Radiation damage and its impact on corrosion in Zirconium-Niobium alloys



Guanze He

Linacre College, University of Oxford

A thesis submitted for the degree of

Doctor of Philosophy

Supervised by:

Prof. Chris Grovenor, Prof. Sergio Lozano-Perez

Hilary Term 2020

Abstract

Zirconium alloys have been successfully used as fuel cladding and structural materials in fission reactors for decades, but the industry's desire to employ high burnup fuels requires an improvement of resistance to in-reactor corrosion. It is therefore essential to understand the mechanisms of radiation-enhanced corrosion of zirconium alloys, and especially why Zr-Nb alloys show improved properties compared to Zircaloys. In order to achieve this goal, the MUZIC-3 (Mechanistic Understanding of Zirconium Corrosion) program was established; a wide collaboration between universities and industrial partners. As part of this program, this project used advanced electron microscopy techniques to investigate in-reactor corroded samples from the Canada Nuclear Laboratory and autoclave corroded samples from Westinghouse.

The characterisation work used the (S)TEM as a primary tool, together with the analytical tools EDX and EELS. The in-reactor samples were Zr – 2.5 Nb samples corroded at 325 °C and 250 °C in the reactor core for 190 days and 2750 days. For comparison, samples corroded in the same primary loop but out of the reactor core, and hence without neutron radiation, have also been studied. In order to further study the mechanism of radiation damage in the metal matrix, in-situ heavy ion radiation in a TEM was carried out on the recrystallised Zr – 1.0Nb and Zr – 2.5Nb alloys provided by Westinghouse™, and proton irradiation was carried out at Dalton Cumbrian Facility (DCF) on as-received Zr – 2.5Nb alloys from CNL. All the TEM samples in this project

were made by Focused Ion Beam (FIB) at either the University of Oxford or the Materials Research Facility (MRF) at the Culham Science Park.

The first section of results presented in this thesis is the characterisation of the metal matrix of the CNL Zr – 2.5Nb alloy. The shape, orientation and number density of radiation-induced Nb precipitates in the α-Zr grains in samples corroded under neutron radiation at 325 °C was analysed. The direct observation of fully coherent Nb nano-precipitates in the α-Zr metal matrix is reported for the first time. A model describing the formation and evolution of the Nb precipitates under neutron irradiation is suggested. The impact on the evolution of the β-Zr phase from the in-reactor conditions is also presented, and it is shown that decomposition from β-Zr to β-Nb is encouraged by neutron irradiation and in-reactor heating.

The second section of the results discusses the mechanisms of radiation damage to the β-Nb SPPs in the metal matrix, as studied by in-situ heavy ion radiation. It was found that due to the combined effect of radiation-induced mixing and local diffusion of solute Nb atoms, the β-Nb SPPs stay very stable under irradiation up to 40 dpa and show very limited Nb redistribution between the SPPs and α-Zr metal matrix. Reasons for the remarkable stability of these Nb-rich phases under radiation are discussed. The characterisation of proton irradiated Zr – 2.5Nb samples is also presented. The results help to understand the mechanisms of radiation-induced Nb precipitation under a

variety of conditions.

The third section presents a study of the corrosion of the decomposed β-Zr regions in the oxide. This is a systematic study of the corrosion behaviour, including morphology changes, oxidation rates of the Nb in the β regions, redistribution of the Nb, and the relation with the formation of other microscopic features such as micro cracks. It is shown that the longer these β regions stay in the metal under neutron radiation, the more decomposed from β-Zr to β-Nb phase they become, and the slower that these regions are oxidised.

With all these factors combined together, the reasons for the improved resistance of the Zr-Nb alloys to in-reactor corrosion is discussed.

Declaration

The research described in this thesis was carried out by the author in the Department of Materials at the University of Oxford between October 2016 and March 2020, under the supervision of Prof. Chris R. M. Grovenor and Prof. Sergio Lozano-Perez. All of the work is original, and where the work of others is included, it has been referenced and acknowledged. No part of this thesis has been submitted for any other degree at this university or elsewhere.

Journal Publication and Conference Presentations

Parts of this thesis have been or plan to be published in peer-reviewed journals.

- He, G., Liu, J., Li, K., (...), Lozano-Perez, S., Grovenor, C., Investigating the stability of second phase particles in Zr-Nb alloys under irradiation, 2019, *Journal of Nuclear Materials*, 526
- He, G., Nordin, H., (…), Lozano-Perez, S., Grovenor, C., The in-reactor corrosion of β-Zr phase in Zr-2.5Nb alloy and its impact on corrosion, to be submitted
- He, G., Karamched, P., (…), Lozano-Perez, S., Grovenor, C., The distribution of radiation induced β-Nb precipitates and its stability in reactor core condition, to be submitted.
- Liu, J., He, G., (…), Lozano-Perez, S., Grovenor, C.R.M., Ex-situ and in-situ studies of radiation damage mechanisms, 2019, *Zirconium in the Nuclear Industry, 19th international syposium*.

- Liu, J., (...), He, G., Lozano-Perez, S., Grovenor, C.R.M., Mechanism of the α-Zr to hexagonal-ZrO transformation and its impact on the corrosion performance of nuclear Zr alloys, 2019, *Acta Materialia*, vol 179
- Liu, J., He, G., (...), Lozano-Perez, S., Grovenor, C., Irradiation-induced amorphization in the zirconium suboxide on Zr-0.5Nb alloys, 2019, *Journal of Nuclear Materials*, vol 513

Selected conference presentations

- G. He, et al., Neutron Radiation Damage of β Phase and its Impact on In-core Corrosion of Zr-Nb alloy, TMS Annual Meeting & Exhibition, 2020, San Diego, US.
- G. He, et al., Radiation damage and corrosion in zirconium alloys, Chinese Materials Conference 2019, Chengdu, China.
- G. He, et al., High-resolution imaging of neutron radiation-induced nano features in fission and fusion materials, Microscience Microscopy Congress 2019, Manchester, UK
- G. He, et al., In-situ TEM observation of second phase particles in zirconium alloys under 1MeV Kr ion irradiation, The 5th Workshop On TEM With In Situ Irradiation, 2018, Huddersfield, UK

Acknowledgement

First, I would like to express my most sincere thanks to my supervisors, Professor Chris Grovenor and Professor Sergio Lozano-Perez, for the great support and guidance through my entire project. It is not always an easy journey pursuing a DPhil degree. There can be as much self-doubt and frustration as happiness from progress and achievements. But the meetings with Chris and Sergio, even a simple chat with several words, can always be cheerful and inspirational. Chris has also provided so many precious opportunities and resources for me to try something of interest, and the outcomes contribute to a good portion of this thesis. I still remember the long hours Sergio spent with me sitting in front of the NVision, 3000F and ARM when he taught me how to use them from the very beginning with every small detail.

I would thank the MUZIC community members for the always friendly discussion and help, especially Dr. Heidi Nordin, Dr. Sousan Abolhassani, Prof. Michael Preuss, Dr. Philipp Frankel, Prof. Arthur Motta, Prof. Adrien Couet, Dr. Suan Otner, Dr. Patrick Burr, Mr. Jonathan Hawes and so on. Special thanks to Dr. Magnus Limback, Dr. Havier Romero and Dr. Jonna Partezana for the great support and excellent work for organising many successful MUZIC meetings.

I have been lucky enough to get access to many advanced facilities all over the world during my project, and always received warm help from the host. These include Dr. Meimei Li, Dr. Mark Kirk, Ed Ryan, Pete Baldo at IVEM Argonne National Lab, Prof. Steve Donnelly, Dr. Jonathan Hinks, Dr. Graeme Greaves, Dr. Anamul Haq Mir at

MIAMI2 facility, Dr. Mohsen Danaie at ePSIC Harwell Science Centre, Dr. Samir de Moraes Shubeita at DCF, and Mrs. Kate Breach, Dr. Alex Cackett, Dr. Monica Jong at MRF Culham Centre. I wouldn't be able to finish my DPhil thesis without your help.

Thanks to the staff at DCCEM who have helped me a lot in the lab, Dr. Neil Young, Dr. Gareth Hughes, Dr. Ian Griffiths, Mrs. Jennifer Holter and Mr. Graham Wyatt.

I would express my special thanks to my MUZIC teammates Dr. Junliang Liu and Ms. Anne Callow. We worked, travelled, attended meeting together for so many times in the last three and a half years, making it such an unforgettable journey.

There have been many inspring discussions and help on specific techniques during my project. I'd like to thank Dr. Kexue Li, Dr. Hongbing Yu, Dr. Phani Karamched, Dr. Jack Haley, Dr. Zhao Shen, Dr. Aakash Varambhia, Dr. Carmen Makepeace, Dr. Jing Hu, Dr. Thomas Aarholt, Dr. Jiale Wang, Dr. Andy London, Mr. Naganand Saravanan. And I'd like to thank many friends in the department for the friendly yet inspirational chat, Mr. Ed Roberts, Mr. Xiaonan Luo, Mr. Yatir Liden, Mr. William Iliffe, Dr. Yang Chen and so on.

Thanks to my friends Dr. Bing Tian, Ms. Sha Li, Mr. Mark Quinlan, Ms. Mariko Nakahara for all the cheering, encouragements and relaxing time we spent together.

I would express my deepest gratefulness to my parents and Qian's mother. I can never finish my thesis without your eternal support.

Finally and most importantly, to my dear wife Qian Xiao, it is your love and understanding that encourages me to make it today.

Table of Contents

Abstract 1

Declaration 4

Acknowledgement 6

Table of Figures 13

Chapter 1 Introduction 26

1.1 Zirconium alloys in the nuclear industry 26

1.2 Zirconium Metallurgy 27

1.3 Different types of zirconium alloys 29

1.3.1 Zircaloy-2 and Zircaloy-4 30

1.3.2 Zirconium-niobium alloys 30

1.4 The MUZIC3 project 34

1.5 Objectives 35

Chapter 2 Literature Review 38

2.1 Corrosion of zirconium alloys 38

2.1.1 General observation, mechanisms, and kinetics 38

2.1.2 Oxide microstructure 42

2.1.3 The corrosion of the Second Phase Particles (SPPs) and β-Zr phase 52

2.2 Radiation damage in zirconium alloys 55

2.2.1 Radiation damage in α-Zr metal matrix 56

2.2.2 Radiation damage to second phase particles 62

2.2.3 Irradiation induced precipitation in the α-Zr matrix 64

2.4 The radiation enhanced corrosion 67

2.5 Emulating neutron irradiation by ion irradiation 70

Chapter 3 Materials, Instruments and Techniques 73

3.1 Materials used in this project 73

3.1.1 Basic microstructure 73

3.1.2 Neutron Irradiation on the CNL Zr – 2.5 wt% Nb alloys 75

3.1.3 Corrosion kinetics of the CNL Zr – 2.5 wt% Nb alloy under reactor conditions 76

3.2 Instruments used in this project 79

3.2.1 Sample preparation by Focused Ion Beam 79

3.2.2 (Scanning) Transmission Electron Microscopy 83

3.2.3 High resolution imaging by TEM and STEM 86

3.2.4 Energy Dispersive X-Ray analysis (EDX) and Electron Energy Loss Spectroscopy (EELS) 87

3.2.5 In-situ irradiation in a TEM 91

3.3 Characterisation techniques used in this project 93

3.3.1 Characterisation of radiation damage in Zr metal by TEM 93

3.3.2 Qualitative and Quantitative analysis by EELS 98

Chapter 4 Neutron Radiation Damage in Dual Phase Zr-Nb alloy 103

4.1 Damage in the α-Zr matrix 104

4.1.1 Radiation-induced Nb precipitates in the α-Zr matrix 104

4.1.2 Dislocation loops 123

4.1.3 The impact on the corrosion of the alloy 125

4.2 Damage in the β phase regions 128

4.2.1 The morphology and microstructure of the β phase 128

4.2.2 The evolution of the β phase under reactor conditions 141

4.2.3 Summary 144

Chapter 5 Emulating neutron radiation damage in the zirconium metal matrix by ion radiation 146

5.1 Investigating the stability of β-Nb SPPs under radiation by in-situ heavy ions 147

5.1.1 Experimental Details 147

5.1.2 Experimental results 157

5.1.3 Discussion 162

5.2 Replicating neutron irradiation induced damage by proton irradiation 171

5.2.1 Irradiation campaign and sample preparation 172

5.2.2 Characterisation of the proton irradiated B166 sample 174

5.2.3 Discussion 175

5.3 Summary 179

Chapter 6 In-reactor corrosion of CNL Zr-2.5Nb alloys 180

6.1 Methods used to study the corrosion of the β phase regions in oxide 183

6.2 Characterisation by STEM HAADF images and EELS 189

6.3 Discussion 201

6.3.1 The corrosion of the β regions in the oxide 201

6.3.2 The oxidation of Nb under different reactor conditions 209

6.3.3 The formation of micro-cracks associated with the β phase 213

6.3.4 The influence of the β phase on the general oxidation of the material 217

6.4 How do the in-reactor conditions change the oxidation of the alloy? 221

Chapter 7 Conclusions and Suggestions for Future Work 222

7.1 Summary of key findings 222

7.2 Suggestions for future work.....226

Table of Figures

Figure 1.1 LWR Fuel assemblies [5] 27

Figure 1.2 Phase diagram of pure zirconium at different pressures and temperatures [9] 28

Figure 1.3 Schematic of hcp cell with some important slip planes marked [6].....29

Figure 1.4 Zr-Nb phase diagram [25] 32

Figure 1.5 Optical Micrographs showing the microstructures of Zr-Nb alloys with varying Nb contents and annealing temperatures [27] 34

Figure 1.6 HAADF images and EDX mapping of alloying Nb and Fe elements in (a) recrystalised Zr-1.0Nb alloy and (b) dual phase CNL Zr-2.5Nb alloy [29].....35

Figure 2.1 Development of zirconium based cladding materials by Westinghouse [5] 39

Figure 2.2 Schematic of the oxidation reactions for uniform corrosion [18] 40

Figure 2.3 Schematic of oxide film growth on zirconium alloys [39].....41

Figure 2.4 Crystal structures of zirconium dioxide [45].....43

Figure 2.5 ASTAR phase map for 120-day RXA Zr-1Nb sample (left) and 46-day annealed Zr-1Nb sample (right) [19] 45

Figure 2.6 Cracks in oxides of RXA Zr-1Nb, annealed Zr-1Nb, and ZIRLO alloys [19] 46

Figure 2.7 Schematic distribution of stresses near wavy metal/oxide surface with the directions of stress labelled. Reproduced from [56] 47

Figure 2.8 Schematic of correlation between porosity network and kinetic transition [22] 49

Figure 2.9 Zr-O phase diagram from first principles calculations[63] 50

Figure 2.10 Different zirconium sub-oxides identified at the metal/oxide interface of ZrFeCr alloy [68] 51

Figure 2.11 Different damage in Ni caused by various irradiation species at 1MeV, shown with the PKA energy (ET) and displacement efficiency (ε) [81] 57

Figure 2.12 BF-STEM image showing the increased ordering of a-loops at increased damage level in proton irradiated Zircaloy-2. a) 2.3 dpa, b)4.7dpa, c)7dpa [101] 60

Figure 2.13 c-loops in Zircaloy-4 neutron irradiated to $8.5 \times 1025 neutrons m2$ at 560K [95] 61

Figure 2.14 Transformation from Laves phase $Zr(Fe,Nb)_2$ to bcc β-Nb with partial amorphisation [97] 64

Figure 2.15 Irradiation induced needle like particles in M5 alloy after neutron irradiation to $13 \times 1025 neutrons m2$ [105] 67

Figure 2.16 Radiation enhanced corrosion shown in Zircaloy-4 corroded at 270 °C. [117] 68

Figure 2.17 Illustration of the corrosion of Zr-1.0Nb alloy in and out of reactor [133] 69

Figure 3.1 An SEM image showing the microstructure of the Zr-2.5 wt% Nb alloy in this study. The radial and hoop directions refer to directions relative to the cladding tube.

.....74

Figure 3.2 A STEM HAADF image showing the typical microstructure of the RXA Zr-2.5Nb alloy. The white spots are the β-Nb and Zr-Nb-Fe SPPs. 76

Figure 3.3 Comparison between the in-flux and out of flux samples corroded at different temperatures. (a) oxide growth curve (b) oxide growth rate curve, with the selected samples marked in red. (Data provided by Heidi Nordin, CNL).....78

Figure 3.4 Steps showing the lift-out of a TEM lamella in a FIB. (a) a protective layer of platinum is deposited on the surface of a bulk sample (b) trenches are made on both sides of the lamella. Then the lamella is attached to a micro-manipulator tip, and undercut to detach from the bulk sample, (c) the lamella is then 'lifted-out' by the micro-manipulator, (d) the lamella is attached to a pin on a half grid, then cut loose from the micro-manipulator.....80

Figure 3.5 SEM images showing the different positions and thickness values of TEM samples for different characterisation purposes. Images (a) and (b) show a lamella attached to a vertical edge of the post and thinned to about 50 nm, while (c) and (d) show a lamella attached on a 'V' shape pin and thinned to about 100 nm to 150 nm. 82

Figure 3.6 A schematic showing the different detectors used in STEM.....85

Figure 3.7 A same region shown in (a) HAADF (b) LAADF (c) BF image and another region shown in (d). The different contrasts in HAADF image (a) shows clearly the distribution of Zr metal matrix; Zr oxide, Nb rich β regions and cracks in the sample. The α grains in the Zr metal are best shown in the BF image (c). The contrast generated

by different thickness of the sample is shown in the HAADF image (d). The boundary circled by the dashed line marks the two different thickness regions, the one on the left is thicker and the one on the right is thinner. This thickness difference is an artefact of FIB milling. 87

Figure 3.8 (a) A schematic layout of the detectors for EDX and EELS in a TEM (b) typical spectra of the EDX and EELS signals from a Zr sample 90

Figure 3.9 The layout of two state-of-the-art in-situ radiation TEM facilities. (a) The IVEM at Argonne National Lab, (b) MIAMI2 at University of Huddersfield. Photos courtesy to Junliang Liu. 93

Figure 3.10 Diagram showing a weak beam dark field imaging condition (g, 3-4g) [154]. 95

Figure 3.11 A series of bright field images of the same region with varying s_g values, and the superposition of these images shown in the centre. The background contrasts in the images around the edge are smoothed out for a better presentation of the features of interest. 96

Figure 3.12 Images showing a region under two different g vectors (a) g = 0002 (b) g = $10\bar{1}0$, and (c) shows the Diffraction Pattern at the zone axis. The features in the white rectangle are the same in (a) and (b), thus not a-loops. But those in the white circle are only visible when g = $10\bar{1}0$, thus are a-loops. 97

Figure 3.13 (a) Low loss spectral image of the region of interest, (b) map of t/λ of the region, (c) line profile as shown in (b) 100

Figure 3.14 White lines of Zr L3, L2 edges and Nb L3, L2 edges as fitted in HyperSpy. 102

Figure 4.1 TEM kinematic bright-field images, high resolution STEM ABF image and STEM EDX mapping of the features of interest in a Zr-2.5Nb sample irradiated to 2 dpa at 325 °C. 106

Figure 4.2 Kinematic Bright-Field images showing the distribution of irradiation-induced features in (a) B56, (b) B70 and (c) B74. The circled black dots are radiation-induced Nb precipitates, the features marked by arrows are hydrides, and the features between the dashed lines are c-loops. It should be noted that not all the Nb precipitates have been circled. The vague black features in the background are surface oxide formed on the TEM foils. 108

Figure 4.3 Histograms showing the size distribution of the Nb precipitates found in B70 and B74 along the long and short axes. 109

Figure 4.4 The angle between the long axis and the α-Zr basal plane against the length of the long axis for each precipitate. A 10% error is added to the measurement. 111

Figure 4.5 TEM kinematic bright field images showing the Nb precipitates at g=0002 in (a) and (b) Zr-2.5Nb alloy irradiated to the fluence of $1.03 \times 1026m - 2$, (c) M5^{TM} irradiated to $1.36 \times 1026m - 2$ [105], (d) E110 irradiated to $3.6 \times 1026m - 2$ [166]. 112

Figure 4.6 (a) A series of HAADF images of different defocus values showing a Nb cluster that is fully coherent to the α-Zr matrix. (b) schematic showing the physical

layout of the serial images when taking under STEM (c) the FFT of the cluster and matrix regions. The cluster is in a B70 sample. 115
Figure 4.7 Kinematic bright field (a) and weak beam dark field (b) images showing the same region containing Nb-rich precipitates in a B74 sample. 118
Figure 4.8 Arrhenius plots of the calculated diffusion coefficients of vacancies along the a and c directions [177], with the two irradiation temperatures used in this study marked..... 121
Figure 4.9 Kinematic bright field images showing the neutron irradiated α-Zr matrix in (a) B70 2 dpa (b) B74 25 dpa. The same g = $10\bar{1}0$ was used in both images..... 124
Figure 4.10 HAADF images at different magnification and EDX line-scan showing Nb segregation to a c-loop in B70 (2 dpa)..... 125
Figure 4.11 A HAADF image showing the oxide region near the metal/oxide interface in a B74 sample, together with three EDX maps showing the appearance of the Nb precipitates in oxide 127
Figure 4.12 Different forms of β phase in different alloys (a) Annealed Zr-1.0 wt% Nb by Westinghouse [19] and (c) the microstructure of the beta Zr grain showing the existence of the omega Zr phase, (b) Zr-Excel alloy from CNL [182] and (d) the microstructure of the beta Zr grain containing omega Zr phase [28] 129
Figure 4.13 TEM bright field and corresponding dark field images showing two morphologies of the β phase, (a) and (b) from B70, (c) and (d) from B74. These β phase regions are found in the metal matrix at the boundary of two α-Zr grains. The dark

contrast (in the bright field images) found in the α-Zr grains are assumed to be surface oxides. 133

Figure 4.14 Cuboidal shape of ω-Zr phase in (a) EXCEL [28] (b) Zr-20Nb alloys [187] 134

Figure 4.15 (a) HAADF image showing a β region in the B70 sample, (b)(c)(d) are components identified by decomposing the low loss spectrum image via PCA and ICA, (b) represents α-Zr, (c) represents β-Nb, and (d) is not identified so I assume it to be the untransformed β-Zr. The spectra corresponding to these components are shown in (e). 136

Figure 4.16 An ω bearing β-Zr grain and its neighbouring α-Zr region, from sample N-3 (Zr - 1.0 wt Nb) which was annealed at 720 °C for 24h. The components are shown in the HAADF image and their corresponding spectra are shown below. 137

Figure 4.17 HAADF images (a) and (d) show the two types of β phase regions commonly seen in the irradiated and unirradiated CNL samples Zr-2.5Nb samples, (b) and (e) show the atomic ratio of Nb to (Nb + Zr), and (c) and (f) show the corresponding values along the selected lines shown in (b) and (e). 139

Figure 4.18 A schematic showing the evolution of β-Zr grain to form β-Nb and α-Zr 140

Figure 4.19 Distribution of the (a) maximum thickness and (b) Nb weight percentage of the β phase regions in different samples 143

Figure 5.1 Typical Nb line-scan profile and the fitted curve of across a β-Nb SPP. The

radius of the SPP is calculated to be 44.5 nm. 151

Figure 5.2 A series of TEM-BF images showing the same region in a sample irradiated by 1MeV Kr ions to 20 dpa at 623K. Two beam condition with g=[0002] was used for the BF images. The straight black lines in the right-hand grain that start to appear at 5 dpa are c-loops. 153

Figure 5.3 HAADF images showing the position of the EDX line-scans taken of the same SPPs before and after irradiation by 1MeV Kr ions to 15dpa at 293K. 155

Figure 5.4 An example of monitoring a single β-Nb particle before and after irradiation by 1MeV Kr ions at 293K. (a) BF image and (b) SADP at 0dpa, (c) BF image and (d) SADP of the same particle after 15dpa. 158

Figure 5.5 Averaged values of the size of β-NB SPPs before and after irradiation at 4 different temperatures, and the percentage size changes. The error bars of the average size of the SPPs represent the estimated errors of the size measurement as described in section 2.4, and the error bars of the relative size change are derived values from the propagation of uncertainty equations. It should be noted that the average size only stands for the particular SPPs investigated in this study, not the general average size of the SPPs in this material. 159

Figure 5.6 Typical EDX line-scan profiles of the Nb Ka signal for SPPs irradiated at (a) 293K, (b) 623K, (c) 873K. Compared to the data at 293K and 873K, more obvious mixing can be seen at the periphery of the SPP at 623K. 160

Figure 5.7 Average value of absolute size changes in β-NB SPPs measured along a and

c directions in the Zr matrix after irradiation to different damage levels at 623 K. The errors of the size change come from the uncertainties in measurement and line-scan profile fitting, as discussed in section 2.4. The errors in dose represent the uncertainties of the damage dose measurement during the in-situ irradiation session. An error of ± 10% in dose is assumed. 162

Figure 5.8 NanoSIMS depth profiles for Nb in the lower half of TEM thin foils irradiated to 20 dpa at 293, 623 and 873 K. The black dashed line indicates the approximate position of the sample surface. The bottom surface of the foils shows Nb segregation only in the 2 samples irradiated at 623 K, and a reduction of counts in the metal bulk..... 166

Figure 5.9 A schematic showing the position of the lift-out TEM lamella with respect to the distribution of the damage profile created by the protons 173

Figure 5.10 The measured temperature of the B166 disc irradiated to 2 dpa 173

Figure 5.11 TEM images showing the microstructure of (a) as received B166 without any irradiation (b) B166 irradiated by protons to 2 dpa..... 175

Figure 5.12 Kinematic bright field images show two grains in proton irradiated B166, (a) and (b), at g = 0002. (c) is from a region in (a), and (d) is from a region in (b). . 176

Figure 6.1 HAADF images (a) and (b) show the morphology of different types of β-Nb in oxide. (a) was taken from a B56 sample and (b) was taken from a B74 sample. (c) shows a β-Nb grain in a B74 sample, consisting of two parts. Diffraction patterns (d) and (e) were taken by nano-beam diffraction in TEM to show the microstructure of the

β-Nb regions circled in 1 and 2 in image (c). 184
Figure 6.2 HAADF images showing the β regions in oxide and the positions where the spectra are extracted (red square) 187
Figure 6.3 Schematic life of β region during in reactor corrosion. The decomposition process in the metal is not illustrated in this image 188
Figure 6.4 An example showing how the oxidation time is determined for a β region D (um) from the metal / oxide interface. The horizontal dashed line corresponds to the total thickness of the oxide grown in time t1. The data points were measured at each time interval during the in-reactor corrosion test. 189
Figure 6.5 HAADF images showing the oxide formed on the samples B74. The layered β-Nb strips in the metal, β-Nb strip newly incorporated in the oxide, and the cracks in the oxide are shown in images on the right 192
Figure 6.6 3D plot of the edge shift of the (a) Zr and (b) Nb in the β phase against time in oxide and damage received in metal 193
Figure 6.7 Oxidation of Nb in β regions plotted against time in the oxide in B74. The labelled yellow circles indicate the typical regions shown in Figure 6.8. 194
Figure 6.8 Typical β regions at different stage of oxidation. (A1) to (E1) are the HAADF images and (A2) to (E2) are Nb mapping extracted from EELS spectral images. 195
Figure 6.9 HAADF images showing the oxide formed on B70, and the 'hollowed' β regions are shown in the high magnification image on the right. 196
Figure 6.10 Oxidation of Nb in the β phase against time in the oxide in B70 196

Figure 6.11 HAADF images showing the oxide formed on samples B56. The ‘hollowed’ β regions are shown in the high magnification image on the right. 197
Figure 6.12 Oxidation of Nb in the β region against time in oxide in the B56. 198
Figure 6.13 HAADF images showing the oxide formed on B96 199
Figure 6.14 Oxidation of Nb in the β regions against time in oxide in B96. 199
Figure 6.15 HAADF images showing the oxide formed on B88 200
Figure 6.16 Oxidation of Nb in β phase against time in oxide in B88. 201
Figure 6.17 'Hollowed structure' β regions in metal (left) and oxide (right) with corresponding elemental maps. These two examples are taken from sample B70 (in-flux corrosion at 325 °C for 192 days). The discrete sphere β-Nb particles can be seen in both metal and oxide. The HAADF image of the oxide and the oxygen mapping show that components in the β region other than β-Nb particles are oxidised rapidly. 203
Figure 6.18 (a) HAADF images showing a β phase region with individual particles on the left side and continuous region on the right side, (b) EELS Nb mapping of the region, (c) Nb L3 edge shift mapping, showing the left side is more oxidised than the right side does. The background colour in (c) is arbitrarily set and does not represent the oxidation status. 204
Figure 6.19 A schematic of the oxidation process of the β phase regions at different stages of decomposition, (a) the starting point, completely β-Zr, (b) some degree of decomposition, the appearance of β-Nb and α-Zr in the β phase region, (c) a completely decomposed β phase region, with only β-Nb. 205

Figure 6.20 Nb L3 Edge Shift in crystal and amorphous β Nb regions as shown in Figure 6.1(c). 207

Figure 6.21 HAADF images showing a β region containing only Nb, evidenced by the EELS spectra taken from the surrounding ZrO_2 and the almost pure β-Nb layer 209

Figure 6.22 Comparison of the oxidation rate of Nb in different samples, (a) B70 vs B56, to show the influence of temperature, (b) B70 vs B96 and (c) B74 vs B88 to show the influence of radiation, (d) B88 vs B96 to show the influence of annealing at 325 °C, and (e) B74 vs B70 to show the combined influence of reactor conditions. 213

Figure 6.23 HAADF images showing micro-cracks formation associated with the β phase. (a)-(c) shows the development of micro-cracks formed on discontinuous β-Nb particles, from individuals to an interconnected network, and (d) shows the single crack formed on large β-Nb strip. The images are not from the same sample, just to show typical morphologies at different state. (a) is from B56, (b) is from B96, (c) is from B70 and (d) is from B74. 215

Figure 6.24 (a) A HAADF image (b) Nb EELS quantity map (c) O EELS quantity map showing the metal / oxide interface in B70. The β-Nb strips in red circles have temporarily stopped the progression of the oxide front, while the region in the blue rectangle shows the unstopped oxide front where the β-Nb strip is absent. There are some isolated unoxidised Zr regions in the oxide right above the Metal / Oxide interface. They are thought to be the result of the complex 3D structure of the metal/oxide interface.....218

Figure 6.25 HAADF images showing the metal / oxide interface follows the shape of the β phase regions above them. The upper yellow dashed line in each image is drawn along the lower boundary of the β region, and the lower yellow dashed line is a copy of its upper counterpart and placed close to the metal / oxide interface. 219

Chapter 1 Introduction

1.1 Zirconium alloys in the nuclear industry

Water cooled reactors using uranium-based fuels have been the mainstream technology in the nuclear industry for decades and are still a competitive option for advanced reactor design. In uranium fuelled reactors, fast neutrons generated by fission reactions need to be slowed down to the thermal region to sustain the chain reaction, which is mainly accomplished by the cooling water. For the sake of neutron economy, neutron loss in the cooling process due to other parts is desired to be as low as possible [1]. The service temperature of reactor cores is commonly around 600 to 700 K. As a safety precaution, cladding materials should have a melting temperature well above the service temperature.

Zirconium based alloys have thus been extensively used as cladding and structural materials because of their relatively low neutron capture cross-sections [2] and high melting point temperature [3]. The basic layout of zirconium cladding uranium fuel assembly is shown in Figure 1.1. In service the zirconium-based tubes separate the fuel pellet and primary coolant.

While zirconium-based alloys have a satisfactory service history, they suffer from several degradation processes which limit their in-core performance. Such degradation mechanisms include grid-to-rod fretting, pellet-cladding interaction, corrosion,

hydriding, irradiation-induced creep and growth and so on [4]. Among all these factors, water side corrosion has drawn lots of attention since it is often the life limiting factor of zirconium-based components. Expanding the in-core lifetime of the fuel assembly is driven by the aim of increasing fuel burn-up for better economic performance, hence improving the corrosion resistance of zirconium-based alloys is desired by the nuclear industry.

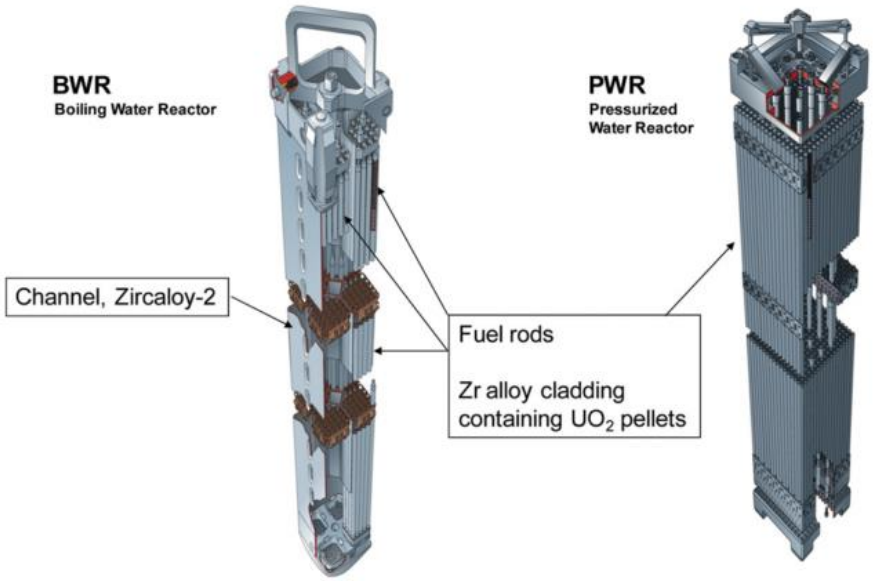


Figure 1.1 LWR Fuel assemblies [5]

1.2 Zirconium Metallurgy

The phase diagram of pure zirconium at different temperature and pressures is given in Figure 1.2. In the pressure range of the service environment, zirconium has two stable phases with different crystal structures; the α phase with the hexagonal closed packed (hcp) structure or β phase with body centered cubic (bcc) structure. The phase boundary

between these two phases is assumed to be around 850 ^{0}C [6]. However, pure zirconium has never been used in the industry due to the inevitable addition of impurities. Some elements are introduced in the manufacturing process, and many elements are added deliberately to improve the property of the alloy [6, 7]. These alloying elements include α phase stabilisers such as Sn, O and β phase stabilisers like Fe, Nb and Cr. The addition of these elements could modify the phase equilibrium of zirconium and affect the properties such as corrosion resistance as well [7]. A more detailed review will be given in Section 1.3.

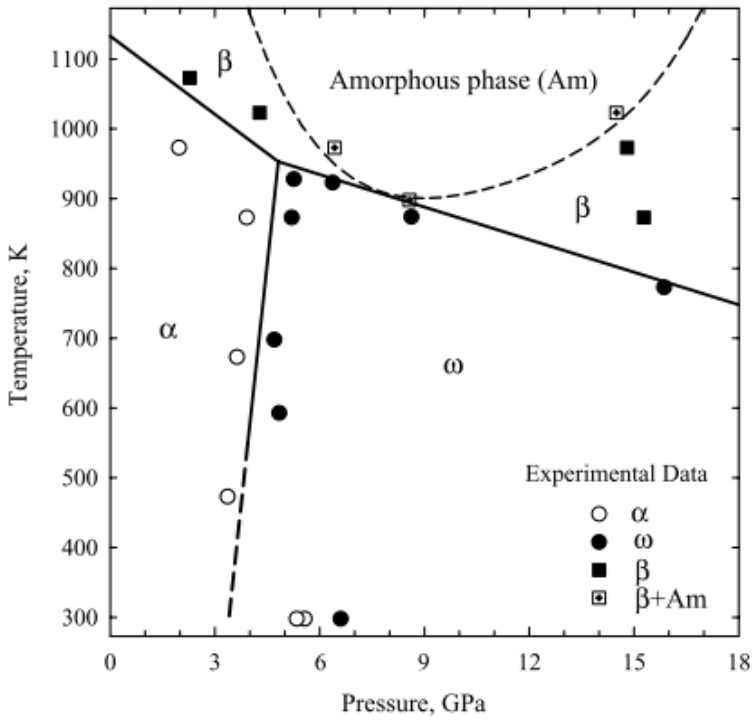


Figure 1.2 Phase diagram of pure zirconium at different pressures and temperatures [9]

In most cases, the properties of zirconium alloys are determined by the hcp structure,

since the α phase is dominant. An elementary cell of α zirconium is given in Figure 1.3. The c/a ratio for zirconium is 1.593, which results in slip taking place on both first-order prism planes and the basal plane. This leads to more complexity of the deformation behaviour in hcp zirconium than those in cubic structures [6]. A more detailed discussion regarding the behaviour of point defects in hcp zirconium induced by radiation will be given in Chapter 2.

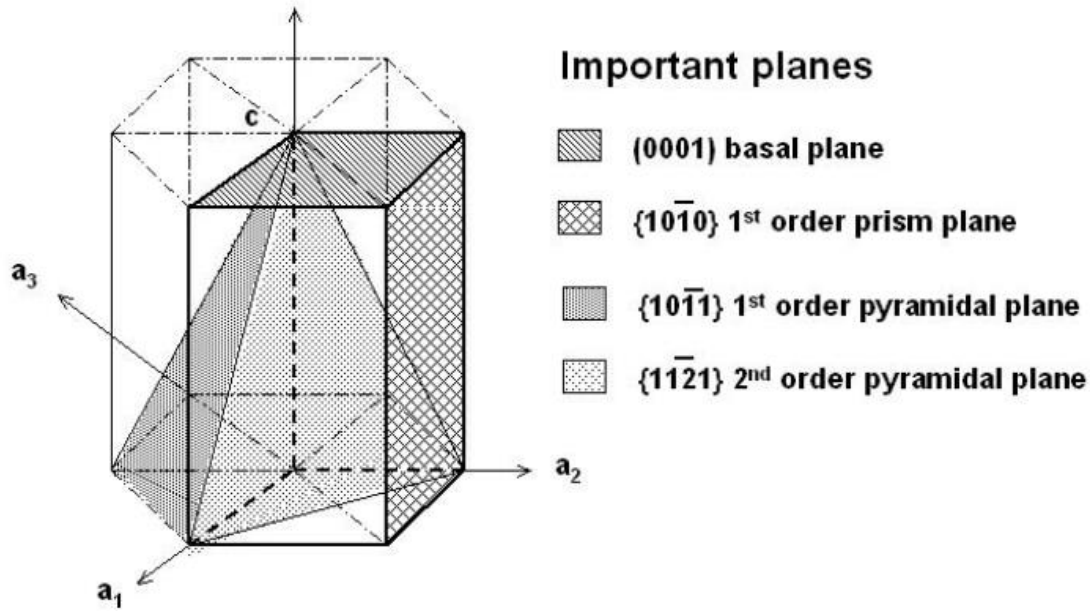


Figure 1.3 Schematic of hcp cell with some important slip planes marked [6]

1.3 Different types of zirconium alloys

After its first introduction by the US Navy in the 1950s and wide spread in the 1960s [3], various types of zirconium alloys have been developed to optimise its in-service performance by adding different types and concentrations of alloying elements into

pure zirconium. Some typical alloys are listed Table 1-1. Based on whether Nb is added, these alloys can be divided into two categories; zircaloys with no niobium content and zirconium-niobium alloys.

1.3.1 Zircaloy-2 and Zircaloy-4

The Zircaloy-2 and Zircaloy-4 alloys feature a relatively high level of tin, as well as iron, nickel, and chromium being the major alloying elements. Zircaloy-2 shows a relatively good corrosion resistance, but nickel results in high level of hydrogen pickup [10]. The improvement was made by replacing nickel with iron to solve the problem, which produced Zircaloy-4 [11]. Zircaloys were widely used to manufacture cladding tubes in both BWRs and PWRs.

1.3.2 Zirconium-niobium alloys

Niobium was added to the zirconium alloy in pursuing new material suited for higher burnup fuels. Examples include E110 and E635 developed in Russia [12], M5 developed in France [13], HANA developed in KOREA[14], Zr-2.5Nb developed and used in Canadian CANDU reactors [15], and ZIRLO and AXIOM by Westinghouse in the USA [16][17]. Zirconium-niobium alloys generally show a good corrosion resistance as the oxide film grows much slower than that in the Zircaloys does [18].

As shown in the phase Zr-Nb diagram, Figure 1.4, the solubility limit for Nb is 0.6 wt%

in α-Zr and about 20 wt% in β-Zr at temperatures lower than 620 °C. Meanwhile, the contents of Nb in commonly used commercial alloys is between 0.8 – 2.5 wt%. As a result, Nb will form precipitates in α-Zr while remaining in solution in β-Zr. The most common precipitates in the α-Zr matrix are approximately spherical β-Nb particles [19]. Such precipitates are also often called second phase particles (SPPs).

Table 1-1 Nominal Composition of Zr alloys [12], [18]–[23]

Alloy	**Application**	**Nominal alloy composition (wt%)**				
		Sn	**Fe**	**Ni**	**Cr**	**Nb**
Zircaloy-2	BWR	1.2-1.7	0.07-0.2	0.03-0.08	0.05-0.15	-
Zircaloy-4	PWR /CANDU	1.2-1.7	0.18-0.24	-	0.07-0.13	-
M5	PWR	-	0.04-0.06	-	-	1.0
ZIRLO	PWR	0.9-1.2	0.1	-	-	1
E110	VVER /RBMK	0	0.006-0.012	-	-	0.95-1.05
E635	VVER /RBMK	1.2-1.3	0.34-0.40	-	-	0.95-1.05
Zr-2.5Nb	CANDU	-	<0.15	-	-	2.4-2.8

Iron is also a common alloying element seen in zirconium niobium alloys and has very

low solubility in α-Zr (~ 0.01 wt%) [24]. A former DPhil student at Oxford, Brian Setiadinata has used atom probe tomography (APT) to study several Zr-1.0Nb samples containing a trace of Fe. According to his study, only around ~ 11 – 12% of the overall iron stays in solution in the matrix, while more iron either forms SPPs or segregates to grain boundaries. As for the iron segregation to SPPs, iron not only forms $Zr(Nb,Fe)_2$ SPPs but also cluster like a halo around β-Nb SPPs [25].

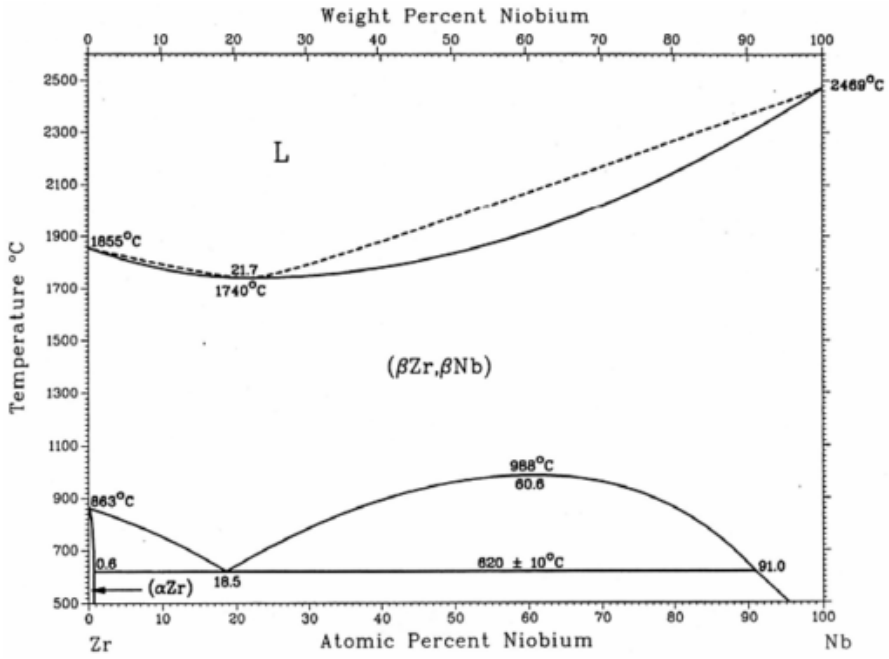


Figure 1.4 Zr-Nb phase diagram [25]

Different fabrication procedures have been applied to produce Zr-Nb alloys with different microstructures. After β quenching, β-Zr phase presents in the alloy, but the β-Zr phase is metastable at temperatures below the monotectoid point and will undergo a decomposition process shown below [26]

$$\beta_{Zr} \rightarrow \alpha + \omega + \beta_{Nb\ enriched} \rightarrow \alpha + \beta_{Nb\ enriched} \rightarrow \alpha + \beta_{Nb}$$

Therefore, the final microstructure of the Zr-Nb alloys is determined by the annealing temperature and content of Nb in the alloy. As shown by Jeong et al., annealing at 570 °C will lead to decomposition of β-Zr and formation of β-Nb in the final structure, while annealing at 640 °C will preserve the β-Zr phase [27], as shown in Figure 1.5.

Based on whether the β-Zr phase presents in the final microstructure, the Zr-Nb alloys can thus be divided into two categories, dual phase alloy with α-Zr and β-Zr both present and recrystalised alloys with only α-Zr presents. Examples of dual phase alloy include the Canadian made Zr-2.5 wt% Nb alloys used in this study and Zr Excel [28]. The alloyed Nb that exceeds the solubility limit in α-Zr mainly stays in the β-Zr phase in these alloys, as illustrated in Figure 1.6.

In comparison, the excess alloying Nb in recrystallised alloys, such as M5^{TM}, ZIRLO, AXIOM etc., mainly stays in the SPPs formed in the α-Zr matrix. In general, there are two types of SPPs; β-Nb SPPs and $Zr(Nb,Fe)_2$ SPPs. It is usually seen that the former type ones are smaller with a round shape while the latter ones are larger, as shown in Figure 1.6.

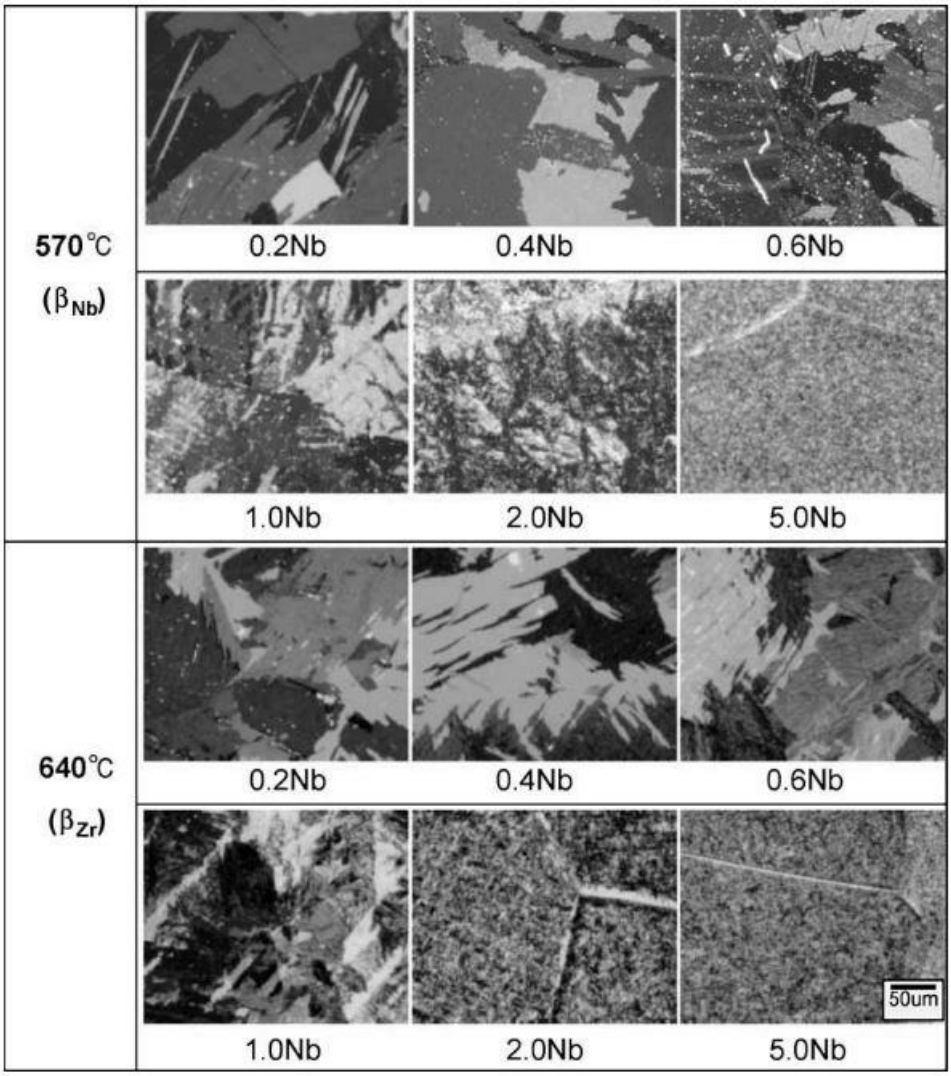


Figure 1.5 Optical Micrographs showing the microstructures of Zr-Nb alloys with varying Nb contents and annealing temperatures [27]

1.4 The MUZIC3 project

In order to better address the degradation problems of zirconium alloys and meet the demand from industry, a consortium called MUZIC (Mechanistic Understanding of Zirconium Corrosion) was founded in 2007. Now it includes academic institutions such as University of Oxford, Manchester and Imperial, Penn State University, Chalmers University, as well as industry leaders such as Westinghouse, EDF and Rolls Royce.

The first and second phases of the project have made a profound contribution to the zirconium research field, generating a large amount of data on some key issues in the corrosion and hydrogen pickup process of zirconium alloys. The kick-off meeting for the MUZIC-3 project was held at Oxford in January 2017. This stage inherits the achievements made in the first and second phase, and aims to make further progress to study the effect of radiation damage on the performance of zirconium alloys. This DPhil project is a part of the MUZIC-3 program.

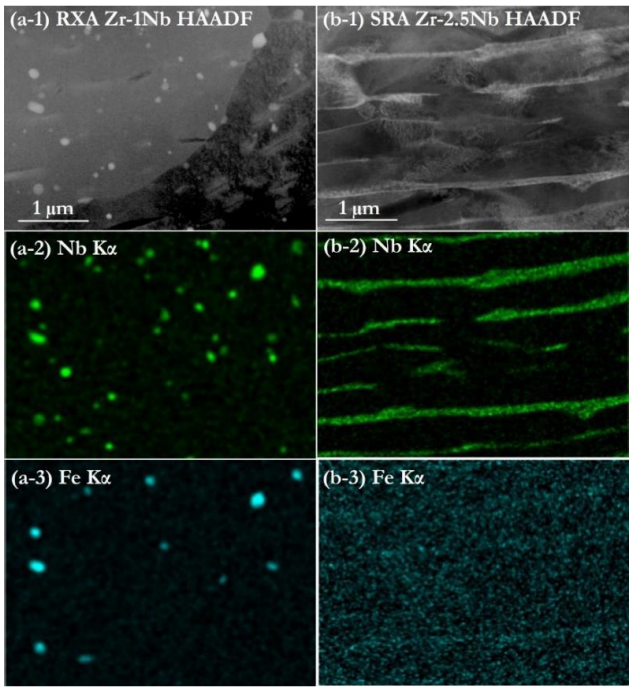


Figure 1.6 HAADF images and EDX mapping of alloying Nb and Fe elements in (a) recrystalised Zr-1.0Nb alloy and (b) dual phase CNL Zr-2.5Nb alloy [29]

1.5 Objectives

The desire of developing high burn-up fuels in modern Water Cooled Reactors requires

the improvement of the in-reactor corrosion resistance of the Zr alloys. As will be discussed in the literature review, the Zr-Nb alloys show a promising resistance to neutron radiation enhanced corrosion, and hence deserve deeper studies on the underlying mechanisms. Among many changing factors that neutron radiation can bring to the material, this project has concentrated on the redistribution of Nb in the metal and oxide during the in-reactor corrosion.

Since a large fraction of the alloying Nb stays in the β phase in the metal in the as-received sample, the evolution of the β phase under reactor conditions is studied. The Zr-Nb alloys also exhibit a unique precipitation of very small (~nm in dimension) Nb rich phases under neutron irradiation. These precipitates will inevitably change the Nb concentration in solid solution in the metal matrix of the samples. These two phenomena occuring in samples corroded in reactor are discussed in Chapter 4.

In addition to the characterisation work carried out on neutron irradiated samples, the Zr-Nb samples irradiated under both in-situ heavy ions and protons are investigated in Chapter 5. Benefiting from the flexibility in settings of the irradiation parameters, this work can help build a deeper understanding of the damage mechanism of the β-Nb SPPs and the formation mechanism of the Nb rich small precipitates in the metal matrix.

In Chapter 6, the corrosion of the β phase in samples corroded in reactor is discussed.

With the aid of state-of-the-art electron microscopy techniques like Electron Energy Loss Spectroscopy (EELS), the oxidation and redistribution of the Nb in the oxide can be studied. Combining the results of Chapter 4 and 6, the impact of neutron irradiation on the corrosion of the samples is discussed.

It is anticipated that with the work presented in this thesis, a deeper understanding of the radiation accelerated corrosion of the Zr-Nb can be achieved, thus helping to develop zirconium alloys with better resistance to the in-reactor corrosion and thus high burn-up fuel designs.

Chapter 2 Literature Review

2.1 Corrosion of zirconium alloys

2.1.1 General observation, mechanisms, and kinetics

Waterside corrosion is one of the major concerns for the in-core performance of zirconium alloys. The corrosion process features the accumulation of oxide on the water facing surface of the metal. There are different types of morphologies of the oxide observed depending on the oxidation environment, among which the most common three types are uniform, nodular and shadow oxide [21]. While the latter two types are occasionally observed in BWRs, a uniform oxide film is widely observed in PWR, BWR and CANDU reactors [21, 30]. In my study, only the uniform oxidation is investigated and all the terms 'oxidation' in the following texts refer to the uniform oxidation unless specifically clarified.

The oxidation process is assessed by measuring the thickness of oxide film against the time for which the alloys stays in the reactor core. An alloy with poorer corrosion resistance will show a larger thickness of the oxide per unit of time. In the convention of the nuclear industry, time in service is usually replaced by the unit burnup, which represents the utilization of the fuel [31]. The measure is consequently converted to oxide thickness against burnup and is more consistent with the design of advanced fuels and reactors [32]. It is a general desire of the industry that the oxide film remains thin with the increase of burnup. This target is gradually approached with the development

of generations of zirconium alloys, as shown in Figure 2.1. The improvements mainly come from optimizing the chemistry and thermal processing procedures [18].

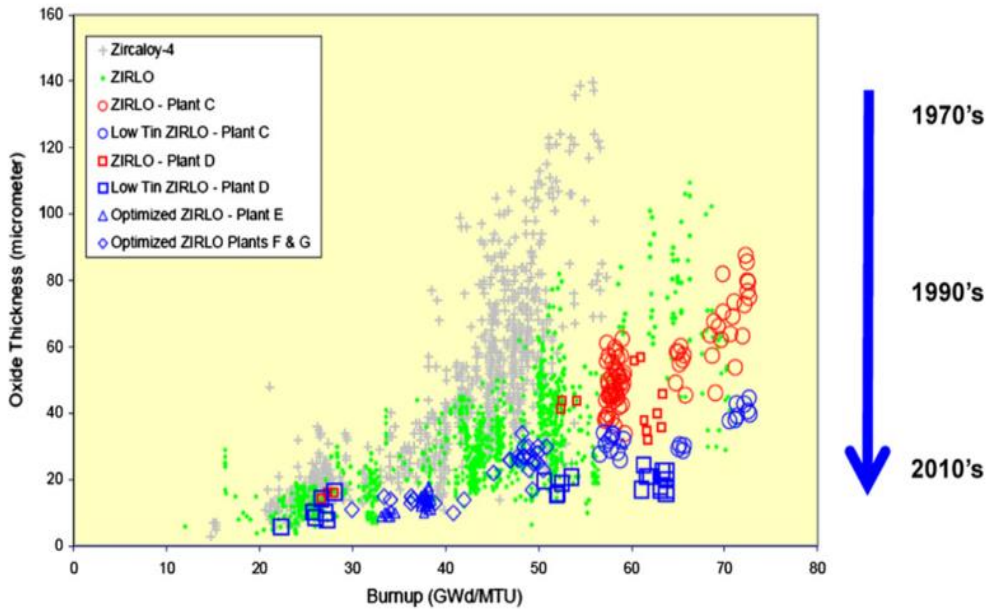


Figure 2.1 Development of zirconium based cladding materials by Westinghouse, the newer generations of the alloys generally show an improved corrosion resistance [5]

In general, the oxidation reaction of zirconium by water can be written as

$$Zr + 2H_2O \rightarrow ZrO_2 + 2H_2$$

This reaction happens instantaneously when zirconium metal contacts the water and an oxide layer forms at the metal/water interface. This oxide layer impedes oxidation by separating the direct contact between metal and water; hence act as a protective layer [33]. Under such circumstances, metallic zirconium is oxidised at the metal/oxide surface while water molecules dissociate at the oxide/water surface respectively. To sustain the overall oxidation reaction, either the zirconium ions or oxidising species needs to be transported through the oxide layer to meet their counterpart. Due to the

nature of zirconium oxide, it is widely accepted that only anions, especially oxygen ions, can diffuse through the oxide by a vacancy mechanism [7, 8]. Furthermore, the diffusion of the anions through oxide is assumed to be the rate controlling factor for oxidation [36, 37].

A model is thus established to illustrate the complete oxidation process, as shown in Figure 2.2.

At the metal/oxide surface, the anodic reaction occurs:

$$Zr + 2O^{2-} \rightarrow ZrO_2 + 2V_O^{2+} + 4e^-$$

At the oxide/water surface, the cathodic reaction occurs:

$$2V_O^{2+} + 4e^- + 2H_2O \rightarrow 2O^{2-} + 4H^+$$

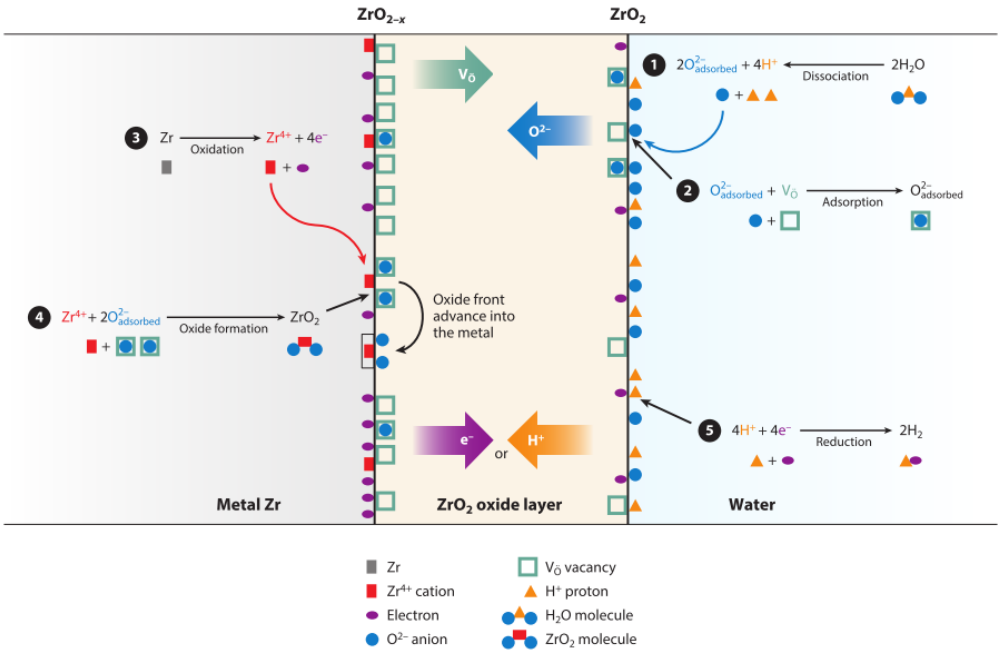


Figure 2.2 Schematic of the oxidation reactions for uniform corrosion [18]

According to this model, the thickness of the oxide should obey a parabolic law [38]. However, this is not always the case. A large number of measurements on the weight gain data during uniform oxidation of zirconium has suggested that the entire process can be roughly divided into three regions [39]. A schematic of this three-step process is shown in Figure 2.3.

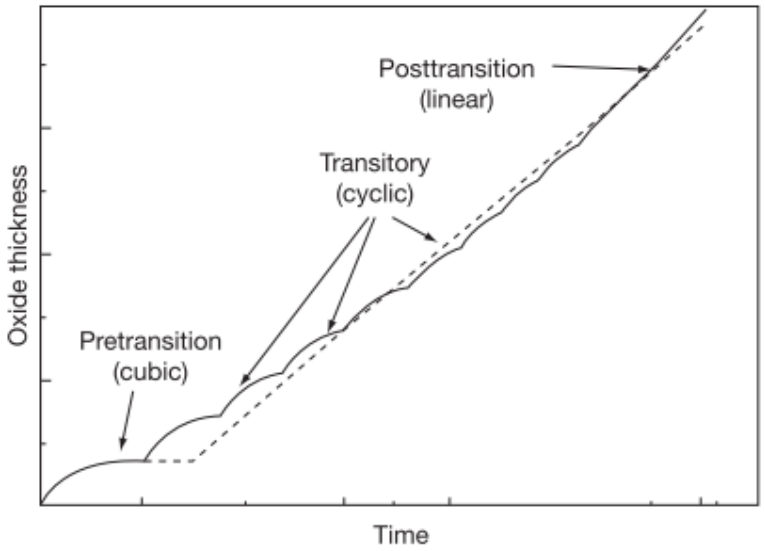


Figure 2.3 Schematic of oxide film growth on zirconium alloys [39]

The first region sees a parabolic or even sub-parabolic growth, like cubic growth for which the oxide thickness shows a ^1/3 dependence on time, as shown in Figure 2.3, corresponding to the oxidation process governed by the Wagner rule. The variances of parabolic and sub-parabolic are found to be related to different types of alloy elements [18]. Nb containing alloys generally show a parabolic growth while Zircaloys containing other alloys usually show a sub-parabolic growth [40, 41]. The slowly

forming oxides in this region are dense and protective regarding the corrosion resistance of the alloy. When the thickness of the oxide reaches some point, the first region transits to a 'transition' region which features the 'breakaway' growth of the oxide. The transition region consists of successive cycles of parabolic growth and in general result in an overall linear nature of the curve [42]. The 'breakaway' growth leads to the oxide layer becoming porous and unprotective. This poor corrosion resistance in turn results in the drastic growth of the oxide layer. The third region, as known as a post-transition region, generally shows a linear growth of the oxide [39].

It is a general desire of the nuclear industry to postpone the occurrence of the breakaway oxide growth as much as possible, as a prerequisite to the pursuit of higher burnup fuel. However, a valid model which could explain the breakaway growth of the oxide thoroughly has not been established. Nevertheless, a huge amount of efforts has been made to unveil such phenomena and many have shown an underlying impact from the microstructure of the oxides. It is thus worthwhile to make an investigation of the microstructural state and evolution of the oxides during the corrosion process.

2.1.2 Oxide microstructure

2.1.2.1 Oxide phases

The only thermodynamically stable phase at the service temperature of zirconium oxide is zirconium dioxide (ZrO_2) [25]. It can exist in three different structures; monoclinic

($m - ZrO_2$ or $\alpha - ZrO_2$) which is stable below 1200℃, tetragonal ($t - ZrO_2$ or $\beta - ZrO_2$) which is stable between 1200℃ and 2372℃, and $\gamma - ZrO_2$ which is face centered cubic and stable beyond 2372℃ up to the melting point [43, 44]. The atomic arrangements for each structure are shown in Figure 2.4.

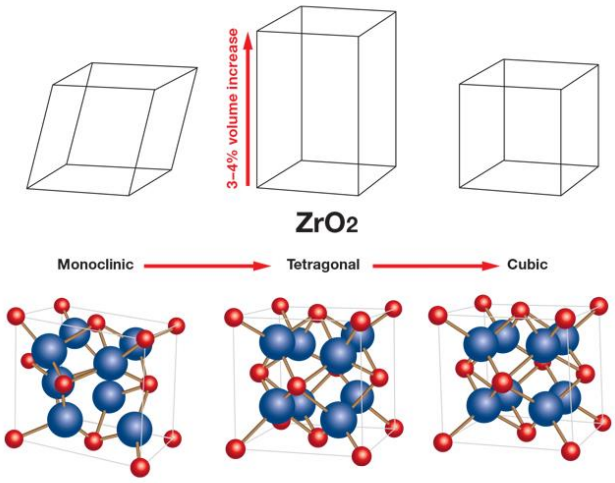


Figure 2.4 Crystal structures of zirconium dioxide [45]

Although tetragonal phase zirconium dioxide is not thermodynamically stable at room temperature or even reactor core temperature, it still exists in the oxide film along with the monoclinic phase [46]. The tetragonal phase is thought to be stabilised by compressive stress in the oxide due to the volume expansion during oxidation (Pilling – Bedworth ratio = 1.55) [47] and the alloying element Sn [48]. Many researchers have shown a preferential formation of $t - ZrO_2$ at the metal/oxide surface and the gradual transition from tetragonal to monoclinic along the direction away from the metal/oxide surface to the oxide/water surface [47–51]. A model has also been proposed to illustrate

the relative existence of tetragonal and monoclinic phases in which two layers coexist in the oxide. The inner layer which is closer to metal/oxide surface is characterised by high fraction of tetragonal phase while the outer layer is dominated by monoclinic phase [52].

It is believed that the distribution of tetragonal and monoclinic phases could affect the oxidation rate [53], with the higher volume fraction of the tetragonal phase the higher the oxidation rate. This is confirmed by the study on Zircaloy-4, ZIRLO and Zr-2.5Nb [54]. A former DPhil student at Oxford, Jing Hu, used the automated crystal orientation mapping (ASTAR) technique on TEM to confirm such behaviour on Zr-1.0Nb alloys as shown in Figure 2.5. The green columnar grains correspond to the monoclinic phase while red equiaxed grains correspond to tetragonal phase. It can be seen that oxide with lower fraction of tetragonal phase (left) has a better corrosion resistance than the one with higher fraction of tetragonal phase (right) [19]. Motta et al. also proposed a model that linked the transition from tetragonal to monoclinic phase to the kinetic transition of oxide growth. They claim that tetragonal phase transforms to monoclinic phase with elongation of the oxide of grains until a critical ratio of 4-5 is reached. This process will repeat in cycles and result in the cyclic kinetic transitions in the corrosion behaviour [55].

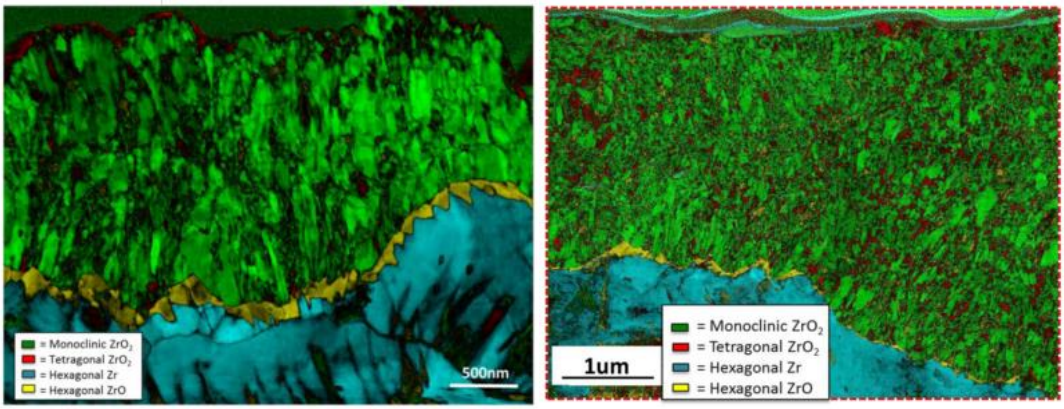


Figure 2.5 A phase map for 120-day RXA Zr-1Nb sample (left) and 46-day annealed Zr-1Nb sample (right) [19]

2.1.2.2 Cracks and Pores

Besides different phases of zirconium dioxide, there are also several important features in the oxide microstructure. These include cracks, pores, sub-oxides and secondary phase particles. They are all thought to have some impact on the oxide growth rate.

Macro cracks are often seen in oxides throughout the entire growth. The most common type is parallel to the metal/oxide surface. A collection of macro cracks in different stages of oxide and types of alloys is given in Figure 2.6. By comparing the crack distribution in the same type of alloy at different times, it can be seen that parallel cracks appear at an early stage of oxidation. After several transitions, parallel cracks group in layers which correspond to the number of transitions. Another important conclusion can be drawn on the relation between crack density and oxidation rate by comparing between different types of alloys. It has been clearly shown that materials with higher oxidation rates, have a higher number density of cracks. This conclusion has also been

confirmed on other alloys such as Zircaloy-2 and Zircaloy-4 [52, 56].

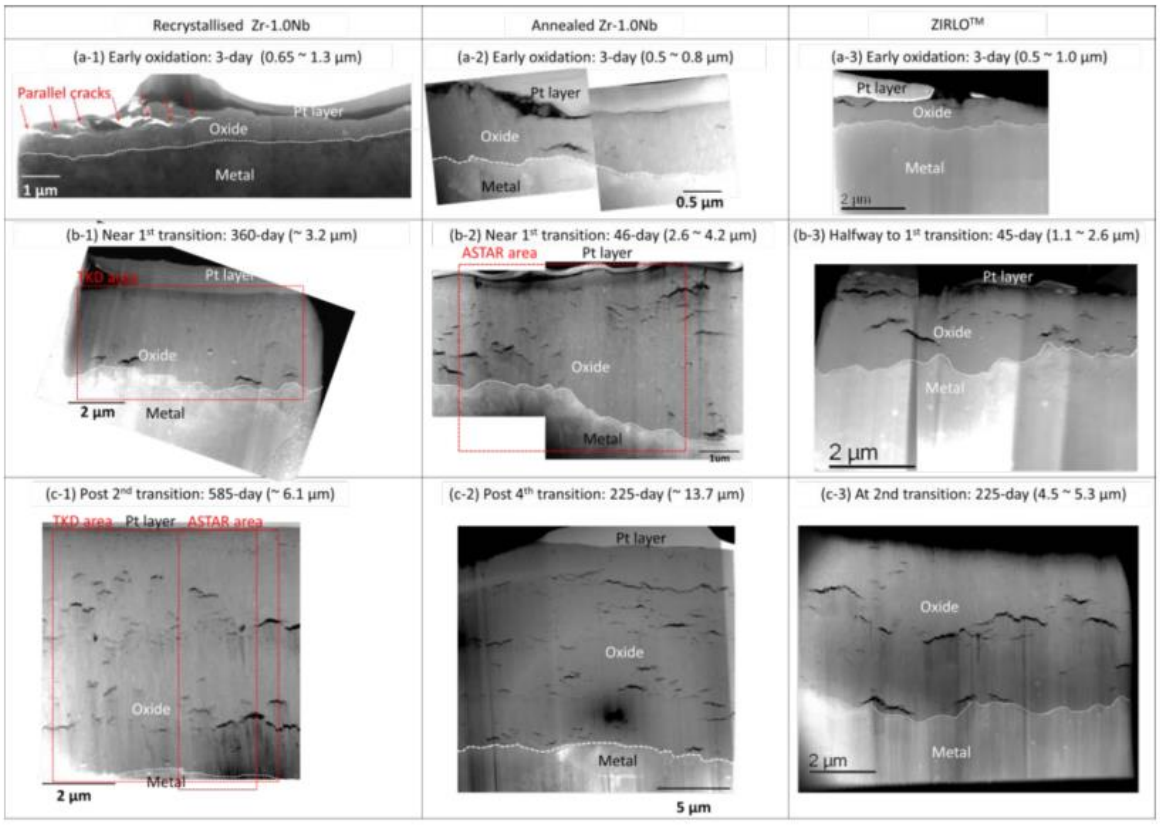


Figure 2.6 Cracks in oxides of RXA Zr-1Nb, annealed Zr-1Nb, and ZIRLO alloys [19]

The formation of these cracks is attributed to the distribution of stress in the oxide. The Pilling-Bedworth ratio of 1.55 and the wavy interface between metal and oxide result in a significant stress difference in different regions of metal and oxide. Stress could be divided into two directions in oxide; parallel and normal to the metal/oxide surface. Parise et al. have established a model to define the local stress in both metal and oxide [57], as shown in Figure 2.7. In the oxide, the parallel stress is always compressive in both convex and concave regions. Meanwhile, the vertical stress is compressive in the

convex region and tensile in the concave region. This vertical tensile stress is believed to be the driving force for the crack formation [56, 57].

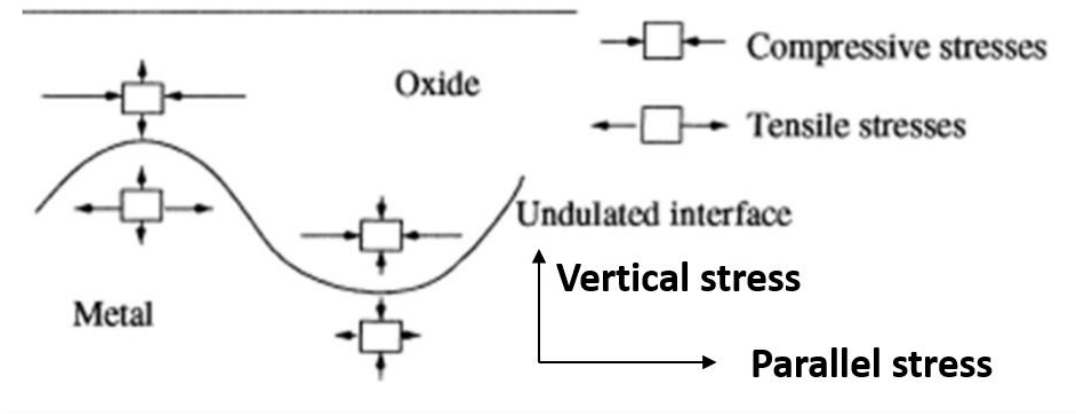


Figure 2.7 Schematic distribution of stresses near wavy metal/oxide surface with the directions of stress labelled. Reproduced from [57]

Due to the correlation between parallel cracks and transition as mentioned earlier (Figure 2.6), researchers in the past suggested that the formation of these lateral cracks are closely associated with the kinetic transition [42, 54, 58]. However, it was later revealed that the formation of these cracks is not correlated with the rapid increase of oxidation rate [59]. Moreover, the authors suggested that these large cracks actually retard the oxidation, as agreed by Yardley et al. with the observation that lateral cracks act as obstacles for oxygen transporting from the oxide/water surface to the metal/oxide surface [60].

Instead of the lateral cracks, small vertical cracks and vertically interconnected pores

are believed to play a vital role in accelerating the oxidation [22]. These features are not easily observed due to relatively low density and small dimensions. They are thought to provide short circuit paths for the oxygen transferring through the oxide [61]. When such short circuit paths connect with each other and with lateral cracks, a network for oxygen transportation is established. This kind of network will let oxygen easily diffuse to the metal/oxide surface and lead to a dramatically increased oxidation rate. According to this mechanism, a positive correlation between porosity density and oxide growth rate could be made, since pores of higher density are more likely to form an interconnected network. This hypothesis has been confirmed by comparing the porosity density of fast corroded annealed Zr-1.0Nb alloy to others by Hu [62]. A model describing the correlation between the formation of such network of porosity and the kinetic transition has been proposed by Ni et al. and shown in Figure 2.8 [22].

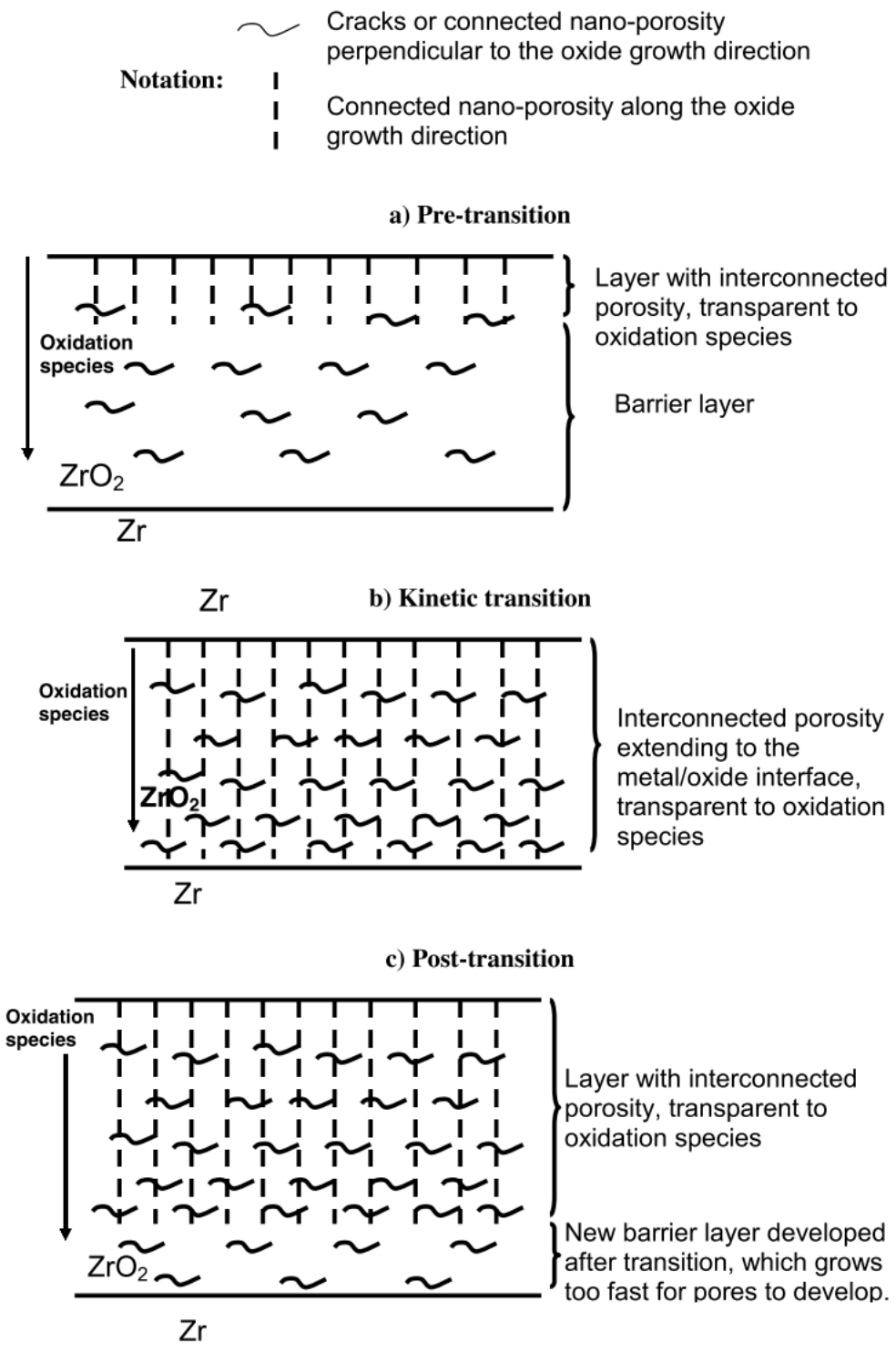


Figure 2.8 Schematic of correlation between porosity network and kinetic transition [22]

2.1.2.3 Sub-oxide

In conventional zirconium-oxide phase diagram, the only thermodynamically stable phase of zirconium oxide is ZrO_2 in the service environment. However, first principles calculations have suggested that combinations of zirconium and oxide with other stoichiometric ratios could also be stable, for instance ZrO [63]. A new phase diagram, which contains much more complex phases was drawn from these first principles calculations and is shown in Figure 2.9. Compared to the zirconium dioxide, many phases on this diagram show a relatively lower content of oxygen. This indicates that such phases might exist between the metal and oxide, where the oxygen activity is lower than that in the bulk oxide.

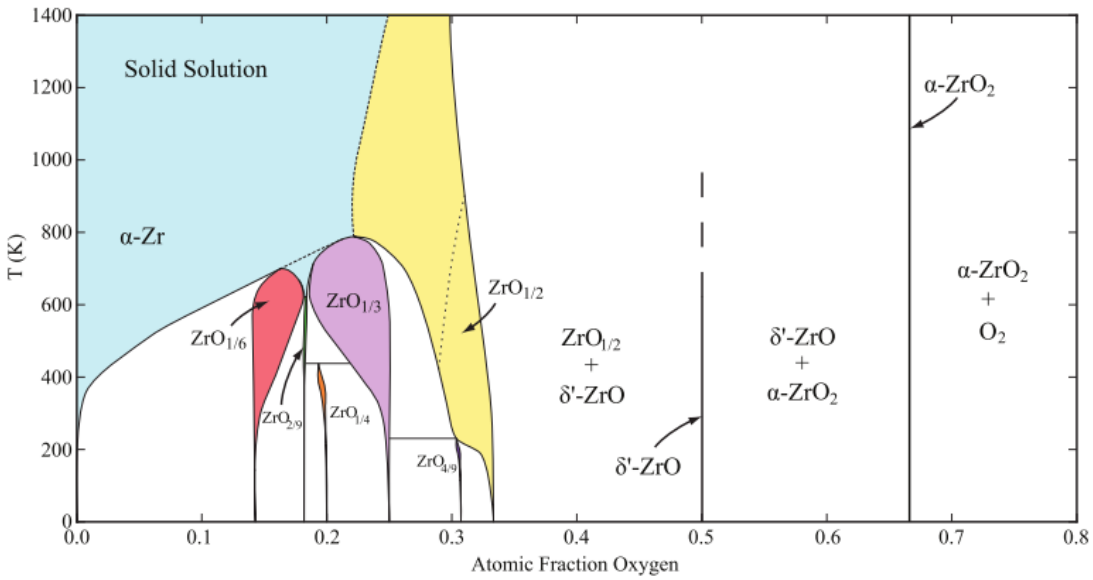


Figure 2.9 Zr-O phase diagram from first principles calculations[64]

Many researchers have identified and characterized a thin layer (~100nm) of sub-oxide

at the metal/oxide surface with state-of-the-art techniques such as (S)TEM and atom probe tomography. Alloys that have been identified to have sub-oxide regions include Zircaloy-2 [65], Zircaloy-4 and ZIRLO [66], Zr-1.0Nb [67], and Zr-2.5Nb [54]. It has been identified that various types of oxide phases, with different level of oxygen content, could exist at the metal/oxide surface [68]. The distribution of such phases generally correlates with the gradually variation of oxygen content. The stoichiometric ratio of oxide to zirconium decreases from the oxide region to metal region. An example containing four regions with different oxygen content level is shown in Figure 2.10.

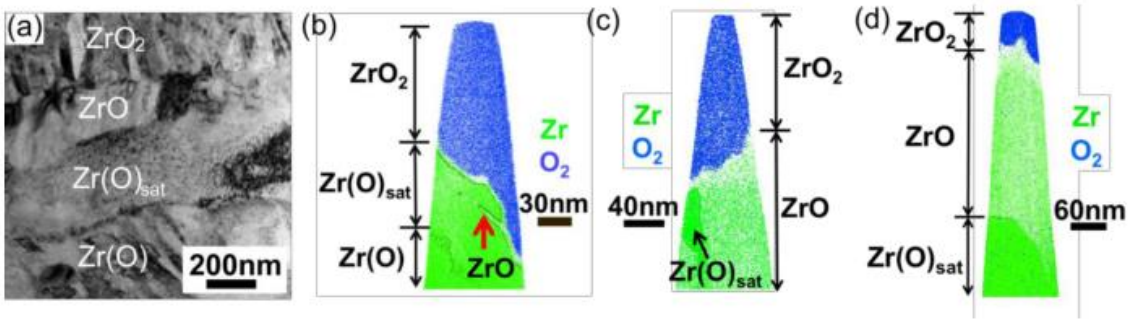


Figure 2.10 Different zirconium sub-oxides identified at the metal/oxide interface of ZrFeCr alloy [69]

Hu et al. have suggested a relation between sub-oxide thickness (ZrO and $Zr(O)_{sat}$) and the oxide growth rate by comparing several types of alloys [19]. It is believed that alloy with better corrosion resistance could form thicker sub-oxides.

2.1.3 The corrosion of the Second Phase Particles (SPPs) and β-Zr phase

The type, size distribution and number density of second phase particles have been shown influential to the oxidation rate of zirconium alloys. Despite this consensus, many reports have suggested that different types of SPPs could lead to great variance in the oxidation behaviour of different alloys. Corrosion experiments conducted on Zircaloy-4 alloy showed that SPPs with larger size (150nm) are beneficial to corrosion resistance [70]. Yet Bojinov et al. showed a slower oxidation rate of Zircaloy-2 was correlated to small SPPs [71]. But this conclusion was contradicted by Tejland et al. who showed that small SPPs could lead to higher oxidation rate of Zircaloy-2 in their work. One possible explanation for this discrepancy is that Bojinov et al mainly discussed the oxidation behaviour before transition while Tejland et al. made their claim regarding the behaviour related to transition. In zirconium-niobium alloys, it has been shown that fine SPPs generally improve the corrosion resistance [19, 72]. In addition, Barberis et al. also showed that a better corrosion resistance could be achieved by increasing the number density of SPPs in the matrix in binary zirconium alloys [73].

Many researchers have proposed different models in order to explain the effect brought by SPPs. From the electrochemical point of view, SPPs are generally nobler than the zirconium matrix and thus serve as the cathodic site when a galvanic reaction pair is formed [74]. This could encourage the preferential oxidation of zirconium metal surrounding the SPPs while allowing the SPPs remain unoxidized, which is confirmed by many publications [25, 68]. Couet et al. used XANES to study the oxidation state of

alloying elements in SPPs and showed that while zirconium is oxidised from the metal/oxide surface, many SPPs remain metallic [76]. Along with the oxidation, an amorphisation process also takes place for the SPPs, as widely observed in Zircaloys, ZIRLO and Zr-Nb alloys [54]. It has been shown that the distances of the amorphous SPPs from the metal/oxide surface (length of time in the oxide) are different for various alloys [54]. A detailed study of the amorphisation of SPPs in Zr-1.0Nb alloys was described in Hu Jing's thesis, showing a process that SPPs transform from crystalline to amorphous with increasing distance from the metal/oxide surface [19]. All these amorphous SPPs were fully oxidised.

The corrosion of the β-Zr phase was studied by Lin et al. in Zr-2.5Nb oxidised in 400 °C steam or 310°C water [77]. Due to the decomposition of the β-Zr in the metal before incorporation into the oxide as discussed in Section 1.3, the corrosion behaviours were discussed separately for β-Zr and β-Nb. It was proposed that the oxidation of β-Zr will lead to the formation of $Nb_2Zr_{x-2}O_{2x+1}$ oxide, and the oxidation of β-Nb will lead to the formation of amorphous Nb_2O_5. For the 'intermedium regime' phase with a varying Nb content higher than the equilibrium Nb concentration in β-Zr and lower than the equilibrium Nb concentration in β-Nb, the oxidation behaviour will be like that of either the β-Zr or β-Nb based on the Nb content. However, due to the limit of available characterisation tools, some important properties such as the oxidation and redistribution of Nb during the process was not presented in detail. Hu Jing has also

studied the corrosion of the β-Zr in annealed Zr-1.0Nb alloy corroded in pure water at 360 °C. It was shown that the β-Zr oxidises relatively fast and the Nb is released to the oxide matrix, but the oxidation process of the β-Zr was not analysed [78].

It should be noted that in addition to the microstructural changes, the redistribution of alloying elements also occurs due to the corrosion of the SPPs and β-Zr phase. It was observed that Nb is released from the SPPs during oxidation [75, 76]. A release of Nb to the oxide matrix from an oxidised β-Zr phase was also reported [19, 81]. A former Oxford DPhil student in MUZIC-2 program, Brian Setiadinata, also made a detailed investigation of the Fe and Nb released to solid solution using atom probe tomography (APT). He has shown that iron segregates to the grain boundaries in metal to form linear features that could be dislocations and clusters, and also the leaching of Nb to the matrix [25]. Yet due to the limited number of APT samples investigated, a valid understanding of Fe and Nb redistribution during oxidation is still lacking.

It has been shown by XANES experiments that these metallic Fe and Nb elements in solid solution also show a 'delayed oxidation' nature like the SPPs do [76]. In the coupled current charge compensation model proposed by Couet et al., these alloying elements in solid solution play an important role in determining the oxidation rate, by creating space charges and providing local electric field to influence the transport of oxidising species through the oxide layer [37].

In general, it is clear that the nature of SPPs and the β-Zr phase could be vital to the oxidation behaviour, by means of both microstructural and microchemical evolution. Therefore, a better understanding of the entire in-service life of SPPs and the β-Zr phase is important for establishment of complete corrosion model of zirconium alloys.

2.2 Radiation damage in zirconium alloys

The energy spectrum of neutrons in fission reactors ranges from the thermal region of tens of meV to fast region of several MeV. As mentioned earlier, zirconium based alloys have relatively low neutron capture cross-sections for thermal neutrons, and hence are a good choice for cladding and structural materials in thermal fission reactors [5]. However, the neutron capture cross-section in the fast region is much higher [2], leading to extensive damage to in-service zirconium structures from this region of the neutron spectrum. Such damage causes significant changes to microstructural and chemical properties and affects the mechanical behaviour of the material. Therefore, the interaction between zirconium based alloys and neutrons with energies higher than 1MeV has always been a key issue of scientific interest to the civil nuclear industry.

In this section, I will start from the basic theories of radiation damage in materials, then move to specific damage behaviour in zirconium based alloys. Both microstructural evolution, for instance the formation of dislocation loops, and microchemical evolution like redistribution of alloy elements will be reviewed. One of the key issues to be

discussed is the radiation induced behaviour of SPPs and the associating chemical changes in the alloy, since this is believed to significantly influence the corrosion and hydrogen pickup behaviour of zirconium alloys [82].

2.2.1 Radiation damage in α-Zr metal matrix

2.2.1.1 Point Defects

When a particle with high energy enters the metal matrix, it will lead to a sequence of events taking place as described below [83]. The incident particle will firstly collide with a lattice atom and transfer some energy to it. If the energy received by the lattice atom is larger than the binding energy between the atom and lattice, this atom will be knocked out from the lattice and become a primary knock-on atom (PKA). The PKA will leave its original site with some momentum and fly through the matrix. Meanwhile, a vacancy is created at the original site of the atom. This interstitial atom and its corresponding vacancy are called a Frenkel Pair. Along the trajectory of the PKA, it will collide with other atoms and transfer some energy to them. These atoms will also be knocked out of the lattice if they receive enough energy. They could also behave similarly to the PKA and might lead to more atoms knocked out from the lattice, which is referred to as a collision cascade. These PKA and other knock-on atoms will lose energy by further collisions and eventually have energy lower than the threshold of the lattice bonding energy. They will eventually terminate as interstitial atoms, which is the end of the cascade process.

It is worth noting that the size of the collision cascade is determined not only by the energy but also by the species of incident particles. For the same type of irradiation particle, higher incident energy will lead to a larger collision cascade. For same incident energy, neutrons and heavy ions will produce larger collision cascades, while light ions such as protons and electrons will produce small collision clusters or even only isolated Frankel pairs, as shown in Figure 2.11.

For the entire sequence of events described above, the primary result of the incident particles is the formation of vacancies and self-interstitial atoms. These point defects will diffuse in the metal matrix and might combine with each other to form more complex microstructural features. Their specific behaviour is vital in determining many effects of irradiation.

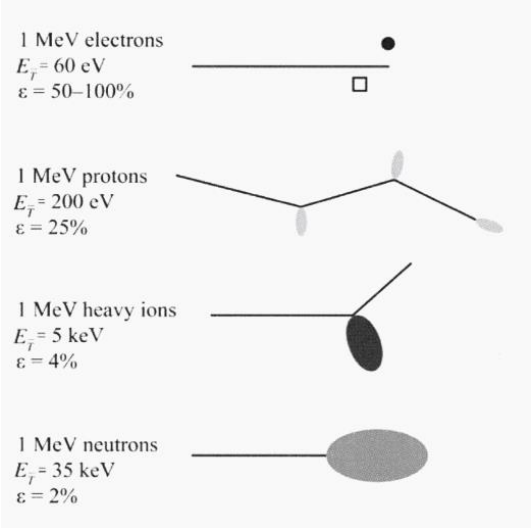


Figure 2.11 Different types and sizes of the damages in Ni caused by various irradiation species at 1MeV, shown with the PKA energy ($E_{\bar{T}}$) and displacement efficiency (ε). Electron irradiation creates Frankel pair, proton irradiation creates small clusters, heavy ion and neutron irradiations create large scale of cascades [83]

In the hcp structure α-Zr, the point defects diffuse anisotropically in different directions [84]. Calculations have shown that diffusion is faster in the basal plane than along the c-direction [6, 7]. Furthermore, Christensen et al. used ab initio and classical simulations to find that SIAs and vacancies diffuse with different rates in the matrix. The order of diffusion rates is; $SIA_{basal} > SIA_{c\ direction} > vacancy_{basal} \sim vacancy_{c\ direction}$ [87]. This anisotropic diffusion of point defects has been described by the DAD (diffusion anisotropy difference) model proposed by Woo et al [88]. It is claimed that this DAD model can successfully explain many radiation induced phenomena related to anisotropic diffusion, such as formation of dislocation loops and irradiation induced growth.

However, some other researchers suggest that the DAD model needs to be modified by considering the contribution of clustering of point defects during diffusion [89]. It has been shown by experiments [90] and simulations [91] that a large fraction of the point defects forms small SIA clusters. Therefore, a model has been proposed based on the PBM (production bias model) by Barashev et al. and is claimed to better explain the features observed in experiments [89].

2.2.1.2 Dislocation loops

The anisotropic diffusion and collapse of point defects results in the formation of dislocation loops in the matrix [92, 93]. Dislocation loops inhabiting different planes

are one of the main features in irradiated zirconium samples, and were observed by TEM decades ago [94]. Two major types are mainly discussed. The first type has a Burgers vector of $\frac{1}{3}\langle 11\bar{2}0\rangle$ and mainly inhabits the prismatic plane $\{10\bar{1}0\}$. It is thus called an a-loop [95]. The second type has a Burgers vector of $\frac{1}{6}\langle 20\bar{2}3\rangle$ and inhabits the basal plane. Thus it is termed a c-loop [96]. These two types of dislocation loop do not appear simultaneously when the metal is irradiated. At a low dose, only a-loops are observed in the matrix while c-loops are absent. At higher dose levels, c-loops start appearing and then increasing in concentration [97].

a-loops

The a-type dislocation loops have been widely found in neutron, electron and ion irradiated samples [94, 98, 99]. It was shown that both interstitial and vacancy loops exist in the irradiated samples, with vacancy loops being elliptical and interstitial loops being more circular. This observation was confirmed by the characterisation of neutron irradiated Zircaloy-2 samples by Northwood et al. [100].

The size and number density of a-loops were shown to be affected by the irradiation dose and temperature. It was demonstrated by Northwood that after an initial increase with dose, both the size and number density saturates at around $10^{25}\, neutrons/m^2$ [101]. Such saturation of loops density was also observed by Griffiths et al. using X-ray diffraction and TEM [102]. In recent research, Harte et al. observed a decrease in

number density at a higher damage level of 7.0 dpa [103]. Temperature can also influence the nature of dislocation loops by affecting the diffusivity of point defects in the matrix. The experiments carried out by Northwood et al. have shown that increasing the temperature would lead to increase of loop size and decrease of number density [100], presumably by increasing the diffusivity of point defects.

The a-loops usually show a clustering behaviour, with loops aligning in rows parallel to the basal plane [104]. Harte et al. have demonstrated that such alignment becomes more significant with increase in the damage level, as shown in Figure 2.12. Such clustering, which features the dark and bright contrast bands parallel to the basal plane, is also termed corduroy contrast [104].

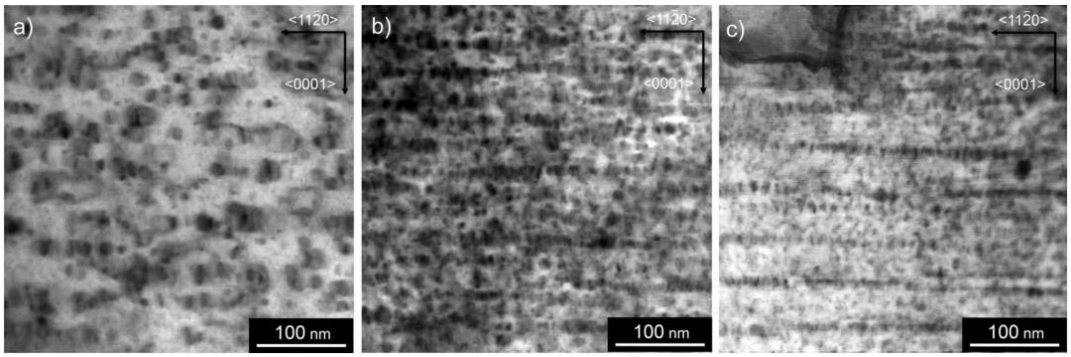


Figure 2.12 BF-STEM image showing the increased ordering of a-loops at increased damage level in proton irradiated Zircaloy-2. a) 2.3 dpa, b)4.7dpa, c)7dpa [103]

c-loops

The existence of c-loops has long been debated and many early researchers concluded

that c-loops do not form during irradiation in zirconium [95, 100]. However, all these experiments were conducted at a relatively low damage level. In later experiments where samples were irradiated to a higher damage level, c-loops were observed and then characterised. These include Jolstons et al. irradiated high purity zirconium to $1.3 \times 10^{25}\, neutrons/m^2$ at 723K [96], Holt et al. irradiated annealed Zircaloy-2 to $6.3 \times 10^{25}\, neutrons/m^2$ at 690K [105], annealed Zircaloy-4 to between $3.5 \times 10^{25}\, neutrons/m^2$ and $8.6 \times 10^{25}\, neutrons/m^2$ at 550-580K [97], and Griffiths et al. irradiated sponge zirconium and Zircaloy-2 and -4 to $6 \times 10^{25}\, neutrons/m^2$ at 644-710K [106]. A typical TEM image of c-loops is shown in Figure 2.13. It has been shown that the number density of c-loops generally increases with the accumulation of radiation damage [102] and they are distributed uniformly in the matrix in most cases [104].

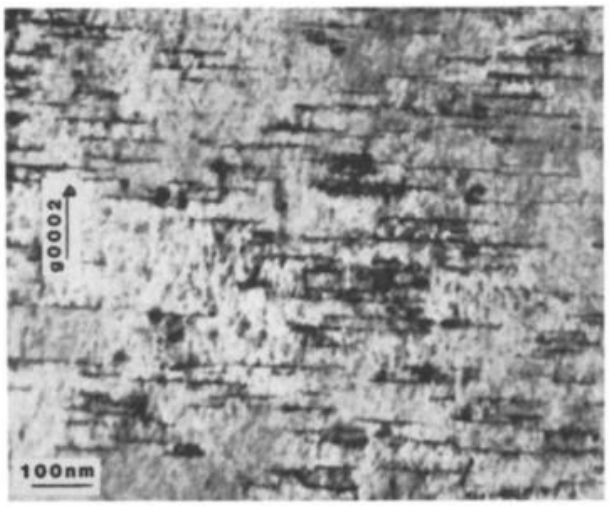


Figure 2.13 c-loops in Zircaloy-4 neutron irradiated to $8.5 \times 10^{25}\, neutrons/m^2$ at 560K [97]

2.2.2 Radiation damage to second phase particles

As discussed in Section 1.3, second phase particles exist in all zirconium alloys and play an important role in determining the mechanical and corrosion behaviour of the alloys. Like the evolution of the zirconium matrix, SPPs also experience microstructural changes during irradiation. In addition, chemical evolution often occurs as well, in the form of redistribution of alloying elements. Therefore, the irradiation impact on SPPs will be discussed in terms of both microstructural and microchemical evolution.

In Zr-Nb alloys before irradiation, there are two types of SPPs existing in the α-Zr matrix. The first is β-Nb with bcc structure and the other type is the Laves phase $Zr(Nb, Fe)_2$ [99, 107]. These two types of SPPs behave differently under irradiation.

Doriot et al. investigated the M5 alloy irradiated in a PWR up to seven cycles. Despite the high damage level, all β-Nb SPPs remained crystalline through the irradiation process [107]. This observation is consistent with results from E110 and E635 alloys [108]. With the accumulation of neutron fluence, the mean size of the β-Nb SPPs increases while the Nb content in the SPPs also drops from 75% to a final value of around 55% [107]. As suggested by Shishov et al. [109] and Kobylyansky et al. [110], the mechanism for this composition change is that Nb atoms are displaced from the SPPs by Zr atoms themselves displaced from collision cascades in the surrounding matrix. These analyses are based on comparisons of the average size of β-Nb SPPs in

initial and irradiated materials rather than the direct observation of the effect of irradiation on individual SPPs, thus might suffer from the possible errors in statistics in the study. The mechanism governing the stability of the β-Nb SPPs under irradiation hence requires further investigation.

Meanwhile, large scale microstructural and microchemical changes were reported for $Zr(Nb, Fe)_2$ SPPs. Doriot et al. reported that the small volume fraction of iron-containing SPPs almost disappeared completely after irradiation, in a material that only contained a few microcrystalline and highly faulted particles deduced to be $Zr(Nb, Fe)_2$ SPPs before irradiation [107]. A more detailed analysis was given in research on E110 and E635 alloys. It was shown that Fe was depleted during irradiation in a similar manner to the process in Zr-Fe-Cr SPPs in Zircaloys [108]. Along with the Fe depletion, the Laves phase $Zr(Nb, Fe)_2$ SPPs transferred into bcc β-Nb SPPs [110]. Shishov et al. studied this transformation by verifying the relative content of Fe and Nb in the SPPs, and showed that the transformation happens if the Fe/(Fe+Nb) content is below 0.3 [111]. In addition to the changes from Laves phase to bcc, some degree of amorphisation was observed at the surface layer of the SPPs [99], as shown in Figure 2.14. A mechanism governing the amorphisation was proposed by Motta et al. [112] suggesting that the depletion of Fe from the SPPs to the metal matrix, due to a new equilibrium concentration of Fe established under irradiation, is the driving force of the amorphisation. However, this is not always the case, especially for irradiation at low

temperatures. Together with other collaborators, I have shown that the amorphisation of the Zr-Nb-Fe SPPs under low temperature in-situ heavy ion irradiation in a TEM does nor require the depletion of Fe [113].

Given all these observations and discussions, the mechanism regarding the evolutions of SPPs under irradiation has not been well explained.

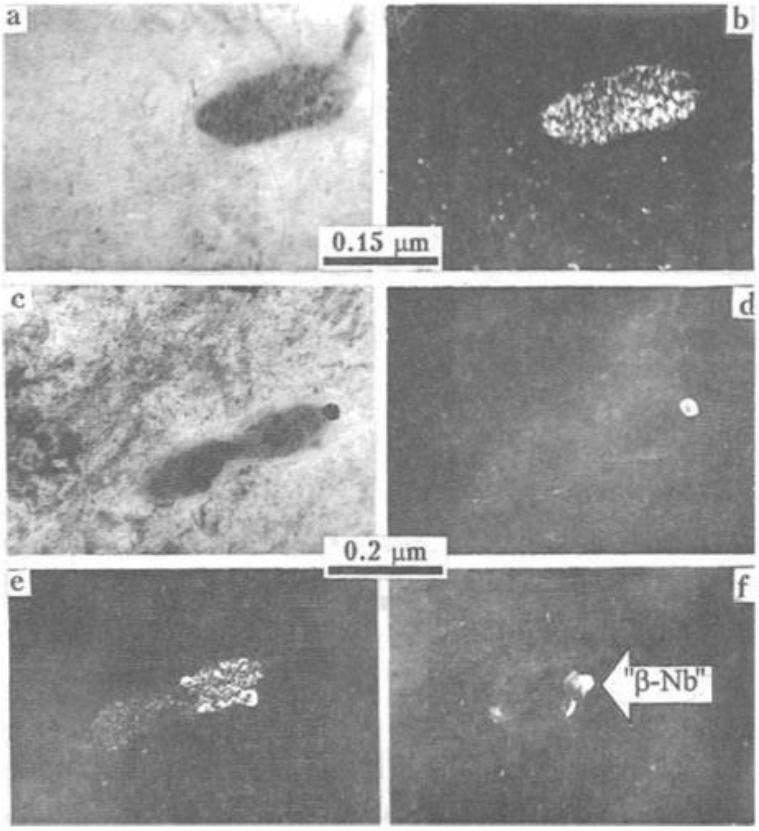


Figure 2.14 Transformation from Laves phase $Zr(Fe,Nb)_2$ to bcc β-Nb with partial amorphisation [99]

2.2.3 Irradiation induced precipitation in the α-Zr matrix

In addition to the evolution of SPPs that already exist before irradiation, irradiation-

induced Nb precipitation is also reported [15, 107, 109]. Due to its low diffusion rate in α-Zr, Nb will become supersaturated in the matrix after heat treatment. During irradiation, the accumulation of defects and the high operating temperature provides extra mobility to the Nb atoms, leading to Nb precipitation [114]. It is reported in the M5 alloy that these precipitates are needle shaped, as shown in Figure 2.15, and appear from the first cycle, that is at a relatively low damage level [107]. Kobylyansky et al. reported similar needle like precipitates in E635 and NSF alloys irradiated by fast neutrons [108]. It was also suggested that such precipitation leads to a Nb content reduction in the Zr matrix even following the dissolution of Nb from the original SPPs [108]. These precipitates were assumed to be bcc β-Nb since they were stable during the post-radiation annealing at 350 °C to 400 °C [107], but a direct observation of the microstructure was not made until recently. Ribis et al. showed in their characterisation work by high resolution TEM that these small precipitates are bcc β-Nb [115]. A similar observation of the microstructure was also reported in the Zr-Nb alloys irradiated by protons at 350 °C [116]. However, the Nb precipitates found in the proton irradiated samples were much larger than those found in the neutron irradiated samples, leading to some doubt on the reliability of direct comparison of these results.

The formation mechanism of these radiation induced Nb precipitates is not well defined. Although some ab-initio simulation work [117] suggested that these precipitates form following an 'in-situ conversion' path 'α-Zr → β-Zr → β-Nb', this path was

contradicted by some other researchers who believed the formation process is 'α-Zr → α-Nb (hcp) → β-Nb' based on the predicted existence of the hcp Nb precipitates from a micro-mechanical point of view [118]. Unfortunately, neither of these two assumptions have been validated by direct observation by electron microscopy, leading it to be an interesting question for discussion.

These precipitates generally grow with the accumulation of radiation damage, but the mechanism is not clearly revealed. Recent characterisation work on the proton irradiated precipitates suggested that the lattice mismatch between the precipitates and the surrounding α-Zr matrix has introduced strains that enhances the diffusion of Nb atoms in local solid solution towards the precipitates [116]. However the size distribution discrepancy between the neutron-induced [107, 108] and proton induced [116] has led to a question that whether this mechanism is also the dominant factor in the neutron irradiated cases.

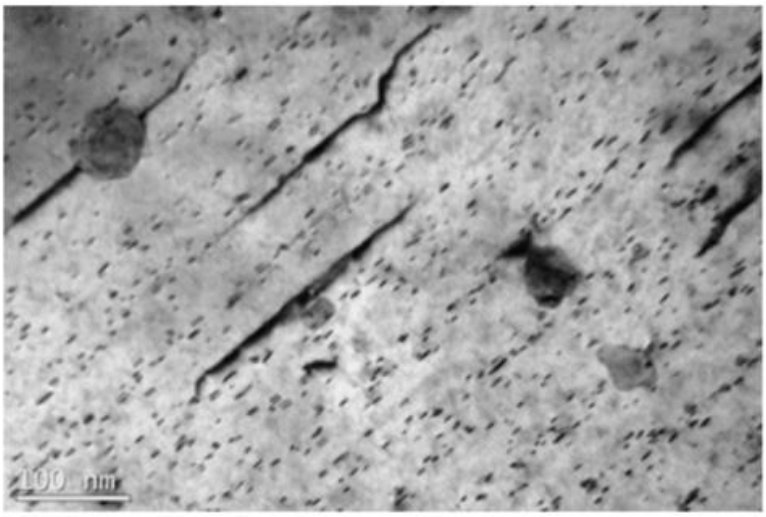


Figure 2.15 Irradiation induced platelet like particles aligning with the basal plane in M5 alloy after neutron irradiation to $13 \times 10^{25}\, neutrons/m^2$ [107]

2.4 The radiation enhanced corrosion

As mentioned earlier, concern about the accelerated corrosion of zirconium alloys in reactor compared to autoclave corrosion is the driving force for the development of new zirconium alloys. Figure 2.16 shows a good example of this phenomenon.

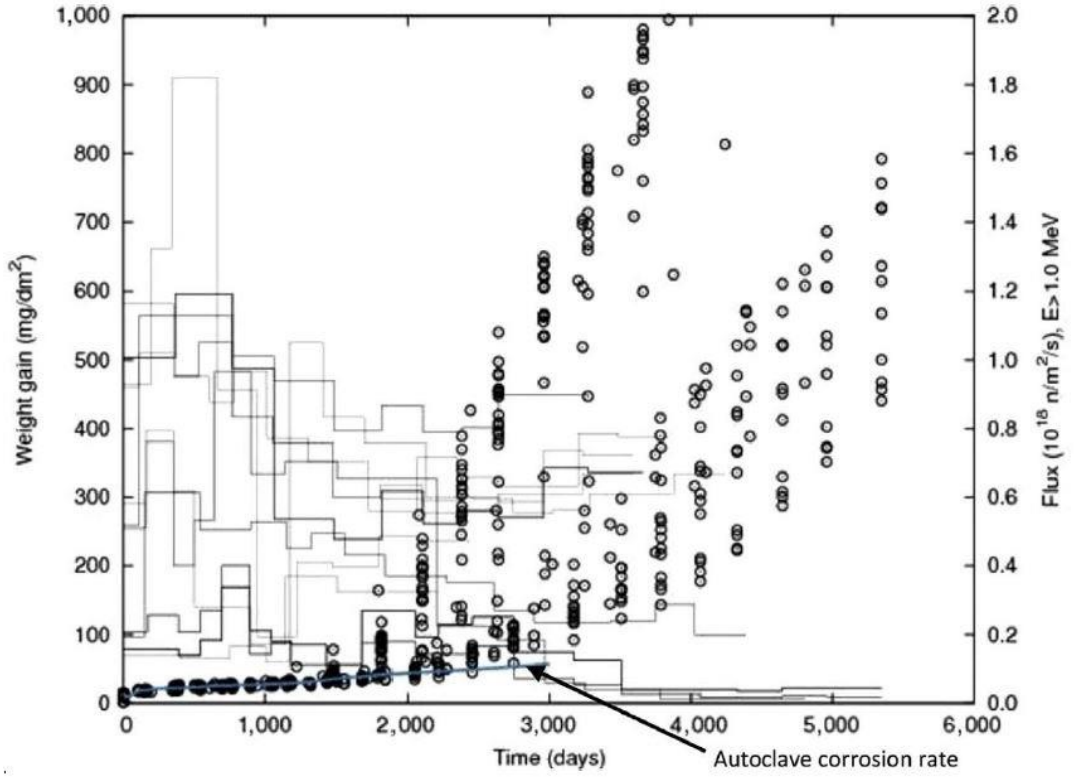


Figure 2.16 Radiation enhanced corrosion shown in Zircaloy-4 corroded at 270 °C. [119]

There are many ways that in-reactor neutron radiation will affect the corrosion behaviour of the zirconium alloys. In the metal matrix, neutron radiation results in formation of dislocation loops [104] which hardens the metal, making it less able to accommodate stress accumulated during oxidation, hence resulting in cracking and accelerated oxide growth. If there is a microstructural texture in the metal, the radiation induced growth of the metal along the c direction [120–122] might lead to a horizontal tensile stress in the oxide that encourages the formation of the cracks vertical to the metal / oxide interface, the least wanted scenario for the sake of corrosion resistance of the alloy [123]. As reviewed in previous sections and in [124–128], radiation can also damage the SPPs in the metal, leading to redistribution of alloying elements into solid

solution in the metal matrix, affecting the local electrical conductivity when incorporated in the oxide and hence the transportation of the oxidising species across the oxide film [18, 37]. If the β-Zr phase is present, in-reactor conditions will lead to the phase decomposition as reviewed in previous sections, and lead to both changes in the micro-mechanical properties of the metal [129] and the corrosion behaviour of the oxide [77]. Some of these factors are summarised and illustrated in Figure 2.17.

The neutron irradiation can also introduce changes to phase distribution, microstructures in the oxide and at the metal / oxide interface formed under irradiation [130–133]. A recent in-situ heavy ion irradiation study showed that the sub-oxide region can become amorphous under intense irradiation [134]. It was also shown that in-situ heavy ion irradiation may result in direct phase transformations in the oxide [29].

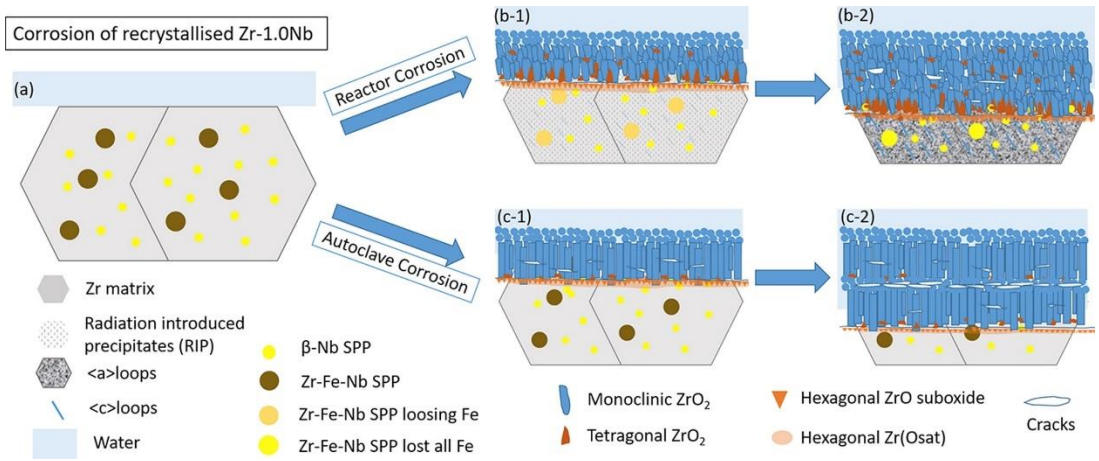


Figure 2.17 Illustration of the corrosion of Zr-1.0Nb alloy in and out of reactor [135]

Based on my sample collection and the techniques I have used, the work presented in this thesis concentrates on studying radiation induced changes in the metal matrix,

including the radiation induced Nb precipitates and formation of the dislocation loops, changes to the SPPs, phase changes to the β-Zr, and correlates their impact on the redistribution of alloying element Nb in the metal and oxide.

2.5 Emulating neutron irradiation by ion irradiation

The fact that neutron irradiated samples can only be obtained by retrieving them from post-reactor materials has limited research in many ways, including consuming both funding and time, lack of flexibility of dose conditions, and limited availability of laboratories due to the high activity of neutron irradiated samples. Therefore, researchers have used other types of radiation species, from electron to ion, to emulate the effects of neutron irradiation. While these charged particles have been shown helpful as a proxy to understand the effects of neutron irradiation [136], care should be paid to avoid the confusion caused by them. In general, there are several issues that should always be borne in mind when using ion irradiation to emulate the effects of neutron irradiation.

Firstly, the recoil spectra for different irradiation species are different. The recoil spectrum is the energy distribution of PKAs during irradiation and can highly influence the size of cascade and types of defects generated [83]. Some researchers have claimed that long term evolutions are not as highly influenced by the differences in recoil spectra as thought before [137]. However, different observations for irradiation damage of SPPs

have suggested that this issue should be taken into account [138].

A more important issue to be considered is the dose rate effect. It has been claimed by Garner et al. that the dose rate is the dominant effect in governing the difference between neutron and ion damage [139]. The influence of dose rate can be undertood by considering two mechanisms; 1. Difference in the number of surviving defects, 2. Difference in the timescale for defects to evolve. With higher dose rate, more defects will be captured by clusters and dislocation loops, rather than by sinks such as grain boundaries and surfaces [140]. A comparison between samples exposed to different dose rates of neutron irradiation was made by Muroga et al. and showed that higher dislocation density at saturation is formed at a higher dose rate [141]. In order to compensate for this difference, a common practice is to use an equivalent temperature according to a concept of 'variable shifts' [142]. The shift from the actual temperature T_1 to the equivalent temperature T_2 can be calculated from

$$T_2 - T_1 = \frac{\frac{kT_1^2}{E_m^V} ln\left(\frac{K_{0_2}}{K_{0_1}}\right)}{1 - \frac{kT_1}{E_m^V} ln\left(\frac{K_{0_2}}{K_{0_1}}\right)}$$

where K_{0_2} and K_{0_1} are the corresponding defect production rates. E_m^V is the migration energy of the vacancies. A good example for the application of this concept is the study the redistribution of Iron in the Zr-Nb-Fe SPPs in neutron and proton irradiated low Tin ZIRLO^{TM} samples [125]. For comparable results between the samples, the neutron irradiation was at 288 °C while the proton irradiation with a higher

damage rate was at 350 °C.

Another interesting issue to be considered is the chemical changes induced by ions accelerated by accelerators. This not only includes the bubbles induced by Xe irradiation as widely observed and described [30], but also the contamination induced by the accelerator itself [143], including the introduction of carbon and oxygen. In investigating the chemistry change in the matrix induced by irradiation, those caused by evolution of SPPs (which are of scientific interest) should be carefully distinguished from those caused by the irradiation event itself.

Chapter 3 Materials, Instruments and Techniques

This chapter discusses the materials, instruments and techniques used in this thesis. The first section will discuss the basic microstructures and irradiation history of the materials. I have used Transmission Electron Microscopy (TEM) as the primary tool, so the second section will talk about the whole analysis process from TEM sample preparation to the more specialised TEM based characterisation methods. The third section discusses specific techniques used in the project, including the conditions used for TEM imaging of irradiation defects, and analysis methods for EELS data.

3.1 Materials used in this project

3.1.1 Basic microstructure

3.1.1.1 CNL Zr – 2.5 wt% Nb alloy

The main type of alloy used in this study is Zr – 2.5 wt% Nb provided by Canadian Nuclear Laboratory (CNL Zr-2.5Nb in short in the following text). The alloy fabrication process involves heating the billets at 1015 °C and then water quenching, then the billets were trepanned and extruded at 815 °C. The tube was then straightened and cold drawn, followed by a final stress release step at 400 °C for 24 hours. This process resulted in a 'dual-phase' microstructure, as shown in Figure 3.1. The α-Zr grains are elongated along the axial and hoop direction of the tube. The Nb enriched (about 20 wt% Nb) β-Zr grains are parallel to the hoop direction, sitting at the α grain boundaries.

The evolution in the α- and β-Zr grains under neutron irradiation will be both studied in this work. One topic is the change of Nb concentration in both phases. However, unlike the β phase regions which have a 20% or even higher Nb concentration, the α-Zr grains have a much lower Nb concentration that cannot easily be detected by TEM-based techniques. Thus the Nb concentration in the α-Zr grains in the as-received CNL Zr-2.5Nb samples was measured to be 0.41 at% by APT. The data is kindly provided by Anne Callow.

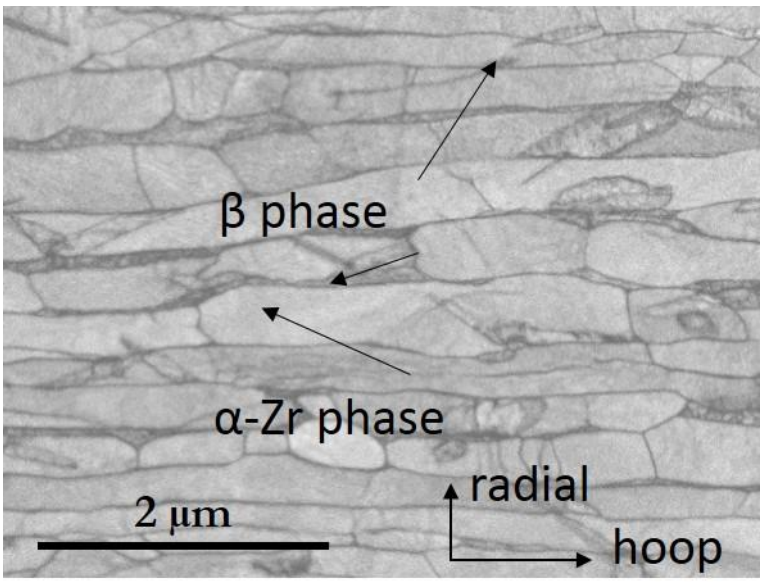


Figure 3.1 An TKD (transmission kichuchi diffraction) band contrast image showing the microstructure of the Zr-2.5 wt% Nb alloy in this study. The radial and hoop directions refer to directions relative to the cladding tube.

3.1.1.2 Recrystalised Zr – 1.0 wt% Nb and Zr – 2.5 wt% Nb alloys

In order to study the underlying mechanisms governing Nb redistribution around the α/β phases under irradiation, a series of experiments were carried out using in-situ

irradiation in a TEM. The materials used in this series of experiments are recrystallised (RXA) Zr-1.0Nb and Zr-2.5Nb alloys provided by Westinghouse^{TM}. The final heat treatment at 560 °C created equiaxed β-Nb and Zr-Nb-Fe phase SPPs in a polycrystalline α-Zr matrix, as shown in Figure 3.2 for the Zr-2.5Nb alloy. The difference in the Zr-1.0Nb alloy is the lower amount of the β-Nb SPPs, due to a lower amount of alloying element Nb, and so is not displayed explicitly. The focus in this study has been on the β-Nb SPPs, which have an initial radius of about 40 nm, and the average grain size in the α-Zr matrix is about 2μm. The composition of these two alloys was measured by Inductively Coupled Plasma Mass Spectrometry (ICPMS), and the main elements are given in Table 3-1.

Table 3-1 Composition of Zr-1.0Nb and Zr-2.5Nb alloys

Material	Nb (wt%)	Fe (wtppm)	H (wtppm)	Zr
Zr-1Nb	1	753	13	balance
Zr-2.5Nb	2.5	440	-	balance

3.1.2 Neutron Irradiation on the CNL Zr – 2.5 wt% Nb alloys

The CNL Zr-2.5Nb alloy samples were irradiated in the Halden Reactor before being retrieved and cut. In addition to the as-received material labelled B166, two types of Halden samples were provided. The first type is the so-called ‘in-flux’ samples which

were put in the reactor core to receive neutron irradiation during corrosion. The second type is the so called 'out of flux' samples, which were put in the primary coolant but out of the reactor core. Thus the out of flux samples were corroded in the same environment as the in-flux samples, but without neutron irradiation. The details of the irradiation and corrosion conditions of the samples can be found in Table 3-2. The conversion factor from neutron fluence to DPA was adopted to be $0.41 \times 10^{25} m^{-2}/dpa$ as calibrated for CANDU reactors [144].

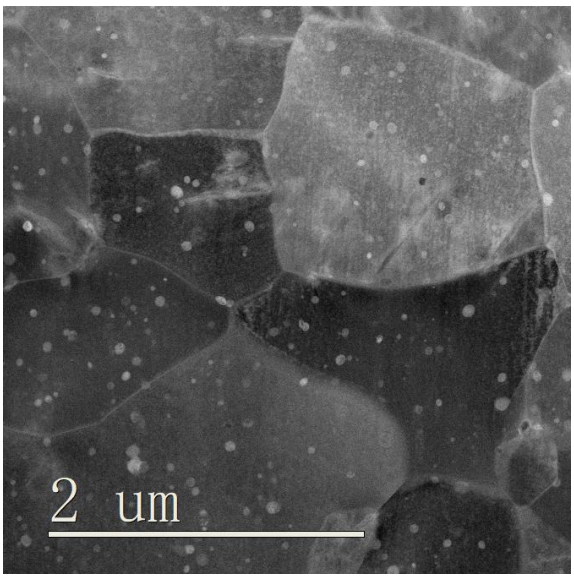


Figure 3.2 A STEM HAADF image showing the typical microstructure of the RXA Zr-2.5Nb alloy. The white spots are the β-Nb and Zr-Nb-Fe SPPs.

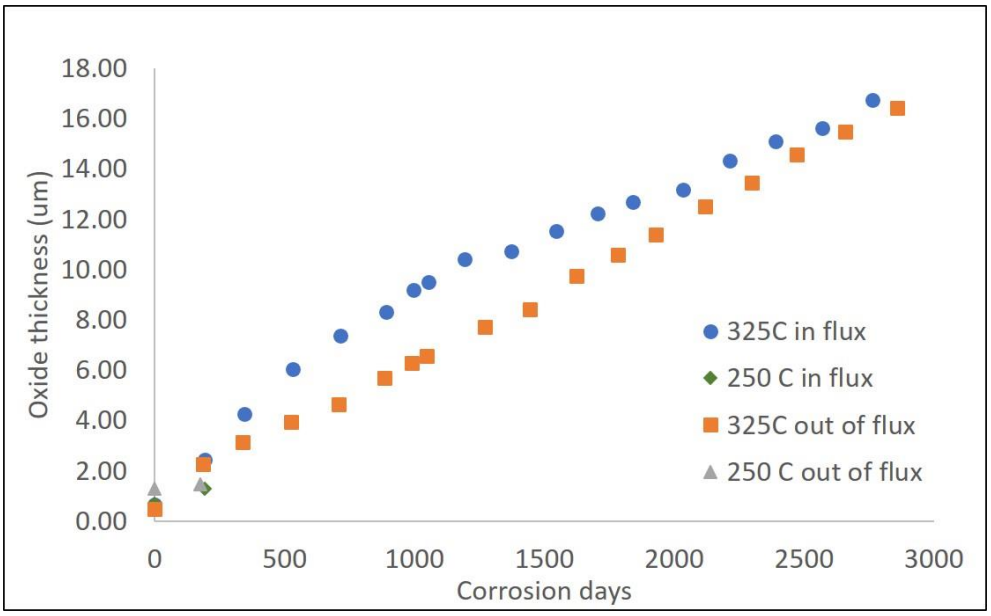
3.1.3 Corrosion kinetics of the CNL Zr – 2.5 wt% Nb alloy under reactor conditions

The growth of the oxide films on the surface of the samples was closely monitored

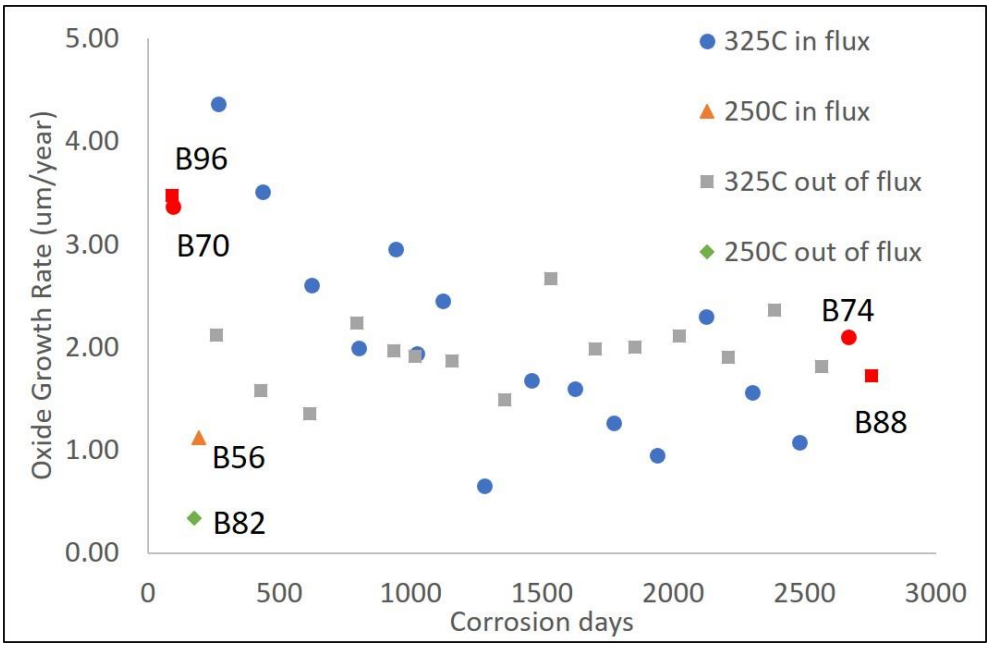
during the in-reactor corrosion. The weight gain due to the formation of oxide was measured at several time intervals over a long time. The calculated oxide thickness from the weight gain is plotted against the corrosion time in Figure 3.3 (a). The oxide growth rate was also calculated by measuring the net growth of the oxide thickness between two neighbouring time intervals and plotted in Figure 3.3 (b). The instantaneous growth rates for selected samples are marked in red. The selection of these samples from the large set shown in the figure was discussed with Dr Heidi Nordin of Canadian Nuclear Laboratory (CNL).

Table 3-2 List of CNL Zr-2.5Nb samples in this study

Samples	**B166**	**B56**	**B82**	**B70**	**B96**	**B74**	**B88**
Corrosion time (days)	---	192	185	192	185	2765	2858
Corrosion temperature (°C)	---	250	250	325	325	325	325
Neutron radiation	---	in flux	out of flux	in flux	out of flux	in flux	out of flux
Neutron flux (/m²/s x 10^{17})	---	4.63	0	4.73	0	4.32	0
Neutron fluence (/m² x 10^{25})	---	0.77	0	0.79	0	10.3	0
Dose rate (x 10^{-7})	---	1.1	0	1.1	0	1.1	0
Dose	---	1.9	0	1.9	0	25.8	0



(a)



(b)

Figure 3.3 Comparison between the in-flux and out of flux samples corroded at different temperatures. (a) oxide growth curve (b) oxide growth rate curve, with the selected samples marked in red. (Data provided by Heidi Nordin, CNL)

Compared to the oxidation kinetics of other alloys presented in the literature review, there are two significant differences in the corrosion of the CNL Zr-2.5Nb alloy. (1)

The ‘break-away’ growth of the oxide film is not significant and (2) the radiation-enhanced oxidation is not significant, as seen in Figure 2.3, Figure 2.16 and Figure 3.3 for comparison. Figure 3.3 (b) shows that the oxidation rate generally decreases with time in the in-flux samples corroded at 325 °C, and remains roughly stable in the out of flux samples corroded at 325 °C. The reason for these behaviours will be discussed in later chapters.

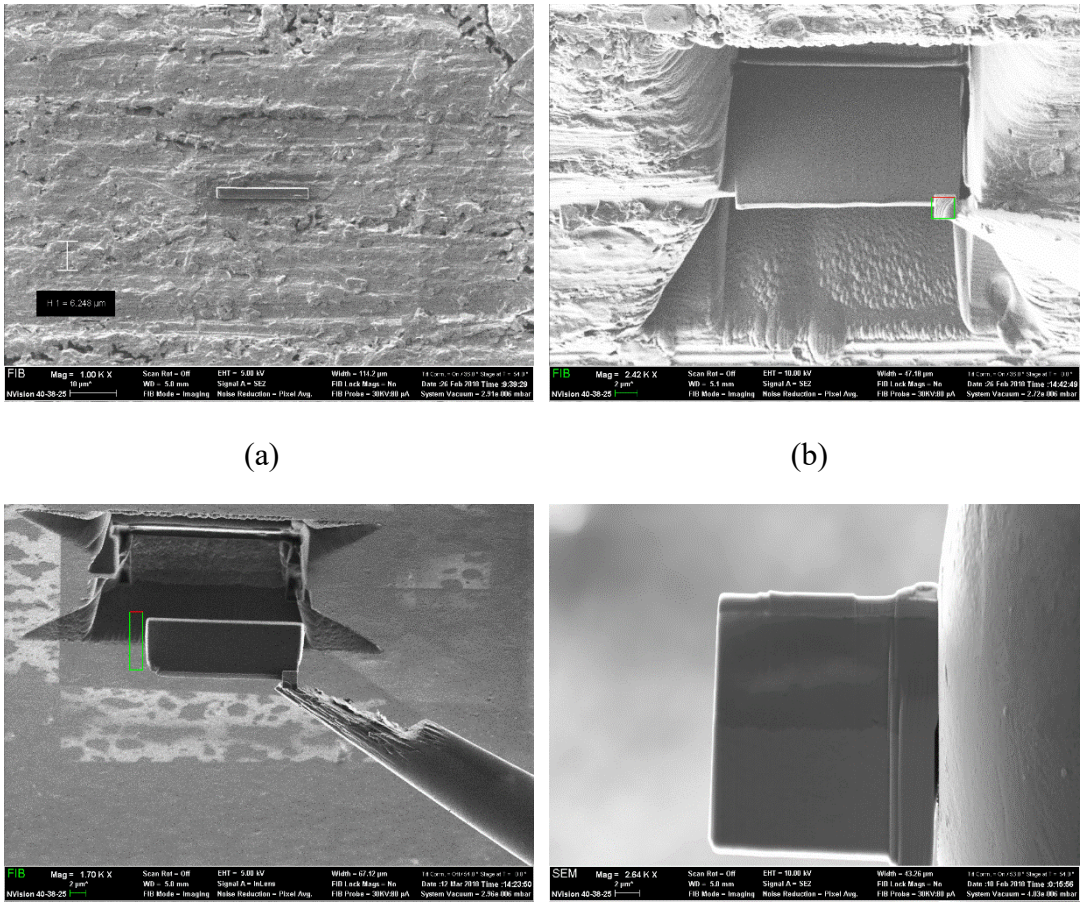
3.2 Instruments used in this project

3.2.1 Sample preparation by Focused Ion Beam

Focused Ion Beam milling has been used to prepare high quality TEM samples since the early 2000s [145, 146]. It benefits from the precise selection of the region of interest and good control of the thickness of the TEM foils. All the TEM samples used in this thesis were made by Focused Ion beam (FIB) milling following the guide in [147]. These ‘cross-section’ TEM lamellae were lifted out in-situ in the FIB chamber and glued to a three post half grid as is illustrated in Figure 3.4. The lamella is about 1.5um thick when extracted and attached to a half grid.

There are generally two positions on the half grid post that are available for attaching the lamella. The first position is on the vertical edge of the post and the lamella is attached like a flag, as shown in Figure 3.5 (a) and (b), and the second position is at the valley of a ‘V’ shaped pin, as shown in (c) and (d). The first position benefits from the

simpleness of the process and is used for most of the samples intended for normal TEM characterisation. The second position, although more effort is required to attach a TEM lamella there, can provide support to the sample on both sides. Thus samples attached to the second position are more immune to bending, which is an advantage for some specific characterisation work such as the in-situ irradiation experiments in the TEM described in Chapter 5.



(a) (b)

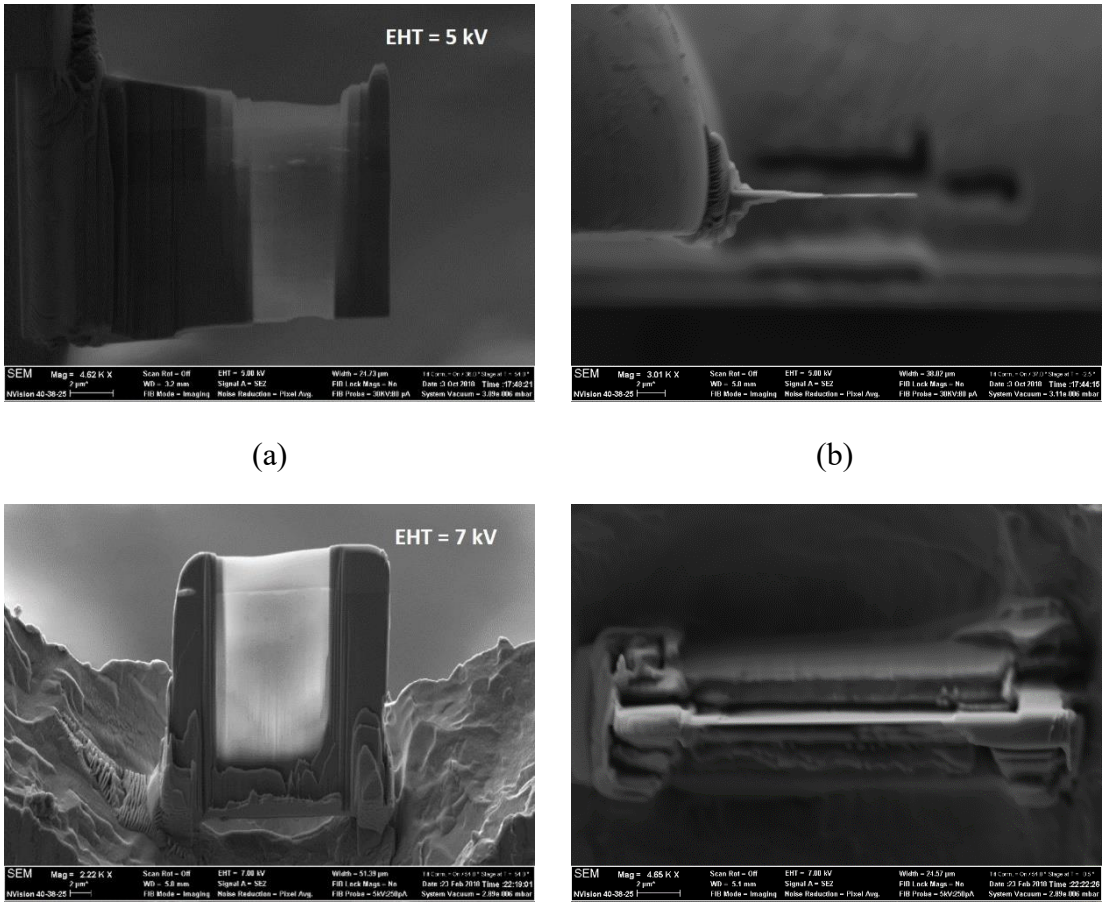
(c) (d)

Figure 3.4 Steps showing the lift-out of a TEM lamella in a FIB. (a) a protective layer of platinum is deposited on the surface of a bulk sample (b) trenches are made on both sides of the lamella. Then the lamella is attached to a micro-manipulator tip, and undercut to detach from the bulk sample, (c) the lamella is then 'lifted-out' by the micro-manipulator, (d) the lamella is attached to a pin on a half grid, then cut loose from the micro-manipulator.

The FIB lamellae are then thinned in the FIB by 30kV gallium ions from the top to an appropriate thickness. Finally they are tilted away from the ion beam by 10° to 15° and the surface of the foil is raster scanned by 2kV or 5kV gallium ions. This last step helps to remove the thin FIB damaged layer on the surface. During the thining down and surface 'cleaning' steps, the thickness of the foil is monitored by observing the transparency in secondary electron images. Based on my experience, the empirical thickness of the Zr metal sample is 100 nm to 150 nm when it is transparent under the 7kV electron beam, and 50 nm to 70 nm when it is transparent under the 5kV e-beam.

It should be noted that the optimum thickness of the sample is determined by the precise nature of the characterisation work that is planned. These following values are based on my personal experience gained in this project. For high resolution imaging, Fresnel contrast imaging and EELS acquisition, samples of 30 nm to 50 nm are ideal. However, for TEM diffraction analysis of radiation defects, the samples are not supposed to be too thin in case the Kikuchi patterns are too weak to follow. A 50 nm to 100nm thick sample is ideal for this type of work. And when the structural integrity of the sample is important, for instance the TEM in-situ radiation experiments for which the lamella will go under a high flux ion beam at high temperatures, the sample may be left relatively thick (100 nm to 150 nm) to avoid fracture. Figure 3.5 (a) shows a sample for EELS work which has been thinned to about 50 nm (electron beam transparent at 5 kV), while

(c) shows a sample for in-situ irradiation experiments deliberately left thicker (electron beam transparent at 7kV).



(a) (b)

(c) (d)

Figure 3.5 SEM images showing the different positions and thickness values of TEM samples for different characterisation purposes. Images (a) and (b) show a lamella attached to a vertical edge of the post and thinned to about 50 nm, while (c) and (d) show a lamella attached on a 'V' shape pin and thinned to about 100 nm to 150 nm.

All the un-irradiated TEM samples in this study have been made using the two FIBs at David Cockayne Centre For Electron Microscopy at Oxford University. An FEI FIB 200 was used to lift out some TEM lamellae, and a ZEISS NVision 40 FIB-SEM was

used to lift out and thin the TEM lamellae. All the neutron irradiated samples, due to their residual radioactivity, were made by an FEI Helios Nanolab 600i FIB at the Materials Research Facility (MRF) at the Culham Science Centre.

3.2.2 (Scanning) Transmission Electron Microscopy

Since its invention, the Transmission Electron Microscope has shown great power in revealing micro- and nano-features in a very wide range of materials. Using the TEM to characterise radiation-induced microstructural changes in samples has been developed and extensively used in the past several decades [104, 148–150]. Working together with other specific detectors, the modern analytical TEMs are also capable of providing microchemical information on small features.

This thesis uses the TEM as the primary tool to study the radiation damage and corrosion process of Zr alloys, generally in two modes. The first is the conventional TEM mode where the sample is illuminated by a parallel or near parallel electron beam [151]. The contrast in the image mainly comes from diffraction of the exiting electron waves, controlled by the arrangement of atoms in the sample. Images of different contrast can thus be obtained by tilting a sample with well-defined crystalline orientation to align the incident beam along chosen directions. The use of specific ‘diffraction conditions’ to reveal the features of interest will be discussed in more depth in Section 3.3.1. All the TEM diffraction analysis work has been carried out on a JEOL-

2100 microscope equipped with a LaB_6 electron source and operating at 200kV. Scanning Transmission Electron Microscopy (STEM) has also been used extensively in this work. Instead of forming a near parallel beam, the electrons are converged by the condenser lenses to form a cone, and the focus point is rastered over the specimen [151]. Detectors are put at different positions below the specimen to capture different portions of the electron exit waves, as illustrated in Figure 3.6. The Annular Dark Field (ADF) detectors capture electron beams diffracted by the lattice plane in the specimen. Based on the semi angle of the beam relative to the optical axis, they can be divided into high angle ADF (HAADF), middle angle ADF (MAADF) and low angle ADF (LAADF) detectors. The Bright Field (BF) detector collects transmitted electrons. Working together with the Annular Bright Field (ABF) aperture, which only blocks the very central portion of the beam, the BF detector can also provide ABF images.

Since the images forming on different detectors come from different portion of the exiting electron beam, the contrast in different images come from different physical interactions of the beam with the specimen. Generally speaking, the highly diffracted beams are generated by the mass variations in the sample, while the moderately diffracted beams are caused by diffraction from the lattice planes the sample [152]. These mass variations in the samples come from two changing factors, the average atomic mass and the thickness of the sample. By assuming the sample imaged is of roughly uniform thickness, the bright regions in the HAADF images correspond to

concentrations of heavier elements. The MAADF and LAADF images provide a combination of mass and diffraction contrast, and the BF images mainly show diffraction contrast. In this thesis, HAADF images have usually been used to identify the precipitates, second phase particles and hydrides since these microscopic features have different average atomic masses from the matrix, and hence show significant mass contrast. Figure 3.7 shows a good example of the different information provided by the different image modes.

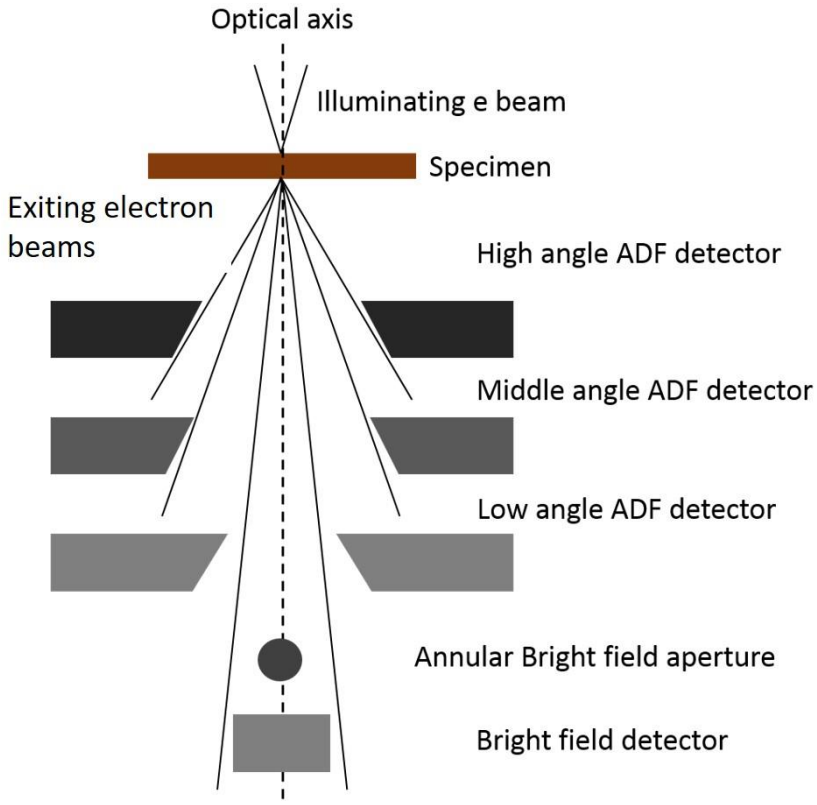


Figure 3.6 A schematic showing the different detectors used in STEM

Several different microscopes have been used in this thesis for STEM analysis. The main machine is a Cs probe corrected JEOL ARM 200F equipped with a cold FEG

source, operating at 200kV. A FEG JEOL 3000 TEM operating in STEM mode has also been used as a supplement. A double corrected JEOL Grand ARM in ePSIC at the Harwell Science Campus, equipped with cold FEG source and operating at 300kV, has also been used to characterise some neutron irradiated samples.

3.2.3 High resolution imaging by TEM and STEM

Some of the features in the alloy like small SPPs and radiation-induced precipitates are smaller than 10nm. This makes the conventional diffraction analysis inefficient in studying the microstructures of these features due to too much contribution from the matrix in the diffraction patterns. Therefore high-resolution imaging that is able to show the lattice planes and even atom columns is the preferred method to use.

In this project, high resolution TEM was carried out on a FEG JEOL 3000 TEM operating at 300kV. The images were taken at a defocus value of about 100nm. High resolution STEM imaging was carried out on a double corrected JEOL Grand-ARM operating at 300kV. By carefully tuning the defocus values, optical sectioning can be achieved so that a series of images can be taken focusing at specific depths in the sample [153]. This enables the study of the microstructural information of small features (about several nm) embedded in a relatively thick (~30 nm) sample.

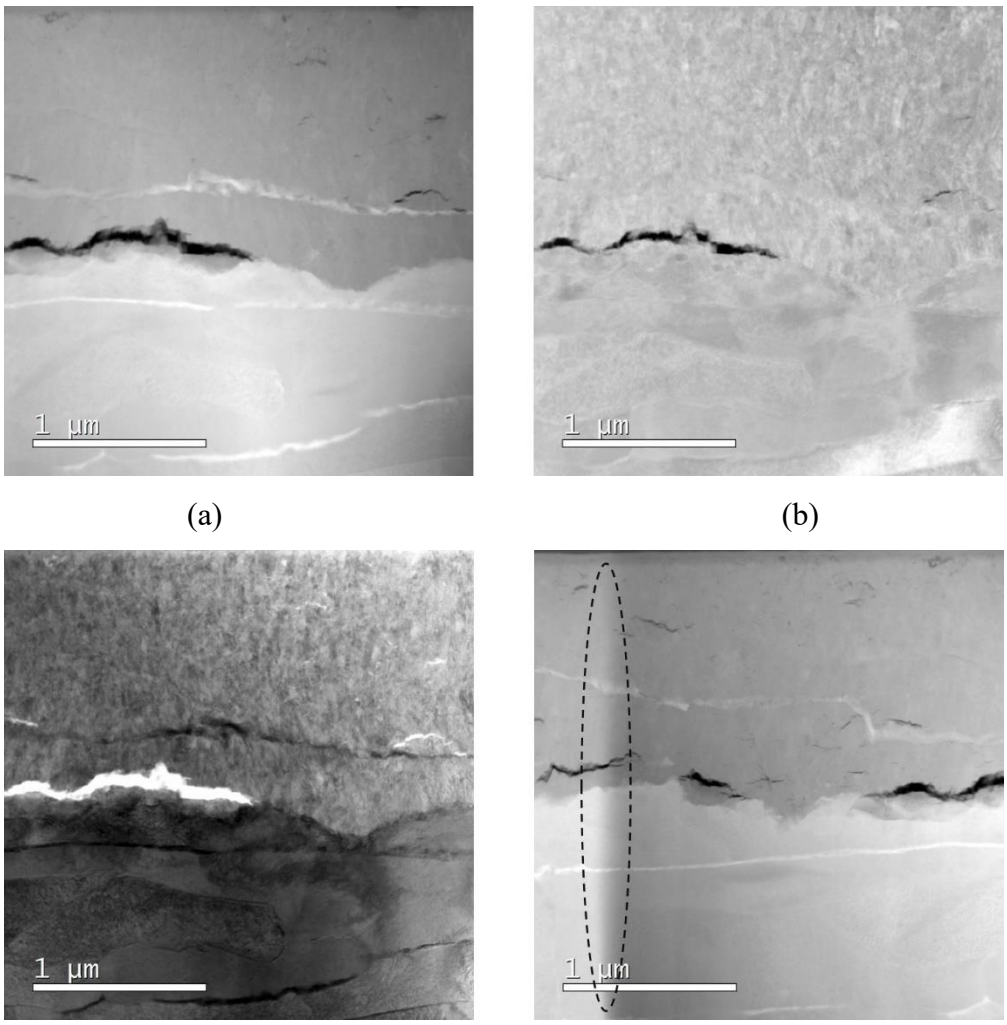


Figure 3.7 A same region shown in (a) HAADF (b) LAADF (c) BF image and another region shown in (d). The different contrasts in HAADF image (a) shows clearly the distribution of Zr metal matrix; Zr oxide, Nb rich β regions and cracks in the sample. The α grains in the Zr metal are best shown in the BF image (c). The contrast generated by different thickness of the sample is shown in the HAADF image (d). The boundary circled by the dashed line marks the two different thickness regions, the one on the left is thicker and the one on the right is thinner. This thickness difference is an artefact of FIB milling.

3.2.4 Energy Dispersive X-Ray analysis (EDX) and Electron Energy Loss Spectroscopy (EELS)

Two analytical techniques, Energy Dispersive X-Ray Spectroscopy (EDX) and

Electron Energy Loss Spectroscopy (EELS), have been used to investigate microchemical information in the TEM. When the electron beam passes through the thin TEM foil, several types of interaction may happen between the electrons and atoms in the specimen. Inelastic scattering will lead to some energy loss of the electrons, which is characteristic to the elements in the specimen. By measuring this electron energy loss spectrum using an image filter, we can determine what elements are in the specimen. A more detailed introduction to the fundamentals of EELS can be found in [154]. Electrons in the inner shells of the atoms in the specimen may also be knocked out by the incident electron beam, leading to electrons in outer shells jumping down to inner shell. These jumps will emit characteristic X-rays, which can be captured to identify the elements in the sample. A more detailed introduction to EDX can be found in [155]. A typical layout of the detectors for EELS and EDX analysis can be seen in Figure 3.8 (a), and typical spectra of both kinds can be seen in Figure 3.8 (b).

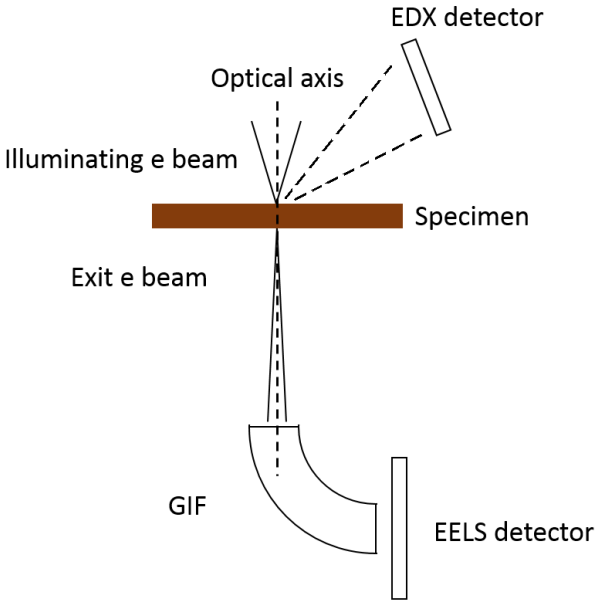
The EELS signals can usually be divided into three regions, around the zero loss peak (ZLP), low loss spectrum and core loss spectrum. The zero loss peak corresponds to the electrons transmitted through the thin specimen without any significant interaction and hence energy loss. The low loss spectrum comes from the energy loss from the plasmon resonance of the valence electrons. It can be used to identify the distribution of different phases [154], as shown in Section 3.3.2 (2). The core loss spectrum comes from the energy loss due to the incident electron interaction with inner shell electrons of the

elements in the specimen and is characteristic to specific elements. It can also be used to measure the valence state of the elements by comparing the fine energy shift of the core loss edges. A good example of measuring the oxidation states of Nb is given in Chapter 6.

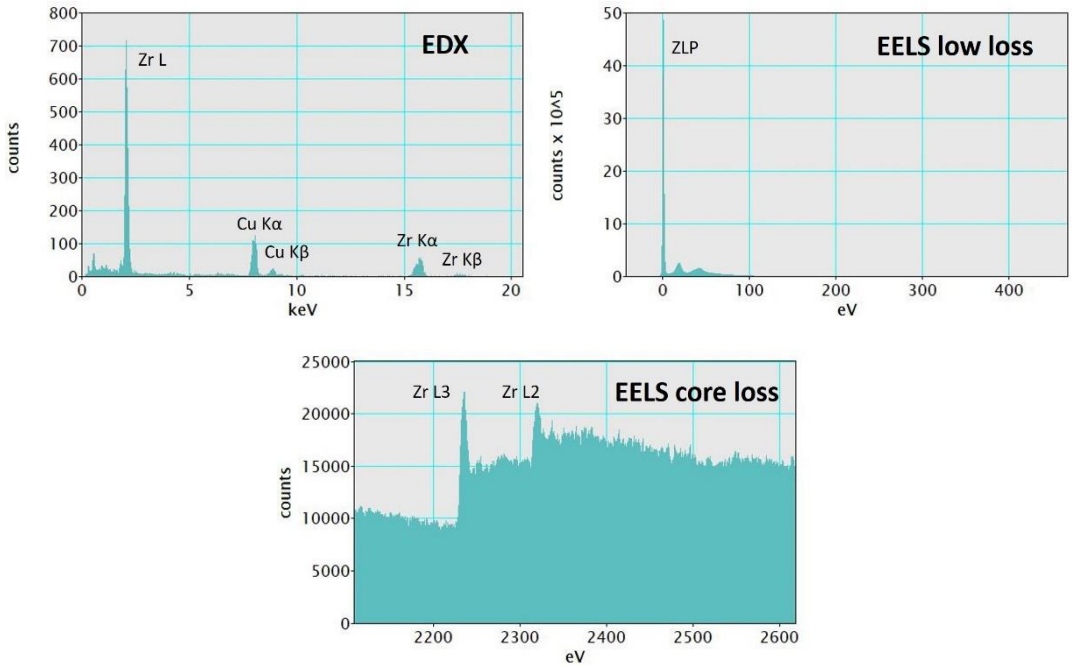
In this work, the EELS signals were always collected using the same set up of the Gatan image filter (GIF). The convergence half angle was always 30 mrad and collection half angle was 40 mrad. The cold FEG gun typically delivered energy spreads of ~ 0.5eV (as measured on the ZLP FWHM). The spectra were usually taken with an energy dispersion of 0.25 eV/pixel. But in cases where the fine analysis of the plasmon peaks were needed, the energy dispersion was set to be 0.05 eV/pixel.

In this work, EDX and EELS signals were usually collected in the spectral images using the Digital Micrograph^{TM} (DM). A spectral image is a HAADF or BF image with a spectrum recorded at each pixel in the image. Therefore the spectrum from a specific microscopic feature in the image can be analysed using the 'picker tool' in the DM. It is a common practice to take at least two spectral images with the EELS, one low loss spectral image with ZLP recorded, and the core loss spectral image. In addition to the EDX spectral image, the line-scan is another useful mode for analysis, especially when the signal is not strong enough so a decent EDX spectral image takes too long to acquire. A good example of using the EDX line-scan for analysis is shown in Section 5.1. Due

to its physical nature, EELS is more sensitive to light elements while EDX is more sensitive to heavy elements. Both techniques have been used collectively in this work.



(a)



(b)

Figure 3.8 (a) A schematic layout of the detectors for EDX and EELS in a TEM (b) typical spectra of the EDX and EELS signals from a Zr sample

All the EELS work in this thesis was carried out on a cold FEG Cs probe corrected JEOL ARM operating at 200kV, equipped with a Gatan GIF Quantum 965 ER. The EDX work has been carried out on several machines, including a JEOL ARM 200 equipped with a 100 mm^2 Centurion EDX detector, a JEOL 2100 equipped with an Oxford instrument 80mm^2 thin window EDX detector, a JEOL 3000 equipped with an Oxford instrument X-MAX EDX detector, and the JEOL Grand ARM equipped with an Oxford Instrument X-MAX 100mm^2 EDX detector. All the EDX results, except the ones from the ARM 200, were analysed by the Oxford Instruments Aztec software. The EDX spectra from the ARM 200 were acquired by Gatan Digital Micrograph software and were analysed by Hyperspy data analysis toolbox. The relevant notebook, which has been specially developed for analysis of the Zr samples in this work, is attached in Appendix A.

3.2.5 In-situ irradiation in a TEM

Researchers using TEM to study microstructural changes in a sample would like to observe these changes in real time, so-called in-situ TEM. By irradiating the TEM sample with one or two beams of high energy ions at the same time as observing it with the electron beam, radiation-induced changes can be directly observed. Figure 3.9 shows the setup of the two state-of-the-art in-situ radiation TEM facilities that I have used in this work.

Compared to studying radiation damage by inspecting neutron-irradiated samples after removal from the reactors, the in-situ technique has several benefits. Firstly, the ion beam in the in-situ TEM can provide a high flux, and hence a high damage dose rate to the sample. Thus the sample can be damaged to a high level very efficiently, for instance it takes less than a day to achieve the same damage level to that achieved in a reactor in one year. Secondly, the heavy ion irradiation will not lead to activation of the sample, leading to a much simpler process for sample handling and post-radiation characterisation. Moreover, the special conditions at the in-situ irradiation facility, for instance extreme radiation temperatures, high flux, different irradiation species and the unique geometry of the sample, may allow us to explore radiation damage behaviours different to those under neutron irradiation conditions in the reactors. By carefully controlling the conditions and comparing to the neutron radiation results, the mechanisms of some processes can be more clearly studied. The relationship between the in-situ irradiation in a TEM and real in-reactor neutron irradiation will be discussed in depth in Chapter 5.

Two sets of in-situ irradiation campaigns were carried out in this work, one at the IVEM facility and one at MIAMI2. The detailed irradiation conditions are described in Section 5.1.1.

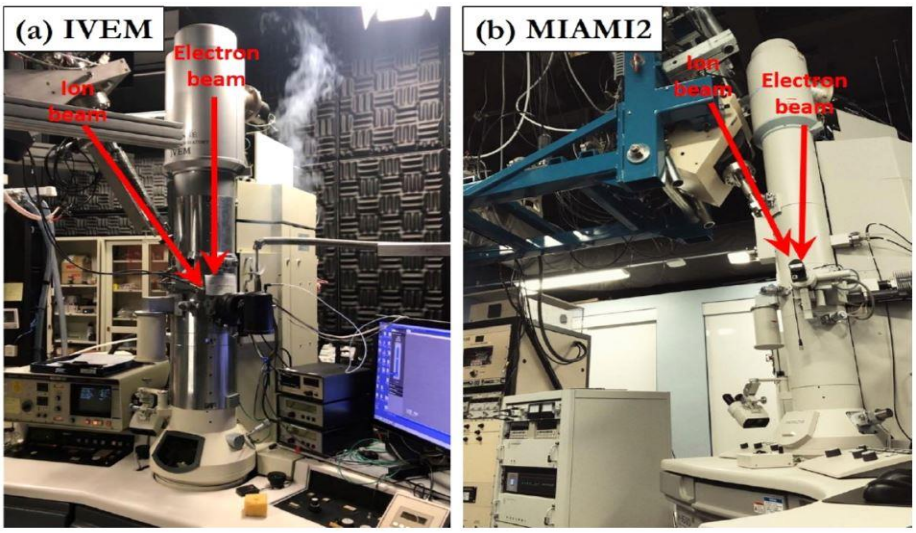


Figure 3.9 The layout of two state-of-the-art in-situ radiation TEM facilities. (a) The IVEM at Argonne National Lab, (b) MIAMI2 at University of Huddersfield. Photos courtesy to Junliang Liu.

3.3 Characterisation techniques used in this project

3.3.1 Characterisation of radiation damage in Zr metal by TEM

Several types of defects can be induced by radiation in the Zr metal matrix, including dislocation loops, radiation-induced precipitates, voids etc. [104]. In this thesis, neutron radiation-induced dislocation loops and precipitates have been investigated since they can have direct impact on the corrosion resistance of the alloy, and these features have been studied using TEM. It is necessary to make sure appropriate imaging conditions were used so valid results can be obtained.

Standard diffraction contrast methods, as described in [149–151], were used to image these defects in this work. Weak Beam Dark Field (WBDF) and Kinematic Bright Field (KBF) imaging were used because these techniques offer different information. WBDF

imaging provides the most accurate size of loops because the contrast is from the highly strained region close to the cores of the defects [150]. However, when the damage level is too high, and the matrix is too strained, WBDF can lead to a 'difficult' background with too many contrast features to deal with. In this case, bright field kinematic imaging is more useful as illustrated in [149]. It is convenient that imaging by both WBDF and KBF can be done at the same time by adjusting the 'Bright tilt' of the electron beam in the TEM, without tilting the sample or changing the position of the objective aperture. The practice in this thesis was always to record both images whenever possible.

It should be noted that establishing a 'true' weak beam condition requires the deviation parameter $|s_g| = \left|\frac{(n-1)\lambda}{2d_{hkl}^2}\right| \geq 0.2nm^{-1}$, where λ is the electron wavelength and d_{hkl} is the interplanar spacing value. In practice, this is achieved by setting the Ewald sphere to cross the reciprocal lattice between high enough reflection spots, for instance (g, 3-4g) or (g, 4-5g). This denotation indicates the dark field image was taken at the condition where the objective aperture was placed at g and the sample was tilted so the Ewald sphere crossed the reciprocal lattice between the spots 3g and 4g, or 4g and 5g. A typical image showing the (g, 3-4g) condition is shown in Figure 3.10.

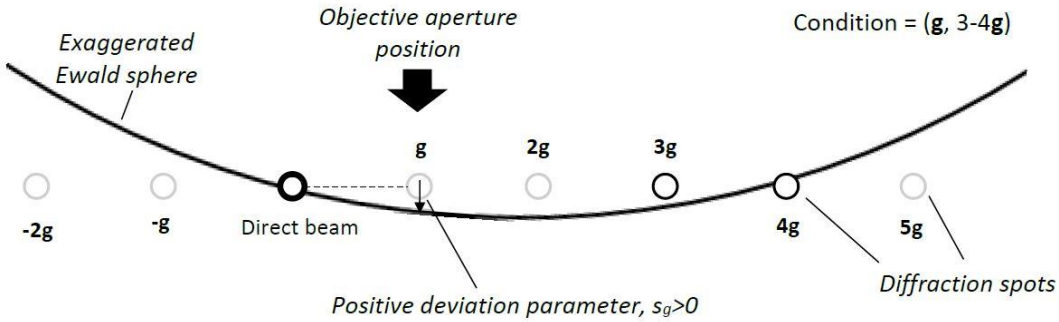


Figure 3.10 Diagram showing a weak beam dark field imaging condition (g, 3-4g) [156].

When taking these images, a script developed by Jack Haley [156] was used to tilt the electron beam precisely to obtain a series of images of slightly different deviation parameter values, sg. The superposition of these serial images allows smoothing of the background, hence a better presentation of the defects, as shown in Figure 3.11.

As mentioned in the previous chapter, there are two types of dislocation loop in the irradiated Zr metal matrix, a-type and c-type. a-type dislocation loops, or a-loops in short, have a Burgers vector of $\frac{1}{3}\langle 11\bar{2}0\rangle$ and mainly inhabit the prismatic plane $\{10\bar{1}0\}$. c-type dislocation loops (c-loops) have a Burgers vector of $\frac{1}{6}\langle 20\bar{2}3\rangle$ and inhabit the basal plane. The characterisation of the dislocation loops in this work mainly concentrated on identifying their existence and measuring the average size.

The invisibility criterion, $\boldsymbol{g}\cdot\boldsymbol{b}=0$, was used to determine the Burgers vector and hence the types of the loops. For a-loops with Burgers vector of $\frac{1}{3}\langle 11\bar{2}0\rangle$, $\boldsymbol{g}=\langle 0002\rangle$ could be used to turn all a-loops invisible and keep the c-loops visible, while selecting

$\boldsymbol{g} = \langle 11\bar{2}0 \rangle$ or $\langle 10\bar{1}0 \rangle$ can be used to make the a-loops visible. Therefore, when the sample was tilted to close to zone axes $\boldsymbol{B} = \langle 11\bar{2}0 \rangle$ or $\langle 10\bar{1}0 \rangle$, four sets of BF and DF images were taken, including $\pm \boldsymbol{g} = \langle 0002 \rangle$ and $\pm \boldsymbol{g} = \langle 10\bar{1}0 \rangle$ or $\langle 11\bar{2}0 \rangle$. The a-loops can then be confirmed and counted by comparing images from two g vectors perpendicular to each other. An example showing the visibility and invisibility of the a-loops in images with different g vectors is given in Figure 3.12.

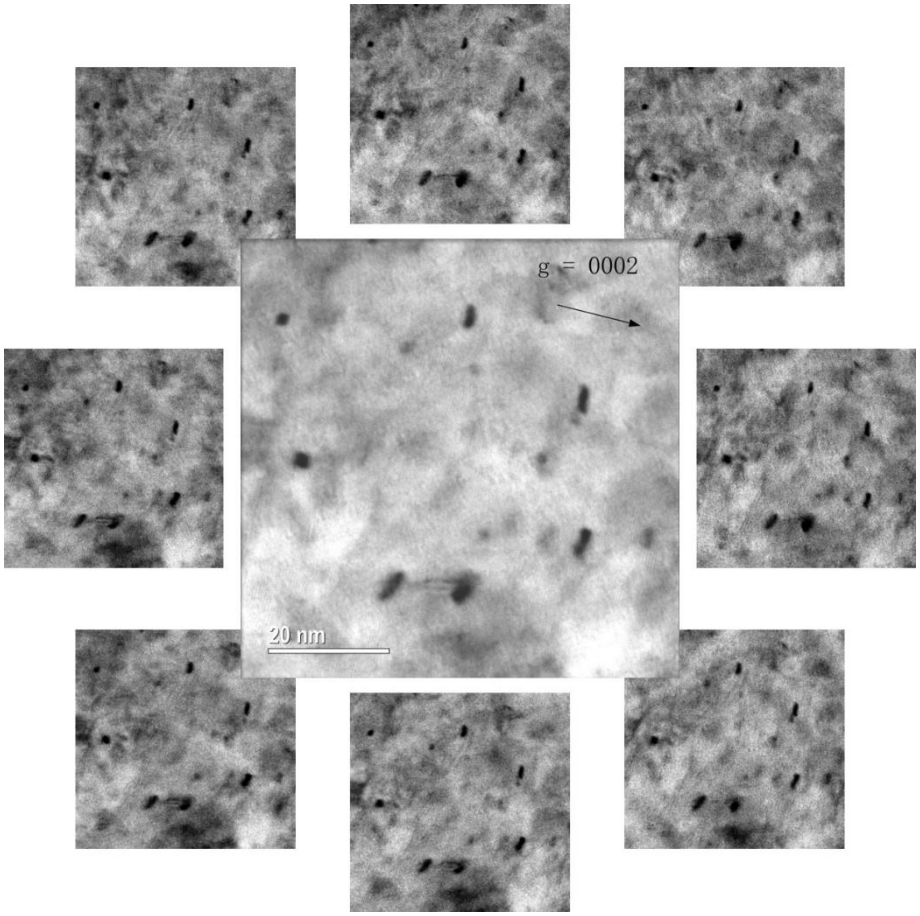
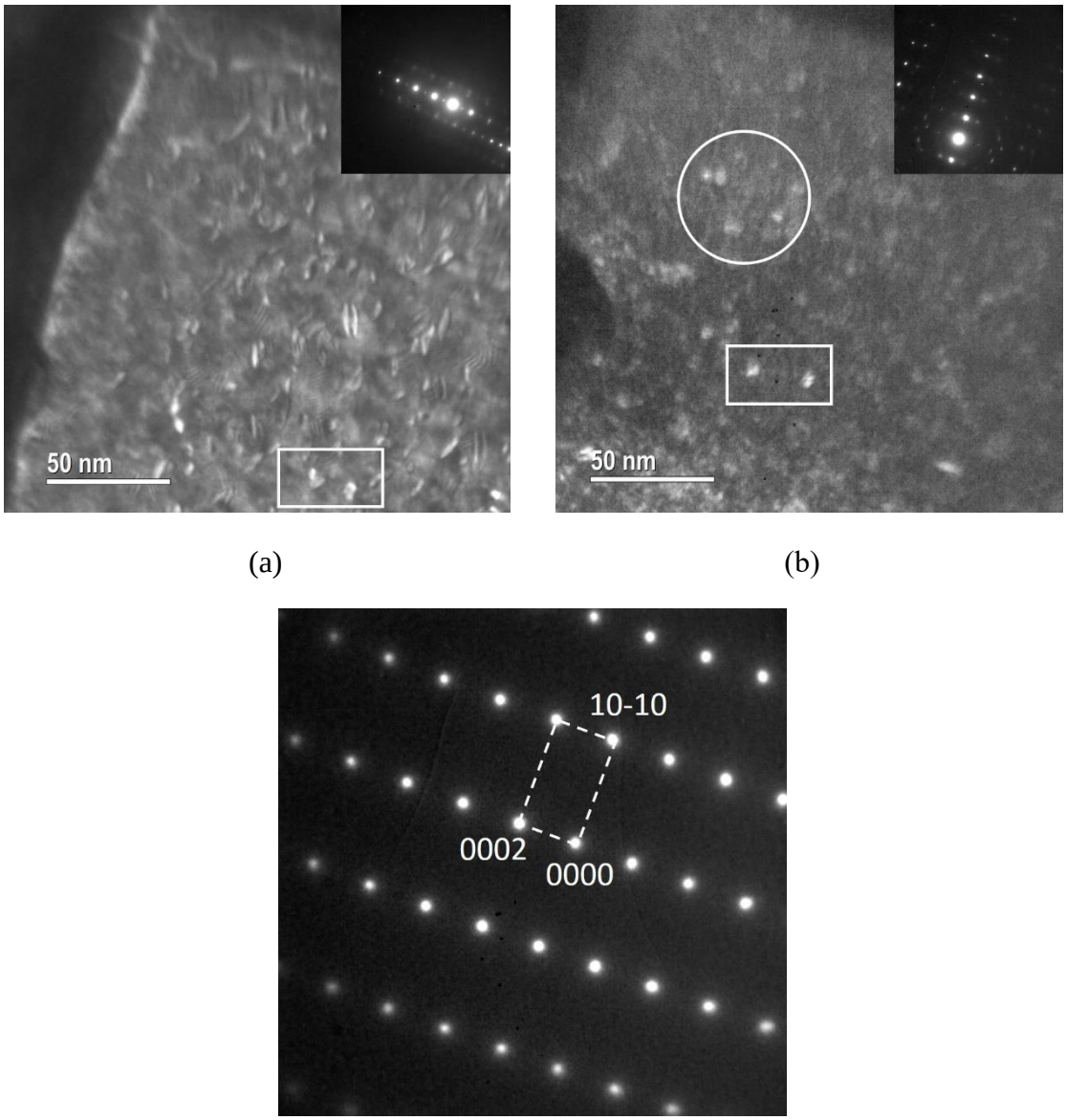


Figure 3.11 A series of bright field images of the same region with varying s_g values, and the superposition of these images shown in the centre. The background contrasts in the images around the edge are smoothed out for a better presentation of the features of interest.



(a) (b)

(c)

Figure 3.12 Images showing a region under two different g vectors (a) g = 0002 (b) g = $10\bar{1}0$, and (c) shows the Diffraction Pattern at the zone axis. The features in the white rectangle are the same in (a) and (b), thus not a-loops. But those in the white circle are only visible when g = $10\bar{1}0$, thus are a-loops.

When $\boldsymbol{g} = \langle 0002 \rangle$ is used, c-loops appear as linear features. Therefore in this thesis, 'average length' and 'linear density' are quantified for c-loops rather than 'average size' and 'number density'. This analysis also shows that the radiation-induced precipitates

can be clearly identified when $\boldsymbol{g} = \langle 0002 \rangle$ and distinguished from a-loops as shown in Figure 3.12 (a) and (b), agreeing with previous researchers [107]. Thus all the measurement of size and number counting of precipitates were also carried out at this condition.

3.3.2 Qualitative and Quantitative analysis by EELS

This section describes how Electron Energy Loss (EELS) spectra are used in this work to identify microstructural and microchemical features in the samples. In general, the tasks can be divided into three categories, as discussed below.

3.3.2.1 Measurement of TEM sample thickness

A sample thin enough is important for the data quality of many TEM based characterisation techniques such as high-resolution imaging and EELS. Thus the thickness of the FIB samples is a major property of interest during sample preparation. Although the rough thickness of a FIB lamella can be judged by the transparency of the image under an SEM probe, direct measurement of the thickness is favoured for the standardisation of the sample preparation process. Moreover, an accurate thickness value is needed when the density of particular microscopic features is measured. For instance, the number densities of radiation induced Nb precipitates in samples damaged to different levels are studied in this project. Therefore, EELS low loss spectra have been used to directly measure the thickness of the TEM samples, based on the method

reviewed by Iakoubovski et al. [157].

For a given low loss spectral image, the 'computer thickness' function in the Digital Micrograph ™ software is used, and the 'log-ratio (relative)' option is selected. The output, as shown in Figure 3.13 (b) below, is a map of the value 't/λ', where t stands for the absolute thickness of the sample and λ stands for the mean free path of inelastic electron scattering. Once the value of λ is known, the absolute thickness can be easily calculated. The mean free path is determined by several factors, including the energy of the incident electrons on the sample, the collection angle and the nature of the sample material itself [158]. A quick calculation of the λ value of the Zr sample under the set-up of the TEM is carried out using a Digital Micrograph™ script developed and kindly provided by David Mitchell [159].

For convenience, only the λ values for the α-Zr metal matrix or ZrO_2 were calculated. For regions containing other small features such as the β phase or hydrides, the thickness is assumed to be roughly the same as the adjacent metal or oxide regions. This approximation is reasonable as the local thickness variation is not large, as shown in the example in Figure 3.13 (c). Under the particular setup of the TEM, the value of λ is calculated to be 117nm. The thickness values along the line varies from 0.42 to 0.44 λ, corresponding to about 50 nm to 52 nm.

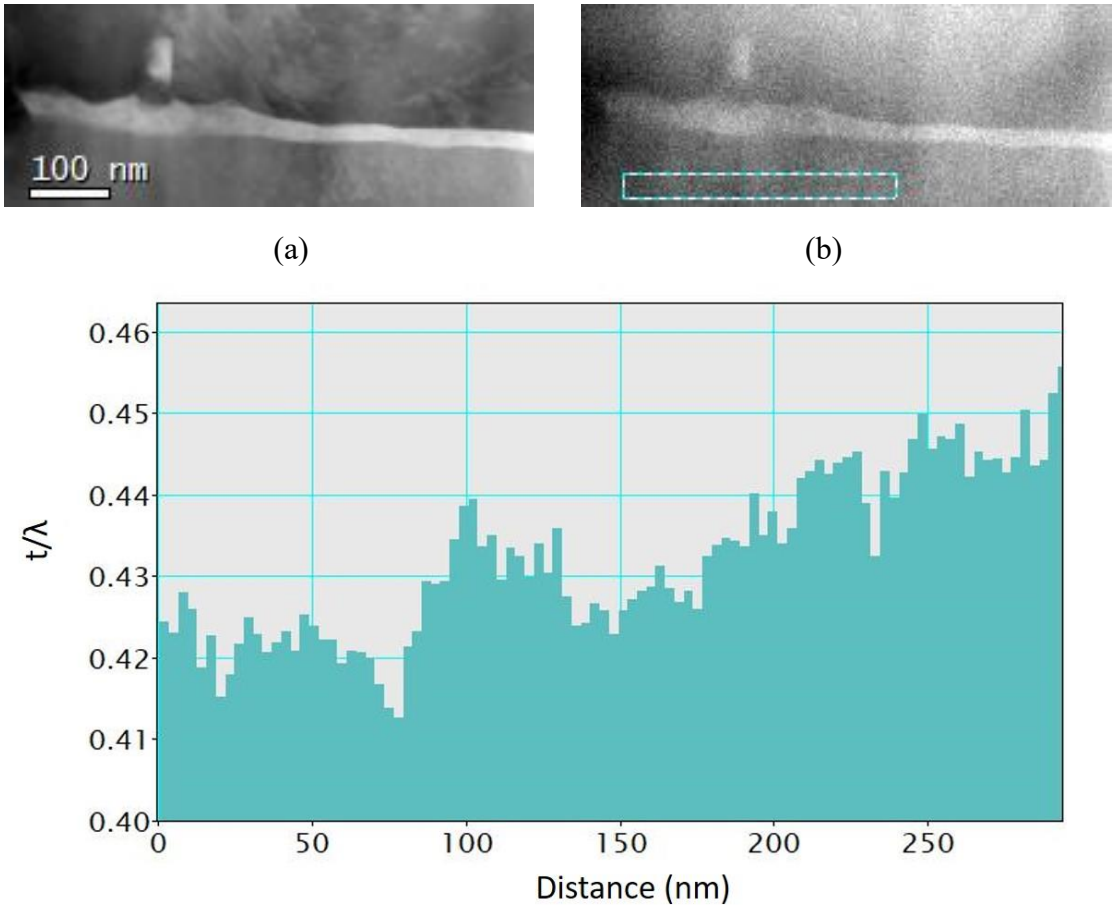


Figure 3.13 (a) Low loss spectral image of the region of interest, (b) map of t/λ of the region, (c) line profile as shown in (b)

3.3.2.2 Identification of nano-size features from the low loss spectrum

As well as the analysis of sample thickness using the low loss spectrum, the plasmon peaks recorded in the low loss regime can provide information on the different phases present in the samples. A good example is the characterisation of the sub-oxide region in corroded zirconium alloys by EELS low loss imaging combined with Multi Linear Least Squares (MLLS) fitting [67, 160]. In this project, the different phases in the β phase regions are identified following the procedure.

As described in Section 1.3, the transformation from β-Zr to β-Nb takes place at the same time as the corrosion of the alloy at elevated temperatures, and the transformed region can be a mixture of α-Zr, β-Nb, ω-Zr and β-Zr phases [161]. Some of these phases can be finely distributed embedded in the α-Zr and β-Zr matrix. Analysis of this fine microstructure usually leads to unreliable MLLS fitting results due to the difficulty of selecting proper reference spectra. To avoid this problem, careful Principle Component Analysis (PCA) and Independent Component Analysis (ICA) have been carried out on the spectral images using the HyperSpy toolbox [162]. By carefully selecting the value of output dimensions, the phases that are not recognised by MLLS can be identified. An example is shown in Figure 4.15 and Figure 4.16. The existence of the ω-Zr phase in the transformed mixture region is excluded by carefully comparing the PCA results from the sample of interest and the reference sample. The HyperSpy notebook that I have specially developed for this type of analysis is attached in Appendix A.

3.3.2.3 Measurement of the concentration and oxidation state change of specific elements using the HyperSpy toolbox

EELS core loss spectra have been used to measure the concentration of Zr, Nb, O and other alloying elements, and to track the oxidation state changes of Zr and Nb during corrosion of the alloys. The intensities and peak positions of the 'white lines' of Zr L edge, Nb L edge and O K edge are calculated using the HyperSpy toolbox. The 'white

lines' are the high intensity peaks at the edges, and are obtained by fitting Gaussian peaks to the background subtracted edges, as shown in Figure 3.14, named after the features acquired on a film in traditional EDX acquisition [163].

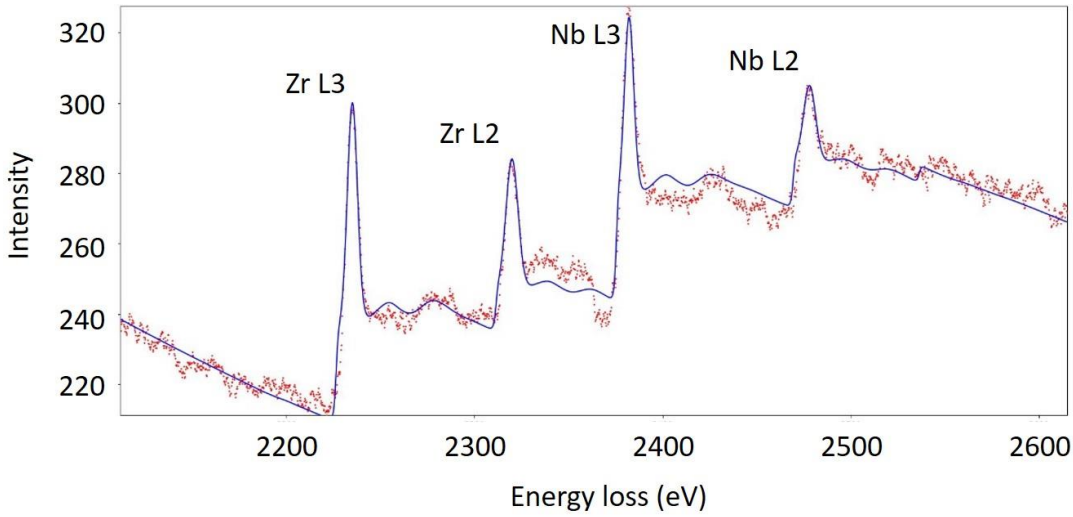


Figure 3.14 White lines of Zr L3, L2 edges and Nb L3, L2 edges as fitted in HyperSpy.

The measurement and calculation of the white lines can also be carried out in Digital Micrograph^{TM} manually, which can be simpler, but using the HyperSpy toolbox benefits from reproducibility in batch processing of large datasets. Moreover, it allows the production of oxidation state maps over an interesting region, as shown in Figure 6.18. The relevant Hyperspy notebook developed by me specifically for this analysis is attached in Appendix A.

Chapter 4 Neutron Radiation Damage in Dual Phase Zr-Nb alloy

As reviewed in previous chapters, the corrosion resistance of some types of Zr alloys can be influenced by neutron radiation, as evidenced by the radiation enhanced oxide growth observed in Zircaloys [39, 119, 164]. At the same time, Zr-Nb alloys have shown less susceptibility to radiation-enhanced oxidation as reported for M5 [165] and Westinghouse Zr-1.0Nb [135]. As shown in Section 3.1, the oxide growth kinetics of the CNL Zr-2.5Nb samples corroded at 325°C also show a limited enhanced oxidation rate at low dose and even a reduced oxidation rate at high dose. It is the aim of this study to reveal why the Zr-Nb alloys, compared to Zircaloys, have a much better resistance to radiation-enhanced corrosion.

While the effects induced by radiation have been studied by many researchers [30, 111, 130, 135, 166], they can be generally divided into two categories: analysis of changes in the metal matrix and changes in the oxide film. Here I concentrate on the changes in the metal matrix induced by exposure to radiation. This chapter discusses the characterisation of radiation damage in the metal matrix of the Zr-2.5Nb alloy. Since it is a dual phase alloy, the changes in the α-Zr matrix and the β phase regions will both be studied and described separately.

4.1 Damage in the α-Zr matrix

The types of radiation-induced damage in the α-Zr matrix generally include the formation of dislocation loops, stacking faults and the dissolution of SPPs [104]. For Zr-Nb alloys, there is also radiation-induced formation of Nb-rich precipitates [11, 12]. This chapter mainly discusses radiation-induced Nb precipitates and the formation of dislocation loops since they are directly related to change of the Nb concentration in solid solution and the hardening of the α-Zr matrix.

4.1.1 Radiation-induced Nb precipitates in the α-Zr matrix

The formation of the nano-size Nb particles has been identified in different forms of Zr-Nb alloys irradiated to high fluences by neutrons [15, 107, 111], yet detailed investigations were only reported recently [115]. Several questions remain unclear regarding the formation, distribution and evolution of these Nb precipitates. Moreover, most previous studies were carried out on recrystallised Zr-Nb alloys in which the excess Nb over the solubility limit is mainly accommodated in β-Nb SPPs. On the contrary, the alloy studied here has gone through β quenching during fabrication, thus most of the excess Nb is in the form of sheets of the β-Zr phase at the α grain boundaries. In this section, neutron radiation-induced Nb precipitates in the α-Zr matrix in this dual phase alloy are characterised.

4.1.1.1 Methods

The first step to characterise these Nb precipitates is to image them in TEM under specific diffraction conditions. Due to the similarity in size and morphology, it is very important to distinguish the precipitates from other radiation-induced features, such as dislocation loops. All the images were taken close to zone axis $\langle 11\bar{2}0 \rangle$ with g = $\langle 0002 \rangle$. This ensures that all a-loops are invisible, and c-loops appear to be lines along basal plane. The Nb precipitates can then be identified. The kinematic bright-field imaging mode was used in all cases since it provides contrast with apparent size close to the physical size of the feature of interest [150].

The quantitative analysis of these precipitates includes calculating the number density and measuring the size distribution in different samples. A series of images at different magnifications were taken to meet different requirements. For calculating the number density of the precipitates, images were taken to cover an area as large as possible, as long as the precipitates can still be counted without ambiguity. Different grains from at least two different TEM lift-out samples from the same corrosion condition were looked at to ensure the minimum of grain-to-grain difference. EELS was used to measure the thickness of the TEM foil to calculate the number density of the precipitates per unit volume. For estimating the size distribution of the precipitates, images were taken at a relatively high magnification to allow for precise measurements. The common magnification used was 300kx to ensure that the corresponding pixel size in a 2048 ×

2048 image was 0.05 nm, beyond the resolving power of the instrument. Thus the minimum size that can be measured with confidence is only determined by the capability of the microscope and the condition of the TEM foil. It is also good practice to set a minimum threshold of the measured size with confidence. Any features observed with size below this threshold are not taken into account due to large measuring uncertainty and limited instrument capability. In this study, any features smaller than 1 nm were excluded.

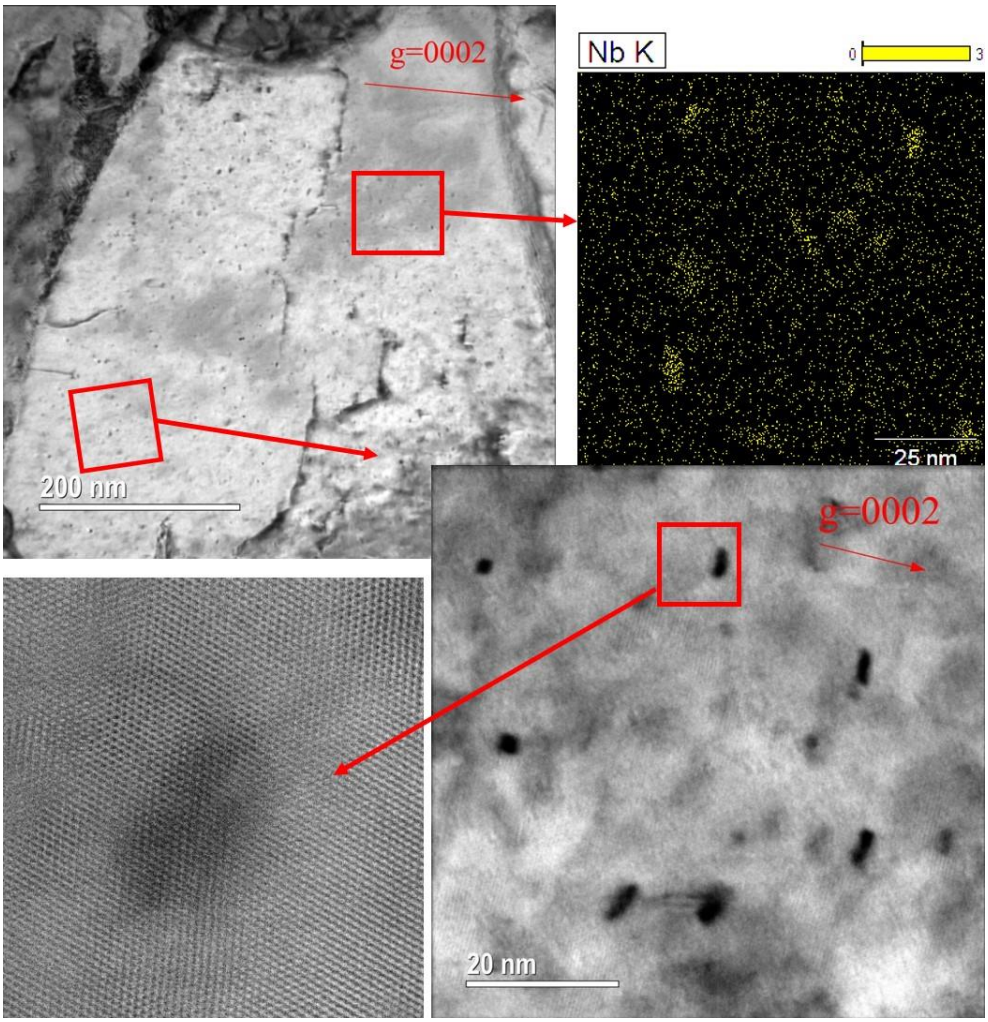


Figure 4.1 TEM kinematic bright-field images, high resolution STEM ABF image and STEM EDX mapping of the features of interest in a Zr-2.5Nb sample irradiated to 2 dpa at 325 °C.

EDX mapping and line-scans were also carried out to help confirm the presence of Nb-rich precipitates. High resolution STEM was also used to help determine the microstructure of these small precipitates. A schematic showing the different scales of the characterisation methodologies is shown in Figure 4.1.

4.1.1.2 Results

Five sets of samples from different conditions have been investigated to study the radiation induced precipitates. These include

(1) B70, 190 days in-flux corrosion at 325 °C, neutron damage to about 2 dpa

(2) B74, 2750 days in-flux corrosion at 325 °C, neutron damage to about 25 dpa

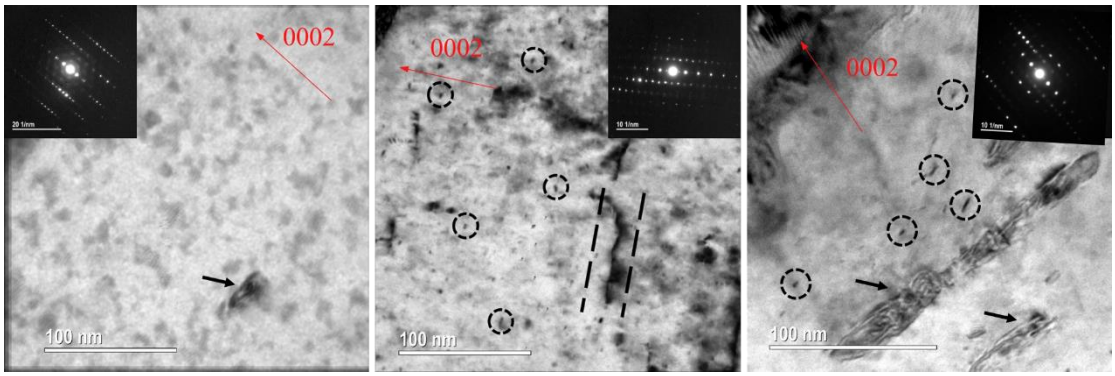
(3) B56, 190 days in-flux corrosion at 250 °C, neutron damage to about 2 dpa

(4) B96, 185 days out-of-flux corrosion at 325 °C, no neutron damage

(5) B88, 2850 days out-of-flux corrosion at 325 °C, no neutron damage.

In the following text, only the material code (B70 etc.) will be used for convenience.

Typical images showing the α-Zr matrix at the same diffraction conditions in three samples are shown in Figure 4.2. After looking at several α-Zr grains from at least two TEM lamella from each sample, it appears that the radiation induced precipitates only exist in B70 and B74. Very few have been seen in B56, not enough for reliable quantification with good statistics. No sign of the precipitates has been seen in B96 or B88. So the following analysis only involves characterisation of B70 and B74 samples.



(a) (b) (c)

Figure 4.2 Kinematic Bright-Field images showing the distribution of irradiation-induced features in (a) B56, (b) B70 and (c) B74. The circled black dots are radiation-induced Nb precipitates, the features marked by arrows are hydrides, and the features between the dashed lines are c-loops. It should be noted that not all the Nb precipitates have been circled. The vague black features in the background are surface oxide formed on the TEM foils.

About 100 Nb precipitates from several different grains have been measured. Almost all the precipitates have an elongated elliptical shape, hence the lengths of the long axis and short axes were both measured. The results are shown in Table 4-1.

Table 4-1 Average lengths and aspect ratio of the radiation induced Nb precipitates detected in B70 and B74 samples

Samples	Average long axis (nm)	Average short axis (nm)	Aspect Ratio
B70 (2 dpa)	5.0 ± 1.3	2.4 ± 0.5	2.2 ± 0.7
B74 (25 dpa)	8.7 ± 3.6	3.2 ± 1.0	2.7 ± 1.4

These values are comparable to the results reported by other researchers at similar damage levels [107]. But merely using the average values to represent the size changes of the precipitates can provide limited information. In order to show more accurately the size distribution, the length values along long and short axes of all precipitates

detected in the two samples are plotted in a histogram, as shown in Figure 4.3.

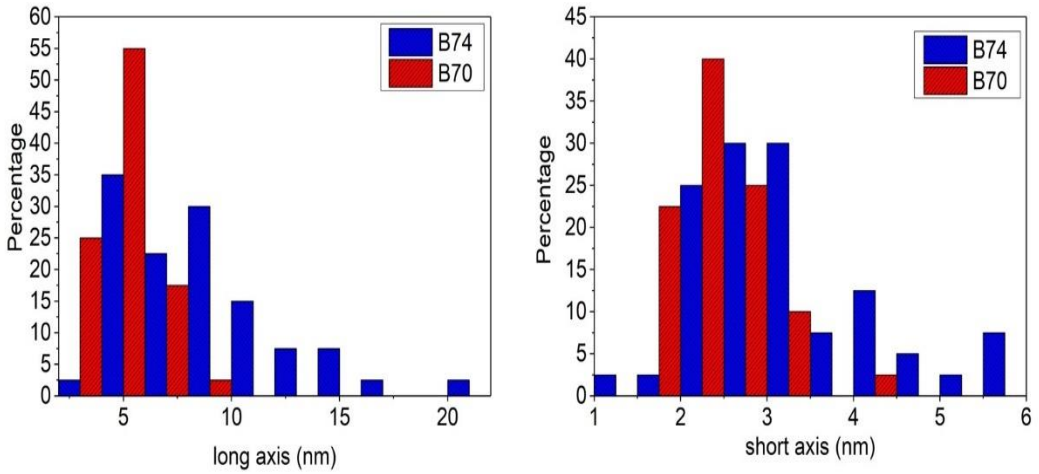


Figure 4.3 Histograms showing the size distribution of the Nb precipitates found in B70 and B74 along the long and short axes.

The distributions of both the long and short axes show a clear tendency to increase with the accumulation of radiation damage. If we adopt the classical 'nucleate-growth' model of the precipitation in a metal matrix [167], this is not surprising considering the much longer time spent under neutron radiation by B74, which allows time for Nb to diffuse towards the growing precipitates. What is interesting to consider is that the average length of the Nb precipitates is already 5 nm at 2 dpa, but only increases to 8.3 nm at 25 dpa. And even for the precipitates formed in B74, most of them have a long axis about 5 nm and short axis about 2 – 3 nm, similar to those found in B70. The distribution also shows a 'broadening' from 2 dpa to 25 dpa. These pieces of observation will be put together below when discussing the formation and evolution of the Nb precipitates in the α-Zr matrix under neutron irradiation.

The number density of the precipitates in both samples has also been calculated, as shown in Table 4-2. The error of the measurements comes from two aspects, counting error and grain-to-grain differences. Although all the counting work was done in images of relatively high magnification and limited ambiguity, it is inevitably difficult to decide whether some features of vague contrast are precipitates or not. It also appears that the density of the precipitates can differ from grain to grain. In order to minimise the impact from this potential source of error, I have taken images from several different grains, and it is ensured that these grains are all far away from the metal / oxide interface (at least 2 μm away and with a layer of α-Zr grains in between) to minimise the impact from the oxidation induced stress accumulation. What is observed is a decrease of the density of precipitates from 2 dpa to 25 dpa. Compared to the results reported on neutron irradiated M5^{TM}, the number density at 2 dpa is similar, while the density was reported to remain roughly the same in the M5 study but decreases at 25 dpa in this study. This discrepancy will be discussed in Section 4.1.1.4.

Table 4-2 Number density of the Nb precipitates found in B70 (2 dpa) and B74 (25 dpa)

Precipitates Number Density	B70 (2 dpa)	B74 (25 dpa)
$\times 10^{22}$ / m^3	1.01 ± 0.25	0.55 ± 0.14

An interesting property to report regarding the Nb precipitates is their orientation distribution with respect to the orientation of the α-Zr matrix. Although there is a debate on whether these Nb precipitates are 'needle' shape [107] or 'platelet' shape [115], it is

generally agreed by these researchers that the long axis of the precipitates lies along the α-Zr basal plane. Since all the images here were taken at $g = \langle 0002 \rangle$, the angles between the long axis of the precipitates and the basal plane can be measured easily. As plotted in Figure 4.4, there is a trend that the longer the precipitate is, the more likely it is to be aligned with the basal plane.

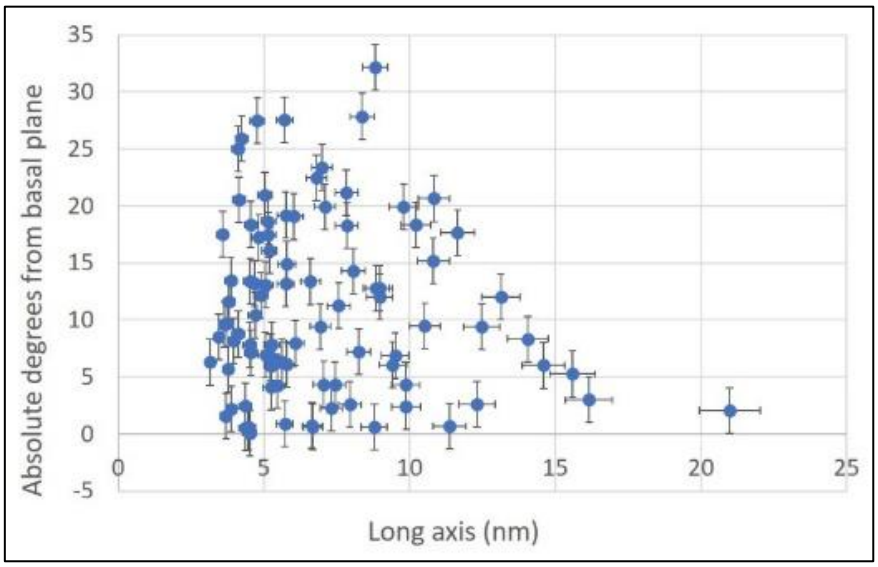
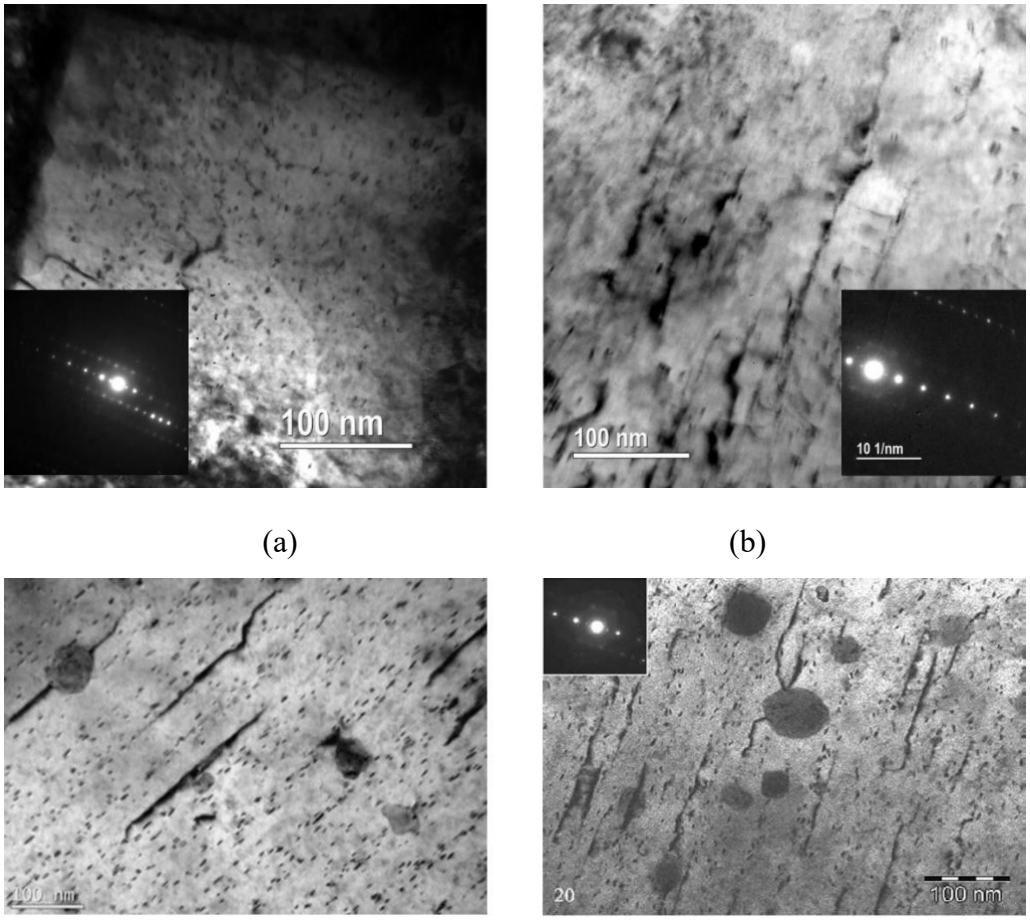


Figure 4.4 The angle between the long axis and the α-Zr basal plane against the length of the long axis for each precipitate. A 10% error is added to the measurement.

The obvious alignment of the Nb precipitates along the basal plane reported by previous researchers [107, 115, 168] is also called the 'rafting' phenomenon. It is compared to the 'rafting' phenomenon observed in Ni super alloys [169, 170] and is assumed to result from the much faster drift of the interstitials to the dislocation loops compared to the drift of the vacancies. In this study, the 'rafting' phenomenon does not always occur, even in the same sample. Figure 4.5 shows a comparison between the precipitate

distribution in the Zr-2.5Nb alloy and other Zr-Nb alloys. Regions (a) and (b) are from two different grains in a same sample, irradiated to about 25 dpa. While the Nb precipitates in (a) show a random distribution, the ones in (b) show some degree of 'rafting'. The main difference between these two regions is the existence of c-loops. When c-loops are present, the Nb precipitates tend to show a good alignment. This is supported by (c) and (d) where c-loops are present in both cases. The implication of this phenomenon will be discussed further in section 4.1.1.4.



(a) (b)

(c) (d)

Figure 4.5 TEM kinematic bright field images showing the Nb precipitates at g=0002 in (a) and (b) Zr-2.5Nb alloy irradiated to the fluence of $1.03 \times 10^{26} m^{-2}$, (c) M5^{TM} irradiated to $1.36 \times 10^{26} m^{-2}$ [107], (d) E110 irradiated to $3.6 \times 10^{26} m^{-2}$ [168].

4.1.1.3 Identification of fully coherent Nb clusters

The number density of the Nb precipitates measured by the TEM diffraction contrast can be compared to the number density of the Nb clusters identified by Atom Probe Tomography (APT). As shown in Table 4-3, the number density of Nb clusters measured by APT is about 10 times of the value measured by TEM in both samples.

Table 4-3 Number density of Nb clusters as measured by TEM and APT in different samples. The APT data is provided by Anne Callow

Sample	Number Density (No. per m^3)	
	By APT	By TEM
B70	1.3×10^{23}	1.0×10^{22}
B74	4.9×10^{22}	5.5×10^{21}

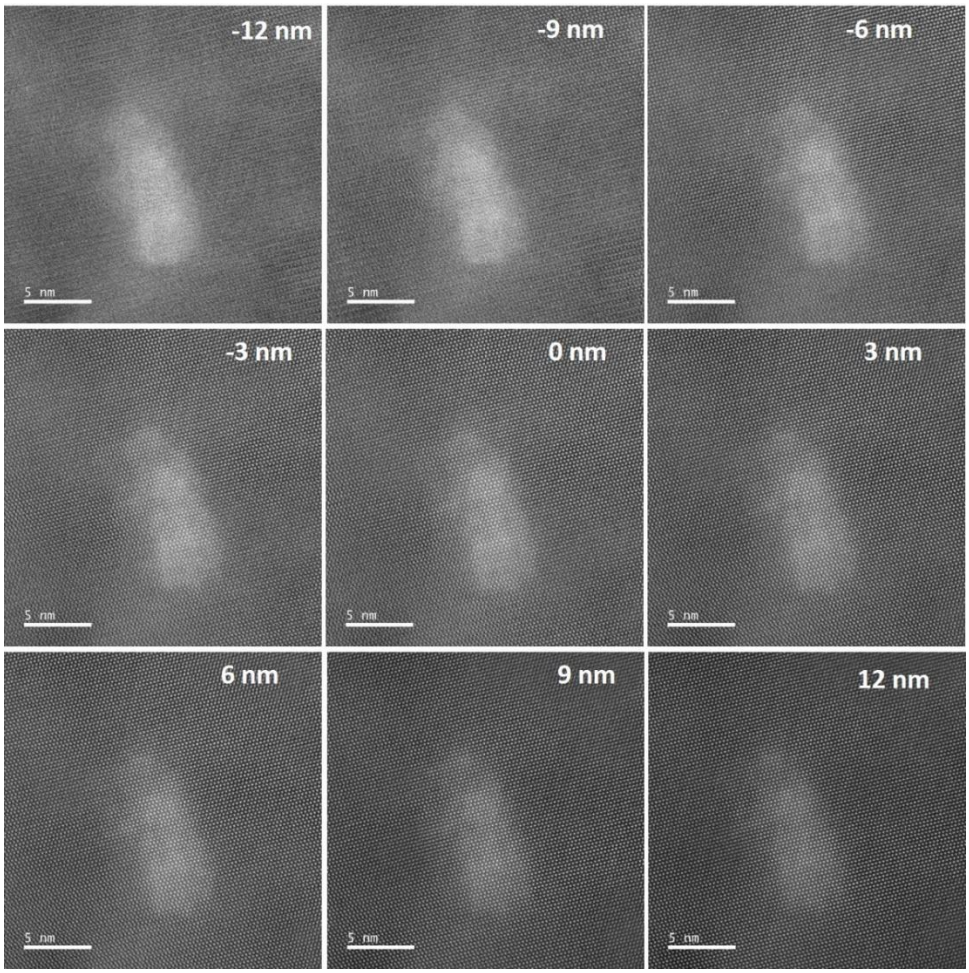
This discrepancy is thought to come from the different imaging / counting mechanisms by TEM and APT. Under TEM kinematic bright-field imaging, only those precipitates that cause sufficient local lattice distortion can produce enough contrast change to be imaged [150]. Meanwhile in APT clusters containing only a few Nb atoms can be identified [171]. This difference gives a hint that there might exist large concentration of Nb clusters that do not cause enough local lattice distortion in the neutron-irradiated α-Zr matrix to be detected by TEM imaging.

To validate this assumption, the neutron irradiated samples were put into the Grand ARM at the Harwell ePSIC facility with lattice imaging capabilities for high resolution

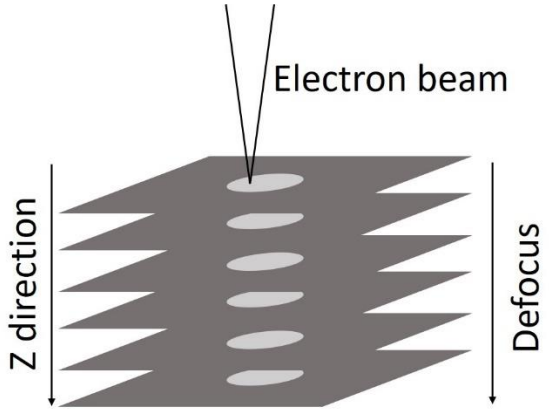
STEM. HAADF images were taken to help locate the Nb clusters in the matrix since this imaging mode only depends on average mass contrast regardless of the microstructure. A technique called 'Optical Sectioning' was used by carefully tuning the defocus value in order to take a series of images of different focus planes across the entire thickness of the TEM foil. Therefore, the information on microstructure changes along the electron beam direction can be revealed. An example of the application of the 'Optical Sectioning' technique for individual dislocations is shown in [153].

It is shown in Figure 4.6 that a Nb-rich cluster has the same lattice structure as the surrounding hcp α-Zr matrix throughout the whole thickness of the TEM foil. This is a direct observation of a fully coherent Nb cluster in the neutron irradiated Zr matrix.

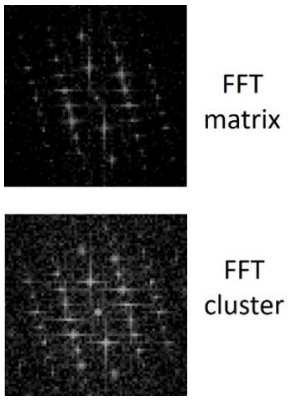
This result agrees well with the assumption made by Matsukawa et al. regarding irradiation-induced Nb precipitation in the α-Zr matrix [118]. Based on the calculations of the obstacle strength of the irradiation induced Nb clusters, they proposed the existence of hcp Nb clusters, but did not provide any direct evidence. The characterisation work presented in this section confirms the existence of coherent hcp Nb clusters.



(a)



(b)



(c)

Figure 4.6 (a) A series of HAADF images of different defocus values showing a Nb cluster that is fully coherent to the α-Zr matrix. (b) schematic showing the physical layout of the serial images when taking under STEM (c) the FFT of the cluster and matrix regions. The cluster is in a B70 sample.

4.1.1.4 The formation and evolution of irradiation induced Nb precipitates

Based on the characterisation of irradiation induced Nb precipitates in five (B56, B70, B74 and B96, B88) samples, the formation and evolution of these precipitates can be discussed. The key observations are reiterated here,

(1) The TEM-detectable Nb precipitates usually form in samples irradiated at 325 °C (B70, B74), while hardly form in samples irradiated at 250 °C (B56). No obvious precipitates were detected in either of the non-irradiated samples (B96 and B88).

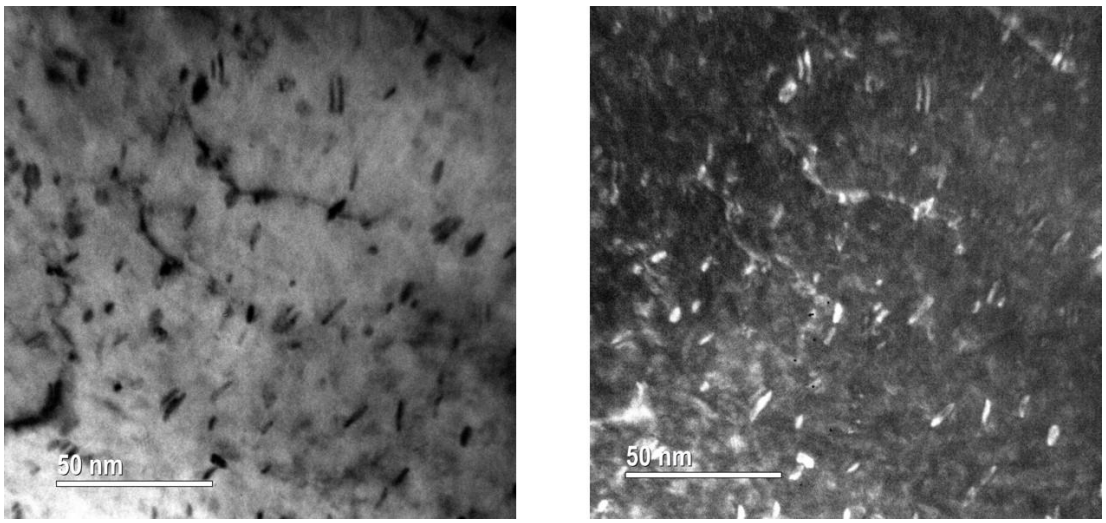
(2) As the radiation damage accumulates from 2 dpa to 25 dpa at 325 °C, the average length of the precipitates increases from 5.0 nm to 8.7 nm, and the aspect ratio increases from 2.2 to 2.7. Meanwhile, the number density of the precipitates decreases from $1.0 \times 10^{22}\, m^{-3}$ to $5.5 \times 10^{21}\, m^{-3}$.

(3) The larger the precipitates are the more likely they are to be well aligned with the basal plane. For precipitates in a same sample the well aligned ones are more likely to be associated with the existence of c-loops.

(4) Nb clusters fully coherent with the α-Zr matrix are identified in samples irradiated at 325 °C and assumed to be present in high concentration based on the comparison between the TEM and APT analysis.

The first thing to make clear is the microstructure of the Nb-rich precipitates formed under irradiation. The clear contrast in kinematic bright field and weak beam dark field TEM images (Figure 4.7) has shown that significant local matrix lattice distortion has

been introduced by these precipitates. This implies that the precipitates detected by TEM are incoherent with the matrix. According to the literature, these Nb-rich precipitates are thought to be bcc β-Nb since they remained stable when the irradiated samples were annealed [107]. The bcc structure was also confirmed by synchrotron diffraction [107], yet the deconvolution of the large β-Nb SPPs existing before irradiation has introduced a large uncertainty of the result. A clearer characterisation by high resolution TEM was reported recently on the neutron irradiated M5^{TM} samples supporting the bcc structure of the precipitates [115]. However, the samples investigated in that paper have been annealed at 450 °C for 960 hours. Such annealing might have introduced substantial changes to the microstructure of the precipitates. Therefore, the microstructure of the Nb-rich precipitates cannot be confirmed with 100% confidence. I have also tried to investigate the microstructure of the Nb precipitates using high resolution STEM imaging but have not found clear evidence supporting the bcc structure. In this discussion, I will adopt the results from the literature and assume the large incoherent precipitates are bcc β-Nb. Therefore, there are two types of precipitates in the neutron irradiated α-Zr matrix, the relatively smaller, fully coherent hcp Nb and the relatively larger, incoherent bcc Nb.



(a) (b)

Figure 4.7 Kinematic bright field (a) and weak beam dark field (b) images showing the same region containing Nb-rich precipitates in a B74 sample.

There is a debate on the formation mechanism of the irradiated-induced bcc Nb precipitates. Unlike the formation of large β-Nb SPPs by the eutectoid reaction during alloy fabrication, the formation of these precipitates takes place at the temperature below the eutectoid point (about 620 °C). It is without any doubt that the formation requires firstly the gathering of Nb atoms so that the local Nb concentration exceeds the solubility limit. But the Zr-Nb phase diagram at equilibrium state [172] does not provide information on the jump from 'Nb enrichment in α-Zr exceeding the solubility limit' to the formation of β-Nb phase below the eutectoid temperature.

In theory, there are two possible paths for this precipitation process, α-Zr → β-Zr → β-Nb or α-Zr → α-Nb → β-Nb. Some previous researchers proposed that the first path is energy preferred based on ab initio calculations [117]. They proposed that an in-situ

transformation of α-Zr → β-Zr → α-Zr + β-Nb [173] happens under irradiation, and the formation of the β-Zr is the intermediate step for precipitation of the β-Nb [117]. However, these irradiation-induced β-Nb precipitates have only been reported in α-Zr matrix with no sign of existence of the β-Zr phase. I have also looked at the β-Zr regions in this neutron irradiation Zr-2.5Nb alloy (discussed in Section 4.2) and have not found signs of the nano platelet Nb precipitates. Moreover, it has been shown in previous research that the bcc – Zr can transform to hcp – Zr [28, 102], not the opposite direction when irradiated below the eutectoid temperature. Therefore, the first path seems unlikely.

The identification of the fully coherent hcp Nb precipitates implies the second path to be more possible. This process involves three steps. Firstly the solute Nb atoms cluster together by diffusion and nucleate an hcp Nb core. Then more solute Nb atoms diffuse towards the core. This direction is determined by thermal dynamics based on the temperature (about 300°C) and Nb concentration of the core (well below the equilibrium value ~90% as measured by APT shown in Table 4-4). As the Nb atoms accumulate and the hcp Nb precipitate grows, the third step happens where the conversion from hcp Nb to bcc Nb occurs. The free energy of the equilibrium bcc structure is lower than that of the hcp structure for Nb precipitates, and the surface to volume ratio reduces with the growth of the precipitates. When the free energy difference overcomes the surface energy, the precipitates will convert from coherent

hcp Nb to incoherent bcc Nb. This process is not only seen in the Zr-Nb system under irradiation. A similar process is seen in the formation of Cu rich precipitates in irradiated or strained ferrite [174–177]. It has been shown that Cu rich precipitates firstly form in the bcc structure (coherent with matrix), then transform into 9R or fcc phases. After the formation of the equilibrium bcc Nb in my samples, further diffusion of Nb atoms in solution will keep the precipitates growing.

The impact of the irradiation is then to be discussed, mainly considering the effect of radiation enhanced diffusion (RED). As seen in the previous paragraph, the diffusion of solute Nb atoms plays an important role in the formation of the Nb rich precipitates. In the equilibrium state without irradiation, diffusion of Nb in the α-Zr matrix is very slow [178]. Under irradiation, large concentrations of SIAs and vacancies are created in the α-Zr matrix. Since the SIAs diffuse much faster than the vacancies [87], some SIAs will escape recombination with the vacancies and diffuse towards other sinks (grain boundaries etc.). As radiation damage continues, an excess of vacancies will be created in the matrix, which is then able to enhance the diffusion of the Nb atoms in solution. The existence of RED explains why the Nb rich precipitates can only be seen in in-flux samples (B70 and B74) but not in out-of-flux samples at the same temperature (B96 and B88).

The impact of temperature on the diffusion of the solute Nb atoms can also be discussed.

Although the diffusion coefficients of Nb atoms under different irradiation conditions have not been calculated, this topic can still be tackled by investigating the diffusion of vacancies in different conditions, since RED is the dominant mechanism. Figure 4.8 shows the diffusion coefficients of vacancies in α-Zr matrix calculated by previous researchers [179]. The diffusion coefficient of vacancies at 325 °C is about 10 times higher than the diffusion coefficient at 250 °C. For a roughly same damage rate at the two temperatures, we might expect that the radiation-enhanced diffusion of the Nb atoms at these two temperatures are roughly 10 times different. This could explain the absence of the precipitates detected by TEM in B56.

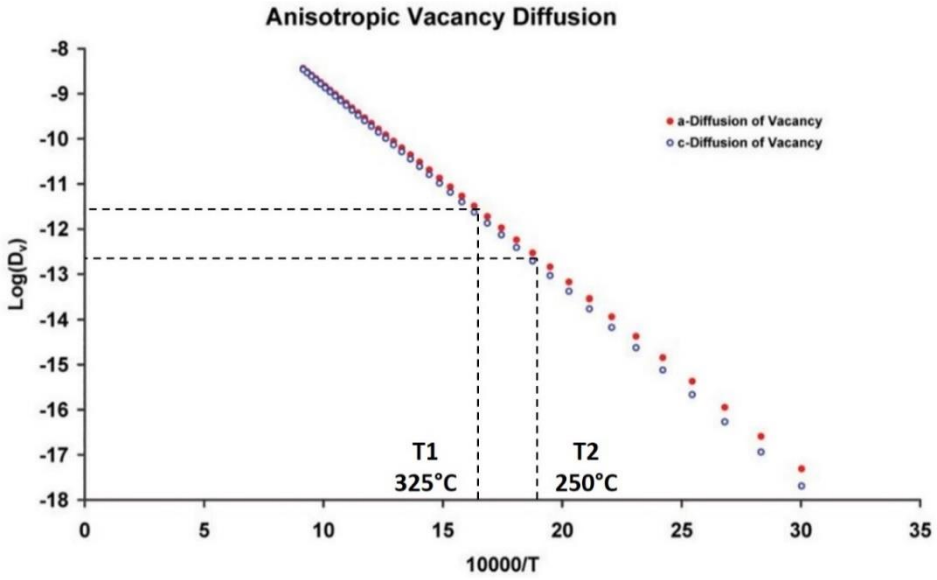


Figure 4.8 Arrhenius plots of the calculated diffusion coefficients of vacancies along the a and c directions [179], with the two irradiation temperatures used in this study marked

The decreased number density of the precipitates from 2 dpa to 25 dpa has indicated that the destruction of the precipitates is occurring simultaneously with the formation

and growth process. The destruction is attributed to neutron-cascade-induced mixing. It is proposed that this cascade-producing irradiation will tend to expel Nb atoms from the smaller precipitates and allow the large ones to survive. This is confirmed by the histograms showing the size distribution of the Nb precipitates found in B70 and B74 along the long and short axes, Figure 4.3. In addition to the increase in average size, the slope towards the larger sizes has also been broadened, indicating the main contribution to the average size increase comes from those relatively large precipitates. It should be noted that this decrease of number density was not reported by researchers studying the neutron irradiated M5^{TM} samples [107]. Instead, they claimed the number densities to be 'constant' from 1 cycle (about 3 dpa) to 7 cycles (about 20 dpa) [107]. But a close look at the data showed that the number densities fluctuate from $1 \times 10^{22} m^{-3}$ to $2 \times 10^{22} m^{-3}$, implying a significant error bar in calculating the number density. This is thought to be a result from the limited volume of samples investigated, after all the TEM foils observed were only several um^3 in volume and only hundreds of precipitates were counted. Nevertheless, the histograms can provide more information about the distributions of the precipitates.

The correlation between the alignment of the precipitates with the basal plane and the size of the precipitates is thought to be a result of the different diffusion rates of the Nb atoms along the basal plane and the c direction. When the Nb clusters are fully coherent with the α-Zr matrix, the long axis can be along any direction, for instance the one

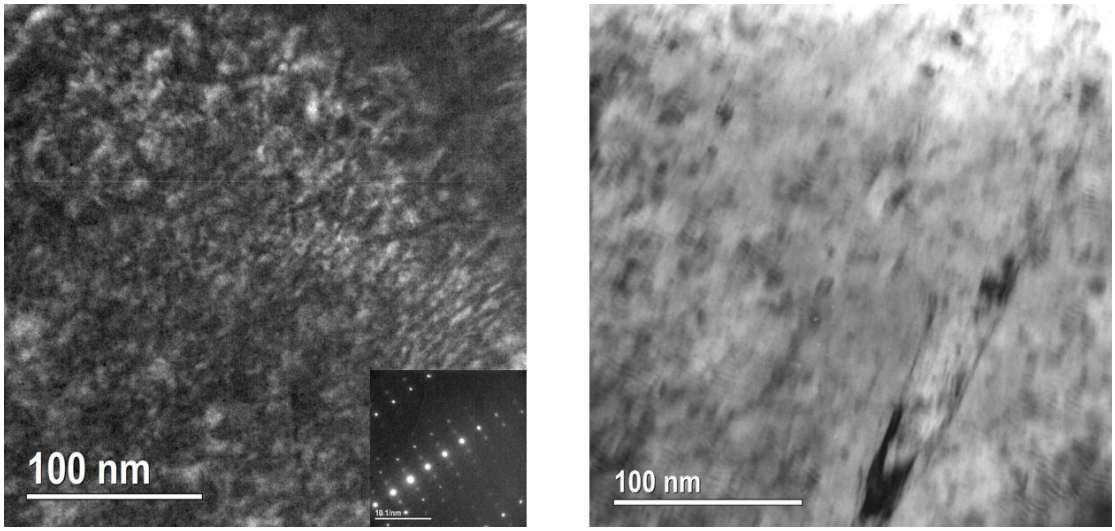
shown in Figure 4.6. But when the clusters turn into bcc precipitates, the shape will gradually be dominated by the newly added Nb atoms diffusing towards them. Since the Nb diffusion rate along the basal plane is reported to be higher than that along the c direction [180], it is not surprising to observe the phenomenon shown in Figure 4.4. This is also supported by the calculation work by Sarce [181].

The preferential diffusion of Nb atoms along certain directions in the Zr matrix is also thought to be the cause of the relation between the 'rafting' phenomenon and the appearance of the c-loops, as shown in Figure 4.5. The preferential diffusion of the SIAs towards the vacancy c-loops leaves a high concentration of vacancies, and hence enhances locally the diffusion of solute Nb atoms. Thus the orientation of the Nb precipitates near the c-loops show a better alignment with the basal plane, while those precipitates far from c-loops show a less aligned distribution due to slower local diffusion of Nb atoms.

4.1.2 Dislocation loops

In addition to the irradiation-induced Nb precipitates, a type and c type dislocation loops are also reported in neutron irradiated Zr-Nb alloys [100, 105, 166]. Here I will only report qualitative rather than quantitative analysis of dislocation loops in the Zr-2.5Nb alloy, mainly due to the poor counting statistics.

In the characterisation of the a-loops, $g = \langle 10\bar{1}0 \rangle$ was used for imaging. To avoid the potential misinterpretation of the contrast by other features such as the surface oxide, the same region was also imaged using $g = \langle 0002 \rangle$ and the 'invisible criteria' was applied to confirm the appearance of the a-loops. Typical images showing the damaged α-Zr matrix are displayed in Figure 4.9. Without precise statistical analysis, it generally appears that the number density of the a-loops has decreased from 2 dpa to 25 dpa. This trend agrees well with previous reports on the correlation of decreased a-loop density and increased c-loop density with the accumulation of radiation damage [103, 182].



(a) (b)

Figure 4.9 Kinematic bright field images showing the neutron irradiated α-Zr matrix in (a) B70 2 dpa (b) B74 25 dpa. The same $g = \langle 10\bar{1}0 \rangle$ was used in both images.

With the $g = \langle 0002 \rangle$ condition, the c-loops intersect the image plane perpendicularly, (and appear to be lines), so the linear density can easily be measured. It was observed that the c-loops were not evenly distributed in all the grains. Even in the same TEM

sample, a high linear density of c-loops can be observed in one grain, while almost no c-loops were detected in another grain. An example is given in Figure 4.5 (a) and (b). This is assumed to be a result of the unevenly distribution of stress in different grains, during the cold work in the manufacturing process [183].

Enrichment of Nb along the c-loops was also observed, as shown in Figure 4.10. It is not clear whether the Nb atoms segregate to the c-loops or the c-loops preferentially form in regions of high Nb concentration. Nevertheless, the Nb-enriched c-loops help to reduce the Nb concentration in solid solution in the matrix.

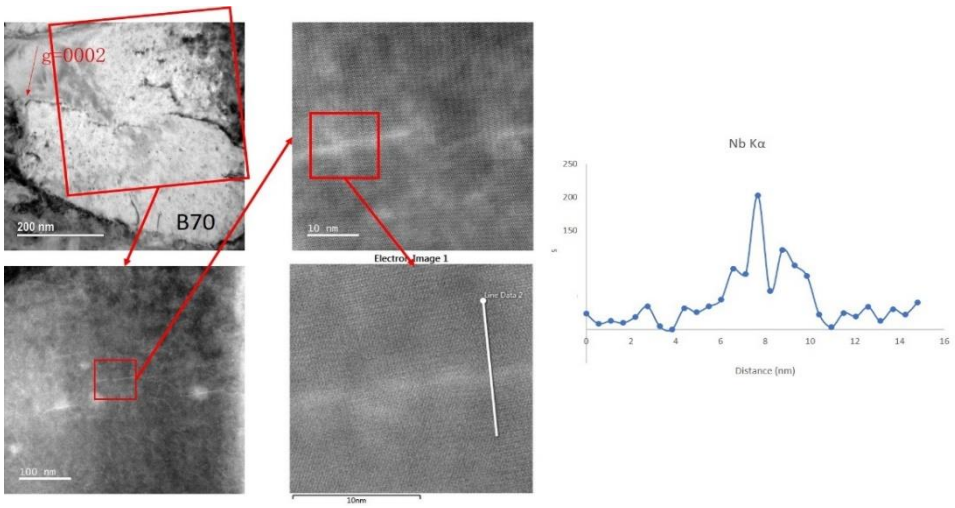


Figure 4.10 HAADF images at different magnification and EDX line-scan showing Nb segregation to a c-loop in B70 (2 dpa)

4.1.3 The impact on the corrosion of the alloy

The formation of the nano-size Nb precipitates and clusters and the Nb enrichment along c-loops can lead to the reduction of Nb in solution in the α-Zr matrix, as shown

by the APT results in Table 4-4. A lower Nb concentration in the metal matrix is proposed to benefit the resistance to oxidation of the alloy [37].

Table 4-4 Nb compositions in matrix and clusters measured by APT, courtesy by Anne Callow

Nb compositions from APT	Nb in matrix (at%)	Nb in clusters (at%)
B166 (starting sample, non-irradiated)	0.45	-
B70	0.27	76
B74	0.17	73

However, there is a remaining question on the actual effect of the radiation-induced reduction of Nb concentration in the metal matrix. If the Nb precipitates formed due to neutron irradiation are oxidised and release Nb back to the oxide matrix instantly, the actual Nb composition at the metal/oxide interface region might not be as low as predicted. Although the 'delayed oxidation' effect is well known for large β-Nb SPPs [135], there is a good chance of rapid oxidation of the much smaller Nb precipitates due to a much higher surface to volume ratio.

In order to investigate the stability of the radiation-induced Nb precipitates and clusters during oxidation, several EDX maps were taken at different regions in the oxide, as shown in Figure 4.11. It is clear that the Nb precipitates could retain their shape and enrichment of Nb up to about 700 nm into the oxide. Therefore, the Nb atoms gathered at the precipitates are not released to the oxide matrix instantly after being incorporated into the growing oxide. According to the C4 model [37], this is beneficial to the

resistance against the oxidation of the alloy.

It should be noted, however, that the precipitates captured in the EDX maps are only the relatively larger (> 5 nm) ones. Despite several attempts to look for the smaller clusters, they were not detected by EDX mapping. This can be a result of either the clusters being too small hence the Nb signals are buried in the signal noise, or the absence of the small clusters in the oxide. It is therefore unclear whether the small precipitates and even the fully coherent Nb clusters will remain stable after being incorporated into the oxide. Nevertheless, the portion of the Nb matrix composition reduction contributed by the Nb trapping in the relatively large Nb precipitates is retained shortly after being oxidised.

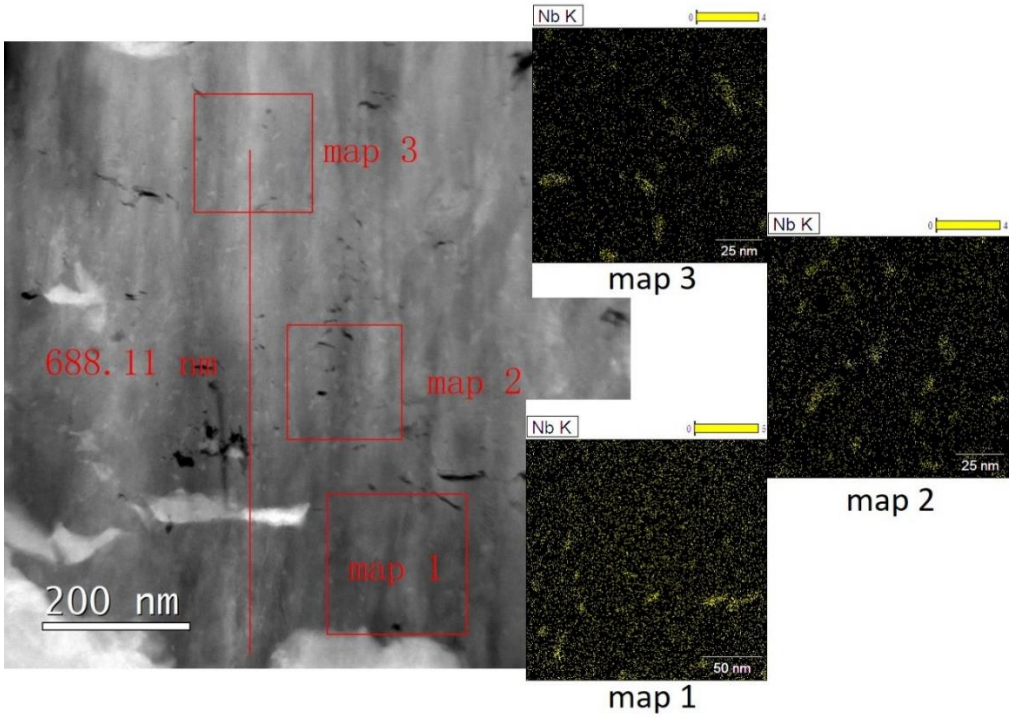


Figure 4.11 A HAADF image showing the oxide region near the metal/oxide interface in B74, together with three EDX maps showing the appearance of the Nb precipitates in oxide

4.2 Damage in the β phase regions

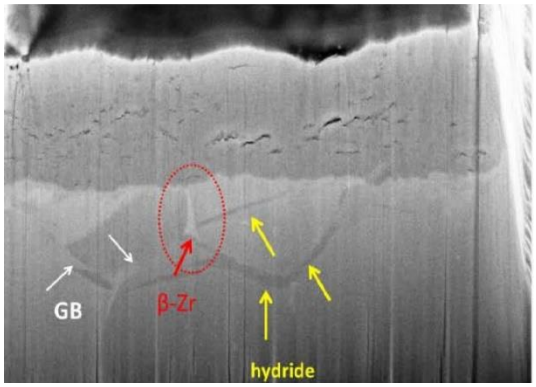
One major difference between the Zr-2.5Nb provided by CNL and other Zr-Nb alloys like Axiom™ from Westinghouse™, M5™ from Framatome etc., and the focus of much of the work in this thesis, is the presence of the β-Zr phase. As shown by Jing Hu in her thesis [19], both the microstructure and resistance to autoclave corrosion can be apparently different between alloys of roughly the same content of alloying Nb (Zr-1.0Nb) with and without the β-Zr phase [19]. It is therefore of great importance to study how these β-Zr phase regions behave under neutron irradiation and how the corrosion resistance is impacted. This section presents the characterisation work of the β phase regions in the metal matrix in the samples corroded in- and out-of neutron flux.

4.2.1 The morphology and microstructure of the β phase

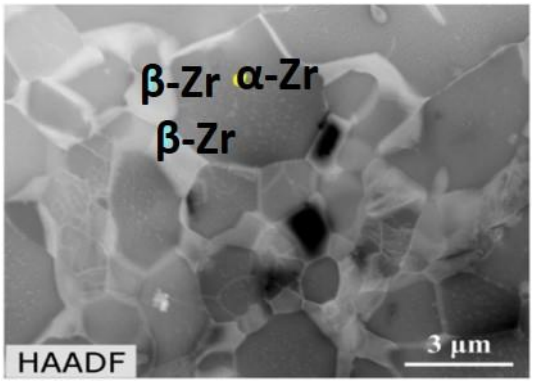
The Nb enriched β-Zr phase usually forms when the alloy contains a Nb content that exceeds the solubility limit (0.6 wt % maximum) in α-Zr and is heat treated above the monotectoid temperature (620 ºC) [172]. The morphology of the β phase varies in different alloys due to the different heat treatment history, as shown in Figure 4.12.

Figure 4.12 (a) shows an SEM image taken on the 'annealed' Zr-1.0Nb provided by Westinghouse™, taken by Jing Hu. The alloy has been through a 24h annealing at 720ºC after the recrystallisation stage at 560ºC. This annealing step has created β-Zr grains, mostly triangular in shape and sitting at the grain boundary triple points. A close

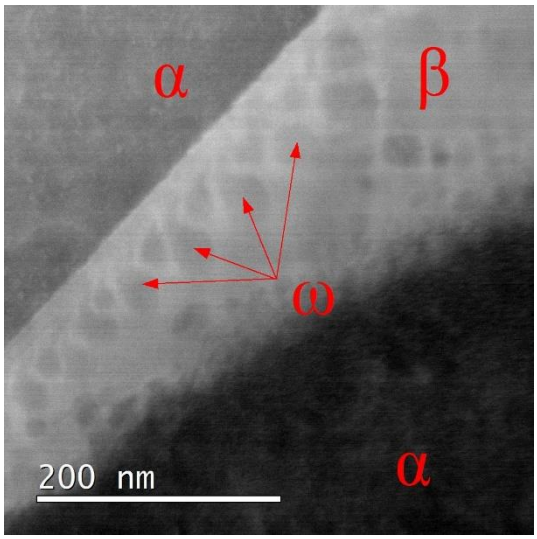
look at these β-Zr grains shows that they have a complex microstructure, consisting of many Nb depleted small squares (assumed to be ω-Zr) in a Nb enriched network (assumed to be β-Zr), as shown in Figure 4.12 (c). A similar microstructure is also seen in β-Zr grains in the Zr-Excel alloy as shown in Figure 4.12 (d). Due to a higher amount of Nb (2.5 wt%) in the alloy, the β-Zr grains take a higher volume fraction, but they still sit at the grain boundaries of the α-Zr grain, as shown in Figure 4.12 (b).



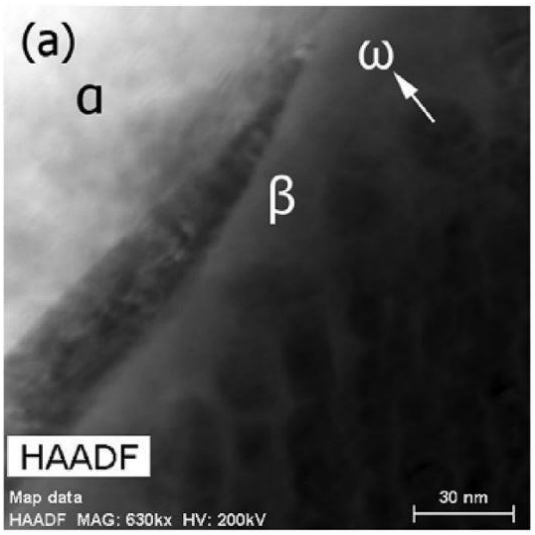
(a)



(b)



(c)



(d)

Figure 4.12 Different forms of β phase in different alloys (a) Annealed Zr-1.0 wt% Nb by Westinghouse [19] and (c) the microstructure of the beta Zr grain showing the existence of the omega Zr phase, (b) Zr-Excel alloy from CNL [184] and (d) the microstructure of the beta Zr grain containing omega Zr phase [28]

Unlike these two cases, the alloy studied in this project is trepanned and extruded at 815 °C, followed by a stress relieving stage at 400 ºC for 24 hours. This results in a unique microstructure where the α-Zr grains are elongated parallel to the hoop direction of the tube, and the β phase sits at the grain boundaries forming a network, as shown in Figure 3.1. A clear difference from the β-Zr grains in the previous two alloys is that most of the β phase regions are parallel to the hoop direction, thus perpendicular to the direction of oxidation.

The microstructure of these β phase regions was investigated by TEM diffraction and STEM EDX/EELS. By looking at more than 50 β phase regions in several different samples, I concluded that they can roughly be divided into two categories judged by the morphology. The first type, as represented in Figure 4.13 (a) and (b), is relatively wide and contains a fragmented internal structure as seen most clearly in the dark field image in (b). The second type, as represented in Figure 4.13 (c) and (d), is thinner and with a more uniform internal structure. It should be noted that these two categories are arbitrarily set and there is no clear-cut boundary between them. Furthermore, some of the β phase regions contain different regions with microstructures characteristic of the two different types.

Now let us consider the decomposition of the β-Zr phase. It is reported by many previous researchers [161, 185–188] that β-Zr is a metastable phase at the irradiation

temperatures (325 °C and 250 °C) and will undergo a transition as below,

$$\beta\ Zr\ \rightarrow\ \omega\ Zr + \beta\ Zr\ (Nb\ enriched)\ \rightarrow\ \beta\ Nb + \alpha\ Zr$$

Neither of these two steps is an instantaneous reaction, therefore the β phase regions found in a sample may very likely be a mixture of several components including β-Nb, α-Zr, ω-Zr and untransformed β-Zr. The morphology and microstructure of the β phase region is thus determined by how far this decomposition reaction has progressed. Since this decomposition is a continuous process, the lack of clear-cut boundary between the two types of microstructure and their co-existence within one β phase region can be easily explained. It is fair to assume that the two types of the β phase regions are actually at different stages of the decomposition process. Then the next question is what stage these β phase regions are at.

To answer this question, it is useful to consider the Nb concentration we expect in the different phases that might be found in the decomposed microstructure. Starting from the final products, the equilibrium Nb concentration in the β-Nb is ~ 80 wt% as shown in the Zr-Nb phase diagram in Figure 1.4, although the ones found in Zr-Nb alloys always have lower values [25]. The Nb concentration in solid solution in the α-Zr matrix is about 0.5 wt% [172], and the equilibrium Nb concentration in β-Zr is about 20 wt% [172]. The intermediate product ω-Zr, is reported to be depleted of Nb compared to β-Zr in many previous publications [28, 161, 185]. In as-received Zr-EXCEL, the Nb concentration in the ω-Zr phase was reported to be about 3 wt% [28]. Therefore, the Nb

concentration detected in the β phase regions can provide an indication of the volume fraction of different phases. If we exclude any α-Zr in the phase mixture, which is a simple task in HAADF images, the higher the Nb concentration the higher fraction of β-Nb and lower fraction of the β-Zr and ω-Zr in the mixture.

The amount of ω-Zr in the β mixture requires some further investigation. All the ω-Zr phase reported previously has a unique cuboidal shape as shown in Figure 4.14. However, this unique feature has not been seen in any of the samples in this study, suggesting the possible absence of the ω-Zr phase. For further validation, EELS low loss spectra were obtained from both the β phase mixture in the samples studied in this project and ω bearing β-Zr grains in the 720 ºC annealed Zr – 1wt% Nb alloy from Westinghouse^{TM}. The plasmon edges from the two spectra are compared to each other as shown in Figure 4.15 and Figure 4.16.

The low loss spectral image is processed by Principal Component Analysis (PCA) and Independent Component Analysis (ICA) for separation of the different components (phases) in the β phase mixture. This is to avoid the possibility that some features (for instance β-Nb particles and ω-Zr if there are some) can have a smaller diameter than the whole sample thickness, and hence form a 'sandwich' structure with other features, resulting in inaccuracy in identifying different components.

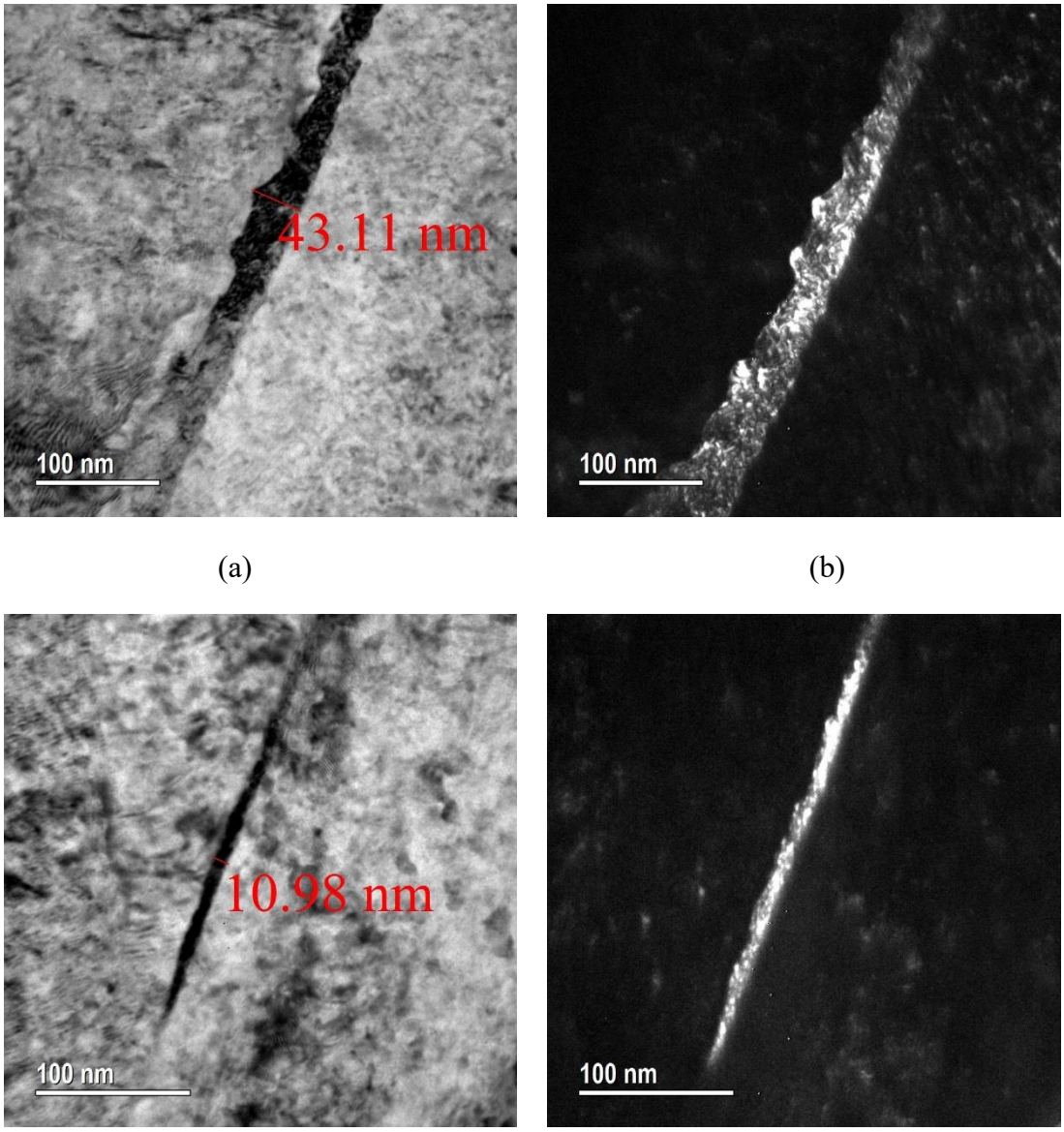
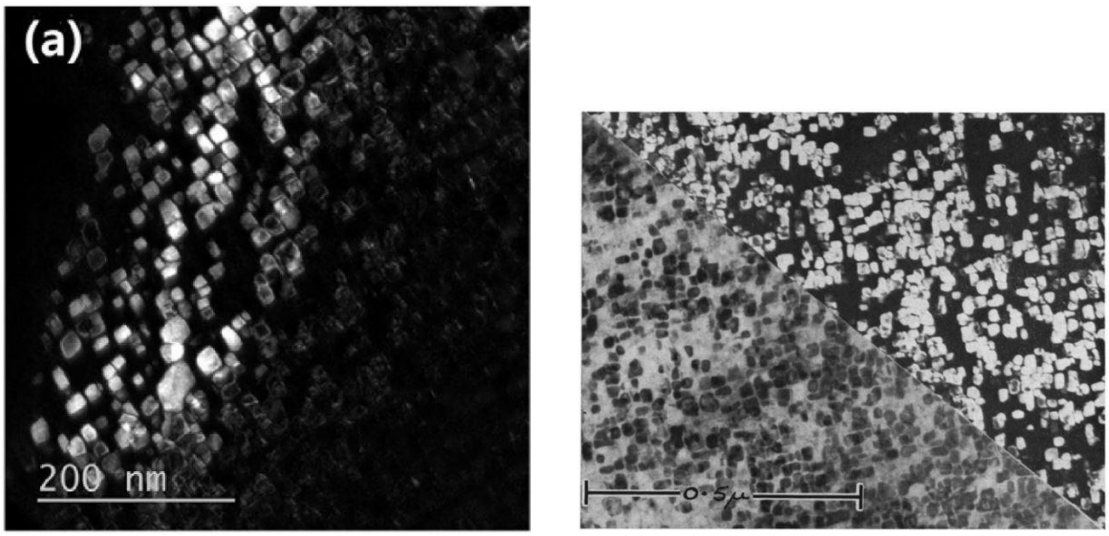


Figure 4.13 TEM bright field and corresponding dark field images showing two morphologies of the β phase, (a) and (b) from B70, (c) and (d) from B74. These β phase regions are found in the metal matrix at the boundary of two α-Zr grains. The dark contrast (in the bright field images) found in the α-Zr grains are assumed to be surface oxides.

Figure 4.15 shows a β phase mixture region consisting of three components. The most obvious one is the surrounding α-Zr matrix as shown in (b). The second component, shown in (c), is associated with higher Nb content as evidenced by the bright contrast

in the HAADF image, and can thus be assumed to be β-Nb. The third component, shown in (d), is not easily recognised. It not only exists in the Nb rich part, but also in the α-Zr regions, and I have assumed it to be the residual of the transformation from β-Zr to β-Nb and α-Zr. This ambiguity in identifying the component in (d) means that the existence of the ω-Zr can still not be ruled out, so comparison to the low loss spectra from samples definitely containing the ω-Zr phase is required.



(a) (b)

Figure 4.14 Cuboidal shape of ω-Zr phase in (a) EXCEL [28] (b) Zr-20Nb alloys [189]

The 'reference' sample is from Zr – 1.0 wt% Nb alloy that has been annealed at 720°C for 24 hours after recrystallisation and provided by Westinghouse^{TM}. This heat treatment has led to the formation of ω bearing β-Zr grains. Low loss EELS spectral images were taken using exactly the same parameters as those for the Zr – 2.5 wt% Nb

samples above, and the data analysis also follows the same procedure. The phase separation results are shown in Figure 4.16. The plasmon edge for the α-Zr phase is at 17.20 eV, the edge for the ω-Zr phase is 17.60 eV, and the edge for the β-Zr phase is 18.50 eV. By comparison, the edge of the unidentified component in Figure 4.15 is 1.9 eV lower than the α-Zr. Therefore, the ω-Zr phase does not appear in the β phase region shown in Figure 4.15. Since several β regions randomly chosen from the Zr - 2.5% Nb samples have been through the same procedure, I would claim with confidence that the ω-Zr phase does not appear in the CNL Zr – 2.5Nb samples.

This observation, although not matching many studies on the β phase mentioned earlier, agrees well with the results reported by Griffiths et al. [161] and Aldridge et al. [189] regarding the ageing of the β phase in similar Zr – 2.5wt% Nb alloy. The absence of the ω phase can be a result of two possibilities; 1) the conversion from ω-Zr to α-Zr and β-Nb is faster than the conversion from β-Zr to ω-Zr, or 2) the ω-Zr phase has not formed in my samples. By looking at tens of β phase regions in the samples and finding no ω-Zr, I tend to believe the second explanation since there will inevitably be some trace of untransformed ω-Zr phase in the first case.

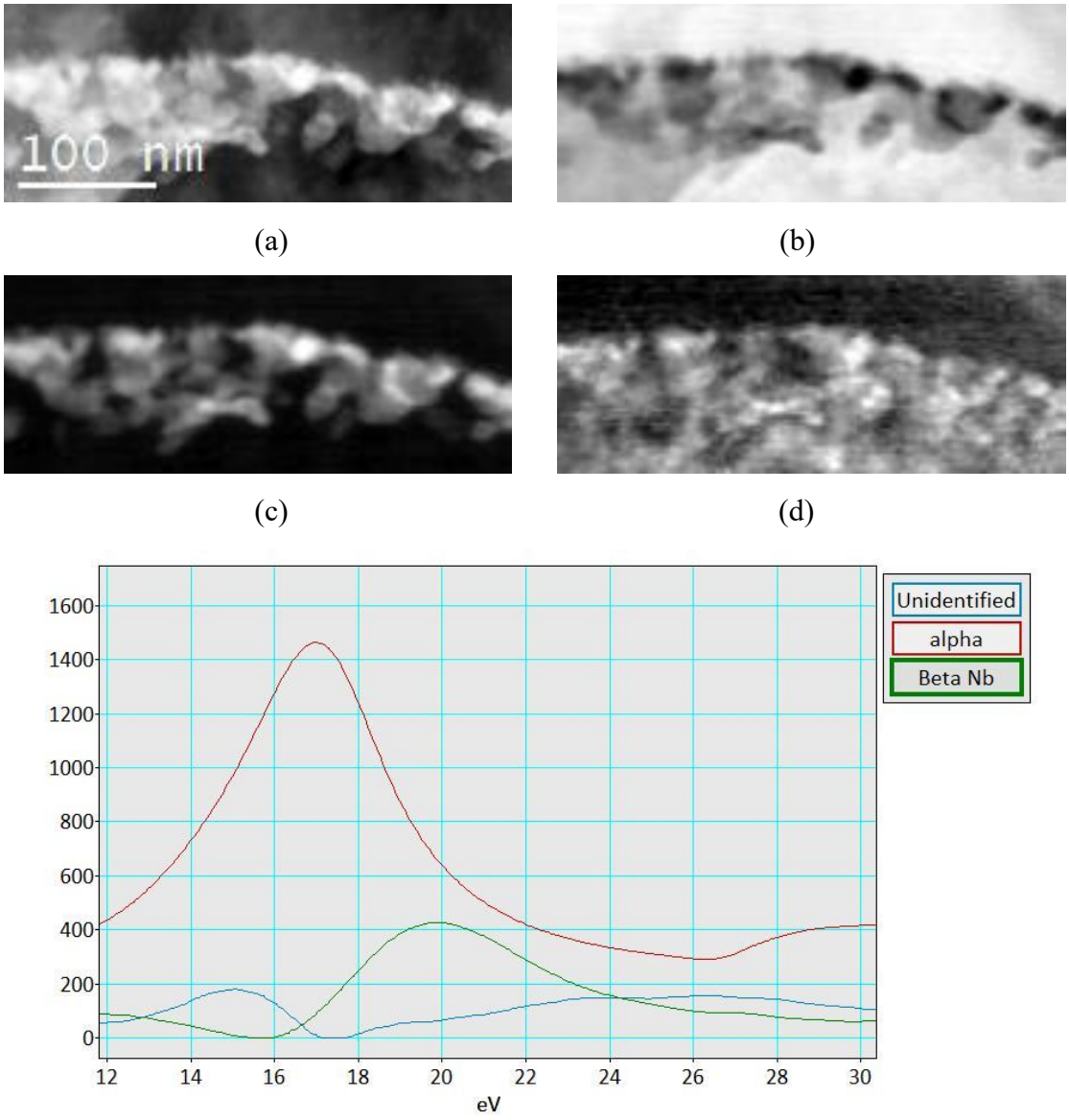
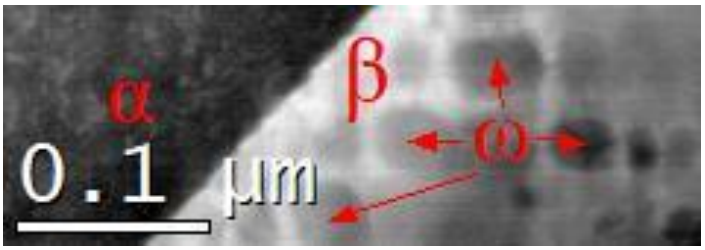
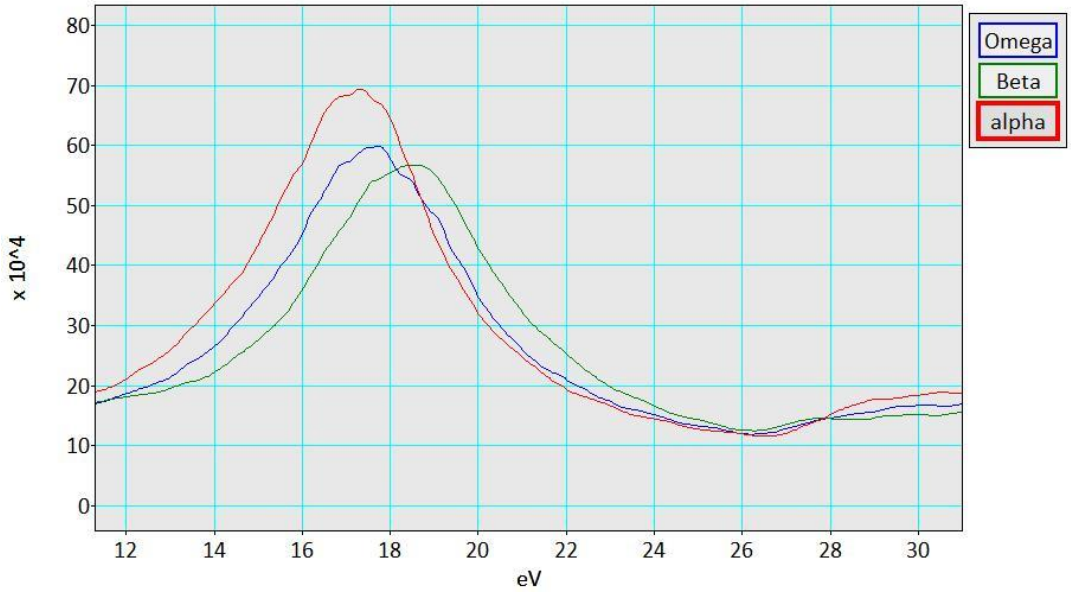


Figure 4.15 (a) HAADF image showing a β region in the B70 sample, (b)(c)(d) are components identified by decomposing the low loss spectrum image via PCA and ICA, (b) represents α-Zr, (c) represents β-Nb, and (d) is not identified so I assume it to be the untransformed β-Zr. The spectra corresponding to these components are shown in (e).



(a)



(b)

Figure 4.16 An ω bearing β-Zr grain and its neighbouring α-Zr region, from sample N-3 (Zr - 1.0 wt Nb) which was annealed at 720 °C for 24h. The components are shown in the HAADF image and their corresponding spectra are shown below.

The lack of ω-Zr formation is likely to be a result of the morphology of the β phase, as suggested by Griffiths [161]. The formation of a Nb depleted ω-Zr particle requires the gathering of Zr atoms and expelling of Nb atoms to the β phase. However, if the nucleation site of the ω-Zr particle is close to the α/β boundary, Zr atoms will preferentially diffuse towards the α-Zr phase rather than the ω phase since the ω-Zr is a meta-stable phase compared to the α-Zr [190]. In the samples studied in this project, the β phase regions are commonly less than 100nm thick, while the β-Zr grains reported

to contain the ω-Zr phase are usually hundreds of nm thick [19, 28]. This assumption is further supported by the observations of the ω denuded regions tens of nm thick at the α / β boundaries [184].

After exclusion of the presence of ω-Zr phase in my samples, the β phase mixture can be simplified to only contain undecomposed β-Zr and the main decomposition product β-Nb. For a given β phase region, the higher the Nb concentration, the higher the fraction of β-Nb, the later stage of decomposition. Therefore, the Nb concentration in the two types of β regions shown in Figure 4.13 are measured to determine the stages of the decomposition reaction.

Two typical β phase regions representing the first and second type of β mixtures are shown in Figure 4.17 (a) and (d). From the EELS spectra taken on these images, the ratio of Nb to (Nb + Zr) is calculated and plotted in (b) and (e). To better present the differences, line profiles are drawn across the β phase mixtures and plotted in (c) and (f). The width and position of the lines are adjusted to ensure that as much of the β region as possible is captured but as little of the matrix as possible. It is obvious from Figure 4.17 (c) and (f) that the Nb concentration in the type 2 β phase mixture is higher than that in the type 1 mixture. The shape of the plot in (c) and (f) also helps to display the morphology and microstructures of the two types of mixtures. The periodicity in (c) indicates the formation of discontinuous Nb rich β-Nb particles, while the plot in (f)

suggests a relatively even distribution of Nb.

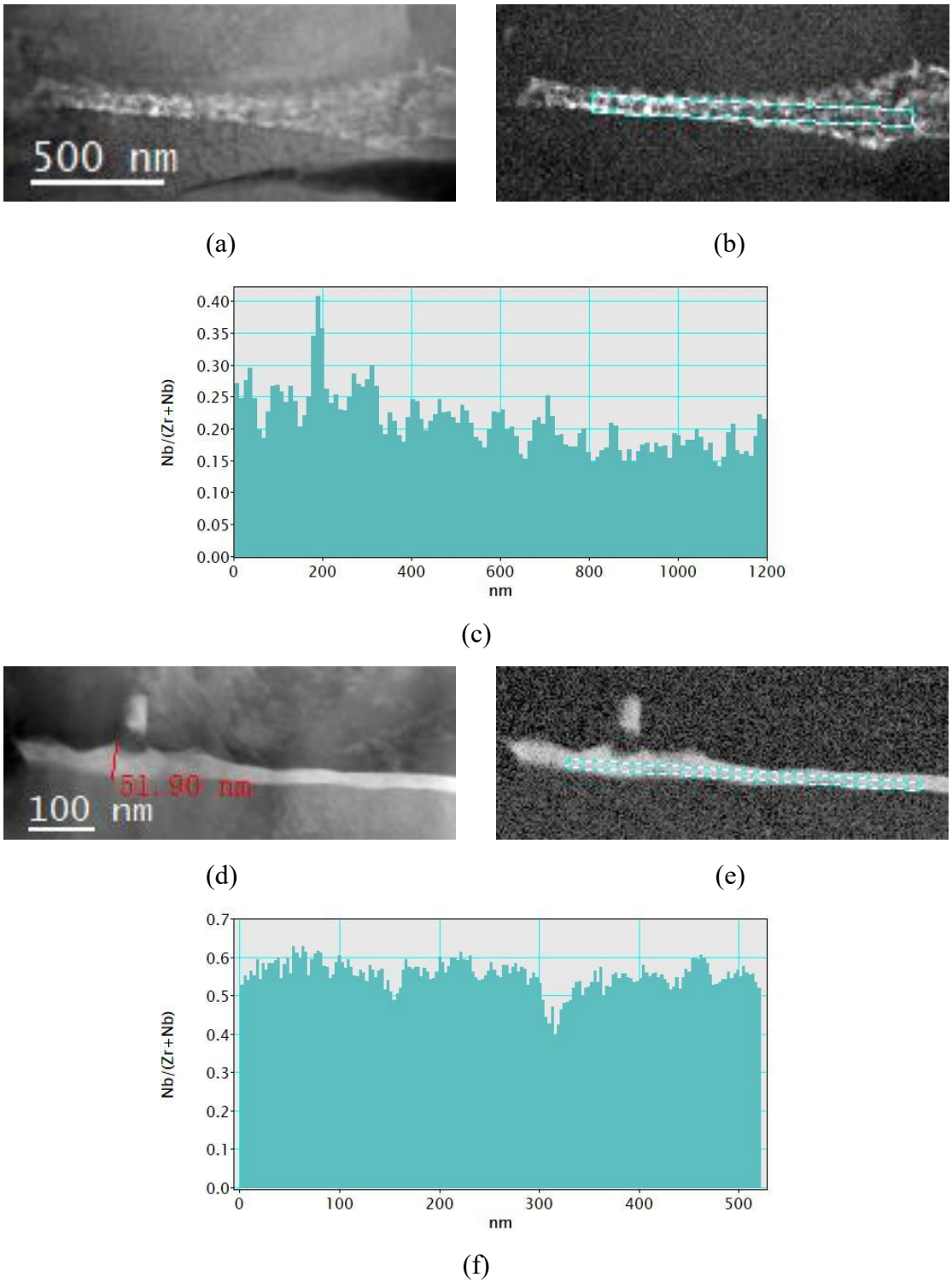


Figure 4.17 HAADF images (a) and (d) show the two types of β phase regions commonly seen in the irradiated and unirradiated CNL samples Zr-2.5Nb samples, (b) and (e) show the atomic ratio of Nb to (Nb + Zr) measured by EELS, and (c) and (f) show the corresponding values along the selected lines shown in (b) and (e).

Therefore, it is fair to claim that the first type represents a less decomposed β phase region while the second type represents a more decomposed β region. A schematic showing the decomposition process of β-Zr is shown in Figure 4.18. The first type of β region corresponds to the partially decomposed stage in the middle and the second type corresponds to much more decomposed stage on the right.

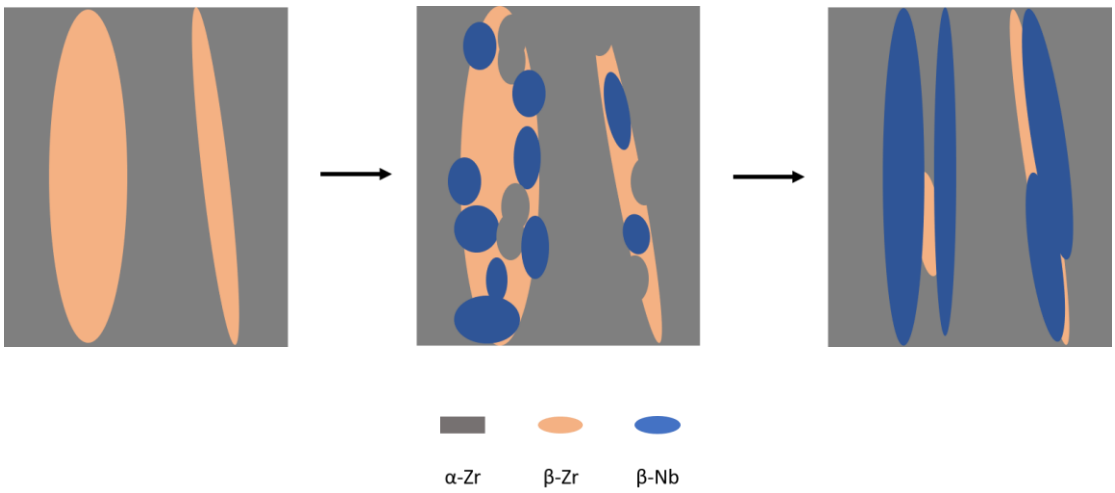


Figure 4.18 A schematic showing the evolution of β-Zr grain to form β-Nb and α-Zr

It is worth re-emphasising that the decomposition of the β-Zr to β-Nb is a continuous process, and the β regions shown in Figure 4.13 and Figure 4.17 are just typical representations of many β regions found in the CNL Zr-2.5Nb samples. While the type 1 and 2 β regions mark the milestones, there are many more β regions with different morphology and Nb concentration corresponding to different stages of the decomposition reaction.

4.2.2 The evolution of the β phase under reactor conditions

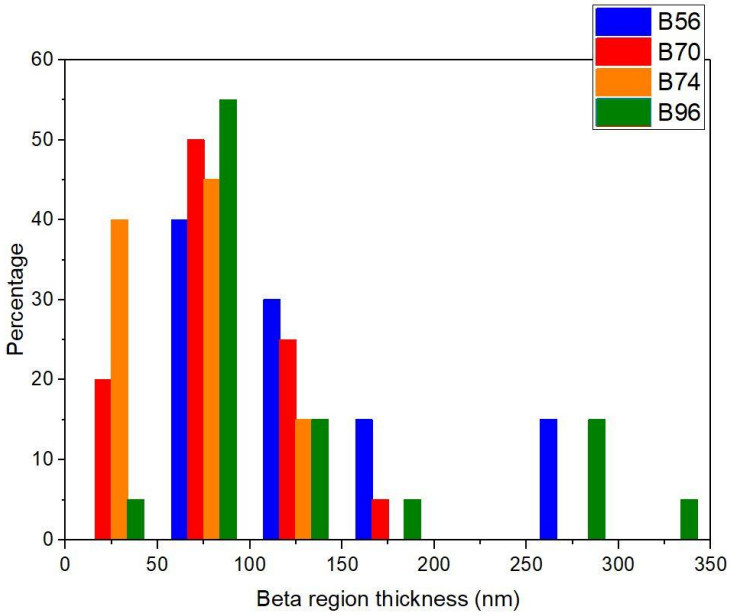
In previous section, the evolution of the β phase in the Zr – 2.5 wt% Nb alloy is discussed and the morphology and Nb concentration at different decomposition stages are identified. The aim of this section is to investigate how in-reactor conditions, including heating and neutron radiation, influence this decomposition process. The morphology and Nb concentration of the β phase regions are compared in four materials, B56, B70, B74 and B96. As listed in Chapter 3, B56 and B70 have both been irradiated for about 190 days, but at different working temperatures. B96 and B70 have both been heated for about 190 days at 325°C, but B96 has not been neutron irradiated. B70 and B74 have both been irradiated at 325°C, but to different damage levels. These three groups can thus provide a direct observation of the impact of both the temperature and neutron radiation.

It should be noted that decomposition of the β-Zr is a dynamic process, and different β regions can be at different stages even in a same sample. Therefore, instead of looking at one or two 'typical' β regions in a sample, tens of β regions are investigated in each sample and the histogram of the morphology and Nb concentration are recorded. The distributions of the histogram in different samples can thus be compared. Another issue to be addressed in advance is how to study the morphology quantitatively. As mentioned earlier, there is no clear-cut boundary between the two typical stages of the β phase regions (as shown in Figure 4.13), leading to the difficulty in categorising the β phase

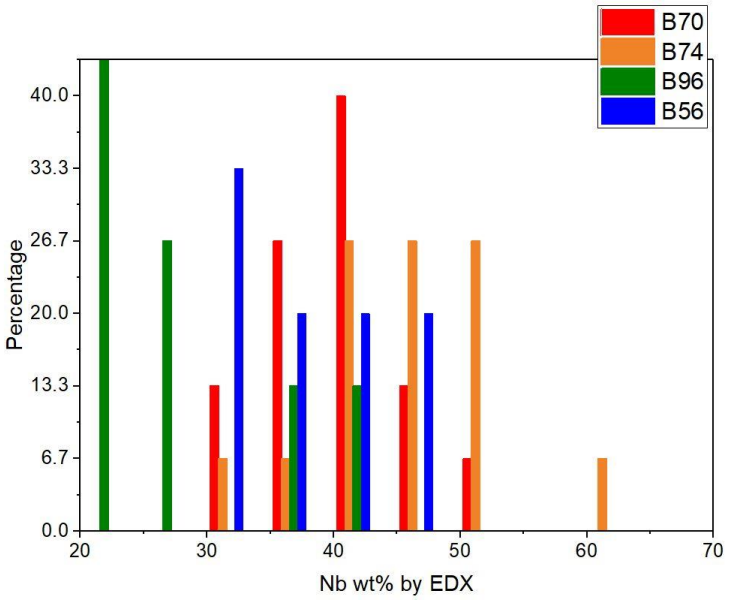
regions studied. The solution is to use the maximum thickness of the β phase regions as measured in the HAADF images (for example Figure 4.17d) as a representative parameter. As shown in Figure 4.17, the more a β-Zr grain is decomposed, the higher the Nb concentration and the thinner the β phase region is. Therefore, a histogram of the maximum thickness and Nb concentration of the β mixtures in different samples is plotted in Figure 4.19. Together with the average values of these two quantities, the stages of decomposition in different samples can be compared and interpreted.

Table 4-5 Average values of the maximum thickness and Nb wt% of the β regions in different samples

Average values	B56 2 dpa, 250°C	B70 2 dpa, 325°C	B74 25 dpa, 325°C	B96, 325°C Out-of-flux,
Maximum Thickness (nm)	133	82	62.5	128
Nb weight percentage (%)	37.1	41	45.9	25.5



(a)



(b)

Figure 4.19 Distribution of the (a) maximum thickness and (b) Nb weight percentage of the β phase regions in different samples measured by EDX

Looking at the comparison between the values of the β region thickness and Nb content from B56 and B70 shows that the decomposition of the β-Zr is faster at higher temperatures. This is not surprising as the decomposition is a thermally activated

process. Comparison between the same values for B70 and B96 has revealed that the conversion from β-Zr to β-Nb is also encouraged under neutron irradiation. In the β-Zr and β-Nb phases that only contain Zr and Nb, the two elements are completely miscible and the lattice parameter of the phase depends on the Nb concentration [189]. Thus the formation of β-Nb is achieved by the enrichment of Nb within β-Zr. The excess point defects generated by neutron radiation can enhance the Nb diffusion, hence encouraging this conversion. Therefore, the irradiated samples tend to be more decomposed into the Nb-enriched β-Nb phase than in non-irradiated samples.

It is also interesting to observe that, compared to the differences between B70 and B56 and B96, the differences are not as large when comparing B70 and B74. This indicates that the β-Zr regions are already substantially decomposed when irradiated for 190 days at 325°C. Nevertheless, this decomposition continues in the longer-term irradiated sample B74, and higher Nb concentrations and smaller thickness values are measured in the β regions.

4.2.3 Summary

The evolution of the β phase in the Zr metal under reactor conditions has been studied. The decomposition of β-Zr into β-Nb and α-Zr occurs during in-core service, and the rate is enhanced at higher temperatures and by neutron radiation. As a result, the longer the time spent in reactor, the more β-Zr is converted to β-Nb and the higher the Nb

concentration is in these β regions. The impact of this evolution of β phase on the corrosion of the alloy is explored in Chapter 6.

Chapter 5 Emulating neutron radiation damage in the zirconium metal matrix by ion radiation

One topic that is always of great interest in the study of nuclear materials is to emulate the effect of neutron radiation by using ion irradiation [136]. While the neutron irradiation of samples can be time consuming and expensive, ion irradiation usually requires much less time and expense for the same level of damage created. The activation of the samples by neutron irradiation can also be avoided partially (by proton irradiation) or fully (by heavy ion irradiation). Moreover, ion irradiation is more flexible in setting irradiation conditions, for instance irradiation temperatures, while the neutron irradiation is restricted by the reactor conditions. This can be useful in some experiments where the mechanisms of some phenomena can be studied by altering the irradiation parameters.

However, there are also some drawbacks to use ion irradiation. For heavy ion irradiation, the limited penetration depth may result in small volume of samples being suitable for characterisation, hence suffering from potential strong free surface effects. Proton irradiation, on the other hand, has a larger penetration depth, but fails to generate the cascades of the same scale as those made by neutron and heavy ion irradiation [83]. Other common challenges include the much higher dose rate than the value in neutron irradiation in reactors and the different energy spectrum of the Primary Knock-on Atom (PKA) and so on. These factors should all be considered when making comparisons

between the results of ion irradiation and neutron irradiation.

This chapter discusses the use of ion irradiation to emulate the effect of neutron irradiation in Zr-Nb alloys, focusing on two phenomena. The first part talks about using in-situ heavy ion irradiation in a TEM to study the stability of SPPs under radiation, and the second part talks about using proton irradiation to study irradiation-induced Nb precipitates. Both results are then compared to those reported in neutron irradiated samples, and the validity of the proxy irradiation is discussed.

5.1 Investigating the stability of β-Nb SPPs under radiation by in-situ heavy ions

In this section, Zr-Nb alloys have been irradiated in-situ by heavy ions in a TEM at different temperatures and to different damage levels. The same SPPs were tracked before and after irradiation to provide direct evidence of the changes that happened to individual SPPs under irradiation. Microstructural and local chemical changes were studied by TEM diffraction and STEM EDX analysis to help better understand the behaviour of these SPPs under irradiation.

5.1.1 Experimental Details

5.1.1.1 Materials and sample preparation

The basic microstructure and composition of the samples used in this in-situ irradiation

study is given in section 3.1.2. All the TEM samples were prepared by focused ion beam (FIB) milling using the in-situ lift-out method [147]. A JEOL 3000F was used for TEM and STEM EDX observations before and after irradiation, and the EELS measurements were used to determine the thickness of the TEM samples using a JEOL ARM200F microscope. Detailed settings of the microscopes can be found in Section 3.2.

5.1.1.2 Heavy ion in-situ irradiation in a TEM

The first set of in-situ irradiation experiments was carried out at the Intermediate Voltage Electron Microscopy (IVEM)-Tandem Facility at Argonne National Laboratory. A Hitachi-9000 microscope (300 kV, LaB_6 source) was used for TEM observations, with in-situ irradiation realised by the intersection of the accelerated ion beam and electron beam at the sample stage in the TEM column. 1 MeV Kr^{2+} ions at a flux of 8×10^{11} $cm^{-2}s^{-1}$ were used to irradiate RXA Zr-2.5Nb at 50 K, 293 K, 623 K and 873 K. The accumulated fluence was 1.2×10^{16} cm^{-2} at 50 K, 1.28×10^{16} cm^{-2} at 293 K, 1.6×10^{16} cm^{-2} at 623 K and 873 K. According to SRIM simulation using the Kinchin-Pease damage calculation model [191], this corresponds to an irradiation dose rate of 0.0015 dpa/s, and a total damage level of 15 dpa at 50 K, 16dpa at 293 K, 20 dpa at 623 K and 873 K. Bright field (BF) and Weak beam dark field (WBDF) images of the entire irradiation session were recorded using a Gatan OneView digital camera. These four temperatures were chosen to not only mimic the behaviour of the SPPs under neutron irradiation in reactor cores, but also study the mechanism (and its temperature

dependence) governing the stability of the SPPs under irradiation.

The second set of experiments was done at the MIAMI2 facility, University of Huddersfield, UK, using a Hitachi-9500 microscope (300 kV, LaB_6 source). 350 keV Kr^+ ions were used to irradiate the Zr-1.0Nb samples at 623 K. Four samples were irradiated to different total fluences at a flux of around 6×10^{11} $cm^{-2}s^{-1}$. These experiments were carried out to study the fluence dependence of the stability of the SPPs under irradiation. Details of the irradiation parameters used at the IVEM and MIAMI2 facilities are presented in Table 5-1.

Table 5-1 Parameters used for IVEM and MIAMI2 irradiation

Sample No.	**1**	**2**	**3**	**4**	**a**	**b**	**c**	**d**	**A**
Irradiation Energy(keV)	1000	1000	1000	1000	350	350	350	350	700
Irradiation temperature (K)	50	293	623	873	623	623	623	623	293
Dose rate (10^{-3}dpa/s)	1.5	1.5	1.5	1.5	1.78	2.88	1.61	2.30	1.1
Dose (dpa)	16	15	20	20	6.4	10.4	20.2	38.8	10

As discussed below, measuring any damage-induced thickness changes in the samples is crucial to interpreting the EDX measurements. To calibrate this effect, an additional experiment on MIAMI2 using 700 keV Kr^{+2} ions with similar parameters to those

described above was carried out, and the sample thickness before and after irradiation measured by the t/λ method in the EFTEM mode [154].

5.1.1.3 EDX line-scans and non-linear curve fitting of line-scan profiles

I have approached the problem of measuring any elemental redistribution in SPPs under irradiation by comparing the STEM EDX line-scan profiles of Zr and Nb from the same SPP before and after irradiation. For each SPP, two line profiles, perpendicular to each other and intersecting at the centre, were acquired. The following measures were taken during EDX acquisition to ensure that the results could be interpreted quantitatively. First the instrument conditions were kept as identical as possible. This included the microscope always being operated at 300 kV, source emission current at the same level, use of the same low background double-tilt holder, using the same probe forming condenser apertures and the same camera length and magnification. Oxford Instrument's Aztec software was used to acquire and analyse all the EDX data, and all the line-scans were taken in 'true line' mode with the background subtracted. The EDX results are presented as raw counts because that makes the study of any diffusional phenomena more reliable than after quantification routines which can introduce artefacts as a result of the very different compositions of the matrix and SPP. The step size was fixed to 0.6nm for all samples, and the dwell time to 10ms.

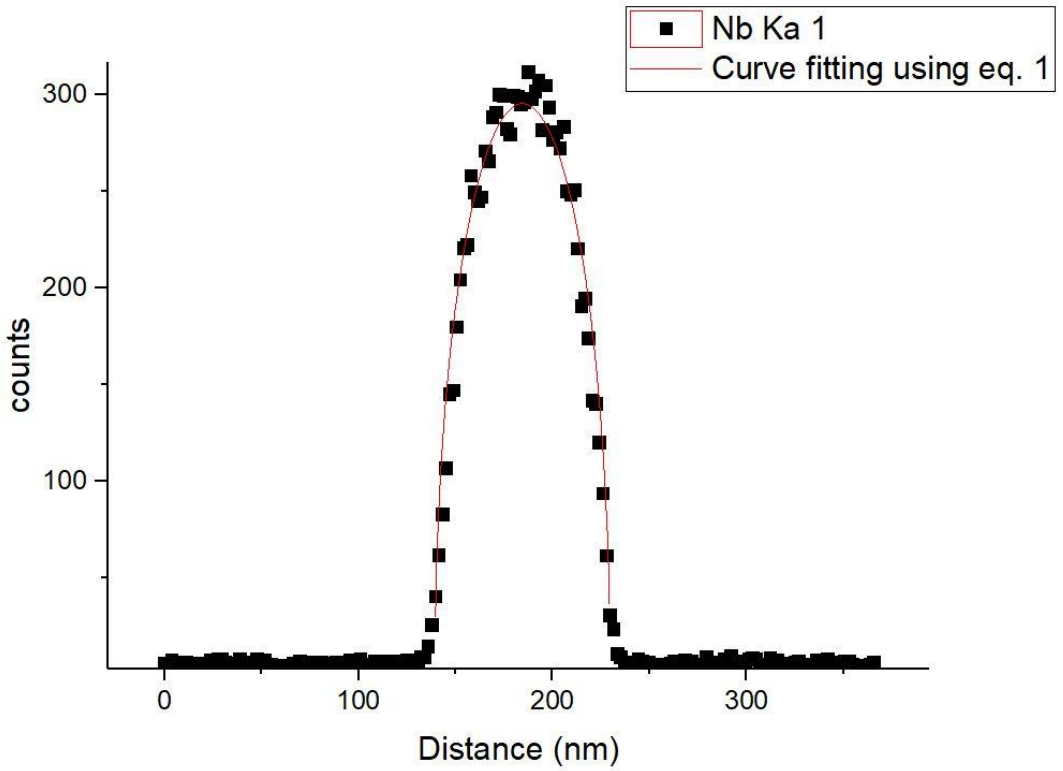


Figure 5.1 Typical Nb line-scan profile and the fitted curve of across a β-Nb SPP. The radius of the SPP is calculated to be 44.5 nm.

To compensate for the effect of irradiation-induced bending, which happened to all the samples during the in-situ experiments, they were always tilted back to the same zone axis before EDX acquisition. Either $[10\bar{1}0]$ or $[11\bar{2}0]$ was used so that orthogonal line-scans could be carried out along the a- and c-directions of the hcp α-Zr matrix. Taking EDX scans directly along a zone axis can result in channelling and a reduction in the reliability of the quantitative data [192], and for this reason, I only used qualitative line profile (counts) for the comparison between samples. In addition, the accumulated radiation damage (dislocations and point defects) could have an effect on the degree of channelling and make the comparison between samples unviable. For this

reason, as shown in Appendix B, the effect of channelling on the EDX Zr signal was compared between unirradiated and irradiated samples. The findings suggest that the effect of irradiation on channelling is negligible (within error), enabling direct comparison of EDX lines-cans over selected SPP before and after irradiation.

A typical line-scan profile of Nb content in an SPP and the neighbouring matrix is shown in Figure 5.1. Quantitative analysis is needed to better understand the degree of elemental redistribution and the underlying damage mechanisms. By assuming that the SPPs are spherical in shape and fully embedded in the TEM foils, the corresponding SPP size along the line scan can be obtained by using non-linear curve fitting of the line-scan profiles using:

$$I = k \times \sqrt{R^2 - (x - x_0)^2} + C \qquad \text{eq.1}$$

where k is a scaling factor, R represents the measured radius of the SPP, x_0 represents the position of the centre of the SPP, C is the background signal intensity outside the particle and I is the signal intensity detected at a point x far from the centre. The background-subtracted intensity should become 0 when x = R, corresponding to the periphery of the SPP.

TEM bright field images can also be used to identify and measure the size of SPPs, and might be considered more straightforward than the method described above. However, it can be difficult to identify the precise shape of SPPs when the images also

contain other features like dislocations and surface oxides, and there are changes to the apparent size of SPPs as a result of sample bending. These effects are illustrated in a set of typical images in Figure 5.2. As a result, EDX results are preferred here for accurate SPP size determination.

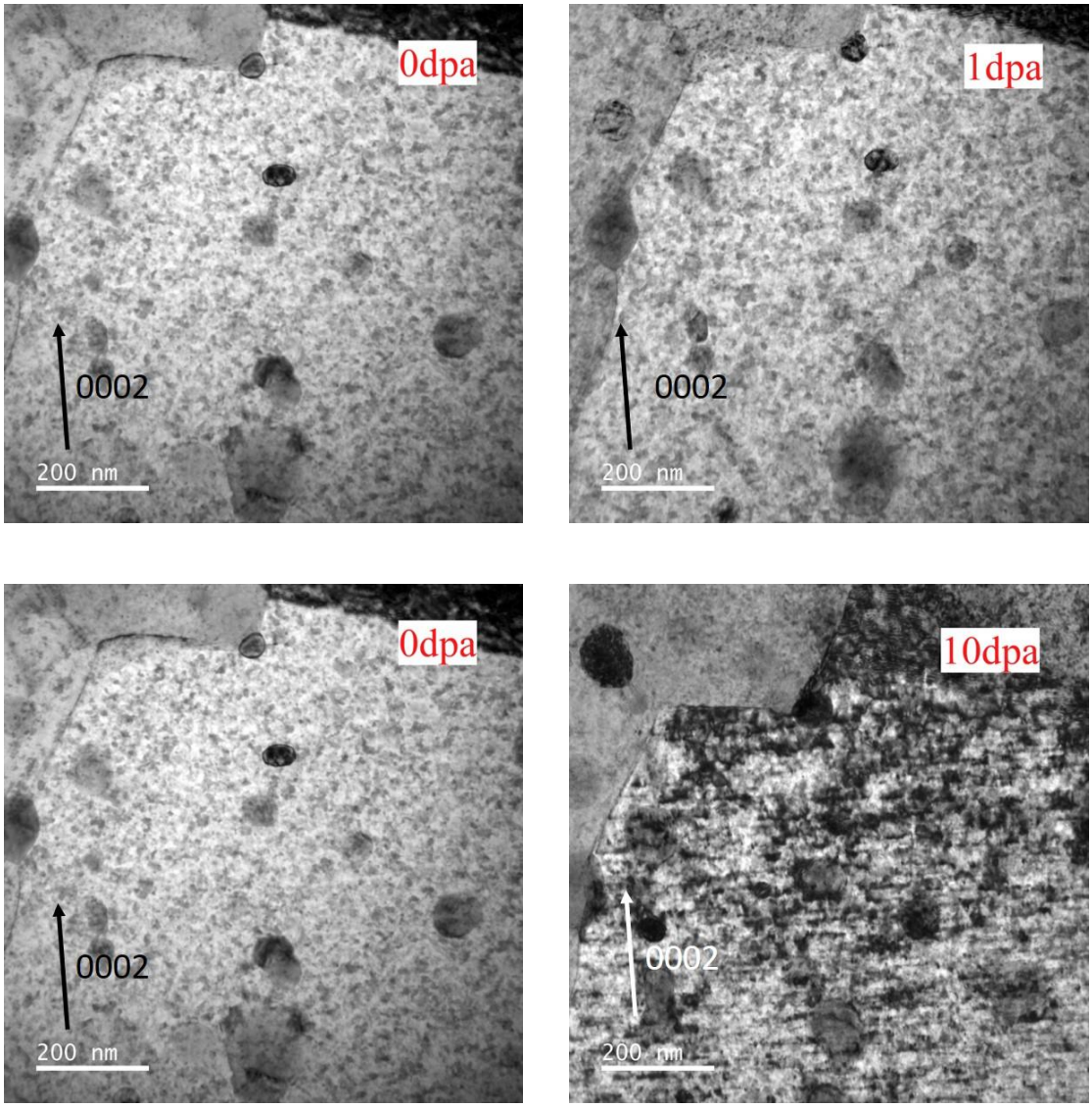


Figure 5.2 A series of TEM-BF images showing the same region in a sample irradiated by 1MeV Kr ions to 20 dpa at 623K. Two beam condition with g=[0002] was used for the BF images. The straight black lines in the right-hand grain that start to appear at 5 dpa are c-loops.

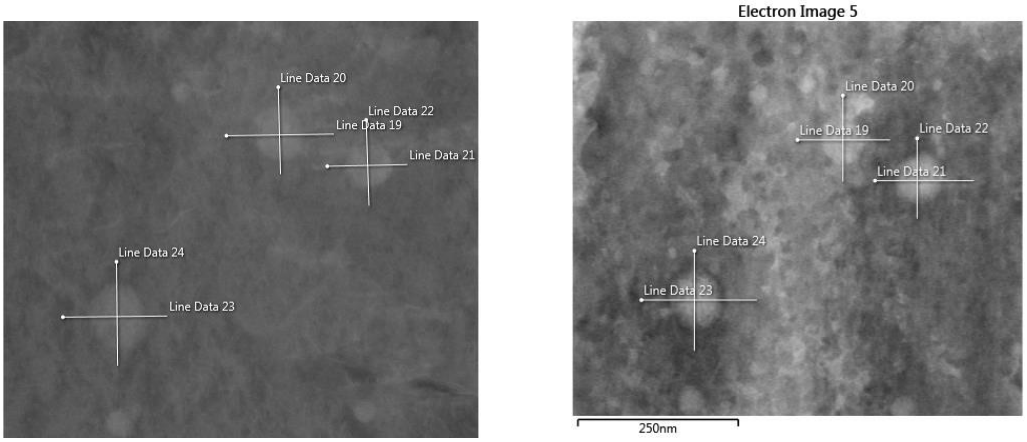
5.1.1.4 Errors in the non-linear fitting of EDX line-scan profiles

Evaluation of possible errors in the fitting of SPP sizes from EDX data needs to be made before any quantitative results can be presented. The first possible error arises from the location of scanned lines over the same SPP in TEM sessions before and after irradiation. To minimise this error, perpendicular lines were carefully drawn across the centre of the particle, as shown in Figure 5.3. It is estimated from analysis of the effect of deliberately misplaced line scans that this introduces to the particle size measurements an error of about 1%. The second type of error comes from the assumption that SPPs are all ideal spheres. To minimise this problem, only SPPs clearly well separated in the initial images, circular in appearance and with diameters smaller than the measured sample thickness were used to increase the likelihood that the SPPs are fully embedded in the TEM foil. The contrast of the SPPs in HAADF images is also a useful guide since for SPPs of the same apparent size a higher contrast with the surrounding matrix indicates that more of the SPP is embedded in the foil. The fitting quality to equation 1 is also helpful, and a minimum threshold of 0.9 is set for the R^2 value of selected SPPs. Considering all these factors, it is estimated that a 5% error should be assumed for all the SPPs radii reported below.

5.1.1.5 Obtaining compositional information from EDX line-scan profiles

In addition to the use of non-linear curve fitting of EDX data to measure size changes, any redistribution of Nb atoms can also be investigated by comparing line-scan profiles

before and after irradiation. Based on the work of Castaing [192], I assume that the TEM foil is thin enough so the ratio of intensities of the X-ray signals of two elements is proportional to the ratio of concentration of these two elements in the region analysed, so by comparing Nb signals in line-scan profiles before and after irradiation, any changes in Nb content can be measured.



before after

Figure 5.3 HAADF images showing the position of the EDX line-scans taken of the same SPPs before and after irradiation by 1MeV Kr ions to 15dpa at 293K.

Direct comparison of Nb signals before and after irradiation requires careful normalisation. In a line-scan profile the data come from both the region containing the SPP and from the Zr matrix. The ratio between the integrated value of Nb signals in the SPP region and the average value of the Zr signal in the matrix was compared before and after irradiation. If the number of Zr atoms in the same region of the matrix is assumed to remain unchanged, any differences in instrumental settings can then be corrected. However, the thickness of the TEM lamella might have been modified by

sample sputtering during in-situ irradiation, and the extent of this sputtering depends on various factors including incident species and energy, the incidence angle of the beam and irradiation temperature [193]. The thickness of each sample can be tracked by EELS [157] before and after irradiation, but this measurement is not always easy especially when surface oxides are forming during irradiation. As a control, a separate sample was irradiated to 10 dpa at room temperature at MIAMI2, sample A in Table 5-1. Using the EFTEM capability on the Hitachi-9500 TEM, the thickness of the foil was measured immediately before and after irradiation, with the sample remaining under vacuum in the same position in the microscope chamber. Zero loss mapping of the same region in the sample was used to compare the thickness of the TEM foil, and after 10 dpa no change in thickness was detected within experimental error (±10 nm). Furthermore, SRIM simulations of Zr sputtering due to 350 keV Kr ions up to 10 dpa indicate the sputtered thickness to be less than 2nm. I am thus confident that changes in sample thickness as a result of sputtering during these in-situ experiments can be considered to be negligible.

In order to study the redistribution of Nb in the TEM foils during in-situ ion implantation, depth profile measurements were performed with a Cameca NanoSIMS50 ion probe with the help from Dr. Kexue Li. A 16 keV primary Cs^+ beam focussed to a nominal diameter of 60 nm was scanned over a measurement area of 3x3 μm on the TEM sample and $^{93}Nb^-$ sputtered secondary ions collected in a double-

focused mass spectrometer. 2D images (planes) with a dwell time of 1000 μs per pixel were generated sequentially. Collecting 400 planes results in a total sputter depth of ~100 nm, penetrating completely through the TEM sample, and allowing analysis of the chemistry of the back surface of the foil. This avoids the artefacts associated with the study of the front surface where steady-state sputtering conditions are not yet established and signal intensities show severe initial transients [194].

5.1.2 Experimental results

Bright field TEM images (Figure 5.4 (a) and (c)) show the morphology of SPPs primarily from diffraction contrast. The scattered black line features in Figure 5.4 (c) are assumed to be a mixture of irradiation-induced dislocations and surface oxides formed during the irradiation session. The crystal structure of the β-Nb SPPs can be monitored by selected area diffraction, as shown in Figure 5.4. Using a selected area aperture diameter so that the SPP covers as much of the area as possible, the diffraction patterns contain reflections from both the α-Zr matrix (connected by white dashed lines in Figure 5.4 (b) and (d)) and the β-Nb SPPs (surrounded by white circles), and we can determine that all of these SPPs are incoherent with the matrix, in agreement with [195]. About 20 β-Nb SPPs were tracked in each sample both before and after irradiation, and it is clear that the β-Nb SPPs retained the same crystal structure after irradiation to 15 dpa at all four temperatures from 50 K to 873 K.

To measure any potential size changes, EDX line-scans were carried out on about 20 β-Nb SPPs in each sample following the method described above to obtain an average value of size changes at each temperature. The results of this analysis are shown in Figure 5.5, and the only temperature at which any size increase in the β-Nb SPPs can be detected outside the error bars is after irradiation at 623 K.

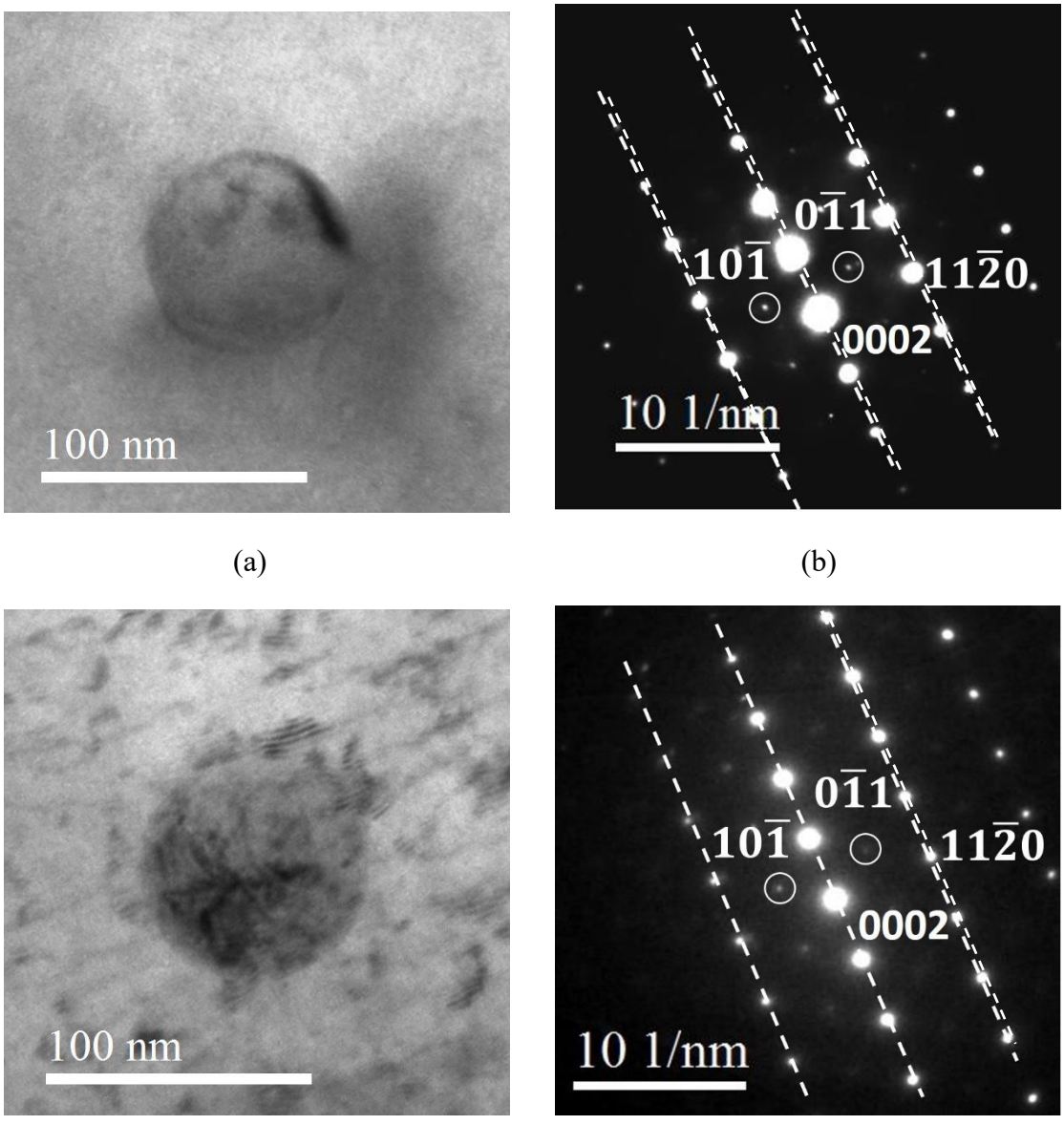


Figure 5.4 An example of monitoring a single β-Nb particle before and after irradiation by 1MeV Kr ions at 293K. (a) BF image and (b) SADP at 0dpa, (c) BF image and (d) SADP of the same particle after 15dpa.

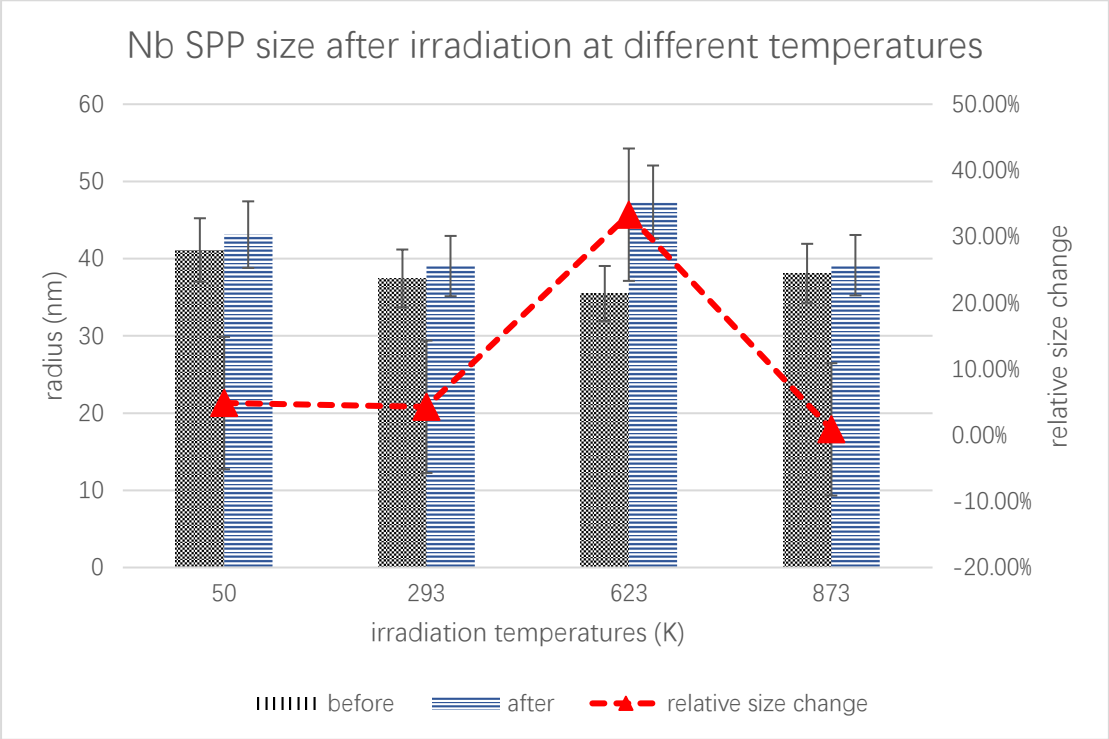
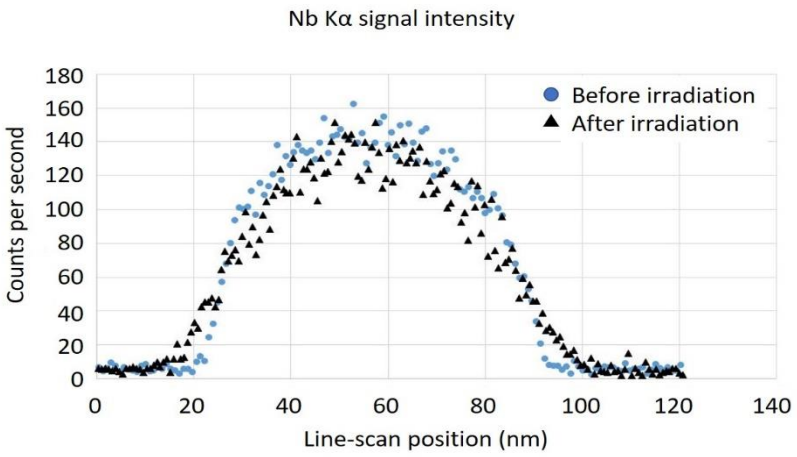
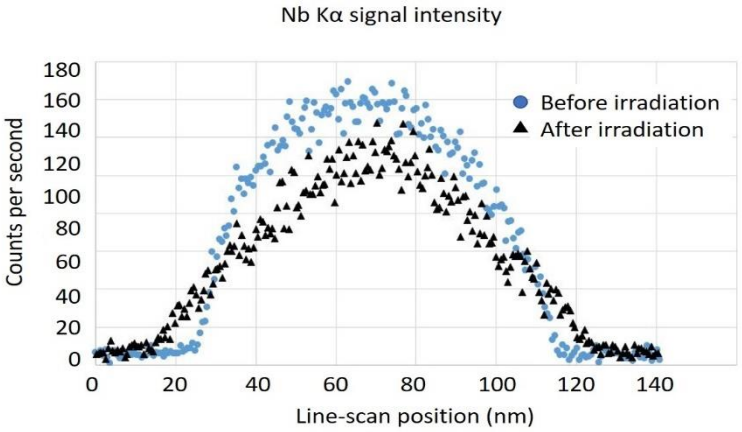


Figure 5.5 Averaged values of the size of β-NB SPPs before and after irradiation at 4 different temperatures, and the percentage size changes. The error bars of the average size of the SPPs represent the estimated errors of the size measurement as described in section 2.4, and the error bars of the relative size change are derived values from the propagation of uncertainty equations. It should be noted that the average size only stands for the particular SPPs investigated in this study, not the general average size of the SPPs in this material.

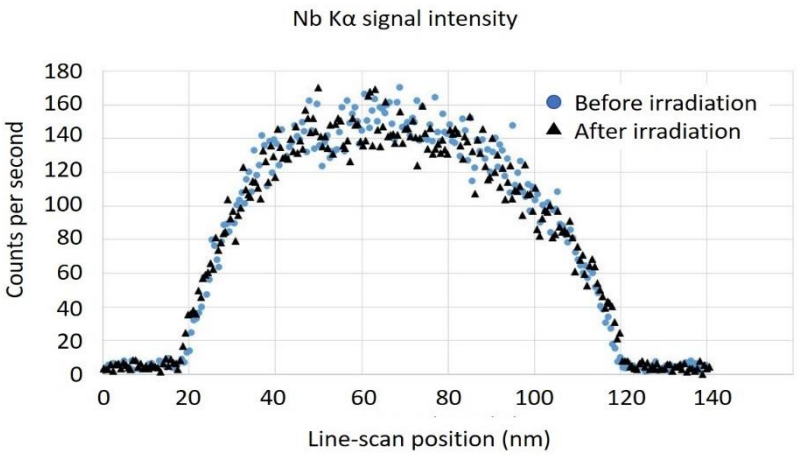
A typical set of line-scan profiles showing compositional changes in SPPs at different temperatures is shown in Figure 5.6. At low temperature (293 K), a change of Nb concentration was only detected at the periphery of this SPP. In the intermediate temperature regime (623 K), a reduction of Nb concentration can be seen in the inner part of the SPP, with an increase of Nb concentration at the outer surface. At higher temperature, the line-scan profiles show very little change even after very high irradiation levels.



(a)



(b)



(c)

Figure 5.6 Typical EDX line-scan profiles of the Nb Ka signal for SPPs irradiated at (a) 293K, (b) 623K, (c) 873K. Compared to the data at 293K and 873K, more obvious mixing can be seen at the periphery of the SPP at 623K.

A further set of samples (a-d) were irradiated to different damage levels at 623 K and again about 20 β-Nb SPPs were characterised by EDX line-scans in each sample before and after irradiation. These EDX line-scans can be divided into two categories; those measured parallel to the a direction (and so lying in the basal plane) and those along the c direction of the α-Zr matrix. The size changes in each direction were calculated separately, and the results are shown in Figure 5.7. It is obvious that the measured increases in size along the c-direction are systematically larger than in the basal plane. This comparison not only is true for the average values, but for every individual SPP examined. Using the assumption discussed above that the thickness of the TEM foil does not change during irradiation, the absolute amount of Nb in each SPP (the sum of all the Nb counts in the SPP in the line-scan profiles) can be compared before and after irradiation. The results show that within the errors discussed above, the Nb content remains unchanged after irradiation.

It is also worth mentioning that using the $[10\bar{1}0]$ or $[11\bar{2}0]$ zone axis for imaging and EDX line-scans has also allowed a careful search for the 'needle/platelet like' irradiation-induced Nb precipitates reported in neutron and proton irradiated Zr-Nb alloys [107, 124]. I have observed no precipitates of this kind in any of the samples examined in this study. A similar result was reported by Motta et al. for the in-situ irradiation of Zr-Nb and Zr model alloys [196]. The implications of this observation will be discussed in Section 5.1.3.

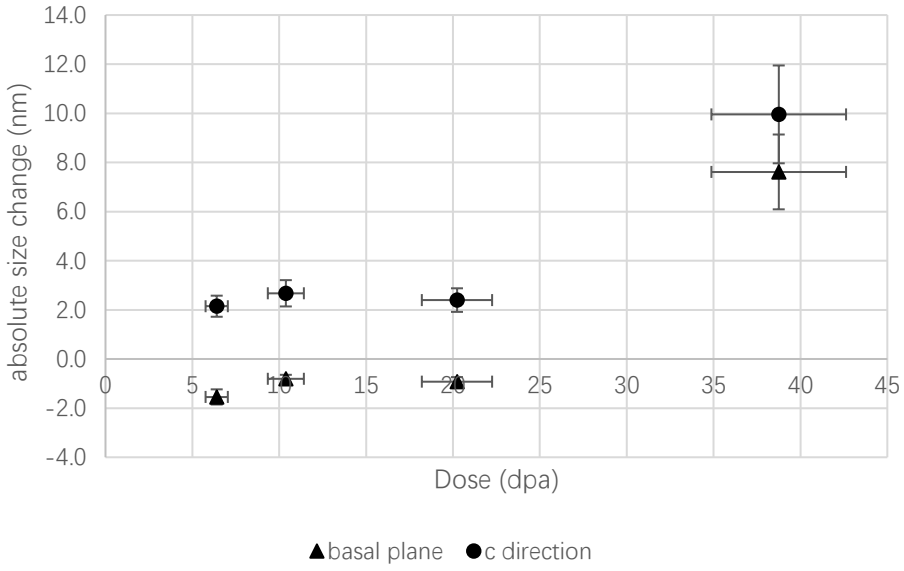


Figure 5.7 Average value of absolute size changes in β-NB SPPs measured along a and c directions in the Zr matrix after irradiation to different damage levels at 623 K. The errors of the size change come from the uncertainties in measurement and line-scan profile fitting, as discussed in section 2.4. The errors in dose represent the uncertainties of the damage dose measurement during the in-situ irradiation session. An error of ± 10% in dose is assumed.

5.1.3 Discussion

There is an extensive discussion in the literature on radiation-induced changes to systems containing more than one phase, like the Zr-Nb alloys I have studied here. It is commonly agreed that phase stability is affected by the redistribution of solute elements governed by competing mechanisms that can be divided into two categories [83]; irradiation-induced mixing that is primarily ballistic in nature, and diffusional processes where the kinetics are strongly temperature dependent. Which of these processes is dominant depends on the precise irradiation conditions.

Ballistic mixing [197] is directly driven by displacement damage from primary and secondary knock-on events. Cascade damage will cause extensive mixing in regions such as the periphery of SPPs where the initial composition changes abruptly [198]. This kind of damage is commonly seen in heavy ion and neutron radiation where dense cascades are generated, and the kinetics of the process depends only on radiation-related parameters such as flux, the energy and mass of the incident particles [199], and is considered athermal.

At the same time, a dynamic equilibrium will be established between the creation of excess concentrations of point defects and defect clusters [197] and diffusional processes that can lead to their annihilation by direct recombination and absorption at sinks. At low temperatures and low initial sink densities, local recombination will be the dominant process for eliminating point defects, and the faster diffusion rate of interstitials will result in them moving not only to annihilate at the slower moving vacancies but also to other sinks like the free surfaces of a TEM sample. As irradiation continues, the interstitial concentration will thus decrease with respect to the vacancies, and radiation enhanced diffusion (RED) via this excess vacancy concentration will gradually become the dominant transport process. At higher temperatures where the diffusion rates are faster [124], coupling between the fluxes of radiation-induced defects and solute and impurity elements to sinks such as surfaces, grain boundaries or interphase boundaries will result in radiation-induced segregation (RIS) [200]. In this

study, the β-Nb particles themselves will act as important sinks of solute Nb atoms, but the sink strength will depend on temperature. The equilibrium concentration of Nb in the β-Nb phase has a minimum value of about 90 wt% at around 890 K and increases rapidly at lower temperatures [172]. However, the initial Nb concentration in the β-Nb SPPs in both alloys used in this study has been directly measured by Atom Probe Tomography to be about 80 wt% [25], i.e. they are not at their equilibrium concentration after alloy manufacture. As a result, one should expect in these experiments the primary flux of Nb atoms in the matrix near an SPP always to be towards the β-Nb SPPs.

At low temperatures RIS will be limited by the low defect mobility and high recombination rate of vacancies and interstitials, but at higher temperatures the increased thermal vacancy concentration leads to enhanced recombination and faster back diffusion of species displaced from the equilibrium phases, limiting the effect of RIS to sinks other than the existing SPPs. At intermediate temperatures, the increased participation of solute atoms in defect fluxes other than directly back into the SPPs can result in more segregation to other sinks. This segregation can also drive the matrix concentration above the solubility limit, inducing additional precipitation of a second phase (like the nano-precipitates mentioned above [110, 124]).

An additional important factor that must be considered in the experiments is that the TEM lamella are so thin that the two large free surfaces must be expected to act as

preferred sinks for defects and may reduce matrix supersaturation of Nb and limit back-diffusion to the SPP/matrix interfaces. Evidence supporting this mechanism comes from two experimental observations; (i) that no radiation-induced Nb precipitates have been created in the matrix in any of the samples studied above, and (ii) that Nb segregation to the free surfaces has been directly measured by SIMS analysis after in-situ damage, but only at 623 K, as shown in Figure 5.8. Matrix nano-precipitation in bulk samples [107, 124] is a result of supersaturated solute atoms segregating into defect clusters in the matrix, but this supersaturation may have been eliminated in the samples by the proximity of the free surfaces [196]. The SIMS result is also direct evidence that this surface segregation process is an important contribution to the overall balance of solute redistribution at the intermediate temperature of 623 K, but at neither 293 K nor at 873 K.

Modelling of the stability of precipitates under radiation damage [199, 201, 202] has been carried out by considering the balance between radiation mixing driven dissolution of SPPs and back-diffusion of solute atoms to their thermodynamically preferred location in the SPPs. This work suggests that SPPs should generally be unstable under irradiation at low temperatures because the rate of diffusion is too slow to compensate for the damage from radiation mixing. The low-temperature limit for stability was predicted by Turkin et al. [199] to be around 900 K for incoherent SPPs (like the β-Nb precipitates studied here) irradiated at 10^{-4} dpa/s, and to lie at even higher

temperatures for higher fluxes. However, this does not match the experimental observations made on β-Nb SPPs under neutron [107] and proton [124] irradiation in the intermediate temperature range (~600 K) where β-Nb SPPs always showed good stability to high damage levels, or my results presented above where the β-Nb shows exceptional crystallographic stability under heavy ion radiation at 10^{-3} dpa/s up to 20 dpa at 50 K, 293 K, 873 K, and some modest spreading in the Nb profile only at 623K.

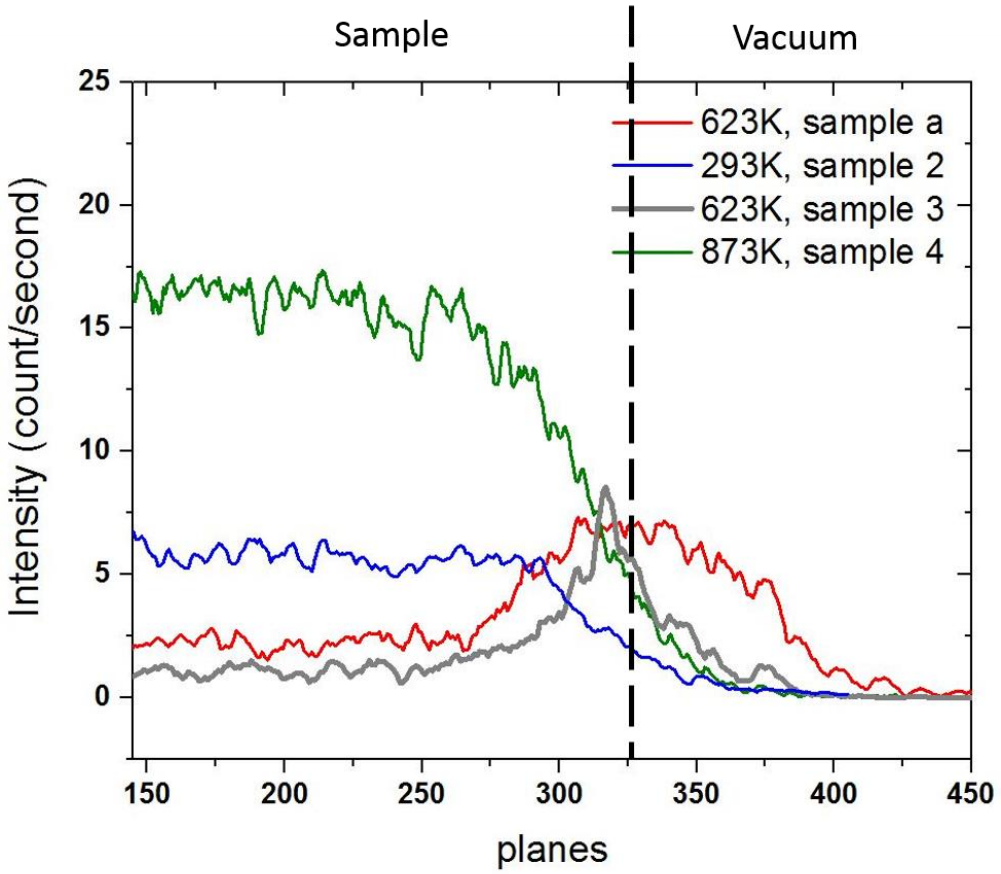


Figure 5.8 NanoSIMS depth profiles for Nb in the lower half of TEM thin foils irradiated to 20 dpa at 293, 623 and 873 K. The black dashed line indicates the approximate position of the sample surface. The bottom surface of the foils shows Nb segregation only in the 2 samples irradiated at 623 K, and a reduction of counts in the metal bulk.

In the experiments reported here, it is supposed that at low temperatures (50 K and 293 K) the observed change of Nb concentration between the SPP and the matrix (Figure 5.6 a) is limited by the low mobility of radiation-induced defects and the high rate of recombination of vacancies and interstitials locally. At higher temperatures, the Nb concentration in the matrix is determined by radiation-enhanced diffusion of solute Nb atoms towards sinks, which in these samples include SPPs, the large free surfaces of the TEM lamella and grain boundaries. At an intermediate temperature (623 K), the solute atoms segregate preferentially to the large free surfaces as shown in Figure 5.8, and the Nb concentration in the matrix decreases. In the high temperature regime (873 K), the diffusion of solute Nb atoms towards free surfaces is suppressed by the well-known reduction in the efficiency of equilibrium segregation mechanisms at higher temperatures captured in the McLean Isotherm [203], so that local back diffusion towards the β-Nb SPPs becomes the dominant mechanism for Nb redistribution.

Combining these factors, a simple model describing the behaviour of β-Nb SPPs under irradiation in this study can be suggested. The incident Kr ions create cascades that form a mixing zone at the SPP/matrix interface seen in the broadened EDX Nb profiles, Figure 5.6 (b) and Figure 5.7. This growth process is opposed by diffusion of Nb atoms back to the damaged SPP, but the driving force for this back diffusion depends on the irradiation temperature because of the strong variations in the equilibrium composition of both matrix and SPP in the phase diagram. Radiation mixing at low temperatures (50

K and 293 K) leaves a narrow mixing zone at the periphery of the SPPs, Figure 5.6 (a). At high temperatures (873 K), surface segregation is suppressed, Figure 5.8, and Nb diffusion in the Zr matrix is so fast that all the radiation mixing is recovered by back diffusion, Figure 5.6 (c). In the intermediate temperature regime (623 K), the balance between back diffusion, diffusional fluxes to other strong sinks like free surfaces and changes in the equilibrium composition of the β-Nb SPPs combine to give apparent growth of the SPPs as measured by EDX line profiles. At this temperature, the increase in SPP size is accompanied by a reduction of Nb concentration within the SPPs, Figure 5.6 (b), but I do not believe that this is evidence for the onset of dissolution because the SPPs retain their bcc structure even after 40 dpa and the amount of Nb redistributed from the SPP to the surrounding matrix is very limited (by comparing the total Nb amounts within the SPPs before and after irradiation). This agrees with the concept of ballistic introduction of Zr atoms into the SPPs [110, 111].

Compared to the mechanisms suggested by previous researchers, the model proposed here underlines the important role of anisotropic local diffusion of Nb in the Zr matrix in determining the behaviour of β-Nb SPPs under irradiation. The known anisotropy of diffusion coefficients for Nb in the basal plane and c direction in the α-Zr matrix [180] can lead to the changes in the shape of the SPPs reported in Figure 5.7. The preferential expansion along the c direction is due to slower back diffusion of radiation-displaced Nb atoms towards the SPPs. The contraction of the SPPs along the basal plane at 623K

up to 20 dpa but then growth at 40 dpa suggests a change in diffusion behaviour that might be related to the formation of lattice defects in the matrix. For instance, Harte et al. [103] showed in proton-irradiated Zircaloy2 samples that segregation of solute elements like Fe, Ni and Cr to a-loops enhances the dissolution of SPPs. Such segregation behaviour was not specifically investigated in this study. Nevertheless, the onset of formation of c-loops cannot account for this change in SPP dimensions since, as shown in Figure 5.2, c-loops appear at 5 dpa and are present in large concentrations at 10 dpa, well before the observed onset of SPP growth at 20 dpa. Some future simulation work might be helpful to explain this phenomenon.

Now it should be considered how this model can help understand the behaviour of β-Nb SPPs in the reactor core environment, where the primary differences compared to the in-situ heavy ion irradiation experiments here are the irradiating species and flux and the operational temperature. Fast neutrons will generate larger cascades than heavy ion damage [83], increasing the size of mixing regions at the outer surface of the SPPs, but the typical dose rate of in-service neutron radiation (about 10^{-7} dpa/s) is so much lower than the high heavy ion flux used here that there will be much longer recovery times between the generation of individual cascades at the same location. The operating temperatures in PWR reactors are around 600 K [5], similar to the intermediate temperature used in this study, but back diffusion of Nb atoms from the matrix towards the SPPs will be much faster at the highest temperature I have used of 873 K. The

absence of free surfaces (the typical grain size is several microns in fuel cladding alloys [107, 110] so grain boundary sinks will typically be much further away than the surfaces of the TEM sample) will encourage radiation-enhanced segregation of displaced Nb atoms from the matrix to SPPs, and further protect the SPPs from dissolution.

With all these factors considered, it is suggested that the results from in-situ irradiation at 623K are representative of the changes to β-Nb SPPs under neutron irradiation. The results of Shishov and others on radiation damage in Russian Zr-Nb alloys have shown size increases from 50 nm to 80 nm after 20 dpa [204] and Nb content reduction [204, 205] under neutron radiation at ~ 600 K. Studies of the in core neutron radiation damage at about 600 K of the French M5^{TM} alloy also show a size increase of SPPs from 35 nm to 50 nm after 5 dpa and a reduction of Nb content from about 80 wt% to 55 wt%. These observations are very similar to my results at 623 K, although I have also shown that the SPPs grow more in the c-direction. Yet there are also some significant differences. The SPP growth reported by Doriot et al. [107] increases with damage up to 5 dpa, then stabilises, while in Figure 5.7 it is shown that the SPPs keep growing to higher damage levels. During low-fluence neutron irradiation, this may be due to Nb diffusion to other radiation-induced defects such as c-loops, or to form nano-precipitates, that will reduce the matrix Nb supersaturation and diffusion towards the SPPs. This effect is largely suppressed in this study due to the presence of the large free surface acting initially as strong sinks. Once these surface sinks are saturated, the equilibrium of the Nb between

the SPPs and matrix then takes longer to reach in the in-situ heavy ion radiation at 623 K than that in neutron radiation under service conditions.

It is also interesting that the SIMS data in Figure 5.8 suggests that there is a measurable reduction of Nb content in the matrix only at 623 K, a factor that has been suggested to be beneficial for the corrosion resistance of Zr-Nb alloys [37].

5.2 Replicating neutron irradiation induced damage by proton irradiation

In the study of the radiation induced Nb precipitates in α – Zr matrix, the results from neutron irradiation (Chapter 4 and [107]) do not always agree with the results from proton irradiation [116] regarding the morphology of the precipitates. This has also led to some ambiguity in understanding the mechanism of precipitation. While there are ongoing discussions about this discrepancy and suggestion of the potential causes, no direct comparison of results from the same material has been reported so far. In this section, the unirradiated, uncorroded sample B166, one of the Zr – 2.5 wt% Nb alloy sets provided by CNL, has been irradiated by protons and then characterised following the same procedures used for the neutron-irradiated samples. The aim is to compare the formation of the radiation-induced precipitates under both types of irradiation, thus help to understand the underlying mechanisms.

5.2.1 Irradiation campaign and sample preparation

The bulk B166 sample was cut into 3mm discs and polished on both sides to give clean surfaces. The final thickness of the discs after polishing was around 100um. The discs were then taken to Dalton Cumbrian Facility and irradiated by 2 MeV protons. The Bragg peak was simulated by SRIM in the Kinchin-Pease model, with the displacement energy of Zr atoms set to be 40 eV, as shown in Figure 5.9. The proton current was adjusted so that the damage rate at 40% depth of the Bragg peak (about 12 um) was 1.5×10^{-5} dpa/s. The total irradiation time was about 37 hours and the total damage at 12 μm was about 2 dpa. The discs were put on a heating stage with enough cooling capability to maintain a reasonably stable irradiation temperature. The measured temperature of the discs through the entire irradiation campaign is shown in Figure 5.10. Since the damage created by proton irradiation is not distributed evenly in depth, cross-section TEM lamella were lifted-out at about 12 μm to 18 μm beneath the surface of the bulk sample, corresponding to 40 % to 60 % of the depth of the Bragg peak. This ensures a relatively even distribution of damage in the TEM foils. It was achieved by FIB lifting-out a deep foil from the bulk sample, cutting off about 12 μm from the top surface, and then further thinning the foil. The geometry is shown in Figure 5.9.

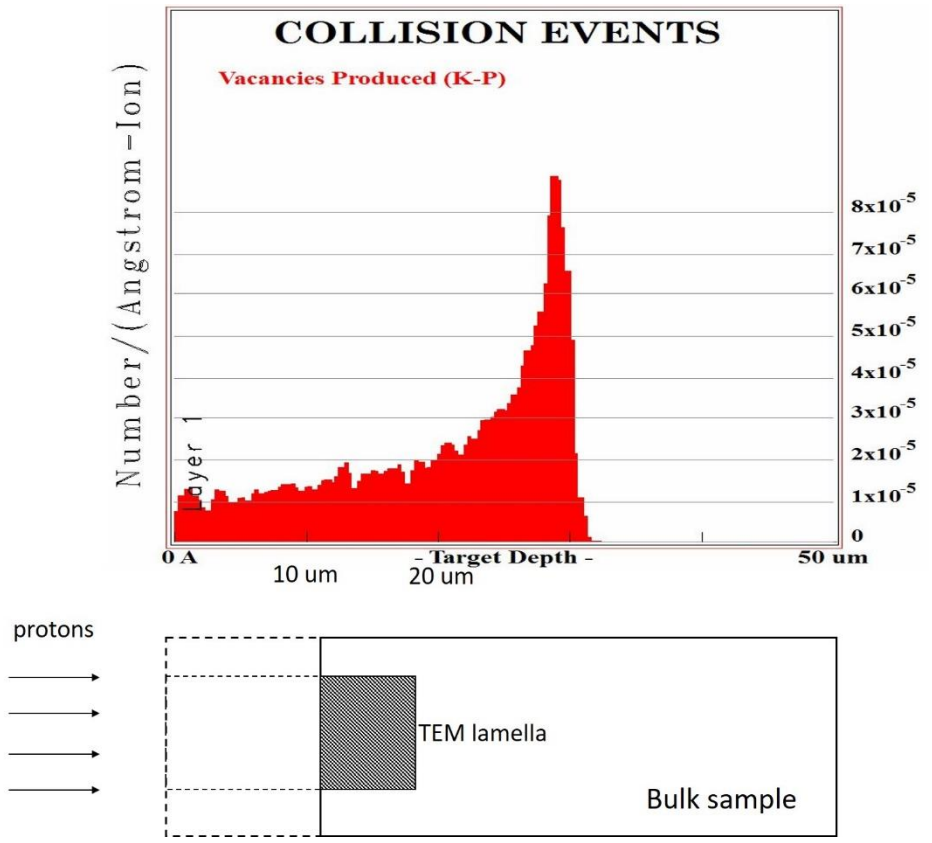


Figure 5.9 A schematic showing the position of the lift-out TEM lamella with respect to the distribution of the damage profile created by the protons

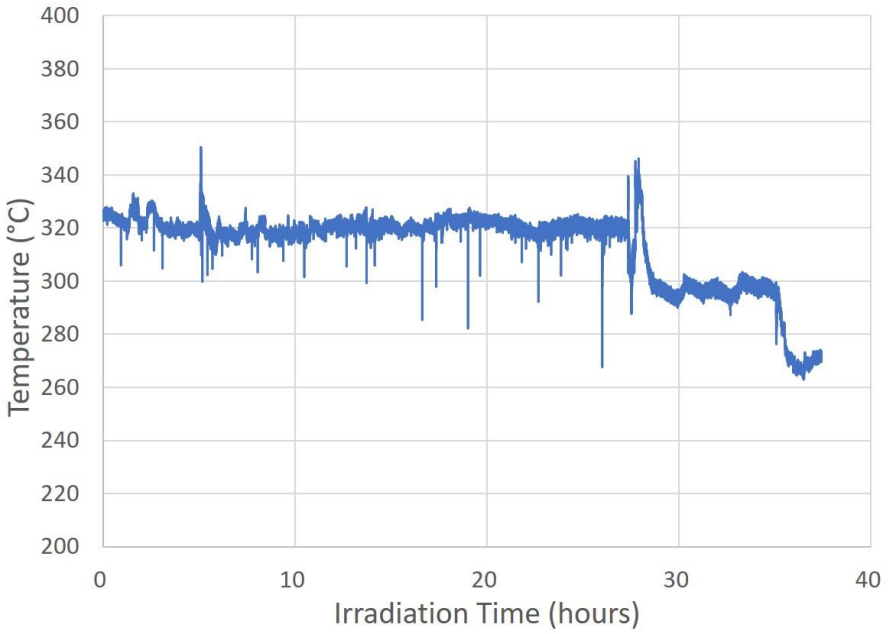
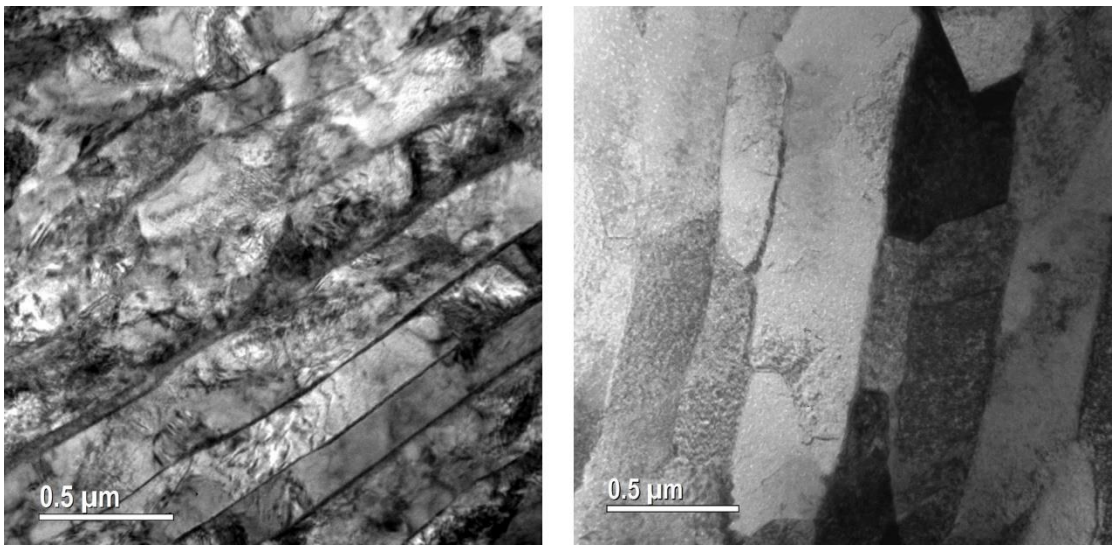


Figure 5.10 The measured temperature of the B166 disc irradiated to 2 dpa

5.2.2 Characterisation of the proton irradiated B166 sample

The characterisation was mainly carried by TEM. Figure 5.11 shows a comparison between the microstructures found in proton irradiated B166 and the as-received B166 material. The basic 'α – β – α' layered structure remains after irradiation. The differences in the width of the α and β grains in the two images are thought to be natural variations from the different locations of the sample rather than a irradiation induced effect.

The kinematic bright field images using $g = \langle 0002 \rangle$ were taken in several grains from two TEM foils of the proton irradiated B166 samples, and two typical grains are shown in Figure 5.12. It is obvious that some c-loops can be seen, while irradiation induced precipitates are not observable. This result is consistent from all the grains investigated. Some small features of a vague contrast seen in (c) and (d) are assumed to be surface oxides formed due to long time sample storage after preparation, as evidenced by the rings in the diffraction patterns. The contrast from these surface oxides are very different from those from the precipitates, as shown in Figure 4.2 and hence are not going to be mistakenly interpreted.



(a) (b)

Figure 5.11 TEM images showing the microstructure of (a) as received B166 without any irradiation (b) B166 irradiated by protons to 2 dpa.

5.2.3 Discussion

The first interesting feedback from the TEM characterisation results is the absence of irradiation-induced Nb precipitates in the α – Zr matrix. This is different not only from what has been reported in neutron-irradiated CNL Zr – 2.5 Nb samples to 2 dpa at 325 °C (B70) in this thesis, but also proton-irradiated Westinghouse^{TM} recrystalised Zr – 0.5 Nb and Zr – 1.0 Nb samples to 1 dpa at 350 °C as reported by Yu et al. [127]. Moreover, Nb rich precipitates were observed by EDX mapping in proton irradiated Low-Sn ZIRLO (Nb bearing) using similar irradiation parameters at the exact same facility (DCF) [206]. But a similar absence of these precipitates is seen in neutron-irradiated CNL Zr – 2.5 Nb samples to 2 dpa at 250 °C (B56). It is therefore of great interest to figure out the reason for this absence of Nb precipitates.

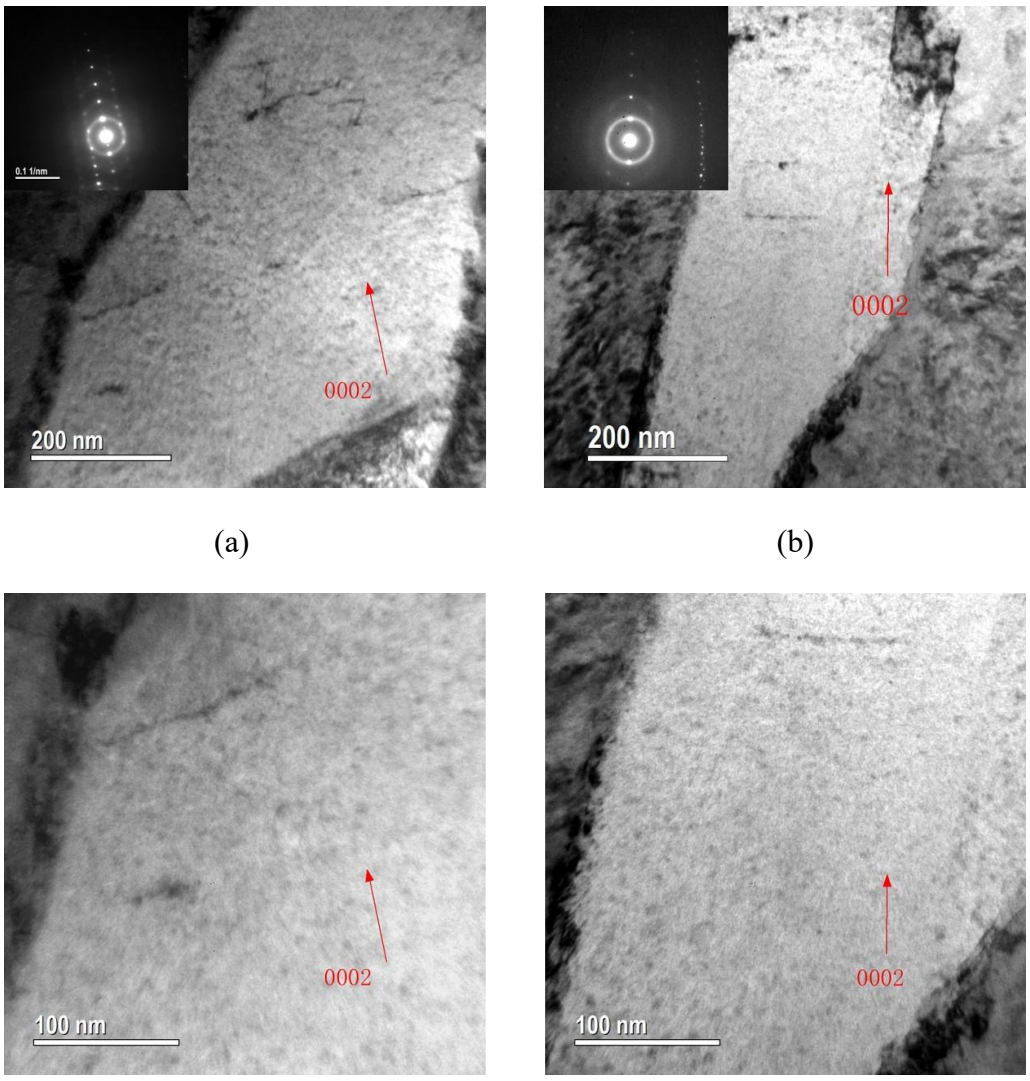


Figure 5.12 Kinematic bright field images show two grains in proton irradiated B166, (a) and (b), at g = 0002. (c) is from a region in (a), and (d) is from a region in (b).

To understand the discrepancy in different cases, two factors that can affect the morphology of the precipitates should be considered, the formation process and the stability under irradiation. As discussed in Chapter 4, the formation of the precipitates that are observable under TEM requires the diffusion of solute Nb atoms towards a nucleation site.

Thus this discrepancy may arise from the different diffusion coefficients of the solute Nb atoms in α – Zr matrix. If the diffusion coefficient in the proton-irradiated CNL Zr – 2.5 Nb samples is much lower than that in neutron irradiated samples at 325 °C, it is not surprising that the precipitates cannot be seen in the proton-irradiated CNL Zr – 2.5 Nb samples.

One major difference in the parameters for the proton and neutron irradiation of the CNL Zr – 2.5 Nb samples is the damage rate. The damage rate is 1.5×10^{-5} dpa/s in the proton irradiated samples, while in the neutron irradiated samples is is 1×10^{-7} dpa/s. As mentioned in Section 2.5, the concept of 'variable shifts' [142] is used to overcome this difference. The shift from the actual temperature T_1 to the equivalent temperature T_2 can be calculated as

$$T_2 - T_1 = \frac{\frac{kT_1^2}{E_m^V} ln\left(\frac{K_{0_2}}{K_{0_1}}\right)}{1 - \frac{kT_1}{E_m^V} ln\left(\frac{K_{0_2}}{K_{0_1}}\right)}$$

where K_{0_2} and K_{0_1} are the corresponding defect production rates. E_m^V is the migration energy of the vacancies, set to be 0.6 eV in this case [207]. Based on the damage rates by protons in this study, the equivalent neutron irradiation temperature for the proton irradiation is calculated to be 210 °C, even lower than the irradiation temperature in B56 samples (250 °C). As discussed in the previous chapter, the Arrhenius curve of the diffusion rate of vacancies in α-Zr matrix is very steep, hence there is a very large temperature dependence of the radiation enhanced diffusion of Nb

atoms. As a result, no observable precipitates can be seen in the proton irradiated CNL Zr – 2.5 Nb samples. A suggested proton irradiation temperature in the future work to mimic the neutron irradiation at 325 °C can also be calculated using this equation. If the damage rate is kept unchanged, the proton irradiation should be carried out at 440 °C.

This claim about the influence of the temperature might be further supported by the results reported by Topping et al. in their proton irradiated ZIRLO samples as mentioned above [206]. The EDX mapping of Nb rich precipitates were presented in two sets of samples irradiated at two temperatures 280 °C and 450 °C. The Nb precipitates in the sample irradiated at 450 °C are much larger than those found in the sample irradiated at 280 °C. As discussed in Chapter 4.1, the small Nb rich precipitates may not be seen under TEM diffraction contrast, where the large ones (~ several nm) can be more clearly identified. It is a pity that no clear TEM images of diffraction contrast using g = 0002 were shown in their results, therefore it is not clear whether those Nb precipitates found under 280 °C irradiation are visible under TEM. Nevertheless, the size distribution of the Nb precipitates could be impacted by the irradiation temperature.

In the meantime, the stability of the precipitates is determined by the different types of interaction between the incident particles and the matrix. As discussed in detail in section 5.1.3, the precipitates are destroyed by cascade-induced mixing and restored by

local backward diffusion. In neutron irradiation, the balance is achieved between the neutron-induced cascades and Nb diffusion towards the precipitates enhanced by radiation. However, in proton irradiation, very little or almost no cascades are created [83], thus the balance cannot be established. Therefore, the precipitates can grow to much larger sizes, as reported by Yu et al. [116].

5.3 Summary

This chapter has shown two case studies of using ion irradiation to emulate the effect of neutron irradiation, particularly regarding the stability of SPPs / precipitates in a binary Zr – 2.5 Nb alloy. In both cases, the results from ion irradiations show some differences from the neutron irradiation results. The cause of these discrepancies is attributed to a series of different irradiation parameters, including the damage rate, irradiation temperature, geometry of the samples and the nature of the irradiating species. It has been shown that only with careful design of the irradiation campaigns and appropriate comparison of the results, the in-situ heavy ion and proton irradiations can be a good method to help understand the mechanisms determining certain phenomena caused by neutron irradiation in the samples.

Chapter 6 In-reactor corrosion of CNL Zr-2.5Nb alloys

The in-reactor corrosion of the CNL Zr-2.5Nb alloy is discussed in this chapter. As described in chapters 2 and 3, this type of Zr alloy exhibits some corrosion behaviour different from other types of Zr alloys; while radiation accelerated oxide growth is usually seen in Zircaloys [165], this phenomenon is not obviously seen in the alloy studied in this project.

Although the corrosion of Zr alloys can be influenced by many factors such as the concentration of alloying elements in solid solution [76], the distribution of nanopores in the oxide [62], the phase distribution in the zirconium oxide [48] and so on, I have concentrated on the evolution of the β-Zr phase during corrosion. The reason to choose this factor for investigation will be discussed in detail in later sections.

The samples used for this study are selected so that the effect of different factors can be identified by making direct comparison of two samples that have experienced changes in only a single parameter. Table 6-1 shows all the samples used.

As discussed in Section 3.1, one significant difference between the microstructures of the CNL Zr-2.5Nb alloy and other commercial models (Zircaloys and Zirlo ^{TM}) is the presence of the β-Zr phase adjacent to the α-Zr grains. It was shown in Section 4.2 that these β-Zr grains go through a decomposition process as they stay in the metal matrix

under reactor conditions. As claimed in Section 4.2, the result of this process is β regions with different distributions of transformed β-Nb, α-Zr and untransformed β-Zr. The longer time the initial β-Zr grains spend in the metal under reactor conditions, the more β-Nb with higher concentration of Nb and less β-Zr are expected in the resulting β regions. Therefore, it is no longer the β-Zr grains that meet the incoming metal/oxide interface but rather the β regions mainly consisting of β-Nb phase. Based on the initial structure of the β-Zr grains and their decomposition process while in the metal, the morphology of the resulting β-Nb phase can vary from discrete particles to continuous sheet, or a combination of these two types, as illustrated in Figure 4.17. For convenience, these β regions will sometimes also be addressed as β-Nb grains later in this chapter, since they commonly have a Nb concentration much higher than 20% which is the equilibrium Nb concentration in β-Zr according to the phase diagram [172], as shown in Figure 4.19.

These β-Nb grains can have an impact on the overall oxidation process for several reasons. Firstly, these β-Nb grains have a high Nb content, therefore can influence the concentration of Nb^{5+} ions in the oxide and the local electrical conductivity. Secondly, as shown by previous research [19] and in this study later, the formation of some of the cracks is related to the existence of the β grains. The layered structure of α-β-α-β grains, as shown in Figure 3.1, indicates that the oxide front will meet the β grains periodically when moving into the metal. Therefore, studying the corrosion behaviour of these β-

Nb grains with different morphologies and distributions is important for understanding the general corrosion behaviour of the material.

Table 6-1 Sample List

Samples	**Irradiation/ Oxidation Days**	**Irradiation temperature (°C)**	**DPA in metal**	**Oxide thickness (um)**
B56	192	250	1.9	1.29
B70	192	325	1.9	2.44
B96	185	325	0	2.26
B74	2765	325	25.2	16.74
B88	2850	325	0	16.43

In this section, the results are presented in the following order. The methods used to study the β phase are firstly discussed, followed by the basic characterisation of the oxides formed in different samples. Then the oxidation processes of the β phase regions, especially the oxidation rates of Nb, are compared between different samples. With all the data and comparisons at hand, the evolution of the β phase in the oxide, and how it is influenced by different factors, is discussed. The last part of this section is a discussion of how the β phase regions affects the general corrosion behaviour of the alloy.

6.1 Methods used to study the corrosion of the β phase regions in oxide

The corrosion of the β phase regions consists of both microstructural and compositional changes, which requires different techniques to be used for characterisation. The microstructural changes, including the change of morphology, crystalline to amorphous transitions and formation of micro-cracks, is identified by STEM HAADF imaging and TEM diffraction analysis, as shown in Figure 6.1. Figure 6.1 (a) and (b) are HAADF images taken on B56 and B74 showing the different morphology of β phase regions in the oxide, corresponding to the type 1 and type 2 β regions as the results of the decomposed β-Zr grains discussed in Section 4.2.2. Figure 6.1 (c) shows a HAADF image of a β-Nb region in the oxide. The contrast between the β-Nb region and Zr oxide is very strong in the lower part of the region, while the contrast in the upper part region is not. By assuming the β-Nb region runs through the whole thickness of the thin TEM specimen, this phenomenon indicates a higher Nb concentration in the lower part of the β region and a lower Nb concentration in the upper region. Diffraction patterns were also taken at the two regions indicated by the red circles, as shown in Figure 6.1 (d) and (e). It shows that region 1 in the lower part is crystalline, but region 2 consists of both a crystalline component and amorphous component. The cracks can also be seen clearly in the HAADF images like Figure 6.1 (a) and (b).

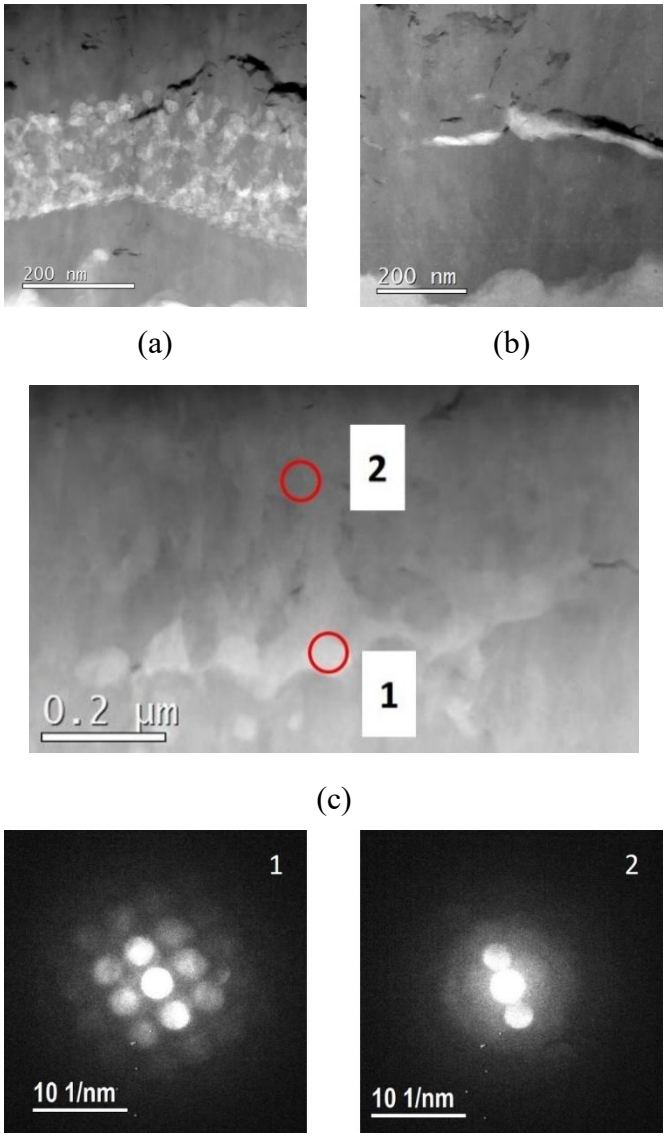


Figure 6.1 HAADF images (a) and (b) show the morphology of different types of β-Nb in oxide. (a) was taken from a B56 sample and (b) was taken from a B74 sample. (c) shows a β-Nb grain in a B74 sample, consisting of two parts. Diffraction patterns (d) and (e) were taken by nano-beam diffraction in TEM to show the microstructure of the β-Nb regions circled in 1 and 2 in image (c).

The change of the content of Zr, Nb and O in the β regions can be identified by quantitative analysis of the EELS data. As described in Chapter 3, the Zr L3, L2 and Nb L3, L2 edges are used to quantify the amounts of these elements and can be subtracted from the same spectral image. The oxygen K edge is used to quantify the O

content. In ideal cases, the spectral image containing the O K edge and the spectral image containing Zr L and Nb L edges should be taken at the same region, with same pixel size and pixel time. But there are cases where I have used different pixel times for core loss spectra O and core loss spectra Zr and Nb, in order to increase the signal intensity in the Zr L and Nb L spectral image. Thus normalisation is required to calculate the relative quantities of the elements. In a spectral image containing regions of zirconium oxide, a small region deep in the oxide far from the metal/oxide interface is selected that contains only zirconium oxide, without any other features such as cracks or β phase. The subtracted oxygen and zirconium contents in this region are forced to be 2:1 to obtain the conversion factor between the two spectral images. Then this factor is applied to the entire spectral images where β regions are included, so the relative quantities of Zr, Nb and O can be calculated.

The oxidation state change of the Zr and Nb in the β phase region is another important feature of interest. EELS core loss spectra are used to determine the oxidation state, as described in Section 3.3.2. Instead of using the absolute edge positions to represent the oxidation state change, the edge shift, which measures the relative position of the edge to the reference point (unoxidized β regions in metal far from the metal/oxide interface), is used to represent the oxidation state. Although using HyperSpy to process the entire spectral image can provide fitting results of the spectrum from each pixel, such work is very time consuming and not necessary for the work of determining the oxidation states

of Nb in different β regions at different depth in the oxide. Instead, an 'average' spectrum is firstly extracted from the spectral image by the 'Picker Tool' in Digital Micrograph^{TM} software and then processed by HyperSpy. To make sure the interpretation of the edge shift is reliable, it is important to clarify how the spectrum is extracted from a large spectral image. Figure 6.2 shows some typical images of the β regions in the oxide from B56 and B74 samples and the spectra are extracted from the rectangular regions. The centre of the rectangle is put at the brightest point in the β region, which represents the point of the highest relative amount of Nb. The boundaries of the rectangle are set to be as large as possible so that a large region of the β phase can be covered and obvious contrast changes within the rectangle are avoided. The output spectrum will be a sum of all the spectra from the pixels covered by the rectangle. This methodology is intended to gather as many pixels as possible to increase the intensity of the spectrum, while ensuring the energy shift of the Nb edge within the rectangle as small as possible. To further rule out the possibility that the edge shift stands for a mixture of different oxidation states of the Nb, the FWHM of the Nb L edges are recorded and compared in each extracted spectrum. It is found that for the Nb L3 edge, the minimum value of the FWHM is 6.25 eV from all the results. Therefore, a threshold of 7 eV is set for the FWHM of the Nb L3 edge in the 'average' spectra. If the FWHM is not larger than 7 eV, the result is regarded reliable. If the FWHM is larger than 7 eV, it means the spectrum contains components of different states of Nb, thus the result will be abandoned and a new 'average' spectrum will be extracted from a different

rectangle in the spectral image, until the 7 eV threshold is met. Once the extracted spectrum is confirmed, the energy shift of Zr L3 edge is also measured. However, it should also be noted that where pixel by pixel oxidation state changes are valuable, for example in Figure 6.18, the entire spectral image will be directly analysed by HyperSpy. Combining all these features together, a comprehensive characterisation of the β regions in the oxide can be achieved.

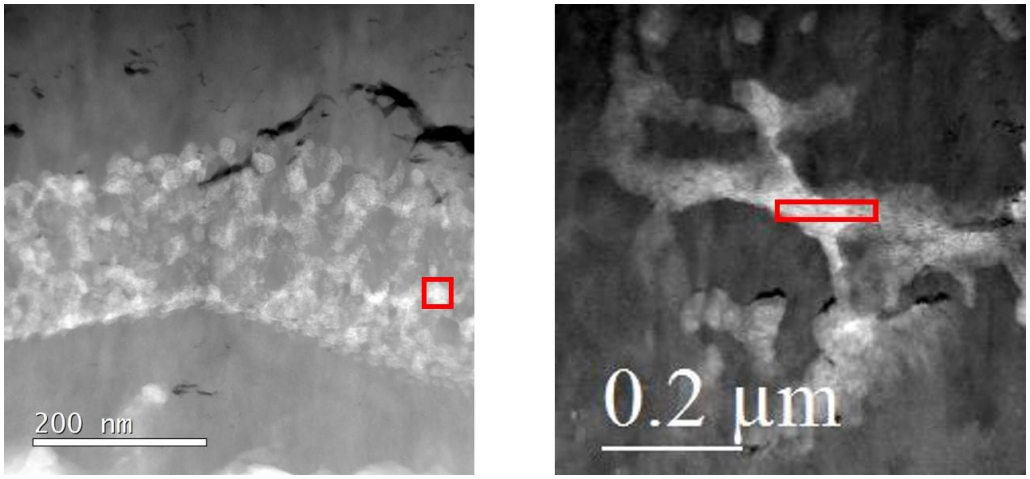


Figure 6.2 HAADF images showing the β regions in oxide and the positions where the spectra are extracted (red square)

Figure 6.3 illustrates the corrosion of one β region under reactor conditions. At first it is embedded in the α-Zr metal matrix while the oxide starts to form at the water facing surface of the metal, as shown in Figure 6.3 (a). The oxide gradually grows inward and after t1 days, the metal / oxide interface reaches this β region, as shown in Figure 6.3 (b). The β region starts to oxidise while the metal / oxide interface keeps growing inward as the time moves beyond t2. After another t2 days, the β region is deeply

embedded in the Zr oxide, as shown in Figure 6.3 (c). When characterising the samples, t2 is calculated based on the distance (D as shown in Figure 6.3) from this β region to the metal / oxide interface, as shown in Figure 6.4.

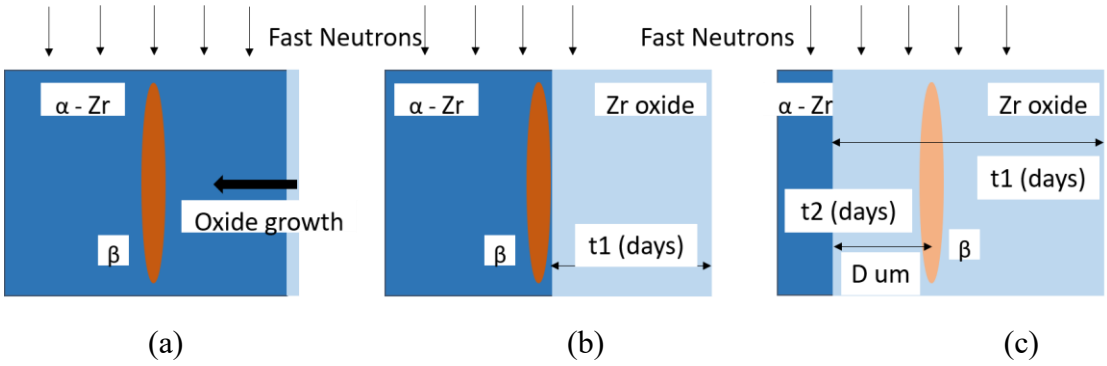


Figure 6.3 Schematic life of β region during in reactor corrosion. The decomposition process in the metal is not illustrated in this image

In this study, the microstructural and microchemical changes to the β regions in different samples are plotted against the oxidation time t2, rather than the distance of from the metal/oxide interface. This is due to the fact the oxide growth rate in different samples are different. Therefore, the β regions at the same depth in the oxide in different samples may have been incorporated in the oxide for different time, and hence are at different states of oxidation. Using the oxidation time rather than distance thus makes the direct comparison between different samples more reasonable.

However, oxidation time is not the only factor considered. The entire corrosion process takes place under fast neutron radiation for in-flux samples, so radiation damage received is another important factor. It should be noted that the effect of the radiation

damage can be different when the β phase regions are in the metal and in the oxide, and the radiation-induced changes to the oxide are predicted to be very limited [135]. By contrast, substantial changes can happen to the β regions in metal under radiation as reported in [208] and in Section 4.2. Therefore, the radiation damage received in the metal, rather than the total radiation damage, is another parameter to be considered for the corrosion of the β regions. It is calculated by multiplying the fast neutron flux by (t1 - t2) days.

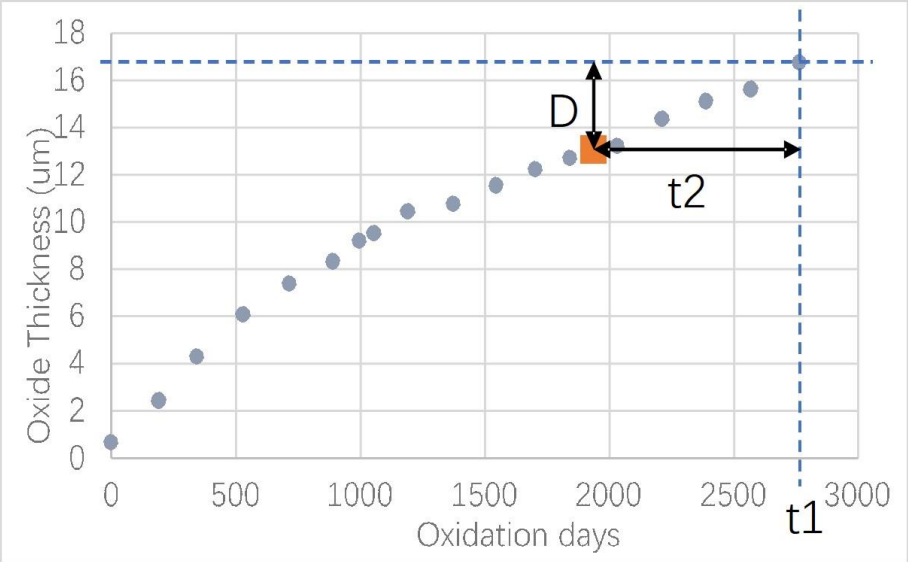


Figure 6.4 An example showing how the oxidation time is determined for a β region D (um) from the metal / oxide interface. The horizontal dashed line corresponds to the total thickness of the oxide grown in time t1. The data points were measured at each time interval during the in-reactor corrosion test.

6.2 Characterisation by STEM HAADF images and EELS

In this section the oxidation process of the β regions and changes happened to them during oxidation are discussed. The results shown first are from the characterisation of

the long time, high temperature in-flux sample (B74), as it contains the β regions oxidised for the longest time.

B74, in flux, 2765 days, 325^{0}C

The exceptionally long time this sample has spent in the reactor has allowed the oxide film to grow to an average thickness of 16.7 μm. In order to cover the entire oxide film, several TEM lamellae were extracted from different depths, and Figure 6.5 shows a stitch of these images. Some general observations can be made by looking at these HAADF images, (1) the metal/oxide interface is relatively flat compared to other Zr-Nb alloys corroded under different conditions [19], (2) β-Nb sheets with obvious bright mass contrast can be seen up to ~3 μm from the metal/oxide interface, (3) lateral cracks can be usually seen ~2 μm from the metal/oxide interface onward, and their distribution shows some periodicity, as is often seen in oxides on Zr alloys [59].

For a more detailed observation of the β regions, EELS mapping was carried out at multiple places across the whole depth of the oxide, including the strips with obvious bright contrast and lateral cracks of different sizes. Using the method described in the previous section, plots of the oxidation states of the Nb and Zr in the β regions as a function of time and neutron damage received in metal can be made, Figure 6.6. While the dependent variable is the shift of the edge position in the spectra, there are two independent variables in these plots. One is the time the β region has spent in the oxide

and the other is the neutron damage levels received when in the metal. The negative days in the plots refer to those data points taken in the metal and calculated in the same manner as those in the oxide. It is clear that neither Zr nor Nb are oxidised in this phase (zero edge shift). After being absorbed into the oxide, the Zr and Nb are gradually oxidised with increasing exposure time. The final edge shift for the Zr is 2 eV when it achieves the 4+ state, to form ZrO_2. The edge shift for Nb is a bit more complicated as there are several oxidation states from 2+ to 5+, and the final edge shift is about 4 eV which marks the formation of Nb_2O_5.

Although the 3-dimensional plot presents the oxidation process based on these two independent variables, it is hard to display in 2 dimensions on a paper. Thus a 2D plot is adopted below, where the only independent variable is the time in the oxide. As shown in Figure 6.7, this type of plot illustrates how fast the Nb in the β region is oxidised, a key question to be answered. The Nb remains un-oxidised as long as ~150 days into the oxide, then gradually oxidises to 5+ state after about 700 days in the oxide. At different stages of the oxidation process, the β phase regions also have different morphologies. Some typical ones are shown in Figure 6.8. The β regions retain the strip shape until about 200 days into the oxide. From ~200 to ~400 days in the oxide, the periphery of the strip shows an obvious reduction of in Nb content while the central part remains unchanged. Micro cracks start to form at the site of the β phase regions at around 500 days, and gradually grow to be major cracks up to 2000+ days in the oxide.

The Nb is retained along the crack flanks during this crack growth process, but with a lower concentration than that in the shortly oxidised β regions.

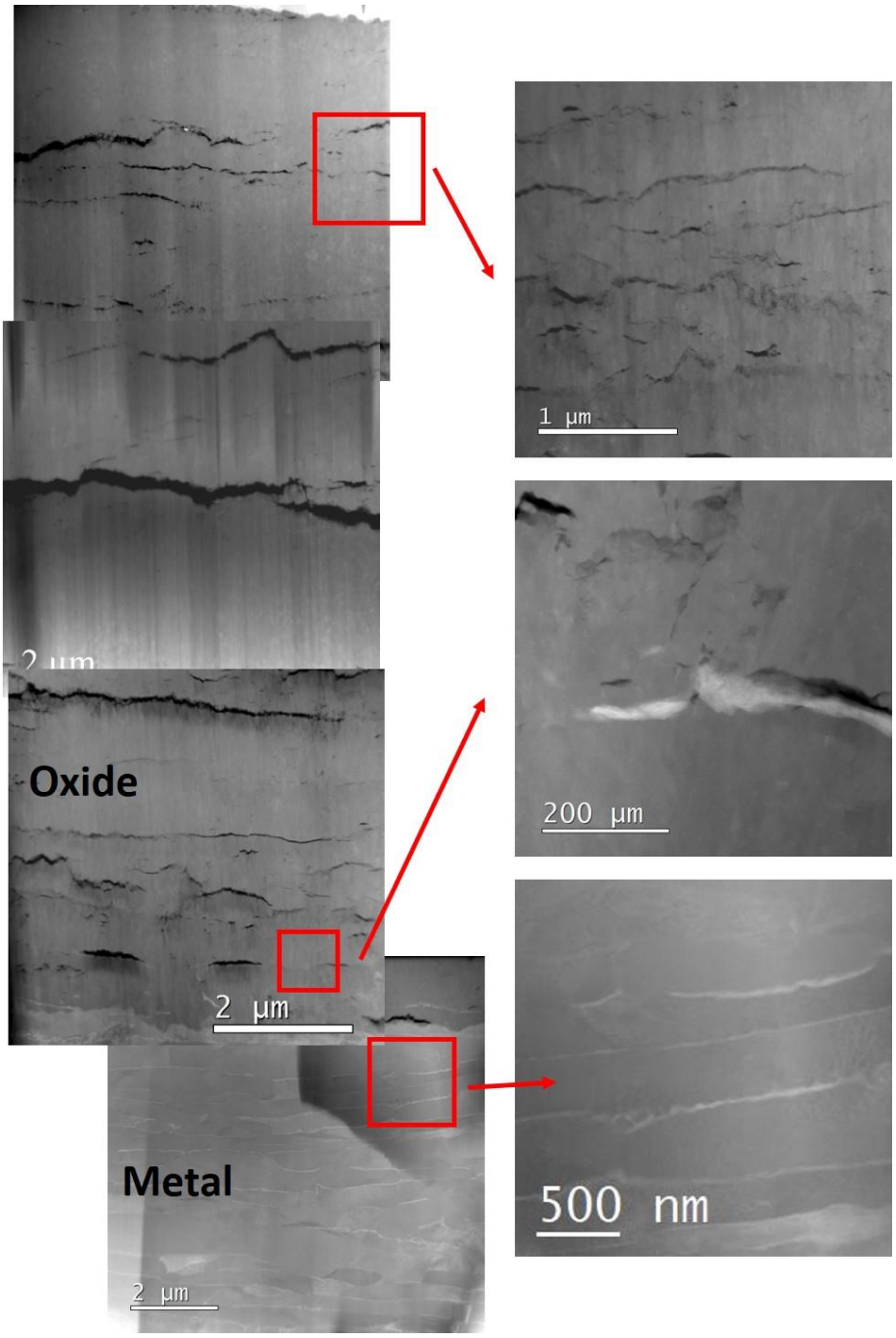
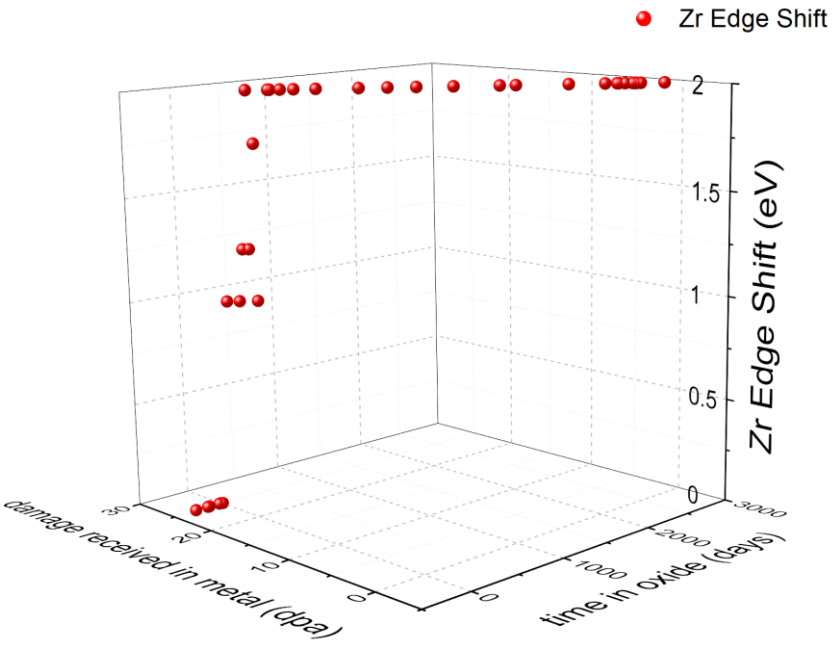
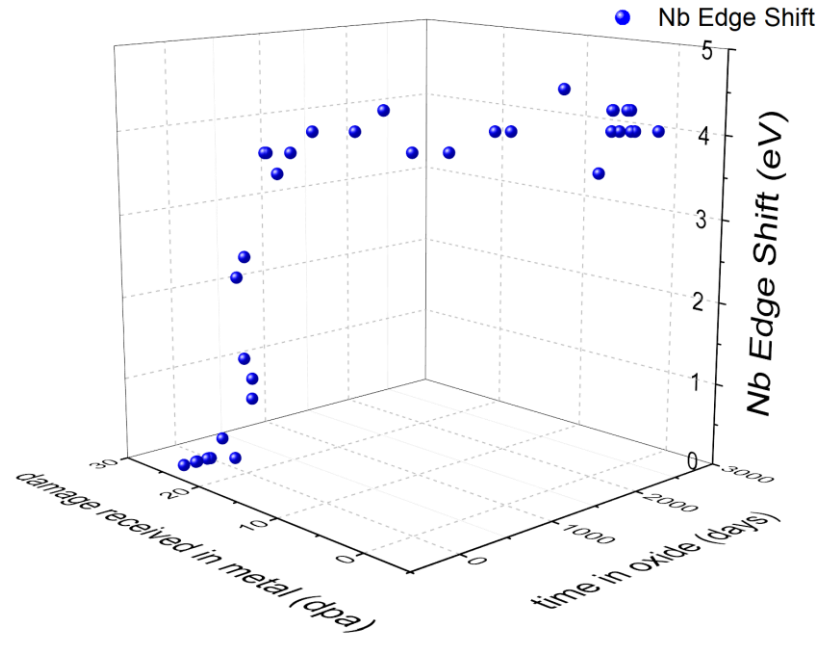


Figure 6.5 HAADF images showing the oxide formed on the samples B74. The layered β-Nb strips in the metal, β-Nb strip newly incorporated in the oxide, and the cracks in the oxide are shown in images on the right



(a)



(b)

Figure 6.6 3D plot of the edge shift of the (a) Zr and (b) Nb in the β phase against time in oxide and damage received in metal

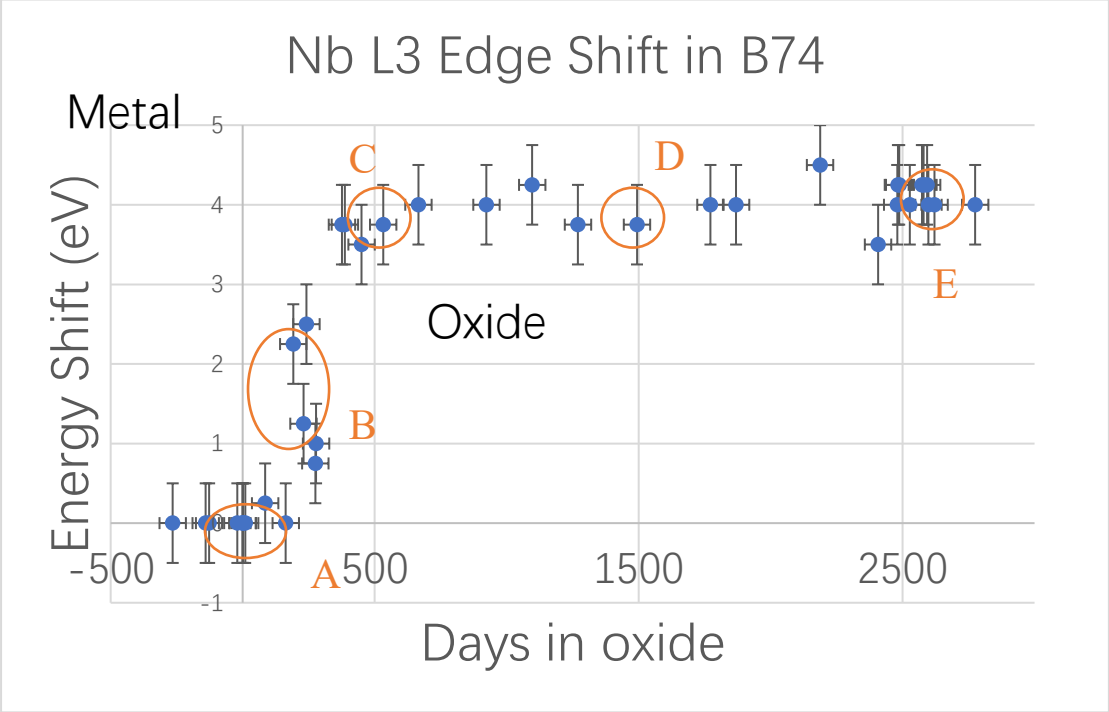
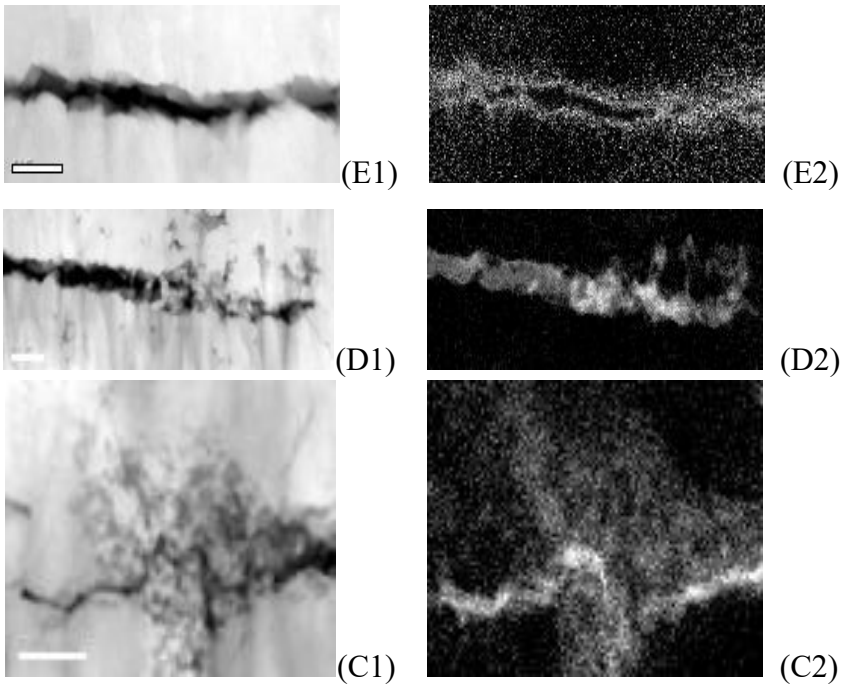


Figure 6.7 Oxidation of Nb in β regions plotted against time in the oxide in B74. The labelled yellow circles indicate the typical regions shown in Figure 6.8.



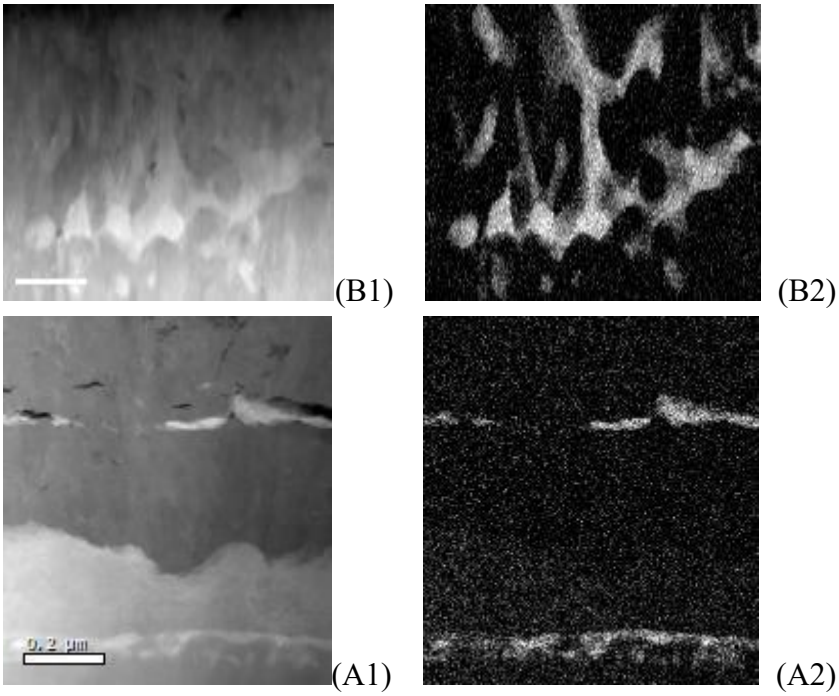


Figure 6.8 Typical β regions at different stage of oxidation. (A1) to (E1) are the HAADF images and (A2) to (E2) are Nb mapping extracted from EELS spectral images.

B70, in flux, 190 days, 325ºC

Following a similar procedure, the oxidation of β regions in the B70 sample is displayed in Figure 6.9. Compared to what is shown in the B74 samples, one of the major differences is the morphology of the β phase regions in the oxide. While the strip shape is well retained for many β regions in B74, they appear to have a 'hollowed' structure in B70, as highlighted by the high magnification image. This mass contrast indicates that this structure consists of both discrete β-Nb particles and regions of ZrO_2. This oxidised β region is thought to correspond to the type 1 β region in the metal matrix as discussed in Section 4.2. When it is incorporated in the oxide, the α-Zr component oxidises quickly, leaving the discrete β-Nb particles surrounded by ZrO_2. The distribution of the cracks in B70 also shows less periodicity compared to that in B74.

The oxidation state of the Nb in the β regions against time in the oxide is plotted in Figure 6.10. The oxidation process takes place almost through the whole thickness of the oxide, and only the data point at the very top surface of the oxide can be regarded as nearly fully oxidised to the 5+ state.

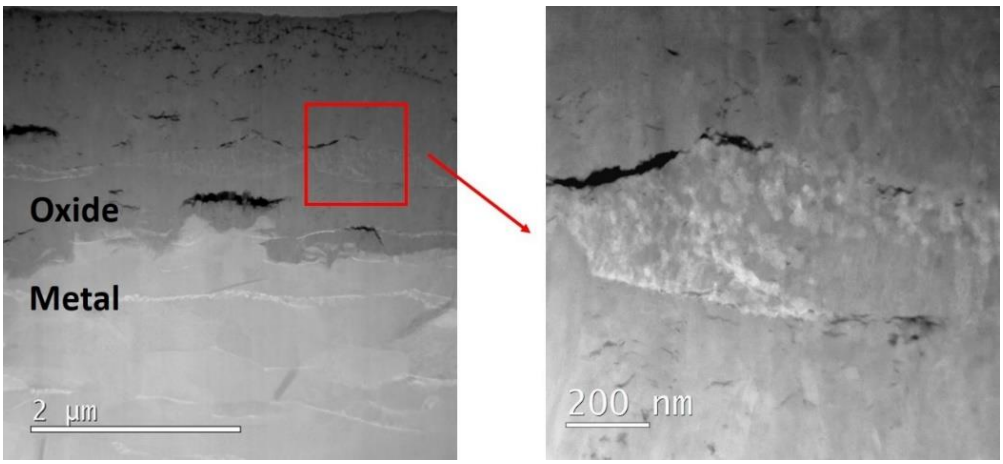


Figure 6.9 HAADF images showing the oxide formed on B70, and the 'hollowed' β regions are shown in the high magnification image on the right.

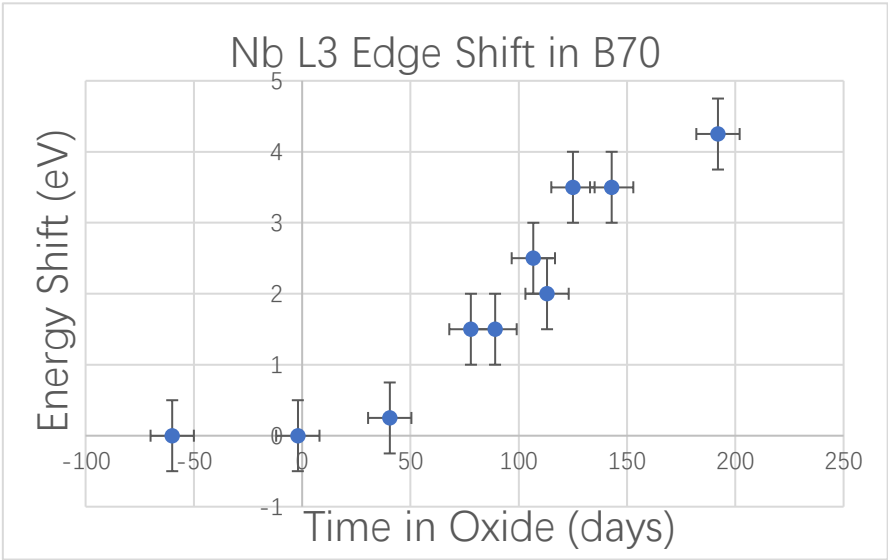


Figure 6.10 Oxidation of Nb in the β phase against time in the oxide in B70.

B56, in flux, 192 days, 250ºC

The TEM samples from B56 show even thinner oxide than that on the B70 sample, and hence fewer β regions in the oxide. Yet they also appear to have a similar 'hollowed' structure. One interesting feature to notice is the unique shape of the metal/oxide interface, which follows the shape of the lower surface of the nearby β regions, as circled in yellow. A further discussion on this feature is given in Section 6.3.4. Like that in B70, the oxidation process of the Nb takes up the entire oxide thickness, and even the data set at the very top surface might not be fully oxidised Nb.

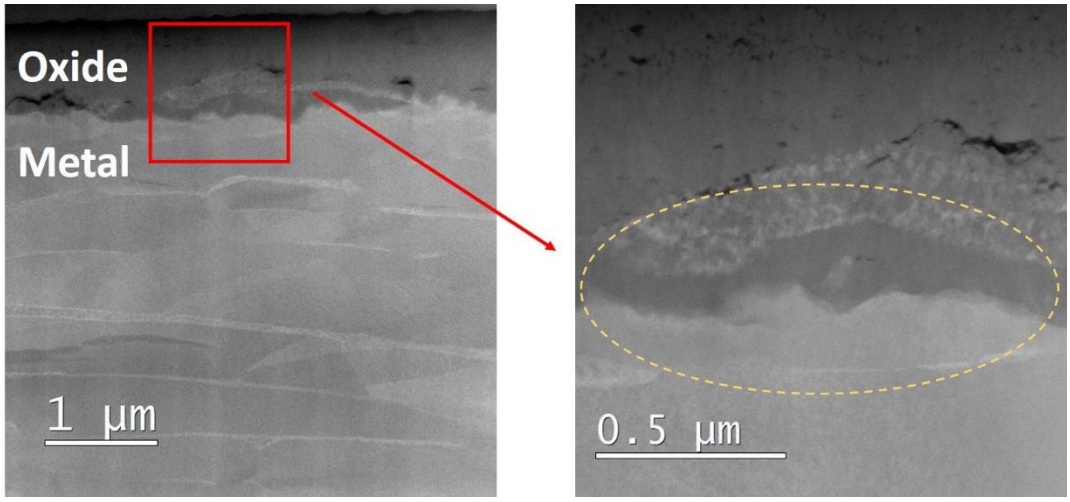


Figure 6.11 HAADF images showing the oxide formed on samples B56. The 'hollowed' β regions are shown in the high magnification image on the right.

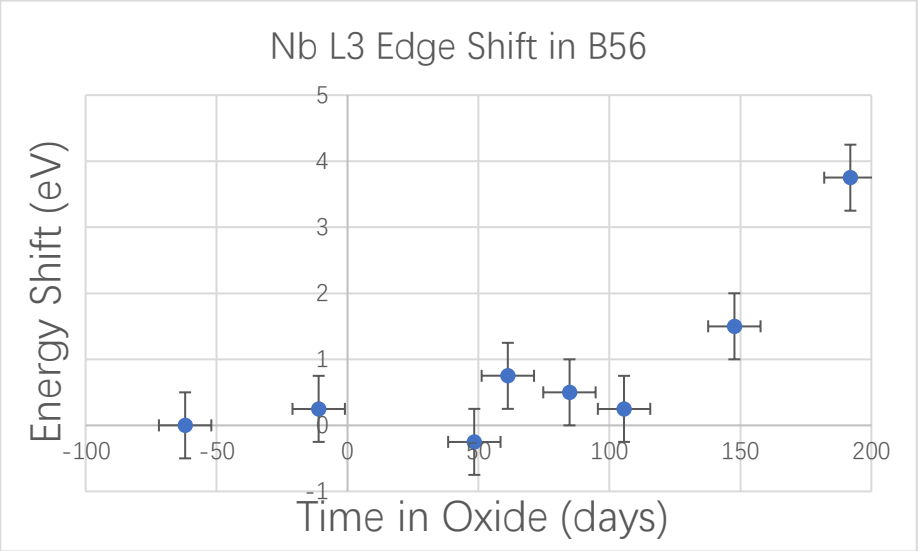


Figure 6.12 Oxidation of Nb in the β region against time in oxide in the B56.

B96, out of flux, 185 days, 325ºC

In addition to characterising the in-flux samples, some out-of-flux samples have also been investigated for comparison. Figure 6.13 shows the oxide formed on the B96 sample corroded out of flux at a similar temperature and length of time as the B70. β regions that retain the original shape and mass contrast can be seen up to ~ 0.5 μm deep into the oxide. The oxidation of Nb is plotted in Figure 6.14, which shows a relatively rapid oxidation process compared to the process in B70. The Nb is oxidised to ~ 2+ state within 50 days into the oxide, and fully oxidised at about 160 days. A layer of oxide with large number of cracks can be seen at the top surface, which is assumed to be the debris of the steam induced oxide film prior to the primary loop corrosion. Such a layer can also be found at the top surface in other samples but might not be as clearly shown as in this case.

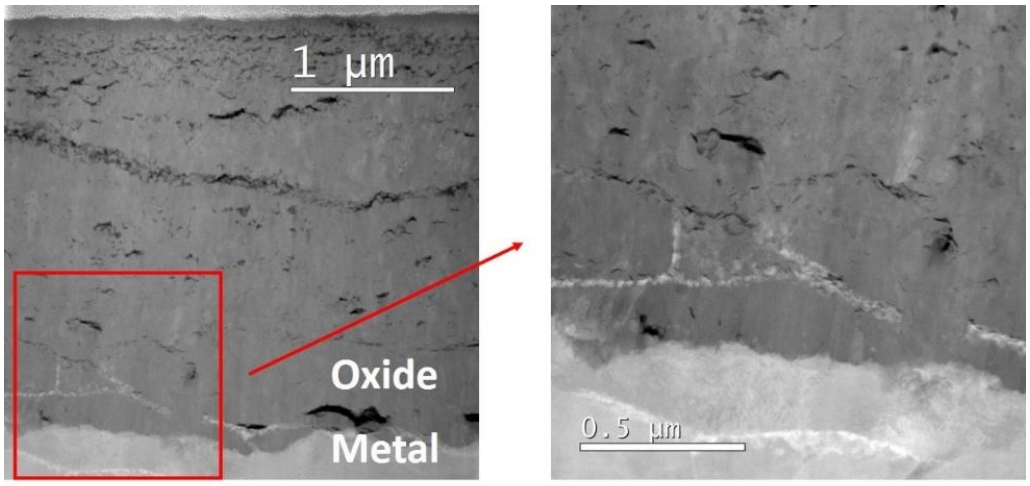


Figure 6.13 HAADF images showing the oxide formed on B96

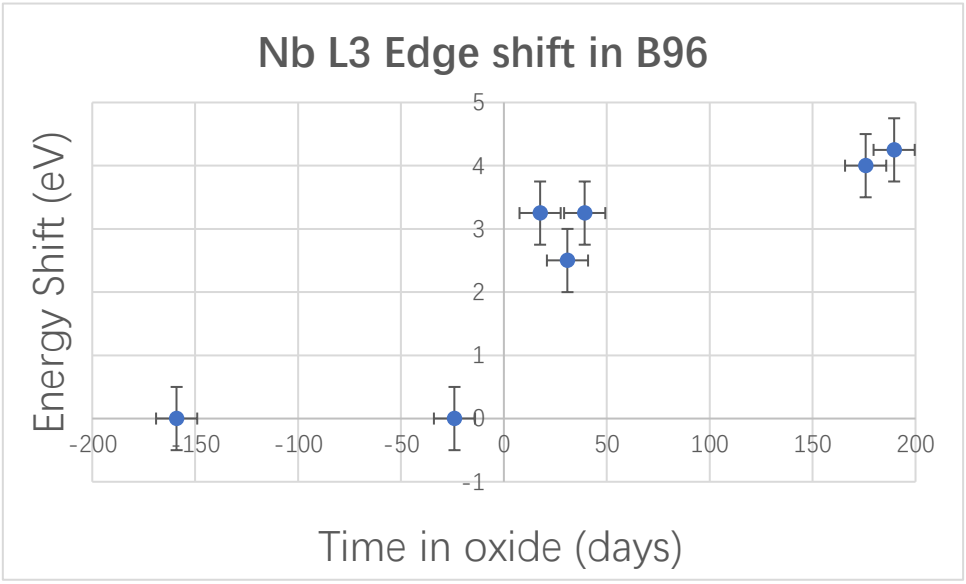


Figure 6.14 Oxidation of Nb in the β regions against time in oxide in B96.

B88, out of flux, 2850 days, 325°C

The long-time corroded, out of flux sample B88 has also been investigated for comparison to the in-flux sample B74. A series of HAADF images in Figure 6.15 shows the oxide film on B88. An obvious difference from what has been seen in B74 is the

large number of cracks / ‘crack like’ features throughout the oxide. Compared to the lateral cracks appearing periodically in B74, these features show less periodicity and uniformity in terms of orientation. The oxidation state of Nb is plotted in Figure 6.16. The Nb remains unoxidised until about 100 days, and is gradually oxidised to the 5 + state at around 500 days.

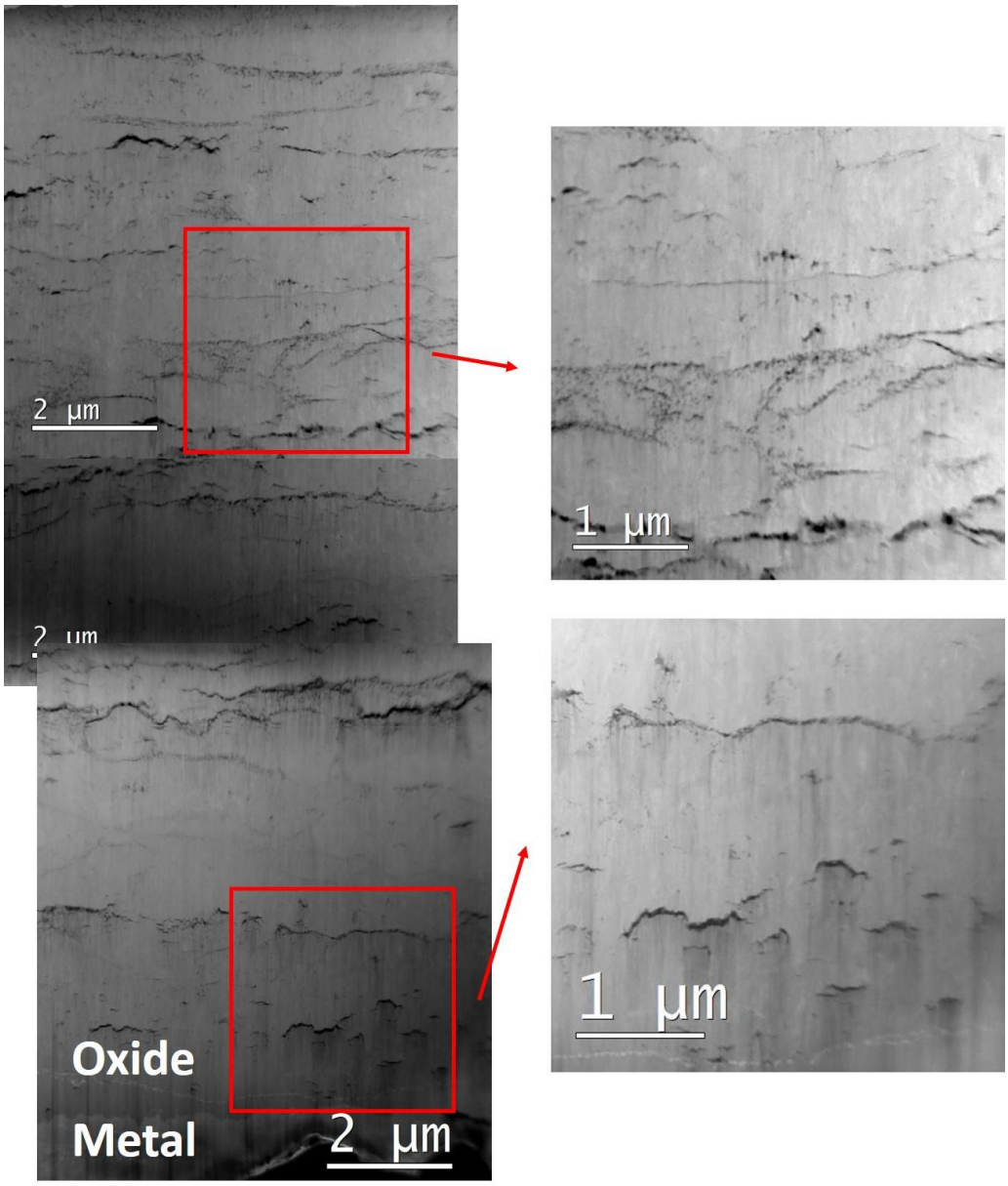


Figure 6.15 HAADF images showing the oxide formed on B88

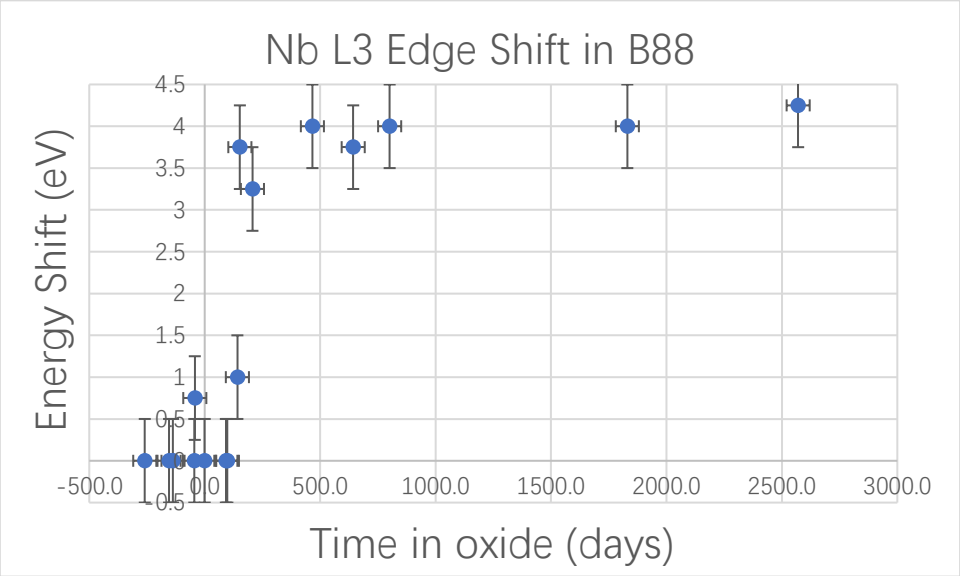


Figure 6.16 Oxidation of Nb in β phase against time in oxide in B88.

6.3 Discussion

6.3.1 The corrosion of the β regions in the oxide

Using the characterisation results from several techniques, the corrosion of the β regions in the oxide can be discussed. As described in Section 4.2, the β region can decompose in the metal during corrosion. This process can be divided into three stages, starting from the β-Zr sheets that form a network along the boundaries of the elongated α-Zr grains that transform to α-Zr and β-Nb. In order to be consistent with the discussion in Section 4.2, these three stages will be called stage zero, stage one and stage two. In stage zero of this decomposition process, the region is mainly β-Zr. Stage one sees the formation of individual small round β-Nb particles, corresponding to the type 1 β region shown in Figure 4.17 (a). Then the large plates of β-Nb form in the final stage, as commonly seen in the type 2 β regions in the long-corroded samples shown in

Figure 4.17 (d). The oxidation takes place simultaneously to this process, and as a result the oxide front can meet the β regions at different stages. The decomposition/corrosion of these β mixture regions are inevitably different depending what they lie in the sample. The oxidation of the β region in stage zero is not investigated in this study due to lack of data points. The shortest corrosion time of my samples is ~190 days, for which most β-Zr grains have decomposed to some extent. The oxidation of the β regions at this stage is assumed to be quite similar to what happens to the β-Zr, featuring rapid oxidation of Zr and Nb with a loss of Nb to the surrounding matrix [19]. But this reaction path is not considered to be what really happens under in-reactor corrosion, since most of the β-Zr grains have already decomposed to some extent before being absorbed into the oxide.

When the β region in stage one is incorporated into the oxide, the β-Nb particles show good resistance to the oxidation, while other components such as the β-Zr and α-Zr are oxidised rapidly. The result is the formation of the 'hollowed structure' mentioned earlier. An example is shown below in Figure 6.17 of the phase mixture in both metal and oxide. After the rapid oxidation of other components, the un-oxidised individual sphere β-Nb particles will be exposed to the surrounding oxide, leading to a relatively rapid oxidation due to their high surface to volume ratio. This type of β region is usually seen in samples B70 and B96 in which the Nb gets fully oxidised in about 190 days after exposure to oxide (t2).

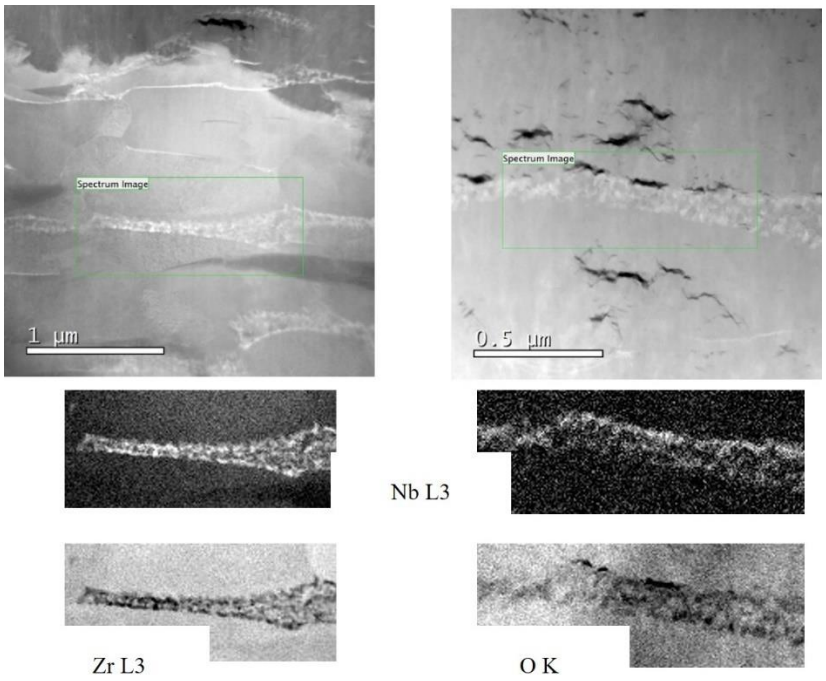


Figure 6.17 'Hollowed structure' β regions in metal (left) and oxide (right) with corresponding elemental maps. These two examples are taken from sample B70 (in-flux corrosion at 325 °C for 192 days). The discrete sphere β-Nb particles can be seen in both metal and oxide. The HAADF image of the oxide and the oxygen mapping show that components in the β region other than β-Nb particles are oxidised rapidly.

The β region at stage two, consisting of large plate of β-Nb and relatively high Nb concentration, is the common starting point of the β phase oxidation in the long-corrosion samples B74 and B88. Several significant steps in oxidising the large β-Nb plate are shown in Figure 6.7 and Figure 6.16. Compared to the oxidation of small individual β-Nb particles, this oxidation process takes much longer due to the smaller surface to volume ratio and higher Nb concentration. A direct comparison between the less Nb enriched discrete particles and the more Nb enriched continuous region is displayed in Figure 6.18. The morphology and Nb concentration clearly determines the rate of oxidation of the Nb-rich phases.

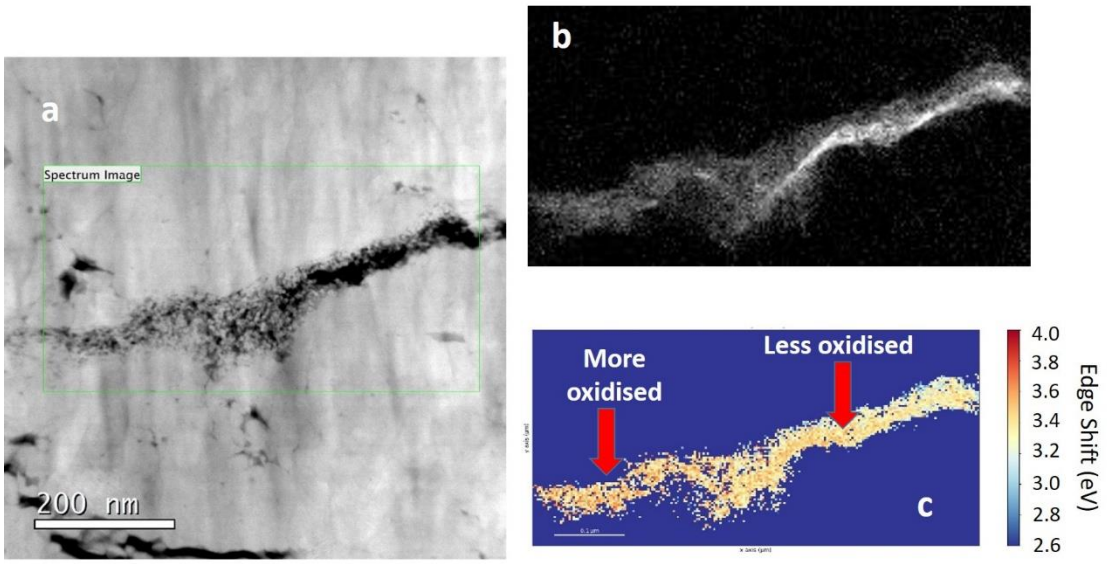


Figure 6.18 (a) HAADF images showing a β phase region with individual particles on the left side and continuous region on the right side, (b) EELS Nb mapping of the region, (c) Nb L3 edge shift mapping, showing the left side is more oxidised than the right side does. The background colour in (c) is arbitrarily set and does not represent the oxidation status.

The difference between the oxidation rates of Nb can be attributed to the different decomposition stages of the β phase regions as they start to oxidise. Figure 6.19 has illustrated the oxidation of the β region at two extreme conditions, (a) undecomposed β-Zr enriched by Nb (stage zero) and (c) fully decomposed β-Nb (stage two). The Nb rich β-Zr is oxidised and dissolved relatively fast, as agreed by previous researchers [81, 209]. On the contrary, the β-Nb in Figure 6.19 (c) remains unoxidised for a while in the oxide and then is oxidised more slowly. When the β region is a phase mixture, as shown in Figure 6.19 (b), the β-Zr and α-Zr will first oxidise to leave discontinuous unoxidised β-Nb particles surrounded by ZrO_2, as the α-Zr and β-Zr oxidise rapidly. These small β-Nb particles will then oxidise at a faster rate than that shown by the larger Nb sheet in (c), due to a higher surface to volume ratio. Therefore the oxidation of Nb is expected

to be fastest in (a) and slowest in (c). However as stated above, cases (a) and (c) are the extreme ends of the real microstructure and hence rarely found in reality. Almost all the β phase regions I have observed are mixture of β-Zr, β-Nb and α-Zr, with different contents and morphology of each component. When the decomposition is at an early stage, the β phase region is towards case (a) in Figure 6.19, thus showing a relatively fast oxidation of Nb, as will be seen in sample B96 compared to B88 and sample B70 compared to B74. By contrast in samples B74 and B88, where the decomposition nearly complete, the mixture is more like case (c) in Figure 6.19, and the oxidation of Nb is much slower.

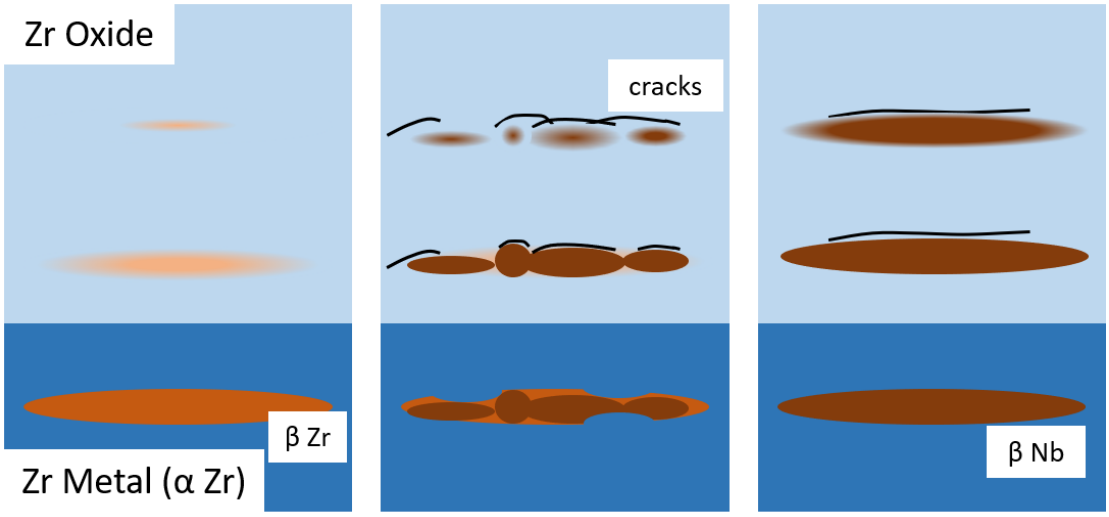


Figure 6.19 A schematic of the oxidation process of the β phase regions at different stages of decomposition, (a) the starting point, completely β-Zr, (b) some degree of decomposition, the appearance of β-Nb and α-Zr in the β phase region, (c) a completely decomposed β phase region, with only β-Nb.

The relatively large β-Nb grains in the oxide coming from the stage two regions in the metal also allows investigation of the relation between the process of oxidation, amorphisation and decomposition. As reported by previous researchers [19, 210], oxidation of the β-Nb particles involves both amorphisation and decomposition, but the order of the process is not clear. The relatively large β-Nb regions seen in the long-corroded samples provide a good chance to study this. As shown in Figure 6.1(c), some areas of the β-Nb regions exhibit a transition from crystalline to amorphous (R1 and R2). While the diffraction pattern of R1 shows only the crystalline spots, the diffraction pattern of R2 shows both crystalline and amorphous components. The EELS spectra from the corresponding regions are shown in Figure 6.20 with the Nb L3 edge shift. It appears that the amorphisation happens when the Nb L3 edge shifts from 2 eV to 3 eV, which I assume is as the Nb is oxidised from 2+ to 4+. A decrease of the Nb concentration is also seen during this process, as shown in Table 6-2. It should be mentioned that the Zr L3 edge shift in the β region is always at 2 eV, showing the Zr has been fully oxidised to 4 +.

However, the depletion of Nb during oxidation is not shown by every data point. An example is given in Figure 6.21 showing a fully oxidised β region found about 13.5 μm from the metal/oxide interface in the oxide in a B74 sample. From the oxidation kinetics plot of B74 we can calculate that this β region has been in the oxide for ~2400 days. The Nb L3 edge shift in the β region is 4.25 eV, indicating that the Nb has been fully

oxidised. However, the EELS spectra from selected regions show that the Zr rather than Nb has been depleted in the β region. A similar case is also found in B96, the high temperature out of flux corroded sample, suggesting that this is not a result only of irradiation. The Nb L3 edge shift in the β region is also found to be 4.25 eV.

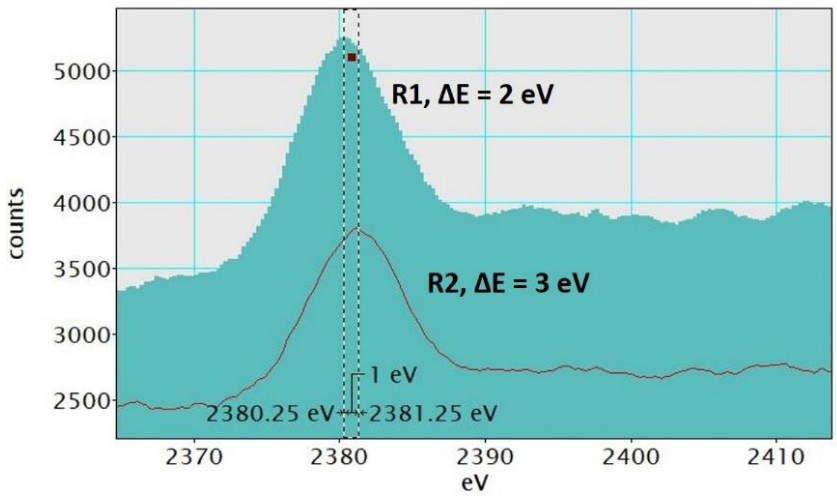


Figure 6.20 Nb L3 Edge Shift in crystal and amorphous β Nb regions as shown in Figure 6.1(c).

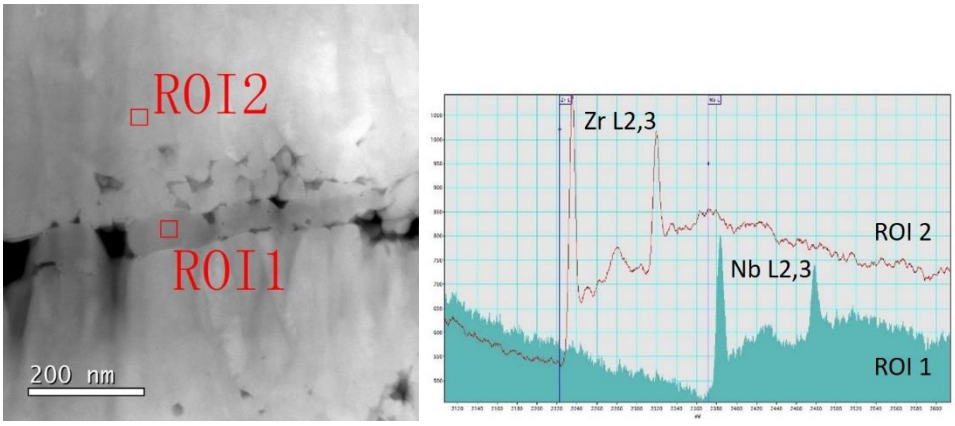
Table 6-2 Relative amounts on Nb in crystalline and amorphous β Nb regions as shown in Figure 6.1(c)

Region	1	2
Nb / (Nb + Zr)	57.4%	44.6%

The results shown in Figure 6.20 and Figure 6.21 suggest a discrepancy in the mobility of Zr and Nb atoms in the β-Nb phases in the oxide. In Figure 6.20, the reduced concentration of Nb in a more oxidised region suggests that Nb atoms are more mobile during oxidation of the β-Nb. However in Figure 6.21, the Zr is seen to be depleted in

a fully oxidised β-Nb region, suggesting a higher mobility of Zr atoms. A possible explanation for this discrepancy might be that the mobility of Zr and Nb atoms in the β phase regions differ at different stages in the oxidation process. When the Nb is oxidised from 2 + to 4 +, it has a higher mobility than the Zr does, corresponding to the depletion of Nb in Figure 6.20. This also results in amorphisation of the β-Nb phase, similar to what has been found happening to other types of intermetallic SPPs in the Zr metal matrix under irradiation [197]. However, when the Nb has been further oxidised to 5 + state, it then has a lower mobility than the Zr does. As a result, the Zr will be depleted, leaving a β region only containing Nb as shown in Figure 6.21. The latter process has rarely been reported perhaps because the Nb has almost been fully depleted in the earlier process in most cases. The appearance of cracks/cavities at the β regions also enhances the redistribution of the Nb, as discussed in the next section. Therefore, whether the second process occurs is determined by how much Nb is retained within a preserved β-Nb grain when oxidised to the 5 + state. As shown in Figure 6.8 (C) (D) and (E), most β-Nb grains gradually dissolve with the depletion of Nb and some Nb is left along the flanks of the cracks. This process happens before the full oxidation of the Nb to the 5 + state, thus we will not interpret the second process as the depletion of Zr. But some β-Nb grains do preserve their shape and some Nb is retained in the grain after amorphisation, as shown in Figure 6.21 (a). This allows the further oxidation of the Nb and the depletion of Zr in the β-Nb grains. It should be emphasised that this analysis is only based on the observed results in this study, which requires further validation by

other work such as modelling studies.



(a) (b)

Figure 6.21 HAADF images showing a β region containing only Nb, evidenced by the EELS spectra taken from the surrounding ZrO_2 and the almost pure β-Nb layer

6.3.2 The oxidation of Nb under different reactor conditions

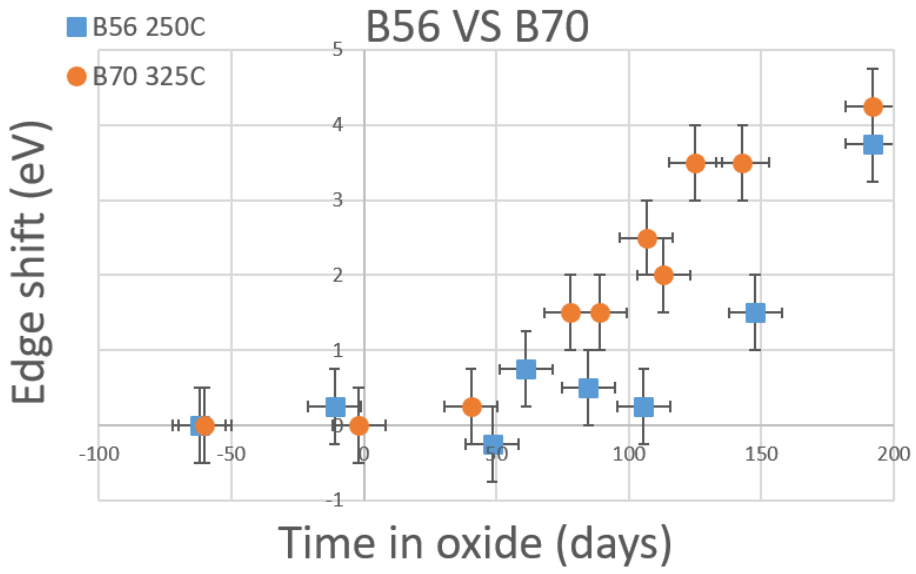
The influence of different factors on the rate of oxidation of the Nb in the β regions can be studied by comparing the EELS plots from specific samples, as shown in Figure 6.22. The comparison between B56 and B70 shows that the Nb is oxidised more slowly at 250 °C than at 325 °C, which is not a surprise considering the transportation of oxidising species is governed by thermally activated diffusion process.

The comparisons between in-flux and out-of-flux samples corroded at same temperature for similar times include B70 vs B96 in Figure 6.22 (b) and B74 vs B88 in Figure 6.22 (c), and show the impact of radiation. In the samples corroded for ~ 190 days, the Nb in irradiated samples is always less oxidised than that in the unirradiated

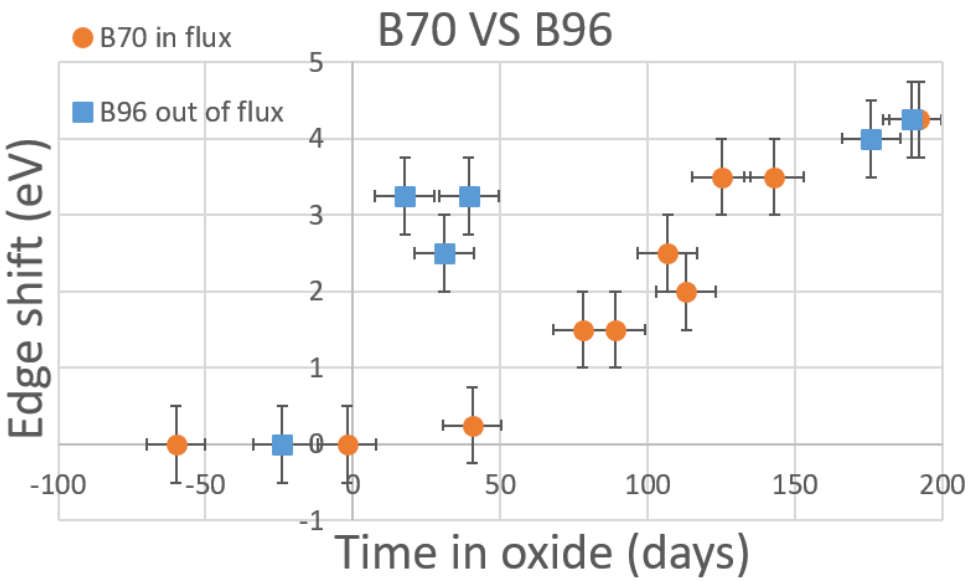
samples. It should be noted in Figure 6.22 that not all the β phase regions studied have been irradiated to 2 dpa in the metal. For instance, there are several data points collected from β regions that have been in the oxide for about 100 days. Their received radiation dose in the metal is about 1 dpa, yet they are even less oxidised than those in the unirradiated oxide for only 50 days. The comparison between the β regions in B74 and B88 is restricted to those incorporated into the oxide for less than 500 days, before the Nb is fully oxidised. Similar to the comparison between B70 and B96, the Nb in the long-time irradiated samples oxidises more slowly than that in the un-irradiated samples. These two comparisons show that neutron radiation is beneficial to the corrosion resistance of the β regions in the alloy. It agrees well with the influence of neutron radiation on the decomposition process from β-Zr to β-Nb, as shown in Figure 4.19 and discussed in Section 4.2.2.

The comparison between B96 and B88 shows the influence of annealing at 325 °C. The β regions incorporated into the B96 oxide for X days have been heat treated for (185 – X) days before they start to oxidise, while those incorporated into the B88 oxide for X days have been heat treated for (2850 – X) days before they start to oxidise. For β regions with roughly the same X values in the two different samples, their annealing times are very different. As shown in Figure 6.22 (d), those β regions with much longer annealing time are oxidised more slowly.

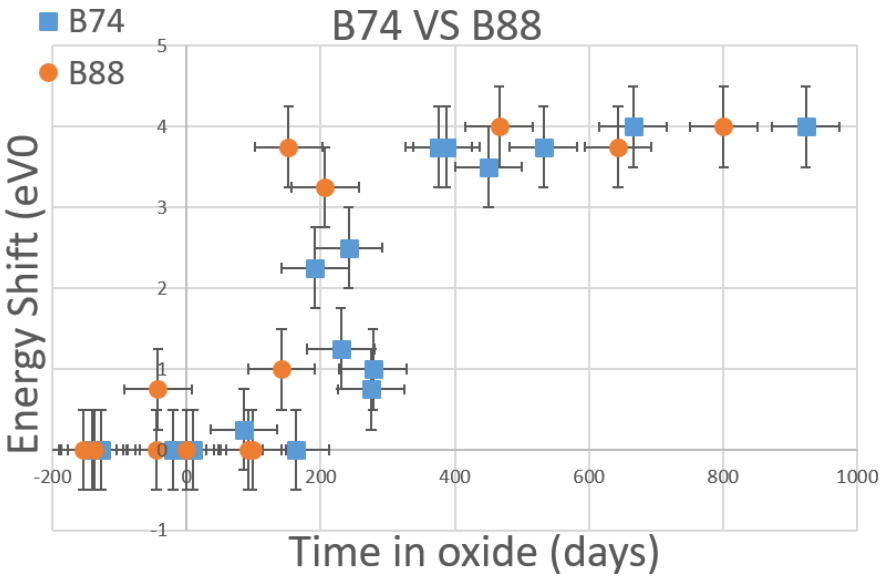
Figure 6.22 (e) shows the comparison between the oxides formed in the first ~200 days in B74 and B70. The Nb in B74 is oxidised much more slowly than in B70. Unlike the other four comparison plots that highlight the influence of only one factor, this comparison involves multiple factors, but it shows what is happening in real reactor-corroded samples. This result correlates well with the weight gain curve of the in reactor corroded samples at 325 °C, in which the oxide growth rate in the first 200 days is about 3.4 um/year, faster than the growth rate after 2500 days which is about 2.1 um/year.



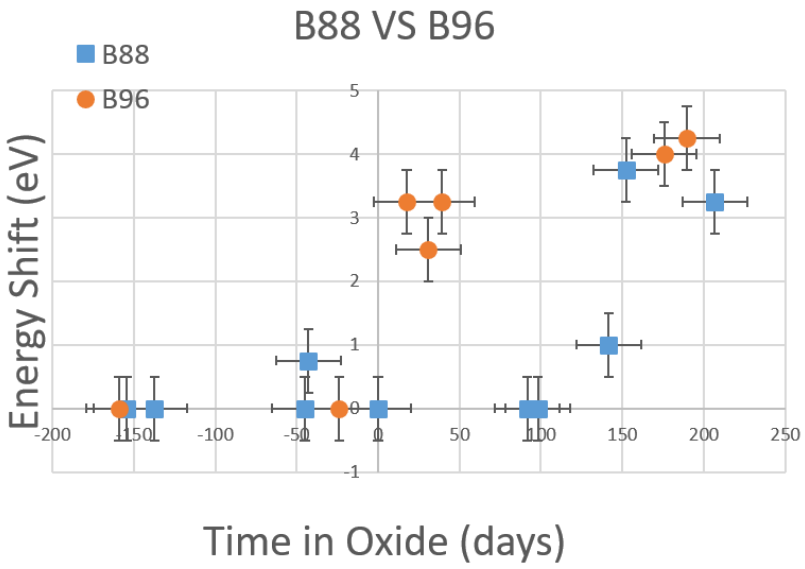
(a)


B70 VS B96
B70 in flux
B96 out of flux
Edge shift (eV)
Time in oxide (days)
5
4
3
2
1
0
-1
-100
-50
0
50
100
150
200

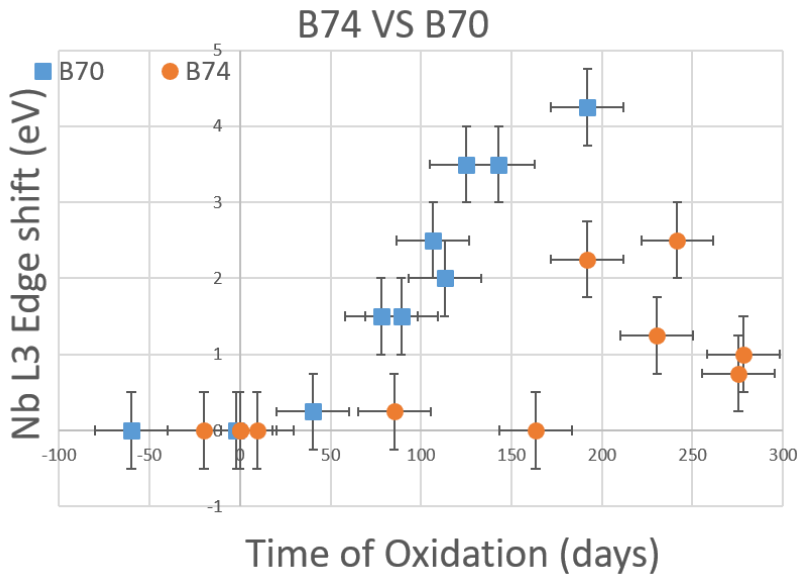
(b)


B74 VS B88
B74
B88
Energy Shift (eV0
Time in oxide (days)
5
4
3
2
1
-1
-200
0
200
400
600
800
1000

(c)



(d)



(e)

Figure 6.22 Comparison of the oxidation rate of Nb in different samples, (a) B70 vs B56, to show the influence of temperature, (b) B70 vs B96 and (c) B74 vs B88 to show the influence of radiation, (d) B88 vs B96 to show the influence of annealing at 325 °C, and (e) B74 vs B70 to show the combined influence of reactor conditions.

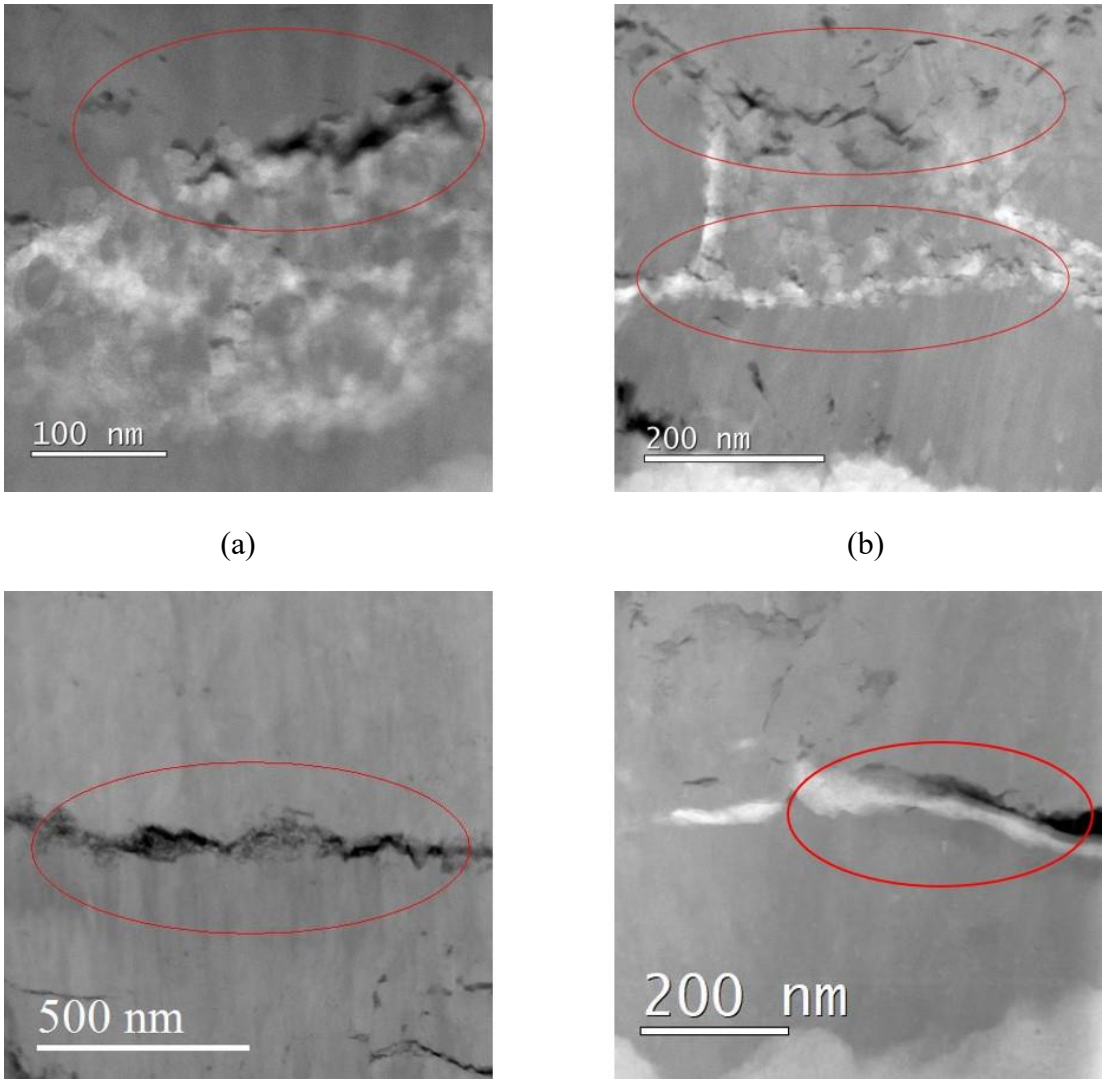
6.3.3 The formation of micro-cracks associated with the β phase

Micro-cracks are commonly found in the oxide formed on various zirconium alloys [41,

59, 211]. They are thought to have substantial impacts on the oxidation kinetics by providing ‘pathways’ [59] or ‘short circuits’ [211] to enhance the rate of oxidising species travelling across the oxide film, hence encouraging earlier transition of the oxidation rate and accelerated oxide growth. The production of these micro-cracks is suggested to be due to the tensile stress along the oxide growth direction in the oxide [57] and common nucleation sites are above unoxidised SPPs and at convex regions of the undulating metal/oxide interface [56]. The large volume fraction of β phase in the Zr-2.5Nb alloy in this study has provided plenty of nucleation sites for micro-cracks, and the formation of micro-cracks associated with these β phase region and their impact is discussed here.

As described earlier, the decomposition of the β-Zr takes place during the formation of the oxide, thus the morphology of the β phase can be roughly divided into three types. The first type, pure β-Zr sheets are rarely seen in this study due to the shortest corroded sample being already ~190 days under reactor conditions. Other researchers have shown that the β-Zr will be rapidly oxidised when incorporated into the oxide and many associated micro-cracks are formed. The second type of β region, which is a mixture of α-Zr, β-Zr and small spherical β-Nb particles, is the most commonly seen case in my samples. With the rapid oxidation of the α-Zr and β-Zr and delayed oxidation of the β-Nb, micro-cracks can be seen at the top of many β-Nb particles, as shown in Figure 6.23 (a). Initially, these cracks are only at the top of individual β-Nb particles and

disconnected from each other. With the progression of oxidation, the cracks gradually connect with each other and form either a network of cracks as shown in Figure 6.23 (b) or a much larger continuous crack as shown in Figure 6.23 (c). The third type, pure β-Nb strips, will lead to formation of relatively large single cracks on the upper surface of the β region, as shown in Figure 6.23 (d).



(a) (b)

(c) (d)

Figure 6.23 HAADF images showing micro-cracks formation associated with the β phase. (a)-(c) shows the development of micro-cracks formed on discontinuous β-Nb particles, from individuals to an interconnected network, and (d) shows the single crack formed on large β-Nb strip. The images are not from the same sample, just to show typical morphologies at different state. (a) is from B56, (b) is from B96, (c) is from B70 and (d) is from B74.

The different distributions of cracks can lead to different oxidation behaviour. A large single cracks might act as an obstacle for diffusion of oxidising species, as suggested by Ni et al. [61], and hence reduce the local oxidation rate. On the other hand, the interconnected small cracks, especially if they have crack directions towards the metal/oxide interface, can provide pathways for fast diffusion of oxidising species, leading to an increase in local oxidation rate.

In addition to the commonly seen cracks adjacent to the top of the β phase regions, an unusual type of crack is also occasionally observed, as shown in Figure 6.21. According to the EELS data, the β strip has been fully oxidised and only Nb and O are retained in the strip, without any retained Zr. A tensile stress in the β-Nb strip in the lateral direction is required for the formation of this kind of crack. Yet the Pilling-Bedworth ratio from Nb to Nb_2O_5 is 2.7 [212], indicating that a compressive, rather than tensile, stress should be generated during oxidation. Thus it is unlikely that the crack forms due to stress accumulation during oxidation. A possible cause of the crack is due to the contraction during cooling of the sample. It has been reported that for monoclinic Nb_2O_5, the thermal expansion coefficient in a, b, c directions are 5.3, 0 and 5.9 $(\times 10^{-6})$ $°C^{-1}$ from 0 to 1000 °C. In monoclinic ZrO_2, the corresponding values are about 6, 3 and 9 $(\times 10^{-6})$ $°C^{-1}$ from 0 to 400 °C [213]. Thus when the oxide is cooled down from the working temperatures around 300 °C, the greater contraction of the ZrO_2 matrix around the β region can generate tensile stresses, and hence cracks. This explanation, if

accepted, makes this type of cracks less of interest since they will not have an impact on the corrosion of the materials during service.

6.3.4 The influence of the β phase on the general oxidation of the material

Now it is the time to discuss how the β phase can affect the oxidation of the material. There are several aspects to be considered.

First, the β phase regions can have a direct impact on the progression of the oxide front towards the fresh metal. Since the 'delayed oxidation' of the β-Nb particles has been proposed by previous researchers [19, 214] and also observed in this work, it is reasonable to assume that the oxide front will be delayed by the β-Nb. While this phenomenon might not be commonly considered in alloys where β-Nb particles are small, the large β-Nb strips in the alloy studied here can provide a substantial effect. Clear evidence for this is shown in Figure 6.24. The oxide front has been temporarily stopped by the β-Nb strips circled in red, and not been stopped where the strips are absent. This phenomenon can be important to the oxidation of the material, especially in long-term corrosion. Due to the 'layered' structure of α-Zr grains and β phase at the grain boundaries and the metallurgical texture in the material, the oxide front will meet the lateral β phase periodically during oxidation. The longer these β phase regions have remained in the metal, the more decomposition will have occurred and the more likely β-Nb strips have formed. As a result, the progress of the oxide front will be periodically

slowed down, contributing to the reduction of oxidation rate in long term corrosion.

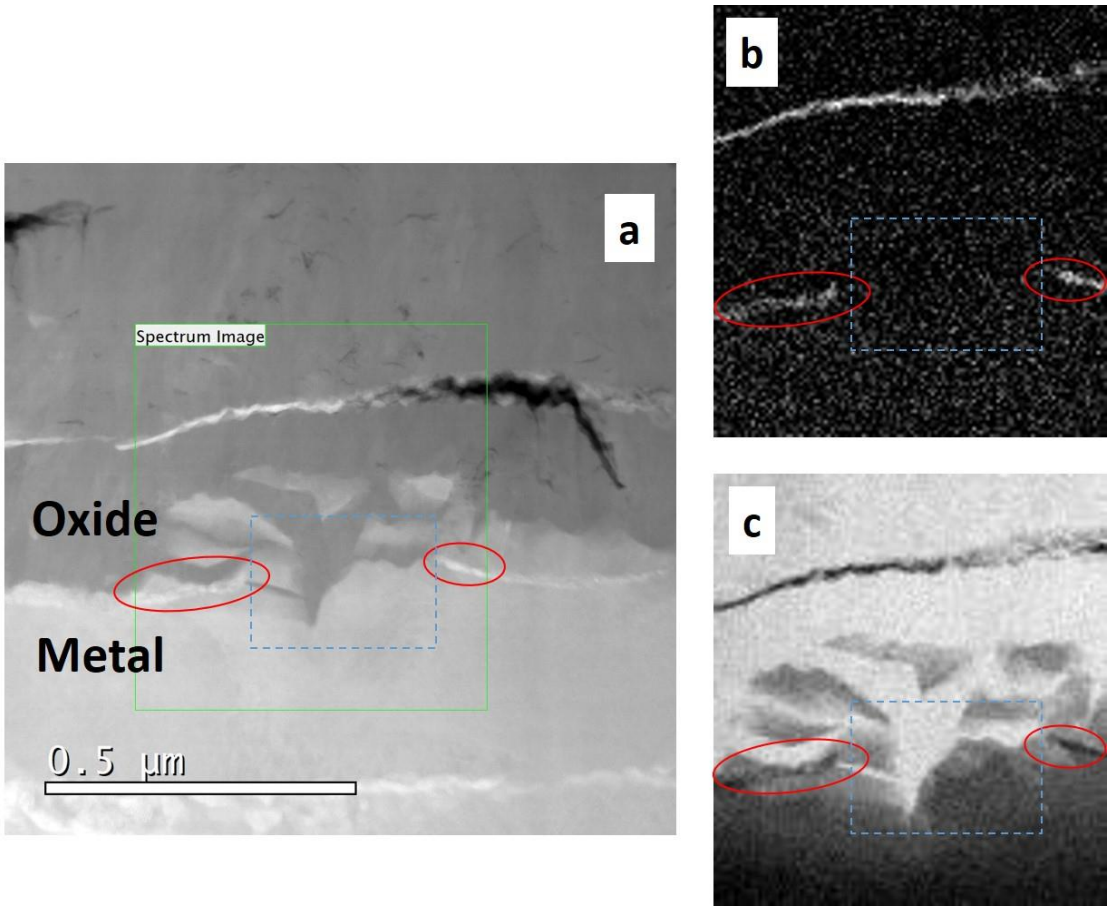


Figure 6.24 (a) A HAADF image (b) Nb EELS quantity map (c) O EELS quantity map showing the metal / oxide interface in B70. The β-Nb strips in red circles have temporarily stopped the progression of the oxide front, while the region in the blue rectangle shows the unstopped oxide front where the β-Nb strip is absent. There are some isolated unoxidised Zr regions in the oxide right above the Metal / Oxide interface. They are thought to be the result of the complex 3D structure of the metal/oxide interface.

The oxide front, or the metal/oxide interface, can not only be obstructed by the β-Nb strips but also follows the shape of the β phase. Figure 6.25 shows HAADF images shows the shape of two β phase regions in the oxide near the metal/oxide interface. It is obvious that the ups and downs of the metal/oxide interface follow the shape of the

lower edge of the β phase regions. This phenomenon may bring in negative effect by leading to an undulating metal/oxide interface which can introduce much larger stresses into the oxide than a flat interface does [214, 215]. It can also be observed that the shape of the metal / oxide interface does not completely copy the shape of the β phase, as shown in the red circle in Figure 6.25. This is thought to be a result of the microscopic features in the oxide between the interface and the β phase, for instance the small β-Nb particle roughly perpendicular to the interface in the red circle. It is not surprising as these features are responsible for affecting the local diffusion of oxidising species. It implies that this impact on the metal/oxide interface from the β phase already incorporated into the oxide is only strong within a short distance from the interface to the β phase, no more than 500 nm as shown in these two images.

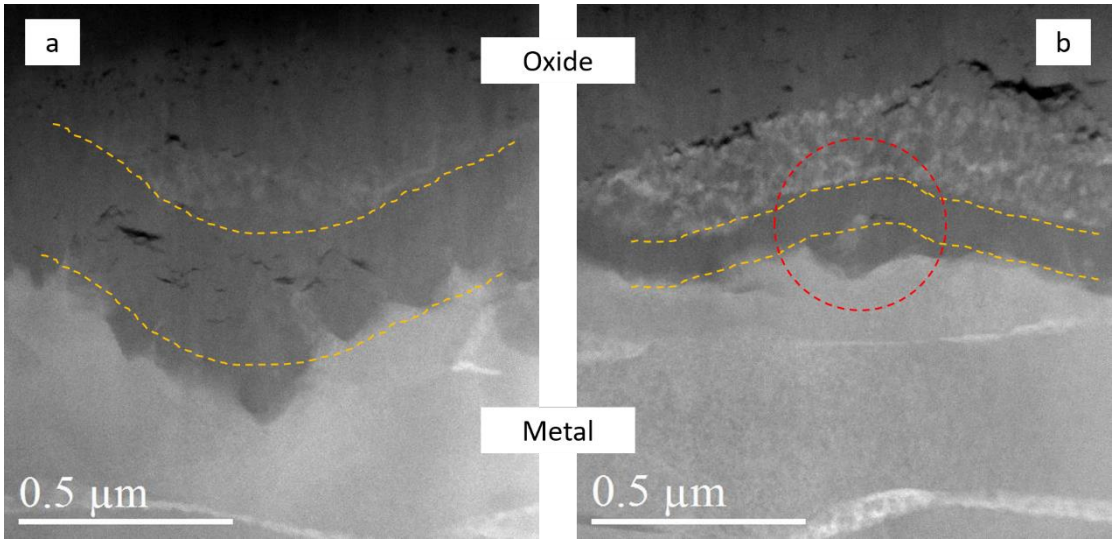


Figure 6.25 HAADF images showing the metal / oxide interface follows the shape of the β phase regions above them. The upper yellow dashed line in each image is drawn along the lower boundary of the β region, and the lower yellow dashed line is a copy of its upper counterpart and placed close to the metal / oxide interface.

Another important factor to be considered is the redistribution of Nb from the β phase to the matrix solid solution, since the Nb ions in solid solution can influence the local electric field and hence the diffusion of oxygen ions [37, 76]. In Figure 6.20, the transport of Nb from the β-Nb phase to Zr oxide solid solution happens when the edge shift of Nb is about 3 eV. If we assume that all the Nb EELS edge shift data in this study were all taken from the β-Nb phase, then the time required for the onset of Nb transport from β phase to solid solution for different samples can be estimated as listed in Table 6-3. It is clear that the further the decomposition of the β phase has progressed, the longer the time is needed for mass transport of Nb from the β phase to solid solution in the bulk oxide.

The relation between the amount of Nb in solid solution in the oxide and the rate of oxidation is suggested by Moorhead et al. [81] by comparing two types of samples, 720 °C Zr-1.0Nb and 580 °C Zr-1.0Nb. The main SPP type in 720 °C Zr-1.0Nb is β-Zr so there is plenty of oxidised Nb in solid solution in the oxide. The main SPP type in 580 °C Zr-1.0Nb is β-Nb, and the content of Nb in the oxide solid solution is lower. By comparing the oxidation kinetics of the pre-transition regime in the two samples, it is shown that 'sufficient' Nb in the oxide solid solution leads to faster oxidation than the sample with 'insufficient' Nb in oxide solid solution. Therefore, the more Nb in solid solution in the oxide, and presumably the earlier the supply of the Nb to the solid solution from the β phase, the faster oxidation is seen.

Table 6-3 Time required for the onset of mass transport of Nb from β to solid solution in different samples

Sample	B56	B70	B96	B74	B88
Conditions	250 °C in flux 190 days	325 °C in flux 190 days	325 °C out of flux 185 days	325 °C in flux 2750 days	325 °C out of flux 2850 days
Time required (days)	190	110	30	300	200

6.4 How do the in-reactor conditions change the oxidation of the alloy?

This question is answered in this section only considering the impact of the β phase as discussed earlier in this chapter. The core factor is the degree of decomposition from β-Zr to β-Nb. The more β-Nb is generated in the metal before it is oxidised, the better the corrosion resistance of the material. This decomposition is enhanced by both neutron radiation and in-service heating. Therefore, the longer the sample sits in the reactor core, the slower the new oxide forms.

Chapter 7 Conclusions and Suggestions for Future Work

7.1 Summary of key findings

The aim of the work reported in this thesis was to explore what changes irradiation will bring to the zirconium metal matrix and how these changes will affect the general corrosion behaviour of Zr-Nb alloys used for fuel cladding in PWRs. Two types of Zr-Nb alloys were studied, a CNL Zr – 2.5Nb alloy containing α-Zr and β-Zr phases, and Westinghouse^{TM} recrystallised Zr – 1.0Nb and Zr – 2.5Nb alloys containing the α-Zr phase and SPPs. Samples irradiated by neutrons, heavy ions and protons have been investigated, and the microstructural and microchemical changes in α-Zr, β-Zr and SPPs studied. These changes were characterised with some advanced electron microscopy techniques. The key observations are listed below.

- The radiation-induced formation of Nb-rich precipitates in α-Zr grains has been investigated in neutron irradiated CNL Zr – 2.5Nb samples irradiated to 2 dpa at 325 °C and 250 °C, and in samples irradiated to 25 dpa at 325 °C. It was found that only in the samples neutron irradiated at 325 °C can the precipitates be observed by TEM bright field and dark field images. No precipitates were observed in samples under neutron irradiation at 250 °C. Under neutron irradiation at 325 °C, these Nb rich precipitates appear to be plate like with the long axis along the basal plane. The formation and evolution process of these Nb precipitates can be divided into several stages, (i) nucleation (ii) fully coherent hcp Nb precipitates and (iii) transformation into larger bcc Nb

precipitates. The growth of these precipitates depends on the radiation-enhanced diffusion of solute Nb towards the precipitates, and hence is temperature dependent. At the same time, some small Nb precipitates are destroyed under neutron radiation by cascade mixing while the larger ones are more likely to survive and grow. As a result, the size distribution of these Nb precipitates is determined by the balance between precipitation, growth and destruction processes. With the accumulation of the radiation dose from 2 dpa to 25 dpa, the average size of the Nb precipitates increases from 5 nm to 8.7 nm, while the size distribution is broadened. The formation of these precipitates has significantly reduced the Nb concentration in solid solution in the α-Zr metal matrix, as evidenced by the APT data on the same samples from Anne Callow.

- It was found both a-type and c-type loops were formed in the samples neutron-irradiated at 325 °C. Solute Nb atoms were shown to segregate to the c-loops.
- Proton irradiation was carried out on the as-received CNL Zr – 2.5Nb alloy samples at 320 °C with a damage rate of 1.5×10^{-5} dpa/s. The absence of radiation induced Nb precipitates in the samples as identified by TEM BF and DF images support the claim in the previous point that the size distribution of the Nb precipitates is influenced by the radiation enhanced diffusion of the Nb atoms in the Zr matrix.
- Irradiation-induced Nb redistribution between the α-Zr matrix and β-Nb SPPs was studied by in-situ heavy ion irradiation on the Westinghouse™

recrystallised Zr-Nb samples in a TEM. It was shown that these β-Nb SPPs could retain their microstructure under irradiation up to 40 dpa. The mechanisms governing the redistribution of Nb atoms between the α-Zr metal matrix and β-Nb SPPs were discussed. It was proposed that the redistribution was induced by the radiation induced mixing occurring at the α/β phase boundaries (periphery of the SPPs) but suppressed by the local diffusion of Nb atoms back to the SPPs. It was thus inferred that under reactor conditions there will be no serious Nb redistribution between the α-Zr matrix and β-Nb SPPs.

- The decomposition of β-Zr phase under neutron irradiation has been studied. The transformation from β-Zr to β-Nb is enhanced under reactor conditions by both neutron irradiation and heating. The morphology changes during the decomposition from a continuous sheet to discrete small β-Nb particles and back to a continuous β-Nb sheet. The β-Nb sheet is thinner than the original β-Zr and has a higher Nb concentration. The ω-Zr phase mentioned in the literature was not identified in the samples corroded at 325 °C.
- The decomposition of the β-Zr phase in the metal matrix before it is incorporated into the oxide results in the different corrosion rate of these β phase regions in the oxide. The more decomposed they are by longer irradiation in the metal, the slower the corrosion rate is. The differences in the decomposition progress of the β phase regions also results in the formation of different shapes of cracks in the oxide, and different rates of Nb release from the β-Zr/β-Nb

regions to the oxide matrix. The β-Nb sheet formed in the metal seems to be able to delay the progress of the metal/oxide interface and hence slow down the overall corrosion rate.

It is thus possible to answer the question 'how will neutron irradiation influence the corrosion of the Zr-Nb alloys, and especially why is the radiation enhanced corrosion in Zr-Nb alloys generally not as fast as in Zircaloys' with these observations. For Zr-Nb alloys containing both α- and β-Zr phases, the influence comes from changes in both α- and β-Zr phases in the metal. In the α-Zr grains, the neutron radiation results in both the precipitation of nanoscale Nb-rich phases and segregation to c-loops, leading to a decrease in the Nb concentration in solution in the metal matrix. According to the C4 model [37], a reduction of Nb concentration is beneficial to reducing the oxidation growth rate in Zr-Nb alloys.

In the β-Zr phase, the radiation enhances the transformation from β-Zr to β-Nb, and the change of morphology of the β phase regions. The more transformed the β phase region is, the slower it is corroded in the oxide and the release of Nb to the oxide matrix is also delayed, and the more likely is the formation of large lateral cracks rather than small interconnected cracks. This will also reduce the general corrosion rate of the alloy by limiting the rate of oxidising species penetrating through the oxide to the metal matrix. The shape of the transformed β-Nb sheets, which are mostly parallel to the metal/oxide

interface, is also benefiting the corrosion resistance since these β-Nb sheets can hinder the progress of the metal/oxide interface. These microscopic findings agree well with the change of oxidation kinetics as shown in the weight gain curve in Figure 3.3

In order to meet the specific characterisation aims of this project, several advanced electron microscopy techniques, including both data acquisition and analysis, have been developed and used. These include using EDX line-scan and curve-fitting of the profiles to study the changes of the SPPs under irradiation, using EELS low loss spectra to study the phase distribution in the β phase regions in Zr metal, and using EELS core loss spectra to study the oxidation of certain elements, with tailored edited HyperSpy notebooks. These can be further improved and used by other researchers.

7.2 Suggestions for future work

For a complete understanding of the underlying mechanisms determining neutron irradiation-induced changes to the zirconium metal matrix and its impact on the corrosion, the following investigations ought to be considered.

1. The hardening of the metal matrix due to the formation of radiation damages has not been studied in-depth in this project. Transmission Kikuchi Diffraction (TKD) scans and Geometrically Necessary Dislocation (GND) analysis on the neutron-irradiated CNL Zr – 2.5Nb TEM samples can be carried out for a systematic investigation.

2. Due to the available choice of irradiation parameters, the proton irradiated samples in this project did not show the most interesting features to compare to those in the neutron irradiated samples. If there is a chance for another proton irradiation campaign, a higher irradiation temperature or lower flux ought to be used and the characterisation work on the samples could be more interesting.
3. The decomposition of the β-Zr phase and the associated Nb redistribution can be better understood using the in-situ irradiation technique carried out on the β-Nb SPPs in this project.
4. The neutron irradiated samples in this project are limited to two damage levels, 2 dpa and 25 dpa. While the comparison is interesting, an additional set of samples irradiated to a intermediate damage level (for instance 10 dpa) may bring some more interesting comparison and insights into the understanding of radiation impacted corrosion of the Zr-Nb alloys.
5. In this project, some EDX/EELS acquisition and analysis methods were developed for better characterisation of the radiation damages in nuclear materials. These techniques can be applied to the study of other radiation damaged materials. A funded collaboration with the National Nuclear Laboratory (NNL) will follow up this project to work together on using the EELS to study radiation damage in a range of materials used in the nuclear industry will be undertaken.

References

[1] S. Glasstone and A. Sesonske, *Nuclear reactor engineering : reactor systems engineering*, 4th ed. Springer Science & Business Media, 1994.

[2] J. Kopecky, J.-C. Sublet, J. A. Simpson, R. A. Forrest, and D. Nierop, *Atlas of Neutron Capture Cross Sections (INDC(NDS)--362)*. International Atomic Energy Agency (IAEA), 1997.

[3] C. R. F. Azevedo, "Selection of fuel cladding material for nuclear fission reactors," *Eng. Fail. Anal.*, vol. 18, no. 8, pp. 1943–1962, Dec. 2011, doi: 10.1016/j.engfailanal.2011.06.010.

[4] INTERNATIONAL ATOMIC ENERGY AGENCY, *Review of Fuel Failures in Water Cooled Reactors, Nuclear Energy Series No. NF-T-2.1*. Vienna: IAEA, 2010.

[5] L. Hallstadius, S. Johnson, and E. Lahoda, "Cladding for high performance fuel," *Prog. Nucl. Energy*, vol. 57, pp. 71–76, May 2012, doi: 10.1016/j.pnucene.2011.10.008.

[6] E. Tenckhoff, "Review of Deformation Mechanisms, Texture, and Mechanical Anisotropy in Zirconium and Zirconium Base Alloys," *J. ASTM Int.*, vol. 2, no. 4, pp. 1–26, Apr. 2005, doi: 10.1520/JAI12945.

[7] A. V. Nikulina and A. G. Malgin, "Impurities and their effect on the structure and properties of zirconium parts in nuclear reactors," *At. Energy*, vol. 105, no. 5, pp. 328–339, Nov. 2008, doi: 10.1007/s10512-009-9104-7.

[8] D. E. Hodgson, M. H. Wu, and R. J. Biermann, *ASM handbook. Volume 2, Properties and selection: nonferrous alloys and special-purpose materials*. ASM International, 1990.

[9] J. Zhang *et al.*, "Experimental constraints on the phase diagram of elemental zirconium," *J. Phys. Chem. Solids*, vol. 66, no. 7, pp. 1213–1219, 2005, doi: 10.1016/j.jpcs.2005.03.004.

[10] W. Yeniscavich, R. A. Wolfe, and R. M. Lieberman, "Hydrogen absorption by nickel enriched zircaloy-2," *J. Nucl. Mater.*, vol. 1, no. 3, pp. 271–280, Oct. 1959, doi: 10.1016/0022-3115(59)90023-6.

[11] S. Kass and W. W. Kirk, "Corrosion and hydrogen absorption properties of nickel-free zircaloy-2 and zircaloy-4," *Trans. Am. Soc. Met.*, vol. Vol: 55, Mar. 1962.

[12] A. V. Nikulina, "Zirconium-Niobium Alloys for Core Elements of Pressurized Water Reactors," *Met. Sci. Heat Treat.*, vol. 45, no. 7/8, pp. 287–292, 2003, doi: 10.1023/A:1027388503837.

[13] J.-P. Mardon, D. Charquet, and J. Senevat, "Influence of Composition and Fabrication Process on Out-of-Pile and In-Pile Properties of M5 Alloy," in *Zirconium in the Nuclear Industry: Twelfth International Symposium*, 100 Barr Harbor Drive, PO Box C700, West Conshohocken, PA 19428-2959: ASTM International, 2000, pp. 505-505–20.

[14] Y. H. JEONG *et al.*, "Out-of-pile and In-pile Perfomance of Advanded Zirconium Alloys (HANA) for High Burn-up Fuel," *J. Nucl. Sci. Technol.*, vol. 43, no. 9, pp. 977–983, Sep. 2006, doi: 10.1080/18811248.2006.9711185.

[15] V. Perovic *et al.*, "Microstructural and microchemical studies of Zr-2.5Nb pressure tube alloy," *J. Nucl. Mater.*, vol. 205, no. C, pp. 251–257, Oct. 1993, doi: 10.1016/0022-3115(93)90087-F.

[16] G. Pan, A. M. Garde, and A. R. Atwood, "Performance and Property Evaluation of High-Burnup Optimized ZIRLO™ Cladding," in *Zirconium in the Nuclear Industry: 17th Volume*, 2015, pp. 607–627, doi: 10.1520/STP154320130008.

[17] A. M. Garde *et al.*, "Advanced Zirconium Alloy for PWR Application," in *Zirconium in the Nuclear Industry: 16th International Symposium*, 2010, vol. 7, no. 9, p. 103030, doi: 10.1520/JAI103030.

[18] A. T. Motta, A. Couet, and R. J. Comstock, "Corrosion of Zirconium Alloys Used for Nuclear Fuel Cladding," *Annu. Rev. Mater. Res.*, vol. 45, no. 1, pp. 311–343, Jul. 2015, doi: 10.1146/annurev-matsci-070214-020951.

[19] J. Hu, "High resolution characterization of corrosion and hydrogen pickup of Zr-Nb cladding alloys", DPhil Thesis, University of Oxford, 2016.

[20] R. Adamson, "Effects of Neutron Irradiation on Microstructure and Properties of Zircaloy," in *Zirconium in the Nuclear Industry: Twelfth International Symposium*, 2000, pp. 15-15–17, doi: 10.1520/STP14292S.

[21] T. R. Allen, R. J. M. Konings, and A. T. Motta, "Corrosion of Zirconium Alloys," in *Comprehensive Nuclear Materials*, vol. 5, no. October, R. J. M. Konings, Ed. Amsterdam: Elsevier Ltd, 2012, pp. 49–68.

[22] N. Ni, "Study of Oxidation Mechanisms of Zirconium Alloys by Electron Microscopy", DPhil Thesis, University of Oxford, 2011.

[23] S. H. Zhang, B. Moniz, and M. Meyer, "ASM handbook Volume 13C: Corrosion: Environments and Industries," ASM International, 2006.

[24] H.-J. Sell, S. Trapp-Pritsching, F. Garzarolli, and S. Dean, "Effect of Alloying Elements and Impurities on in-BWR Corrosion of Zirconium Alloys," *J. ASTM Int.*, vol. 3, no. 1, p. 12372, Jan. 2006, doi: 10.1520/JAI12372.

[25] B. Setiadinata, "Corrosion and Hydrogen Pickup Mechanisms of Zirconium Alloys", DPhil Thesis, University of Oxford, 2016.

[26] G. Choudhuri *et al.*, "Influence of Fe content on corrosion and hydrogen pick up behavior of Zr–2.5Nb pressure tube material," *J. Nucl. Mater.*, vol. 441, no. 1–3, pp. 178–189, Oct. 2013, doi: 10.1016/J.JNUCMAT.2013.05.026.

[27] Y. H. Jeong, H. G. Kim, and T. H. Kim, "Effect of β phase, precipitate and Nb-concentration in matrix on corrosion and oxide characteristics of Zr–xNb alloys," *J. Nucl. Mater.*, vol. 317, no. 1, pp. 1–12, Apr. 2003, doi: 10.1016/S0022-3115(02)01676-8.

[28] H. Yu, K. Zhang, Z. Yao, M. A. Kirk, F. Long, and M. R. Daymond, "Metastable phases in Zr-Excel alloy and their stability under heavy ion (Kr2+) irradiation," *J. Nucl. Mater.*, vol. 469, pp. 9–19, Feb. 2016, doi: 10.1016/j.jnucmat.2015.11.020.

[29] J. Liu, "High resolution structural analysis of irradiated zirconium alloys", DPhil Thesis, University of Oxford, 2019.

[30] B. Cox, "Some thoughts on the mechanisms of in-reactor corrosion of zirconium alloys," *J. Nucl. Mater.*, vol. 336, no. 2, pp. 331–368, 2005, doi: 10.1016/j.jnucmat.2004.09.029.

[31] United States Nuclear Regulatory Commission, "Backgrounder on High Burnup Spent Fuel." [Online]. Available: https://www.nrc.gov/reading-rm/doc-collections/fact-sheets/bg-high-burnup-spent-fuel.html.

[32] World Nuclear Association, "Advanced Nuclear Power Reactors | Generation III+ Nuclear Reactors." [Online]. Available: http://www.world-nuclear.org/information-library/nuclear-fuel-cycle/nuclear-power-reactors/advanced-nuclear-power-reactors.aspx.

[33] A. Couet, A. T. Motta, A. Ambard, and D. Livigni, "In-situ electrochemical impedance spectroscopy measurements of zirconium alloy oxide conductivity: Relationship to hydrogen pickup," *Corros. Sci.*, vol. 119, pp. 1–13, 2016, doi: 10.1016/j.corsci.2016.12.008.

[34] J. Belle and M. W. Mallett, "Kinetics of the High Temperature Oxidation of Zirconium," *J. Electrochem. Soc.*, vol. 101, no. 7, p. 339, Jul. 1954, doi: 10.1149/1.2781278.

[35] H. A. Porte, J. G. Schnizlein, R. C. Vogel, and D. F. Fischer, "Oxidation of Zirconium and Zirconium Alloys," *J. Electrochem. Soc.*, vol. 107, no. 6, p. 506, Jun. 1960, doi: 10.1149/1.2427733.

[36] B. Cox, "Rate controlling processes during the pre-transition oxidation of zirconium alloys," *J. Nucl. Mater.*, vol. 31, no. 1, pp. 48–66, May 1969, doi: 10.1016/0022-3115(69)90043-9.

[37] A. Couet, A. T. Motta, and A. Ambard, "The coupled current charge compensation model for zirconium alloy fuel cladding oxidation: I. Parabolic oxidation of zirconium alloys," *Corros. Sci.*, vol. 100, pp. 73–84, 2015, doi: 10.1016/j.corsci.2015.07.003.

[38] K. R. Lawless, "The oxidation of metals," *Reports Prog. Phys.*, vol. 37, no. 2, pp. 231–316, Feb. 1974, doi: 10.1088/0034-4885/37/2/002.

[39] E. Hillner, D. . Franklin, and J. . Smee, "Long-term corrosion of Zircaloy before and after irradiation," *J. Nucl. Mater.*, vol. 278, no. 2, pp. 334–345, 2000, doi: 10.1016/S0022-3115(99)00230-5.

[40] A. Yilmazbayhan, A. T. Motta, R. J. Comstock, G. P. Sabol, B. Lai, and Z. Cai, "Structure of zirconium alloy oxides formed in pure water studied with synchrotron radiation and optical microscopy: relation to corrosion rate," *J. Nucl. Mater.*, vol. 324, no. 1, pp. 6–22, Jan. 2004,

doi: 10.1016/J.JNUCMAT.2003.08.038.

[41] A. T. Motta, M. J. Gomes da Silva, A. Yilmazbayhan, R. J. Comstock, Z. Cai, and B. Lai, "Microstructural Characterization of Oxides Formed on Model Zr Alloys Using Synchrotron Radiation," in *Zirconium in the Nuclear Industry: 15th International Symposium*, 2009, pp. 486-486–21, doi: 10.1520/STP48151S.

[42] J. S. Bryner, "The cyclic nature of corrosion of zircaloy-4 in 633 K water," *J. Nucl. Mater.*, vol. 82, no. 1, pp. 84–101, Jun. 1979, doi: 10.1016/0022-3115(79)90042-4.

[43] J. P. Abriata, J. Garcés, and R. Versaci, "The O−Zr (Oxygen-Zirconium) system," *Bull. Alloy Phase Diagrams*, vol. 7, no. 2, pp. 116–124, Apr. 1986, doi: 10.1007/BF02881546.

[44] Materials Design, "Temperature-Dependent Phase Transitions of ZrO_2." [Online]. Available: http://www.materialsdesign.com/appnote/temperature-dependent-phase-transitions-zro2.

[45] Glidewell Laboratories, "BruxZir® Full-Strength vs. BruxZir Anterior - Choosing Between Transformation Toughening and Light Transmission," 2017. [Online]. Available: http://glidewelldental.com/education/chairside-dental-magazine/volume-11-issue-3/bruxzir-full-strength-vs-anterior.

[46] J. Godlewski, J. Gros, M. Lambertin, J. Wadier, and H. Weidinger, "Raman Spectroscopy Study of the Tetragonal-to-monoclinic Transition in Zirconium Oxide Scales and Determination of Overall Oxygen Diffusion by Nuclear Microanalysis of O," in *Zirconium in the Nuclear Industry: Ninth International Symposium*, 1991, pp. 416-416–21, doi: 10.1520/STP25520S.

[47] E. Polatidis *et al.*, "Residual stresses and tetragonal phase fraction characterisation of corrosion tested Zircaloy-4 using energy dispersive synchrotron X-ray diffraction," *J. Nucl. Mater.*, vol. 432, no. 1–3, pp. 102–112, Jan. 2013, doi: 10.1016/j.jnucmat.2012.07.025.

[48] A. Garner *et al.*, "The effect of Sn concentration on oxide texture and microstructure formation in zirconium alloys," *Acta Mater.*, vol. 99, pp. 259–272, 2015, doi: 10.1016/j.actamat.2015.08.005.

[49] J. Godlewski, "How the Tetragonal Zirconia is Stabilized in the Oxide Scale that is Formed on a Zirconium Alloy Corroded at 400°C in Steam," in *Zirconium in the Nuclear Industry: Tenth International Symposium*, 1994, pp. 663-663–21, doi: 10.1520/STP15214S.

[50] P. Barberis, "Zirconia powders and Zircaloy oxide films: tetragonal phase evolution during 400°C autoclave tests," *J. Nucl. Mater.*, vol. 226, no. 1–2, pp. 34–43, Oct. 1995, doi: 10.1016/0022-3115(95)00108-5.

[51] A. J. G. Maroto *et al.*, "Growth and characterization of oxide layers on zirconium alloys," *J. Nucl. Mater.*, vol. 229, pp. 79–92, Apr. 1996, doi: 10.1016/0022-3115(95)00233-2.

[52] H. El Kadiri *et al.*, "Transformations and cracks in zirconia films leading to breakaway oxidation of Zircaloy," *Acta Mater.*, vol. 61, no. 11, pp. 3923–3935, Jun. 2013, doi: 10.1016/j.actamat.2013.02.052.

[53] F. Garzarolli, H. Seidel, R. Tricot, and J. Gros, "Oxide Growth Mechanism on Zirconium Alloys," in *Zirconium in the Nuclear Industry: Ninth International Symposium*, 1991, pp. 395-395–21, doi: 10.1520/STP25519S.

[54] A. Yilmazbayhan, E. Breval, A. T. Motta, and R. J. Comstock, "Transmission electron

microscopy examination of oxide layers formed on Zr alloys," *J. Nucl. Mater.*, vol. 349, no. 3, pp. 265–281, Mar. 2006, doi: 10.1016/j.jnucmat.2005.10.012.

[55] A. Motta *et al.*, "Microstructure and Growth Mechanism of Oxide Layers Formed on Zr Alloys Studied with Micro-Beam Synchrotron Radiation," in *Zirconium in the Nuclear Industry: Fourteenth International Symposium*, 100 Barr Harbor Drive, PO Box C700, West Conshohocken, PA 19428-2959: ASTM International, 2005, pp. 205-205–28.

[56] P. Tejland and H.-O. Andrén, "Origin and effect of lateral cracks in oxide scales formed on zirconium alloys," *J. Nucl. Mater.*, vol. 430, no. 1–3, pp. 64–71, Nov. 2012, doi: 10.1016/j.jnucmat.2012.06.039.

[57] M. Parise, O. Sicardy, and G. Cailletaud, "Modelling of the mechanical behavior of the metal–oxide system during Zr alloy oxidation," *J. Nucl. Mater.*, vol. 256, no. 1, pp. 35–46, Jul. 1998, doi: 10.1016/S0022-3115(98)00045-2.

[58] P. Bossis, G. Lelie`vre, P. Barberis, X. Iltis, and F. Lefebvre, "Multi-Scale Characterization of the Metal-Oxide Interface of Zirconium Alloys," in *Zirconium in the Nuclear Industry: Twelfth International Symposium*, 2000, pp. 918-918–27, doi: 10.1520/STP14334S.

[59] N. Ni, S. Lozano-Perez, J. M. Sykes, G. D. W. Smith, and C. R. M. Grovenor, "Focussed ion beam sectioning for the 3D characterisation of cracking in oxide scales formed on commercial ZIRLO™ alloys during corrosion in high temperature pressurised water," *Corros. Sci.*, vol. 53, no. 12, pp. 4073–4083, Dec. 2011, doi: 10.1016/j.corsci.2011.08.013.

[60] S. S. Yardley *et al.*, "An investigation of the oxidation behaviour of zirconium alloys using isotopic tracers and high resolution SIMS," *J. Nucl. Mater.*, vol. 443, no. 1, pp. 436–443,

2013, doi: 10.1016/j.jnucmat.2013.07.053.

[61] N. Ni *et al.*, "Porosity in oxides on zirconium fuel cladding alloys, and its importance in controlling oxidation rates," *Scr. Mater.*, vol. 62, no. 8, pp. 564–567, Apr. 2010, doi: 10.1016/j.scriptamat.2009.12.043.

[62] J. Hu *et al.*, "Hydrogen pickup during oxidation in aqueous environments: The role of nano-pores and nano-pipes in zirconium oxide films," *Acta Mater.*, vol. 180, pp. 105–115, Nov. 2019, doi: 10.1016/J.ACTAMAT.2019.09.005.

[63] R. J. Nicholls *et al.*, "Crystal Structure of the ZrO Phase at Zirconium/Zirconium Oxide Interfaces," *Adv. Eng. Mater.*, vol. 17, no. 2, pp. 211–215, Feb. 2015, doi: 10.1002/adem.201400133.

[64] B. Puchala and A. Van der Ven, "Thermodynamics of the Zr-O system from first-principles calculations," *Phys. Rev. B*, vol. 88, no. 9, p. 094108, Sep. 2013, doi: 10.1103/PhysRevB.88.094108.

[65] Yoshitaka Nishino, A. R. Krauss, Yuping Lin, and D. M. Gruen, "Initial oxidation of zirconium and Zircaloy-2 with oxygen and water vapor at room temperature," *J. Nucl. Mater.*, vol. 228, no. 3, pp. 346–353, Apr. 1996, doi: 10.1016/0022-3115(95)00194-8.

[66] N. Ni *et al.*, "How the crystallography and nanoscale chemistry of the metal/oxide interface develops during the aqueous oxidation of zirconium cladding alloys," *Acta Mater.*, vol. 60, no. 20, pp. 7132–7149, Dec. 2012, doi: 10.1016/j.actamat.2012.09.021.

[67] J. Hu *et al.*, "Identifying suboxide grains at the metal–oxide interface of a corroded Zr–1.0%Nb alloy using (S)TEM, transmission-EBSD and EELS," *Micron*, vol. 69, pp. 35–42, Feb.

2015, doi: 10.1016/j.micron.2014.10.004.

[68] B. de Gabory, Y. Dong, A. T. Motta, and E. A. Marquis, "EELS and atom probe tomography study of the evolution of the metal/oxide interface during zirconium alloy oxidation," *J. Nucl. Mater.*, vol. 462, pp. 304–309, 2015, doi: 10.1016/j.jnucmat.2015.03.043.

[69] Y. Dong, A. T. Motta, and E. A. Marquis, "Multi-scale Characterization of Oxidized Zirconium Alloys," in *Microscopy and Microanalysis*, 2016, vol. 22, no. S3, pp. 1496–1497, doi: 10.1017/S1431927616008321.

[70] F. Garzarolli, W. Goll, A. Seibold, and I. Ray, "Effect of In-PWR Irradiation on Size, Structure, and Composition of Intermetallic Precipitates of Zr Alloys," in *Zirconium in the Nuclear Industry: Eleventh International Symposium*, 1996, pp. 541-541–16, doi: 10.1520/STP16189S.

[71] M. Bojinov, L. Hansson-Lyyra, P. Kinnunen, T. Saario, and P. Sirkia¨, "In-Situ Studies of the Oxide Film Properties on BWR Fuel Cladding Materials," in *Zirconium in the Nuclear Industry: Fourteenth International Symposium*, 2005, pp. 367–385, doi: 10.1520/STP37516S.

[72] G. Sabol, G. Kilp, M. Balfour, and E. Roberts, "Development of a Cladding Alloy for High Burnup," in *Zirconium in the Nuclear Industry: Eighth International Symposium*, 1989, pp. 227–244, doi: 10.1520/STP18868S.

[73] P. Barberis *et al.*, "Role of the Second-Phase Particles in Zirconium Binary Alloys," in *Zirconium in the Nuclear Industry: Thirteenth International Symposium*, 2002, pp. 33-33–26, doi: 10.1520/STP11382S.

[74] H. Weidinger, H. Ruhmann, G. Cheliotis, M. Maguire, T.-L. Yau, and T.-L. Yau, "Corrosion-

Electrochemical Properties of Zirconium Intermetallics," in *Zirconium in the Nuclear Industry: Ninth International Symposium*, 1991, pp. 499–535, doi: 10.1520/STP25525S.

[75] B. de Gabory and A. Motta, "Structure of Zircaloy 4 oxides formed during autoclave corrosion," in *ANS LWR Fuel Performance Meeting (TopFuel)*, 2013.

[76] A. Couet, A. T. Motta, B. de Gabory, and Z. Cai, "Microbeam X-ray Absorption Near-Edge Spectroscopy study of the oxidation of Fe and Nb in zirconium alloy oxide layers," *J. Nucl. Mater.*, vol. 452, no. 1, pp. 614–627, 2014, doi: 10.1016/j.jnucmat.2014.05.047.

[77] Y. Lin and O. Woo, "Oxidation of β-Zr and related phases in Zr–Nb alloys: an electron microscopy investigation," *J. Nucl. Mater.*, vol. 277, no. 1, pp. 11–27, Jan. 2000, doi: 10.1016/S0022-3115(99)00153-1.

[78] J. Hu *et al.*, "Understanding Corrosion and Hydrogen Pickup of Zirconium Fuel Cladding Alloys: The Role of Oxide Microstructure, Porosity, Suboxides, and Second-Phase Particles," in *Zirconium in the industry: 18th international symposium*, 2018, pp. 93–126, doi: 10.1520/STP159720160071.

[79] D. Pecheur, "Oxidation of β-Nb and Zr(Fe, V)2 precipitates in oxide films formed on advanced Zr-based alloys," *J. Nucl. Mater.*, vol. 278, no. 2–3, pp. 195–201, Apr. 2000, doi: 10.1016/S0022-3115(99)00253-6.

[80] H. Kim, J. Park, and Y. Jeong, "Ex-reactor corrosion and oxide characteristics of Zr–Nb–Fe alloys with the Nb/Fe ratio," *J. Nucl. Mater.*, vol. 345, no. 1, pp. 1–10, Oct. 2005, doi: 10.1016/J.JNUCMAT.2005.04.061.

[81] M. Moorehead, Z. Yu, L. Borrel, J. Hu, Z. Cai, and A. Couet, "Comprehensive investigation

of the role of Nb on the oxidation kinetics of Zr-Nb alloys," *Corros. Sci.*, vol. 155, pp. 173–181, Apr. 2019, doi: 10.1016/J.CORSCI.2019.04.017.

[82] P. Huang, S. Mahmood, and R. Adamson, "Effects of Thermomechanical Processing on In-Reactor Corrosion and Post-Irradiation Mechanical Properties of Zircaloy-2," in *Zirconium in the Nuclear Industry: Eleventh International Symposium*, 1996, pp. 726–758, doi: 10.1520/STP16199S.

[83] G. S. Was, *Fundamentals of radiation materials science: metals and alloys*. Springer Science & Business Media, 2007.

[84] D. J. Bacon, "A review of computer models of point defects in hcp metals," *J. Nucl. Mater.*, vol. 159, pp. 176–189, 1988, doi: 10.1016/0022-3115(88)90092-X.

[85] Q. Peng, W. Ji, H. Huang, and S. De, "Stability of self-interstitial atoms in hcp-Zr," *J. Nucl. Mater.*, vol. 429, no. 1–3, pp. 233–236, Oct. 2012, doi: 10.1016/j.jnucmat.2012.06.010.

[86] G. D. Samolyuk, A. V. Barashev, S. I. Golubov, Y. N. Osetsky, and R. E. Stoller, "Analysis of the anisotropy of point defect diffusion in hcp Zr," *Acta Mater.*, vol. 78, pp. 173–180, 2014, doi: 10.1016/j.actamat.2014.06.024.

[87] M. Christensen *et al.*, "Diffusion of point defects, nucleation of dislocation loops, and effect of hydrogen in hcp-Zr: Ab initio and classical simulations," *J. Nucl. Mater.*, vol. 460, pp. 82–96, 2015, doi: 10.1016/j.jnucmat.2015.02.013.

[88] C. H. Woo, "Theory of irradiation deformation in non-cubic metals: Effects of anisotropic diffusion," *J. Nucl. Mater.*, vol. 159, pp. 237–256, 1988, doi: 10.1016/0022-3115(88)90096-7.

[89] A. V. Barashev, S. I. Golubov, and R. E. Stoller, "Theoretical investigation of microstructure evolution and deformation of zirconium under neutron irradiation," *J. Nucl. Mater.*, vol. 461, pp. 85–94, 2015, doi: 10.1016/j.jnucmat.2015.02.001.

[90] B. von Guerard, H. Peisl, and IUCr, "Agglomeration of point defects in copper after neutron irradiation at 4.6 K," *J. Appl. Crystallogr.*, vol. 8, no. 2, pp. 161–161, Apr. 1975, doi: 10.1107/S0021889875009958.

[91] R. E. Stoller, "1.11 – Primary Radiation Damage Formation," in *Comprehensive Nuclear Materials*, Elsevier Ltd, 2012, pp. 293–332.

[92] N. de Diego, Y. N. Osetsky, and D. J. Bacon, "Structure and properties of vacancy and interstitial clusters in α-zirconium," *J. Nucl. Mater.*, vol. 374, no. 1–2, pp. 87–94, Feb. 2008, doi: 10.1016/j.jnucmat.2007.07.011.

[93] C. Varvenne, O. Mackain, and E. Clouet, "Vacancy clustering in zirconium: An atomic-scale study," *Acta Mater.*, vol. 78, pp. 65–77, Oct. 2014, doi: 10.1016/j.actamat.2014.06.012.

[94] P. M. Kelly and R. G. Blake, "The characterization of dislocation loops in neutron irradiated zirconium," *Philos. Mag.*, vol. 28, no. 2, pp. 415–426, Aug. 1973, doi: 10.1080/14786437308217463.

[95] A. Jostsons, P. M. Kelly, and R. G. Blake, "The nature of dislocation loops in neutron irradiated zirconium," *J. Nucl. Mater.*, vol. 66, no. 3, pp. 236–256, May 1977, doi: 10.1016/0022-3115(77)90113-1.

[96] A. Jostsons, R. G. Blake, J. G. Napier, P. M. Kelly, and K. Farrell, "Faulted loops in neutron-irradiated zirconium," *J. Nucl. Mater.*, vol. 68, no. 3, pp. 267–276, 1977, doi: 10.1016/0022-

3115(77)90251-3.

[97] R. A. Holt and R. W. Gilbert, "〈c〉 Component dislocations in annealed Zircaloy irradiated at about 570 K," *J. Nucl. Mater.*, vol. 137, no. 3, pp. 185–189, 1986, doi: 10.1016/0022-3115(86)90218-7.

[98] D. O. Northwood, V. Fidleris, R. W. Gilbert, and G. J. C. Carpenter, "Dislocation loop generation and irradiation growth in a zirconium single crystal," *J. Nucl. Mater.*, vol. 61, no. 2, pp. 123–130, 1976, doi: 10.1016/0022-3115(76)90076-3.

[99] S. Averin, V. Panchenko, A. Kozlov, L. Sinelnikov, V. Shishov, and A. Nikulina, "Evolution of Dislocation and Precipitate Structure in Zr Alloys Under Long-Term Irradiation," in *Zirconium in the Nuclear Industry: Twelfth International Symposium*, 2000, pp. 105-105–17, doi: 10.1520/STP14297S.

[100] D. O. Northwood *et al.*, "Characterization of neutron irradiation damage in zirconium alloys — an international 'round-robin' experiment," *J. Nucl. Mater.*, vol. 79, no. 2, pp. 379–394, 1979, doi: 10.1016/0022-3115(79)90103-X.

[101] D. O. Northwood, "Comments on 'in-pile dimensional changes in neutron irradiated zirconium base alloys,'" *J. Nucl. Mater.*, vol. 64, no. 3, pp. 316–319, 1977, doi: 10.1016/0022-3115(77)90087-3.

[102] M. Griffiths, J. Mecke, and J. Winegar, "Evolution of Microstructure in Zirconium Alloys During Irradiation," in *Zirconium in the Nuclear Industry: Eleventh International Symposium*, 1996, pp. 580–603, doi: 10.1520/STP16191S.

[103] A. Harte *et al.*, "The effect of matrix chemistry on dislocation evolution in an irradiated Zr

alloy," *Acta Mater.*, vol. 130, pp. 69–82, 2017, doi: 10.1016/j.actamat.2017.03.024.

[104] M. Griffiths, "A review of microstructure evolution in zirconium alloys during irradiation," *J. Nucl. Mater.*, vol. 159, no. C, pp. 190–218, 1988, doi: 10.1016/0022-3115(88)90093-1.

[105] R. A. Holt and R. W. Gilbert, "c-Component dislocations in neutron irradiated zircaloy-2," *J. Nucl. Mater.*, vol. 116, no. 1, pp. 127–130, 1983, doi: 10.1016/0022-3115(83)90301-X.

[106] M. Griffiths, R. W. Gilbert, V. Fidleris, R. P. Tucker, and R. B. Adamson, "Neutron damage in zirconium alloys irradiated at 644 to 710 k," *J. Nucl. Mater.*, vol. 150, no. 2, pp. 159–168, 1987, doi: 10.1016/0022-3115(87)90071-7.

[107] S. Doriot *et al.*, "Microstructural Evolution of M5 TM Alloy Irradiated in PWRs up to High Fluences—Comparison With Other Zr-Based Alloys," in *Zirconium in the Nuclear Industry: 17th Volume*, 2015, pp. 759–799, doi: 10.1520/STP154320120179.

[108] G. P. Kobylyansky *et al.*, "Irradiation-induced growth and microstructure of recrystallized, cold worked and quenched Zircaloy-2, NSF, and E635 alloys," *J. ASTM Int.*, vol. 5, no. 4, pp. 564–582, Apr. 2008, doi: 10.1520/stp48156s.

[109] V. Shishov *et al.*, "Influence of Structure—Phase State of Nb Containing Zr Alloys on Irradiation-Induced Growth," *J. ASTM Int.*, vol. 2, no. 8, pp. 666–685, 2005, doi: 10.1520/JAI12431.

[110] G. P. Kobylyansky *et al.*, "Radiation Damage of E635 Alloy Under High Dose Irradiation in the VVER-1000 and BOR-60 Reactors," *J. ASTM Int.*, vol. 8, no. 1, pp. 827–850, Apr. 2011, doi: 10.1520/JAI102941.

[111] V. N. Shishov, P. Barberis, and S. W. Dean, "The evolution of microstructure and

deformation stability in Zr–Nb–(Sn,Fe) alloys under neutron irradiation," *J. ASTM Int.*, vol. 7, no. 7, pp. 37–67, 2010, doi: 10.1520/JAI103005.

[112] A. Motta, F. Lefebvre, and C. Lemaignan, "Amorphization of Precipitates in Zircaloy under Neutron and Charged-Particle Irradiation," in *Zirconium in the Nuclear Industry: Ninth International Symposium*, 1991, pp. 718–740, doi: 10.1520/STP25536S.

[113] J. Liu *et al.*, "Ex-situ and in-situ studies of radiation damage mechanisms in Zr-Nb alloys," in *Zirconium in the Nuclear Industry - 19th International Symposium*, 2019.

[114] F. Onimus and J. L. Béchade, "4.01 – Radiation Effects in Zirconium Alloys," in *Comprehensive Nuclear Materials*, 2012, pp. 1–31.

[115] J. Ribis, S. Doriot, and F. Onimus, "Shape, orientation relationships and interface structure of beta-Nb nano-particles in neutron irradiated zirconium alloy," *J. Nucl. Mater.*, vol. 511, pp. 18–29, Dec. 2018, doi: 10.1016/J.JNUCMAT.2018.08.042.

[116] Z. Yu *et al.*, "Microstructure and microchemistry study of irradiation-induced precipitates in proton irradiated ZrNb alloys," *Acta Mater.*, vol. 178, pp. 228–240, Aug. 2019, doi: 10.1016/J.ACTAMAT.2019.08.012.

[117] X. K. Xin, W. S. Lai, and B. X. Liu, "Point defect properties in hcp and bcc Zr with trace solute Nb revealed by ab initio calculations," *Journal of Nuclear Materials*, vol. 393, no. 1. pp. 197–202, 15-Aug-2009, doi: 10.1016/j.jnucmat.2009.06.005.

[118] Y. Matsukawa *et al.*, "The effect of crystallographic mismatch on the obstacle strength of second phase precipitate particles in dispersion strengthening: bcc Nb particles and nanometric Nb clusters embedded in hcp Zr," *Acta Mater.*, vol. 102, pp. 323–332, Jan. 2016,

doi: 10.1016/J.ACTAMAT.2015.09.038.

[119] B. F. Kammenzind, J. A. Gruber, R. Bajaj, and J. D. Smee, "Neutron Irradiation Effects on the Corrosion of Zircaloy-4 in a Pressurized Water Reactor Environment," in *Zirconium in the Nuclear Industry: 18th International Symposium*, 2018, pp. 448–490, doi: 10.1520/stp159720160085.

[120] M. Léger and R. G. Fleck, "Irradiation growth in Zr-2.5Nb," in *Zirconium in the Nuclear Industry: Sixth International Symposium*, 1984, pp. 409–426, doi: 10.1520/STP34483S.

[121] H. Willard, "Irradiation Growth of Zircaloy (LWBR Development Program)," in *Zirconium in the Nuclear Industry*, 1984, pp. 452-452–29, doi: 10.1520/STP34486S.

[122] J. Williams, E. C. Darby, and D. C. C. Minty, "Irradiation growth of annealed Zircaloy-2," in *Zirconium in the Nuclear Industry: Sixth International Symposium*, 1984, pp. 376–393, doi: 10.1520/STP34481S.

[123] B. Cox, "Processes occurring during the breakdown of oxide films on zirconium alloys," *J. Nucl. Mater.*, vol. 29, no. 1, pp. 50–66, Jan. 1969, doi: 10.1016/0022-3115(69)90126-3.

[124] E. Francis *et al.*, "Effect of Nb and Fe on damage evolution in a Zr-alloy during proton and neutron irradiation," *Acta Mater.*, vol. 165, pp. 603–614, Feb. 2019, doi: 10.1016/J.ACTAMAT.2018.12.021.

[125] E. M. Francis *et al.*, "Iron redistribution in a zirconium alloy after neutron and proton irradiation studied by energy-dispersive X-ray spectroscopy (EDX) using an aberration-corrected (scanning) transmission electron microscope," *J. Nucl. Mater.*, vol. 454, no. 1–3, pp. 387–397, Nov. 2014, doi: 10.1016/j.jnucmat.2014.08.034.

[126] A. Harte *et al.*, "Nano-scale chemical evolution in a proton-and neutron-irradiated Zr alloy," *J. Nucl. Mater.*, vol. 487, pp. 30–42, 2017, doi: 10.1016/j.jnucmat.2017.01.049.

[127] Z. Yu, A. Couet, and M. Bachhav, "Irradiation-induced Nb redistribution of ZrNb alloy: An APT study," *J. Nucl. Mater.*, vol. 516, pp. 100–110, Apr. 2019, doi: 10.1016/J.JNUCMAT.2019.01.015.

[128] H. Yu, J. Liang, Z. Yao, M. A. Kirk, and M. R. Daymond, "Effect of heavy ion irradiation on thermodynamically equilibrium Zr-Excel alloy," *J. Nucl. Mater.*, vol. 488, pp. 33–45, May 2017, doi: 10.1016/j.jnucmat.2017.03.003.

[129] Q. Dong, H. Qin, Z. Yao, and M. R. Daymond, "Irradiation damage and hardening in pure Zr and Zr-Nb alloys at 573 K from self-ion irradiation," *Mater. Des.*, vol. 161, pp. 147–159, Jan. 2019, doi: 10.1016/J.MATDES.2018.11.017.

[130] A. Garner *et al.*, "Investigating the Effect of Zirconium Oxide Microstructure on Corrosion Performance: A Comparison between Neutron, Proton, and Nonirradiated Oxides," in *Zirconium in the Nuclear Industry: 18th International Symposium*, 2018, no. January, pp. 491–523, doi: 10.1520/STP159720160069.

[131] P. Wang and G. S. Was, "Oxidation of Zircaloy-4 during in situ proton irradiation and corrosion in PWR primary water," *J. Mater. Res.*, vol. 30, no. 09, pp. 1335–1348, May 2015, doi: 10.1557/jmr.2014.408.

[132] X. Iltis, F. Lefebvre, and C. Lemaignan, "Microstructure Evolutions and Iron Redistribution in Zircaloy Oxide Layers: Comparative Effects of Neutron Irradiation Flux and Irradiation Damages," in *Zirconium in the Nuclear Industry: Eleventh International Symposium*, 1996,

pp. 242–265, doi: 10.1520/STP16176S.

[133] S. Abolhassani *et al.*, "TEM Examinations of the Metal-Oxide Interface of Zirconium Based Alloys Irradiated in a Pressurized Water Reactor," in *Zirconium in the Nuclear Industry: Fourteenth International Symposium*, 2008, pp. 467–494, doi: 10.1520/stp37521s.

[134] J. Liu *et al.*, "Irradiation-induced amorphization in the zirconium suboxide on Zr-0.5Nb alloys," *J. Nucl. Mater.*, vol. 513, pp. 226–231, Jan. 2019.

[135] J. Hu *et al.*, "Effect of neutron and ion irradiation on the metal matrix and oxide corrosion layer on Zr-1.0Nb cladding alloys," *Acta Mater.*, vol. 173, pp. 313–326, May 2019, doi: 10.1016/J.ACTAMAT.2019.04.055.

[136] G. Was, "Challenges to the use of ion irradiation for emulating reactor irradiation," *J. Mater. Res.*, vol. 30, no. 9, pp. 1158–1182, 2015, doi: 10.1557/jmr.2015.73.

[137] A. Souidi, M. Hou, C. S. Becquart, L. Malerba, C. Domain, and R. E. Stoller, "On the correlation between primary damage and long-term nanostructural evolution in iron under irradiation," *J. Nucl. Mater.*, vol. 419, no. 1–3, pp. 122–133, Dec. 2011, doi: 10.1016/J.JNUCMAT.2011.08.049.

[138] A. T. Motta, "Amorphization of intermetallic compounds under irradiation — A review," *J. Nucl. Mater.*, vol. 244, no. 3, pp. 227–250, Apr. 1997, doi: 10.1016/S0022-3115(96)00740-4.

[139] F. A. Garner, H. L. Heinisch, R. L. Simons, and F. M. Mann, "Implications of neutron spectrum and flux differences on fission-fusion correlations at high neutron fluence," *Radiat. Eff. Defects Solids*, vol. 113, no. 1–3, pp. 229–255, Mar. 1990, doi:

10.1080/10420159008213068.

[140] C. Abromeit, "Aspects of simulation of neutron damage by ion irradiation," *J. Nucl. Mater.*, vol. 216, pp. 78–96, Oct. 1994, doi: 10.1016/0022-3115(94)90008-6.

[141] T. Muroga, H. Watanabe, and Y. Yoshida, "Correlation of fast neutron, fusion neutron and electron irradiations based on the dislocation loop density," *J. Nucl. Mater.*, vol. 174, no. 2–3, pp. 282–288, Nov. 1990, doi: 10.1016/0022-3115(90)90241-E.

[142] G. S. Was, "8.3.5 Irradiation Variable Shifts," in *Fundamentals of radiation materials science: metals and alloys*, Springer Science & Business Media, 2007, pp. 426–432.

[143] J. G. Gigax, H. Kim, E. Aydogan, F. A. Garner, S. Maloy, and L. Shao, "Beam-contamination-induced compositional alteration and its neutron-atypical consequences in ion simulation of neutron-induced void swelling," *Mater. Res. Lett.*, vol. 5, no. 7, pp. 478–485, Nov. 2017, doi: 10.1080/21663831.2017.1323808.

[144] R. Holt and R. Fleck, "The Contribution of Irradiation Growth to Pressure Tube Deformation," in *Zirconium in the Nuclear Industry: Ninth International Symposium*, 1991, pp. 218-218–12, doi: 10.1520/STP25509S.

[145] S. Lozano-Perez and J. M. Titchmarsh, "TEM investigations of intergranular stress corrosion cracking in austenitic alloys in PWR environmental conditions," *Mater. High Temp.*, vol. 20, no. 4, pp. 573–579, 2003, doi: 10.1179/mht.2003.066.

[146] Y. Z. Huang, S. Lozano-Perez, R. M. Langford, J. M. Titchmarsh, and M. L. Jenkins, "Preparation of transmission electron microscopy cross-section specimens of crack tips using focused ion beam milling," *J. Microsc.*, vol. 207, no. 2, pp. 129–136, Aug. 2002, doi:

10.1046/j.1365-2818.2002.01050.x.

[147] S. Lozano-Perez, "A guide on FIB preparation of samples containing stress corrosion crack tips for TEM and atom-probe analysis," *Micron*, vol. 39, no. 3, pp. 320–328, Apr. 2008, doi: 10.1016/J.MICRON.2007.12.003.

[148] X. Yi, M. L. Jenkins, K. Hattar, P. D. Edmondson, and S. G. Roberts, "Characterisation of radiation damage in W and W-based alloys from 2 MeV self-ion near-bulk implantations," *Acta Mater.*, vol. 92, pp. 163–177, Jun. 2015, doi: 10.1016/j.actamat.2015.04.015.

[149] M. Kirk *et al.*, "Characterization of irradiation defect structures and densities by transmission electron microscopy," *J. Mater. Res.*, vol. 30, no. 09, pp. 1195–1201, May 2015, doi: 10.1557/jmr.2015.19.

[150] M. L. Jenkins, "Characterisation of radiation-damage microstructures by TEM," *J. Nucl. Mater.*, vol. 216, pp. 124–156, Oct. 1994, doi: 10.1016/0022-3115(94)90010-8.

[151] D. B. Williams and C. B. Carter, *The Transmission Electron Microscope*. Boston, MA: Springer US, 2009.

[152] S. J. Pennycook and P. D. (Peter D. Nellist, *Scanning transmission electron microscopy : imaging and analysis*. Springer, 2011.

[153] H. Yang, J. G. Lozano, T. J. Pennycook, L. Jones, P. B. Hirsch, and P. D. Nellist, "Imaging screw dislocations at atomic resolution by aberration-corrected electron optical sectioning," *Nat. Commun.*, vol. 6, pp. 1–7, 2015, doi: 10.1038/ncomms8266.

[154] R. F. Egerton, *Electron energy-loss spectroscopy in the electron microscope*. Springer, 2011.

[155] D. Shindo and T. Oikawa, *Analytical Electron Microscopy for Materials Science*. Springer

Japan, 2002.

[156] J. C. Haley, “TEM of neutron, proton and self-ion irradiation damage in FeCr alloys”, DPhil Thesis, University of Oxford, 2018.

[157] K. Iakoubovskii, K. Mitsuishi, Y. Nakayama, and K. Furuya, “Thickness measurements with electron energy loss spectroscopy,” *Microsc. Res. Tech.*, vol. 71, no. 8, pp. 626–631, Aug. 2008, doi: 10.1002/jemt.20597.

[158] C. Lee, Y. Ikematsu, and D. Shindo, “Measurement of mean free paths for inelastic electron scattering of Si and SiO2,” *J. Electron Microsc. (Tokyo).*, vol. 51, no. 3, pp. 143–148, May 2002, doi: 10.1093/jmicro/51.3.143.

[159] D. R. G. Mitchell, “DiffTools: Electron diffraction software tools for DigitalMicrograph™,” *Microsc. Res. Tech.*, vol. 71, no. 8, pp. 588–593, Aug. 2008, doi: 10.1002/jemt.20591.

[160] J. Sayers, S. Lozano-Perez, R. J. Nicholls, and S. Ortner, “A high-resolution characterization of the oxide-metal interface in Zircaloy-4 and its relation to the oxidation and hydrogen pickup mechanisms,” *J. Nucl. Mater.*, vol. 525, pp. 72–82, Nov. 2019, doi: 10.1016/j.jnucmat.2019.07.008.

[161] M. Griffiths, J. E. Winegar, and A. Buyers, “The transformation behaviour of the β-phase in Zr–2.5Nb pressure tubes,” *J. Nucl. Mater.*, vol. 383, no. 1–2, pp. 28–33, Dec. 2008, doi: 10.1016/J.JNUCMAT.2008.08.003.

[162] E. P. Francisco de la Peña Vidar Tonaas Fauske, Pierre Burdet, Petras Jokubauskas, Magnus Nord, ··· Andreas Garmannslund, “hyperspy/hyperspy: HyperSpy v1.5.2.” Zenodo, 2019, doi: 10.5281/zenodo.3396791.

[163] T. Manoubi, M. Tencé, and C. Colliex, “Quantification of white lines in Electron Energy Loss Spectroscopy (EELS),” *Ultramicroscopy*, vol. 28, no. 1–4, pp. 49–55, Apr. 1989, doi: 10.1016/0304-3991(89)90269-6.

[164] V. Bouineau, G. Bénier, D. Pêcheur, J. J. Thomazet, A. Ambard, and M. Blat, “Analysis of the Waterside Corrosion Kinetics of Zircaloy-4 Fuel Cladding in French PWRs,” *Nucl. Technol.*, vol. 170, no. 3, pp. 444–459, Jun. 2010, doi: 10.13182/NT10-A10330.

[165] G. L. Garner, B. A. Hilton, and E. Mader, “2007 LWR Fuel Performance/Top Fuel : September 30th - October 3, 2007, San Francisco, California.,” in *2007 LWR Fuel Performance Meeting / TopFuel 2007 “Zero by 2010,”* 2007.

[166] P. Bossis, D. Pecheur, K. Hanifi, J. Thomazet, and M. Blat, “Comparison of the High Burn Up Corrosion on M5 and Low Tin Zircaloy 4,” in *Zirconium in the Nuclear Industry: Fourteenth International Symposium*, 2005, pp. 494–525, doi: 10.1520/STP37522S.

[167] W. D. Callister and D. G. Rethwisch, *Materials Science and Engineering*, 8th SI Ver. WILEY, 2011.

[168] V. N. Shishov, “The Evolution of Microstructure and Deformation Stability in Zr–Nb–(Sn,Fe) Alloys Under Neutron Irradiation,” in *Zirconium in the Nuclear Industry: 16th International Symposium*, 2012, pp. 37–66, doi: 10.1520/stp152920120003.

[169] L. Zhou, S. X. Li, C. R. Chen, Y. C. Wang, Q. S. Zang, and K. Lu, “Three-dimensional finite element analysis of stresses and energy density distributions around γ′ before coarsening loaded in the [1 1 0]-direction in Ni-based superalloy,” *Mater. Sci. Eng. A*, vol. 352, no. 1–2, pp. 300–307, Jul. 2003, doi: 10.1016/S0921-5093(02)00901-2.

[170] T. Murakumo, T. Kobayashi, Y. Koizumi, and H. Harada, "Creep behaviour of Ni-base single-crystal superalloys with various γ′ volume fraction," *Acta Mater.*, vol. 52, no. 12, pp. 3737–3744, Jul. 2004, doi: 10.1016/j.actamat.2004.04.028.

[171] C. A. Williams, E. A. Marquis, A. Cerezo, and G. D. W. Smith, "Nanoscale characterisation of ODS-Eurofer 97 steel: An atom-probe tomography study," *J. Nucl. Mater.*, vol. 400, no. 1, pp. 37–45, May 2010, doi: 10.1016/j.jnucmat.2010.02.007.

[172] J. P. Abriata and J. C. Bolcich, "The Nb−Zr (Niobium−Zirconium) system," *J. Phase Equilibria*, vol. 3, no. 1, pp. 34–44, Jun. 1982, doi: 10.1007/BF02873409.

[173] H. R. Wenk, I. Lonardelli, and D. Williams, "Texture changes in the hcp → bcc → hcp transformation of zirconium studied in situ by neutron diffraction," *Acta Mater.*, vol. 52, no. 7, pp. 1899–1907, Apr. 2004, doi: 10.1016/j.actamat.2003.12.029.

[174] R. Monzen, M. L. Jenkins, and A. R. Sutton, "The bcc-to-9R martensitic transformation of Cu precipitates and the relaxation process of elastic strains in an Fe-Cu alloy," *Philos. Mag. A Phys. Condens. Matter, Struct. Defects Mech. Prop.*, vol. 80, no. 3, pp. 711–723, 2000, doi: 10.1080/01418610008212077.

[175] P. J. Othen, M. L. Jenkins, and G. D. W. Smith, "High-resolution electron microscopy studies of the structure of Cu precipitates in α-Fe," *Philos. Mag. A Phys. Condens. Matter, Struct. Defects Mech. Prop.*, vol. 70, no. 1, pp. C1-24, 1994, doi: 10.1080/01418619408242533.

[176] S. Lozano-Perez, M. L. Jenkins, and J. M. Titchmarsh, "Evidence for deformation-induced transformations of Cu-rich precipitates in an aged FeCu alloy," *Philos. Mag. Lett.*, vol. 86, no. 6, pp. 367–374, Jun. 2006, doi: 10.1080/09500830600815365.

[177] G. M. Worrall, J. T. Buswell, C. A. English, M. G. Hetherington, and G. D. W. Smith, "A study of the precipitation of copper particles in a ferrite matrix," *J. Nucl. Mater.*, vol. 148, no. 1, pp. 107–114, Mar. 1987, doi: 10.1016/0022-3115(87)90525-3.

[178] G. M. Hood, H. Zou, R. J. Schultz, and N. Matsuura, "Nb diffusion in single-crystal α-Zr," *Defect Diffus. Forum*, vol. 143–147, pp. 55–60, 1997, doi: 10.4028/www.scientific.net/DDF.143-147.55.

[179] C. H. Woo and X. Liu, "Atomistic calculation of point-defect diffusion anisotropy and irradiation growth in α-zirconium," *Philos. Mag.*, vol. 87, no. 16, pp. 2355–2369, Jun. 2007, doi: 10.1080/14786430601185085.

[180] V. P. Ramunni and A. M. F. Rivas, "Diffusion calculations with two atomic models in h.c.p Zr-Nb diluted alloys," *Mater. Chem. Phys.*, vol. 197, pp. 163–180, Aug. 2017, doi: 10.1016/J.MATCHEMPHYS.2017.05.022.

[181] A. Sarce, "Stability of precipitates in the anisotropic α-Zr matrix under irradiation," *J. Nucl. Mater.*, vol. 185, no. 2, pp. 214–223, Nov. 1991, doi: 10.1016/0022-3115(91)90338-8.

[182] M. Griffiths and R. W. Gilbert, "The formation of c-component defects in zirconium alloys during neutron irradiation," *J. Nucl. Mater.*, vol. 150, no. 2, pp. 169–181, 1987, doi: 10.1016/0022-3115(87)90072-9.

[183] M. Griffiths, M. H. Loretto, and R. E. Smallman, "Electron damage in zirconium: II. Nucleation and growth of c-component loops," *J. Nucl. Mater.*, vol. 115, no. 2, pp. 323–330, 1983, doi: 10.1016/0022-3115(83)90323-9.

[184] H. Yu, Z. Yao, and M. R. Daymond, "The stability of thermodynamically metastable phases

in a Zr-Sn-Nb-Mo alloy: Effects of alloying elements, morphology and applied stress/strain," *J. Nucl. Mater.*, vol. 493, pp. 84–95, Sep. 2017, doi: 10.1016/J.JNUCMAT.2017.06.004.

[185] V. Perovic, A. Perovic, G. C. Weatherly, and G. R. Purdy, "The distribution of Nb and Fe in a Zr-2.5 wt% Nb alloy, before and after irradiation," *J. Nucl. Mater.*, vol. 224, no. 1, pp. 93–102, 1995, doi: 10.1016/0022-3115(95)00044-5.

[186] G. K. Dey, R. N. Singh, R. Tewari, D. Srivastava, and S. Banerjee, "Metastability of the β-phase in Zr-rich Zr-Nb alloys," *J. Nucl. Mater.*, vol. 224, no. 2, pp. 146–157, Aug. 1995, doi: 10.1016/0022-3115(95)00047-X.

[187] J. O. Stiegler, J. T. Houston, and M. L. Picklesimer, "Transmission electron microscopy of omega phase in a Zr-15 % Nb alloy," *J. Nucl. Mater.*, vol. 11, no. 1, pp. 32–40, 1964, doi: 10.1016/0022-3115(64)90118-7.

[188] S. Banerjee and R. Krishnan, "Martensitic transformation in zirconium-niobium alloys," *Acta Metall.*, vol. 19, no. 12, pp. 1317–1326, 1971, doi: 10.1016/0001-6160(71)90068-X.

[189] S. A. Aldridge and B. A. Cheadle, "Age hardening of Zr-2.5 wt % Nb slowly cooled from the (α +β) phase field," *J. Nucl. Mater.*, vol. 42, no. 1, pp. 32–42, 1972, doi: 10.1016/0022-3115(72)90004-9.

[190] G. Aurelio, A. F. Guillermet, G. J. Cuello, and J. Campo, "Structural properties and high-temperature reactions of the metastable Ω phase in Zr-Nb alloys," *J. Nucl. Mater.*, vol. 341, no. 1, pp. 1–11, May 2005, doi: 10.1016/j.jnucmat.2004.12.001.

[191] J. Ziegler, "The Kinchin-Pease Model for Vacancy Production," in *SRIM - The Stopping and*

Range of Ions in Matter, 15th ed., Lulu, 2015.

[192] R. Castaing, "Application of electron probes to local chemical and crystallographic analysis," University of Paris, 1951.

[193] J. A. Hinks, "Transmission electron microscopy with in situ ion irradiation," *J. Mater. Res.*, vol. 30, no. 09, pp. 1214–1221, May 2015, doi: 10.1557/jmr.2014.384.

[194] K. L. Moore, M. Schröder, and C. R. M. Grovenor, "Imaging Secondary Ion Mass Spectroscopy," in *Handbook of Nanoscopy*, Weinheim, Germany: Wiley-VCH Verlag GmbH & Co. KGaA, 2012, pp. 709–744.

[195] G. Yuan, L. Zhang, Q. Yue, H. Gu, G. Li, and J. Shen, "Microstructural characteristics of β precipitates in Zr–1Nb alloy," *Mater. Chem. Phys.*, vol. 165, pp. 87–90, Sep. 2015, doi: 10.1016/J.MATCHEMPHYS.2015.08.058.

[196] A. T. Motta, J. A. Faldowski, L. M. Howe, and P. R. Okamoto, "In situ studies of phase transformations in zirconium alloys and compounds under irradiation," 1996, vol. 1295, pp. 557–579.

[197] A. T. Motta and C. Lemaignan, "A ballistic mixing model for the amorphization of precipitates in Zircaloy under neutron irradiation," *J. Nucl. Mater.*, vol. 195, no. 3, pp. 277–285, 1992, doi: 10.1016/0022-3115(92)90519-Q.

[198] K. C. Russell, "Phase instability under cascade damage irradiation," *J. Nucl. Mater.*, vol. 206, no. 2–3, pp. 129–138, Nov. 1993, doi: 10.1016/0022-3115(93)90120-N.

[199] A. A. Turkin, A. V. Buts, and A. S. Bakai, "Construction of radiation-modified phase diagrams under cascade-producing irradiation: application to Zr–Nb alloy," *J. Nucl. Mater.*, vol. 305,

no. 2, pp. 134–152, 2002, doi: 10.1016/S0022-3115(02)01027-9.

[200] G. S. Was and P. L. Andresen, "Radiation damage to structural alloys in nuclear power plants: mechanisms and remediation," in *Structural Alloys for Power Plants*, Woodhead Publishing, 2014, pp. 355–420.

[201] R. S. Nelson, J. A. Hudson, and D. J. Mazey, "The stability of precipitates in an irradiation environment," *J. Nucl. Mater.*, vol. 44, no. 3, pp. 318–330, Sep. 1972, doi: 10.1016/0022-3115(72)90043-8.

[202] P. Wilkes, "Phase stability under irradiation — a review of theory and experiment," *J. Nucl. Mater.*, vol. 83, no. 1, pp. 166–175, Aug. 1979, doi: 10.1016/0022-3115(79)90602-0.

[203] McLean Donald, *Grain boundaries in metals*. Oxford: Oxford University Press, 1957.

[204] V. Shishov *et al.*, "Influence of Zirconium Alloy Chemical Composition on Microstructure Formation and Irradiation Induced Growth," in *Zirconium in the Nuclear Industry: Thirteenth International Symposium*, 2002, pp. 758–780, doi: 10.1520/STP11415S.

[205] V. N. Shishov *et al.*, "Structure-phase state, corrosion and irradiation properties of Zr-Nb-Fe-Sn system Alloys," *J. ASTM Int.*, vol. 5, no. 3, pp. 724–743, 2008, doi: 10.1520/JAI101127.

[206] M. Topping *et al.*, "The effect of irradiation temperature on damage structures in proton-irradiated zirconium alloys," *J. Nucl. Mater.*, vol. 514, pp. 358–367, Feb. 2019, doi: 10.1016/j.jnucmat.2018.12.006.

[207] R. C. Pasianot and A. M. Monti, "A many body potential for α-Zr. Application to defect properties," *J. Nucl. Mater.*, vol. 264, no. 1–2, pp. 198–205, Jan. 1999, doi: 10.1016/S0022-3115(98)00477-2.

[208] H. Yu, Q. Dong, Z. Yao, H. K. Zhang, M. A. Kirk, and M. R. Daymond, "In-situ study of heavy ion irradiation induced lattice defects and phase instability in β-Zr of a Zr–Nb alloy," *J. Nucl. Mater.*, vol. 522, pp. 192–199, Aug. 2019, doi: 10.1016/J.JNUCMAT.2019.05.028.

[209] R. A. Ploc, "Mechanism of deuterium pickup in Zr–2.5Nb alloy," *Mater. High Temp.*, vol. 17, no. 1, pp. 29–34, Jan. 2000, doi: 10.1179/mht.2000.006.

[210] C. Proff, S. Abolhassani, and C. Lemaignan, "Oxidation behaviour of zirconium alloys and their precipitates – A mechanistic study," *J. Nucl. Mater.*, vol. 432, no. 1–3, pp. 222–238, Jan. 2013, doi: 10.1016/j.jnucmat.2012.06.026.

[211] P. Tejland *et al.*, "Oxidation Mechanism in Zircaloy-2—The Effect of SPP Size Distribution," in *Zirconium in the Nuclear Industry: 17th international syposium*, 2015, pp. 373–403, doi: 10.1520/STP154320130052.

[212] C. A. C. Sequeira, *High temperature corrosion : fundamentals and engineering*. Wiley-Blackwell, 2019.

[213] R. P. Haggerty, P. Sarin, Z. D. Apostolov, P. E. Driemeyer, and W. M. Kriven, "Thermal Expansion of HfO2 and ZrO2," *J. Am. Ceram. Soc.*, vol. 97, no. 7, pp. 2213–2222, Jul. 2014, doi: 10.1111/jace.12975.

[214] D. Pecheur, F. Lefebvre, A. T. Motta, C. Lemaignan, and J. F. Wadier, "Precipitate evolution in the Zircaloy-4 oxide layer," *J. Nucl. Mater.*, vol. 189, no. 3, pp. 318–332, Aug. 1992, doi: 10.1016/0022-3115(92)90385-X.

[215] M. Parise, O. Sicardy, and G. Cailletaud, "Modelling of the mechanical behavior of the metal-oxide system during Zr alloy oxidation," *J. Nucl. Mater.*, vol. 256, no. 1, pp. 35–46,

Jul. 1998, doi: 10.1016/S0022-3115(98)00045-2.

[216] M. Parise, I. Touet, and O. Sicardy, "Oxidation of Zirconium Alloys. Crystallographic Texture of Zirconia: Interpretation and Mechanical Consequences," *Textures Microstruct.*, vol. 30, no. 3–4, pp. 247–263, 1998, doi: 10.1155/tsm.30.247.

Appendix A

In [ ]:
```
%matplotlib qt
%config IPCompleter.greedy=True
import hyperspy.api as hs
import numpy as np
import matplotlib.pyplot as plt
import gc
gc.enable()
```

In [ ]:
```
#Opens a dialogue to load an image (in this case, the survey image from DM)
image=hs.load()
```

In [ ]:
```
#this will plot the results inside the notebook (handy for offline work or to keep re
%matplotlib inline
```

In [ ]:
```
image.plot()
```

In [ ]:
```
# The path contaning the directories is defined and the low loss and core loss image:

path = r"C:\Users\Guanze He\OneDrive - Nexus365\Documents\Data\ARM\20190727 B88-1 EEL
import os
os.chdir(path)
ll = hs.load("EELS spectrum image zlp.dm3")
cl = hs.load("EELS spectrum image O.dm3")
cl2 = hs.load("EELS spectrum image Zr.dm3")
#cl3 = hs.load("EELS Spectrum Image.dm3")
```

In [ ]:
```
#The low loss image is aligned for energy and the same correction applied to all the
#alpha and beta angles are added to core loss image for further calculations

ll.align_zero_loss_peak(calibrate=True, also_align=[cl,cl2])
cl.set_microscope_parameters(200, convergence_angle=31.48, collection_angle=41.0)
cl2.set_microscope_parameters(200, convergence_angle=31.48, collection_angle=41.0)
#cl3.set_microscope_parameters(200, convergence_angle=31.48, collection_angle=41.0)
```

In [ ]:
```
cl.plot()
```

In [ ]:
```
#This command will remove spikes (X-rays) from the datasets (it helps with PCA)
cl.spikes_removal_tool()
```

In [ ]:
```
#Now spike removal for cl2
cl2.plot()
```

In [ ]:
```
cl2.spikes_removal_tool()
```

In [ ]:
```
#Now that the data is energy aligned and spikes free, it can be saved
```

In [ ]:
```
#If we want to save the data in another folder, we specify it here
path = r"C:\Users\Guanze He\OneDrive - Nexus365\Documents\Data\ARM\20190727 B88-1 EEL

os.chdir(path)
```

In [ ]:
```
ll.save("zlp aligned.rpl")
cl.save("Core loss aligned O.rpl")
cl2.save("Core loss aligned Zr.rpl")
#cl3.save("Core loss aligned 3.rpl")
```

In [ ]:
```

```

In [ ]:
```
#PCA
```

In [ ]:
```
cl.print_summary_statistics()
```

In [ ]:
```
#If negative values found in cl, find the minimum e.g. -85, and add it to all pixels
cl=cl+
```

In [ ]:
```
#If decomposition, pca, etc is necessary, do the next steps
#This is to perform PCA with Poissonian normalization (recommended for EELS data)
cl.decomposition(normalize_poissonian_noise=True)
#cl2.decomposition(normalize_poissonian_noise=True)
#cl3.decomposition(normalize_poissonian_noise=True)
```

In [ ]:
```
#to plot the PCA results
cl.plot_decomposition_results()
```

In [ ]:
```
#To create a denoised dataset with a given number of components (chosen after examin
#sc=cl.get_decomposition_model(12)
sc=cl.get_decomposition_model(components=[0,1,2,3,4])
```

In [ ]:
```
sc.plot()
```

In [ ]:
```
path = r"C:\Users\Guanze\Desktop\20180812 B56-1\EELS\Region 2\hyperspy"

os.chdir(path)
```

In [ ]:
```
sc.save("Core loss O reconstructed.rpl")

```

In [ ]:
```

```

In [ ]:
```
cl2.print_summary_statistics()
```

In [ ]:
```
cl2=cl2+17
```

In [ ]:
```
cl2.decomposition(normalize_poissonian_noise=True)
```

In [ ]:
```
cl2.plot_decomposition_results()
```

In [ ]:
```
#sc2=cl2.get_decomposition_model(11)
sc2=cl2.get_decomposition_model(components=[0,1,2])
```

In [ ]:
```
sc2.plot()
```

In [ ]:
```
path = r"C:\Users\Guanze\Desktop\20180812 B56-1\EELS\Region 2\hyperspy"

os.chdir(path)
```

In [ ]:
```
sc2.save("Core loss reconstructed Zr.rpl")
```

In [ ]:
```
1
```

In [ ]:
```
1 #ICA
```

In [ ]:
```
1 cl.blind_source_separation(4)
```

In [ ]:
```
1 cl.plot_bss_results()
```

In [ ]:
```
1 #If we want to save the data in another folder, we specify it here
2 path = r"C:\Users\Guanze He\OneDrive - Nexus365\Documents\Data\ARM\20190727 B88-1 EEl
3
4 os.chdir(path)
```

In [ ]:
```
1 cl.export_bss_results(loading_format='tif', factor_format='msa')
```

In [ ]:
```
1 cl.export_bss_results(loading_format='jpg')
```

In [ ]:
```
1
```

In [ ]:
```
1 cl2.blind_source_separation(4)
```

In [ ]:
```
1 cl2.plot_bss_results()
```

In [ ]:
```
1 #If we want to save the data in another folder, we specify it here
2 #Need to save to two different folders for two sets of BSS result
3 path = r"C:\Users\Guanze\OneDrive - Nexus365\Documents\Data\ARM\20190726 B88-1\EELS\I
4
5 os.chdir(path)
```

In [ ]:
```
1 cl2.export_bss_results(loading_format='tif', factor_format='msa')
```

In [ ]:
```
1 cl2.export_bss_results(loading_format='jpg')
```

In [ ]:
```
1
```

In [ ]:
```
1 # Let's see if there is any info in the low-loss region
```

In [ ]:
```
1 ll1=ll.isig[5.0:]
```

In [ ]:
```
1 ll1.print_summary_statistics()
```

In [ ]:
```
1 ll1=ll1+115
```

In [ ]:
```
1 ll1.plot()
```

In [ ]:
```
1 path = r"C:\Users\Guanze\OneDrive - Nexus365\Documents\Data\ARM\20190726 B88-1\EELS\I
2
3 os.chdir(path)
```

In [ ]:
```
1 ll1.spikes_removal_tool()
```

In [ ]:
```
ll1.decomposition(normalize_poissonian_noise=True)
```

In [ ]:
```
ll1.plot_decomposition_results()
```

In [ ]:
```
sc0=ll1.get_decomposition_model(components=[0,1,2,3,4,5,10,11,12,13])
```

In [ ]:
```
sc0.save("Zero loss free.rpl")
```

In [ ]:
```
ll1.blind_source_separation(5)
```

In [ ]:
```
ll1.plot_bss_results()
```

In [ ]:
```
path = r"C:\Users\Guanze\OneDrive - Nexus365\Documents\Data\ARM\20190726 B88-1\EELS\I

os.chdir(path)
```

In [ ]:
```
ll1.export_bss_results(loading_format='tif', factor_format='msa')
```

In [ ]:
```
ll1.export_bss_results(loading_format='jpg')
```

In [ ]:
```
#SI crop
#to crop the spectrum image in two dimension
#0:100 from pixel 0 to 100
#0:100.0 from 0 to 100nm
#also work if the unit in SI image is in um, 0:0.1
```

Curve fitting for quantification

In [ ]:
```
hs.preferences.gui()
```

In [ ]:
```
sc.add_elements(('O','Fe'))
```

In [ ]:
```
sc.estimate_poissonian_noise_variance()
```

In [ ]:
```
#del m
```

In [ ]:
```
m=sc.create_model(ll=sczlp)
```

In [ ]:
```
m.components
```

In [ ]:
```
#run this after getting a fitting result from smart fit/mpfit
#m.enable_fine_structure()
m.disable_fine_structure()
```

In [ ]:
```
m.plot()
```

In [ ]:
```
m.fit(fitter="mpfit", bounded=True)
```

In [ ]:
```
m.gui()
```

In [ ]:
```
m.fit(fitter="mpfit", bounded=True)
```

In [ ]:
```

```

In [ ]:
```
sc2.add_elements(('Zr','Nb'))
```

In [ ]:
```
sc2.estimate_poissonian_noise_variance()
```

In [ ]:
```
#del m2
```

In [ ]:
```
m2=sc2_cropped.create_model(ll=sczlp)
```

In [ ]:
```
m2.components
```

In [ ]:
```
#run this after getting a fitting result from smart fit/mpfit
#m.enable_fine_structure()
m2.disable_fine_structure()

```

In [ ]:
```
m2.plot()
```

In [ ]:
```
#m2.smart_fit()
```

In [ ]:
```
#m2.enable_fine_structure()
```

In [ ]:
```
m2.fit(fitter="mpfit", bounded=True)
```

In [ ]:
```
m2.gui()
```

In [ ]:
```
components = hs.model.components1D

#GNbL2 = hs.model.components1D.Gaussian()
#GNbL2.name = "Nb L2 White Line"
GNbL3 = hs.model.components1D.Gaussian()
GNbL3.name = "Nb L3 White Line"
GZrL2 = hs.model.components1D.Gaussian()
GZrL2.name = "Zr L2 White Line"
GZrL3 = hs.model.components1D.Gaussian()
GZrL3.name = "Zr L3 White Line"


m2.append(GZrL2)
m2.append(GZrL3)
#m2.append(GNbL2)
m2.append(GNbL3)


GZrL2.centre.bmin = 2316.0

GZrL2.centre.bmax = 2321.0


GZrL3.centre.bmin = 2231.0

GZrL3.centre.bmax = 2235.0


GNbL3.centre.bmin = 2379.0

GNbL3.centre.bmax = 2384.0


m2.components
```

In [ ]:
```
#m2.smart_fit()
```

In [ ]:
```
m2.fit(fitter="mpfit", bounded=True)
```

In [ ]:
```
import numpy as np
```

In [ ]:
```
thevalue=np.nanmean(m2.red_chisq.data)
```

In [ ]:
```
sc2_cropped.estimate_poissonian_noise_variance(gain_factor=thevalue)
```

In [ ]:
```
m2.red_chisq.plot()
```

In [ ]:
```
sc2_cropped.metadata.Signal.Noise_properties.variance.data+=1
```

In [ ]:
```
 m2.multifit(fitter="mpfit", bounded=True)
```

In [ ]:
```
del samf
```

In [ ]:
```
samf = m2.create_samfire(workers=None, ipyparallel=False)
```

In [ ]:
```
samf.metadata.goodness_test.tolerance = 1000
```

In [ ]:
```
samf.strategies
```

In [ ]:
```
samf.strategies.remove(1)
```

In [ ]:
```
samf.strategies
```

In [ ]:
```
samf.refresh_database()
```

In [ ]:
```
m2.plot()
```

In [ ]:
```
#m2.smart_fit()
```

In [ ]:
```
m2.fit(fitter="mpfit", bounded=True)
```

In [ ]:
```
samf.plot()
```

In [ ]:
```
samf.start(fitter='mpfit', bounded=True)
```

In [ ]:
```
ZrL3_centre = GZrL3.centre.as_signal()
#ZrL2_centre = GZrL2.centre.as_signal()
NbL3_centre = GNbL3.centre.as_signal()

ZrL3_centre.plot(cmap='RdYlBu_r',vmin=2231.0,vmax=2236.0)
#ZrL2_centre.plot(cmap='RdYlBu_r',vmin=2316.0,vmax=2321.0)
NbL3_centre.plot(cmap='RdYlBu_r',vmin=2379.0,vmax=2384.0)
```

In [ ]:

```
#Move the cursor to the point to quantify
m.quantify() #the oxide model/dataset
m2.quantify() #the Zr dataset
import math

O_signal = m.components.O_K.intensity.value
Fe_signal = m.components.Fe_L3.intensity.value

Zr_signal = m2.components.Zr_L3.intensity.value
Nb_signal = m2.components.Nb_L3.intensity.value

#'value' is for a single spectrum, 'signal' is for multiple spectra for the whole ma

O_std = m.components.O_K.intensity.std
Fe_std = m.components.Fe_L3.intensity.std
Zr_std = m2.components.Zr_L3.intensity.std
Nb_std = m2.components.Nb_L3.intensity.std


O_at =(O_signal/(O_signal+Fe_signal+Zr_signal+Nb_signal)*100)
Fe_at =(Fe_signal/(O_signal+Fe_signal+Zr_signal+Nb_signal)*100)
Zr_at = (Zr_signal/(O_signal+Fe_signal+Zr_signal+Nb_signal)*100)
Nb_at = (Nb_signal/(O_signal+Fe_signal+Zr_signal+Nb_signal)*100)


#Errors in the fitting

O_at_std = O_at*O_std/O_signal
Fe_at_std = Fe_at*Fe_std/Fe_signal
Zr_at_std = Zr_at*Zr_std/Zr_signal
Nb_at_std = Nb_at*Nb_std/Nb_signal

#Relative errors including cross section
O_total_std = O_at*math.sqrt(0.1**2+(O_std/O_signal)**2)
Fe_total_std = Fe_at*math.sqrt(0.1**2+(O_std/Fe_signal)**2)
Zr_total_std = Zr_at*math.sqrt(0.1**2+(Zr_std/Zr_signal)**2)
Nb_total_std = Nb_at*math.sqrt(0.1**2+(Nb_std/Zr_signal)**2)


#print("\nRelative quantification:\nO %at = ",round(O_at,2),"\xb1",round(O_at_std,1),
#Now including the 10% relative error of the cross section
#print("\nRelative quantification with cross-section errors:\nO %at = ",round(O_at,1,
```

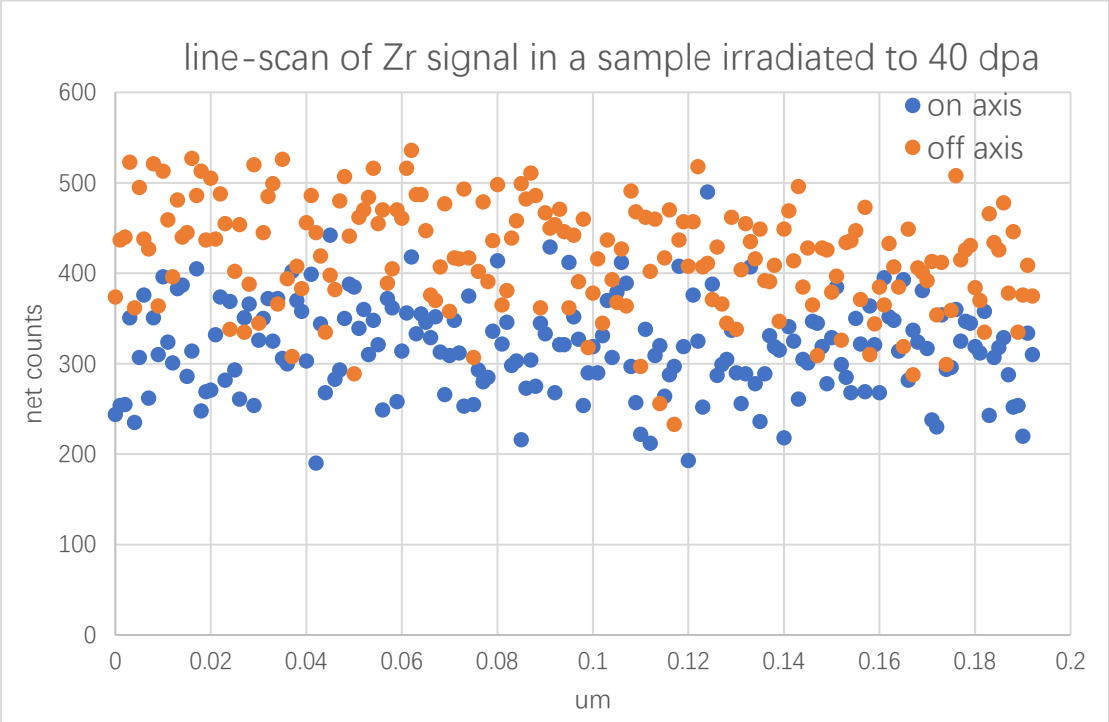
In [ ]:

```
1
```

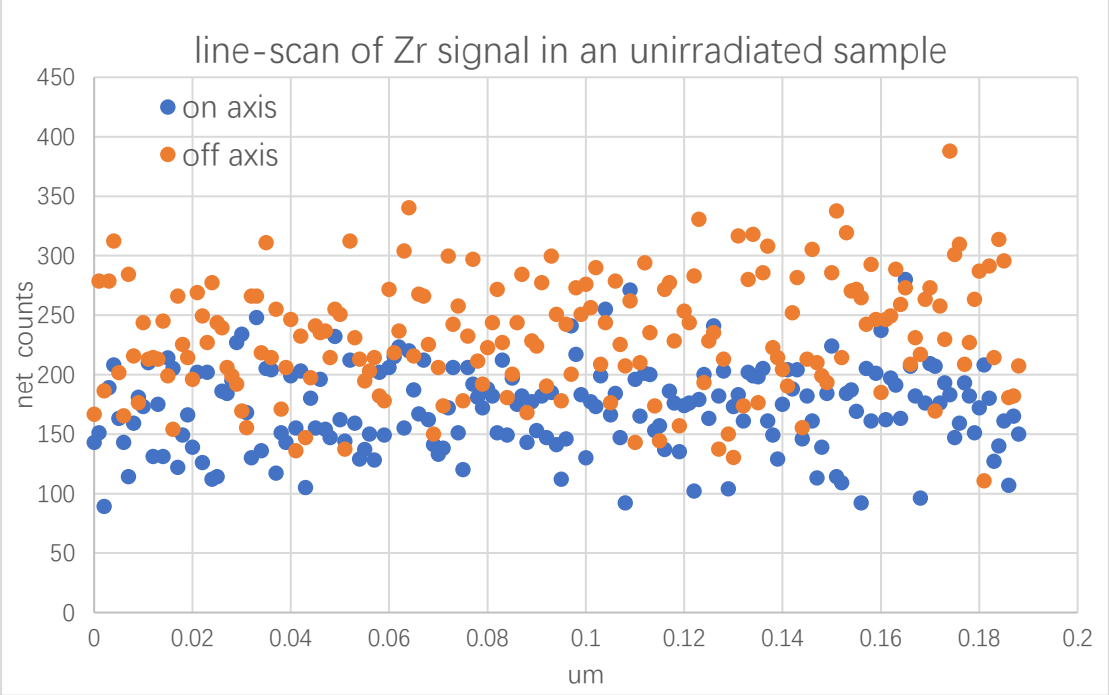
Appendix B

In order to evaluate how the radiation-induced disorder affected the channelling in our EDX measurements (always carried out with the sample in a low-index zone-axis), we have carried out an experiment to compare the channelling effect in irradiated and unirradiated samples. The irradiated sample is the sample d in this study, which has faced the highest damage (38.8 dpa) by heavy ion. The unirradiated sample is of the same material. The same zone axis, $[10\bar{1}0]$, was used to acquire a line-scan in both samples. Then the samples were tilted 4º away from the zone axis, and a second line-scan was acquired on the same region. Similar to the protocols described in section 2.3, all the parameters used in taking the line-scans were kept the same for each scan. The net Zr counts were compared between these two line-scans to illustrate the channelling effect. The figures below show the Zr net counts line-scan profiles from on and off axis EDX scanning on irradiated and unirradiated samples. The difference in net counts between samples is caused by differences in local thicknesses and relative position in the holder respect to the EDX detector.

As shown in the table below, the signal intensity change (ratio) between on-axis and off-axis scans in the irradiated and unirradiated samples is negligible within error, suggesting that the radiation induced disorder is not affecting the results and our comparison between irradiated and unirradiated samples is reasonable.



(a)



(b)

Figure 1 Net Zr counts when EDX line-scans were taken in the same place in (a) irradiated sample, (b) unirradiated sample.

Table 1 Average net counts of Zr in different case. The errors of the measured counts

are standard deviation of all the data points, and the errors of the ratio is calculated by error transfer function.

	Irradiated	Unirradiated
On axis counts	318 ± 51	171 ± 36
Off axis counts	420 ± 59	233 ± 49
On/off ratio	0.76 ± 0.16	0.74 ± 0.22